ISSN en trámite

Geofísica Internacional

Revista Trimestral Publicada por el Instituto de Geofísica de la Universidad Nacional Autónoma de México

México
Volume 51 Number 1
January - March
2012

— Geofísica Internacional —

GEOFÍSICA INTERNACIONAL, Año 51, Vol. 51, Núm. 1, enero - marzo de 2012 es una publicación trimestral, editada por la Universidad Nacional Autónoma de México, Ciudad Universitaria, Alcaldía Coyoacán, C.P. 04150, Ciudad de México, a través del Instituto de Geofísica, Circuito de la Investigación Científica s/n, Ciudad Universitaria, Alcaldía Coyoacán, C.P. 04150, Ciudad de México, Tel. (55)56 22 41 15. URL: http://revistagi.geofisica.unam.mx, correo electrónico: revistagi@igeofisica.unam.mx. Editora responsable: Andrea Rostan Robledo. Certificado de Reserva de Derechos al uso Exclusivo del Título: 04-2022-081610251200-102, ISSN: en trámite, otorgados por el Instituto Nacional del Derecho de Autor (INDAUTOR). Responsable de la última actualización Saúl Armendáriz Sánchez, Editor Técnico. Fecha de la última modificación: 31 de diciembre 2011, Circuito de la Investigación Científica s/n, Ciudad Universitaria, Alcaldía Coyoacán, C.P. 04150, Ciudad de México.

Geofísica Internacional

Vol. 51, Núm. 1, enero-marzo de 2012

Contents

Geofísica
Internacional

Precursors to eruptions of Popocatépetl Volcano, Mexico.
Ana Lillian Martin Del Pozzo

Geofísica Internacional (2012) 51-1: 5-15

Original paper

Estimation of soil petrophysical parameters based on electrical resistivity values obtained from lab and in-field measurements

Omar Delgado Rodríguez*, María Ladrón de Guevara Torres, Vladimir Shevnin and Albert Ryjov

Received: January 20, 2010; accepted: October 13, 2011; published on line: December 16, 2011

Resumen

El conocimiento de los parámetros petrofísicos del suelo es muy útil para la agricultura y análisis de impacto ambiental. Por lo tanto, es importante desarrollar técnicas y metodologías que ayuden a obtener mapas petrofísicos del suelo de manera rápida y económica. Este trabajo muestra dos técnicas para la estimación del contenido de arcilla, porosidad y capacidad de intercambio catiónico a partir de mediciones eléctricas. La primera, basada en mediciones de resistividad del suelo (SRM) realizadas en laboratorio; la segunda técnica, ERT&WRM, mediante la aplicación de Tomografía de Resistividad Eléctrica (ERT) y mediciones en campo de resistividad en muestras de agua subterránea (WRM). Se realizó un estudio geoeléctrico en un sitio areno-limoso y los resultados alcanzados fueron comparado con los obtenidos mediante la técnica de análisis textural de Bouyoucos. La técnica SRM mostró ser más precisa y menos productiva que la técnica ERT&WRM. Los resultados obtenidos proponen una nueva aplicación de los métodos geoeléctricos en estudios de agricultura precisa, tanto para análisis de muestras de suelo en laboratorio utilizando la técnica SRM como para evaluar grandes extensiones de suelo agrícola utilizando la técnica ERT&WRM.

Palabras clave: tomografía de resistividad eléctrica, modelación petrofísica, contenido de arcilla, porosidad, CIC.

Abstract

Knowledge of soil petrophysical parameters is very useful for agricultural and environmental impact analysis. Therefore, it is important to develop techniques and methodologies to help obtain soil petrophysical maps both quickly and inexpensively. This paper shows two techniques for estimating clay content, porosity and cation exchange capacity from electrical measurements. The first one, based on soil resistivity measurements (SRM), is performed in the laboratory. The second technique, ERT&WRM, uses the Electrical Resistivity Tomography (ERT) and groundwater resistivity measurements (WRM) in the field. A geoelectrical study was carried out in a sandy-loam site and the results were compared to those determined by particle size analysis using the Bouyoucos technique for textural analysis. The SRM technique was more accurate but slower than the ERT&WRM technique. The obtained results suggest a new application of geoelectrical methods for precision farming, both for analysis of soil samples in the laboratory using SRM technique and to evaluate large tracts of agricultural land using ERT&WRM technique.

Key words: electrical resistivity tomography, petrophysical modeling, clay content, porosity, CEC.

O. Delgado Rodríguez*
Instituto Mexicano del Petróleo
Eje Central Lázaro Cárdenas 152
07730, México D.F.
*Corresponding author: odelgado@imp.mx

Ma. Ladrón de Guevara Torres
Instituto Politécnico Nacional
Centro Interdisciplinario de Investigación
para el Desarrollo Integral Regional - CIIDIR
Unidad Oaxaca, México

V. Shevnin
Moscow State University
Faculty of Geology
Moscow, Russia

A. Ryjov
Moscow State Geological Prospecting Academy
Geophysical Faculty
Moscow, Russia

Introduction

Usually, the planting and harvesting of diverse agricultural products involve large tracts of land. On the other hand, cultivation practice has always indicated that there are differences among nearby parcels, reflecting in the productivity of crops.

In several countries (e.g., USA, France, Germany) many techniques are used in carrying out research in order to determine the main soil parameters and their temporal variations; this procedure is known as Precision Farming (PF). The results of PF are used to exploit the farm soils in a more efficient way, allowing an increase of crops without using chemical fertilizers and pesticides, thus reducing the environmental impacts on agricultural activity (Robert, 2002).

PF has a great challenge: the study and mapping of soil parameters as rapidly and accurately as possible. Geophysical methods, specifically electrical and electromagnetic methods, are effective, quick, and inexpensive for the implementation of PF process (Sudduth *et al.*, 2000) in the determination of the boundaries among genetic types of soils (Pascual *et al.*, 1995), and changes in the degree of salinization (Williams and Baker, 1982) or moisture (McKenzie *et al.*, 1989).

A new technology has been developed by the Mexican Petroleum Institute (Shevnin *et al.*, 2006, 2007) based on electrical measurements made in both the laboratory and the field, that allows the determination of clay content, porosity and Cation Exchange Capacity (CEC). Soil samples taken at different study depths are subjected to electrical measurements in the lab to determine their petrophysical parameters, while the resistivity values calculated by the Electrical Resistivity Tomography (ERT) method, and groundwater salinity obtained in field, enabling the determination of petrophysical sections and maps for the entire study site. This inversion process starts with an initial model that includes previous information of the petrophysical parameters, which could be supplied from electrical measurements performed in the lab using soil samples collected from the site.

This paper describes two techniques for the estimation of clay content, porosity and CEC both from electrical measurements made in soil samples in the lab and from the resistivity values obtained with the implementation of ERT method in field. As a practical example, we present the results achieved at a site located in Oaxaca, Mexico.

Materials and methods

Water resistivity measurements (WRM)

The field procedure for performing the WRM is very simple: once the sampling point (e.g. pit or well) is identified a water sample is collected. Afterwards, by using a combo portable resistivity meter (e.g., Hanna HI98130) the readings of water conductivity (σ), in mS/cm, and temperature, in °C are taken. Conductivity values, σ, in mS/cm are converted to electrical resistivity values, ρ_w, in Ohm.m by:

$$\rho_w \text{ (Ohm.m)} = 10^* (1/\sigma \text{ (mS/cm)}) \quad (1)$$

Using a GPS, the UTM coordinates of the sampling point must be taken for graphical representation. Subsequently, the values are corrected at a reference temperature of 20°C by the expression (Sorensen and Glass, 1987).

$$\rho_{w20} = \rho_w(T) [1 + \alpha (T - T_0)] \quad (2)$$

Where:

T = water temperature (°C)

α = temperature coefficient equal to 0.0177 1/°C (Beklemishev, 1963)

T_0 = reference temperature equal 20°C

ρ_w = water resistivity measured in field (Ohm.m)

ρ_{w20} = water resistivity corrected at 20°C (Ohm.m)

The temperature 20°C is selected for being the reference value in the process of petrophysical modeling.

Taking into account the linear function (logarithmic scale) of water resistivity versus salinity, for a reference temperature equal to 20°C, it is possible, for salinities below 10 gl^{-1}, to estimate the water salinity from water electrical resistivity using the relation:

$$C = 6 / \rho_{w20} \quad (3)$$

Where C is the salt content (NaCl equivalent) in gl^{-1}.

The C value will be used in the process for determining petrophysical parameters.

Electrical Resistivity Tomography (ERT) method

The Vertical Electrical Sounding method, worldwide known since the beginning of the 1920's, was created by the Schlumberger brothers in France. They made a design using four electrodes (two for electric current injection and the other two for measuring potential difference). By increasing the distance between current electrodes, the study depth will increase as well (Keller and Frischknecht, 1966). Technically the method is very simple; it is currently used primarily for near surface studies. In 1990, a new stage in the development of this method began with the emergence of technology called Electrical Resistivity Tomography (ERT) or resistivity imaging. Such profile measurements allow two-dimensional interpretation, using software such as Res2DInv (Loke and Barker, 1996a, b). This two-dimensional interpretation has several good features making the interpretation results suitable for a good visualization. The resulting model has the same number of layers with same thicknesses along each profile (Figure 1), giving great advantage for processing and mapping of interpreted data.

The results obtained from ERT method are interpreted resistivity sections and maps (correlation of different profiles). Cross-sections have less interpolation between measuring points than maps. For map construction interpolation between profiles is needed. However, maps have less resistivity interval than sections (electrical properties vary more with depth than in horizontal direction). As a result we have higher resolution in maps (horizontal behavior of soil resistivity), leading us to locate weaker anomalies.

Soil Resistivity Measurements (SRM) at lab.

Ryjov and Sudoplatov (1990) presented a model that includes components of unconsolidated formations and electrochemical resistivity estimation of free water and water in the pores of the formation, resulting in the estimation of the rock resistivity. In this theoretical model solid grains of sand and clay make up an insulating skeleton where their capillaries are seen as hollow cylinders with different radii. The sand component contains a porous system of cylindrical channels (so-called wide pores) with radii rangind between 10^{-3} and 10^{-4} m, which are much larger than the thickness of the electrical double layer The micropores of the clay component are very narrow, and their average radii lie between 10^{-7} and 10^{-8} m, which is close to the thickness of the electrical double layer. The thickness of the electrical double layer depends on the water salinity and increases with decreasing salt concentration. At near-surface conditions, when the salt concentration changes from 0.02 to 2 gl^{-1}, the thickness of the electrical double layer varies in the range of $0.3 - 3 \times 10^{-8}$ m. The total volume of pores for sand and clay is taken into account separately by means of the

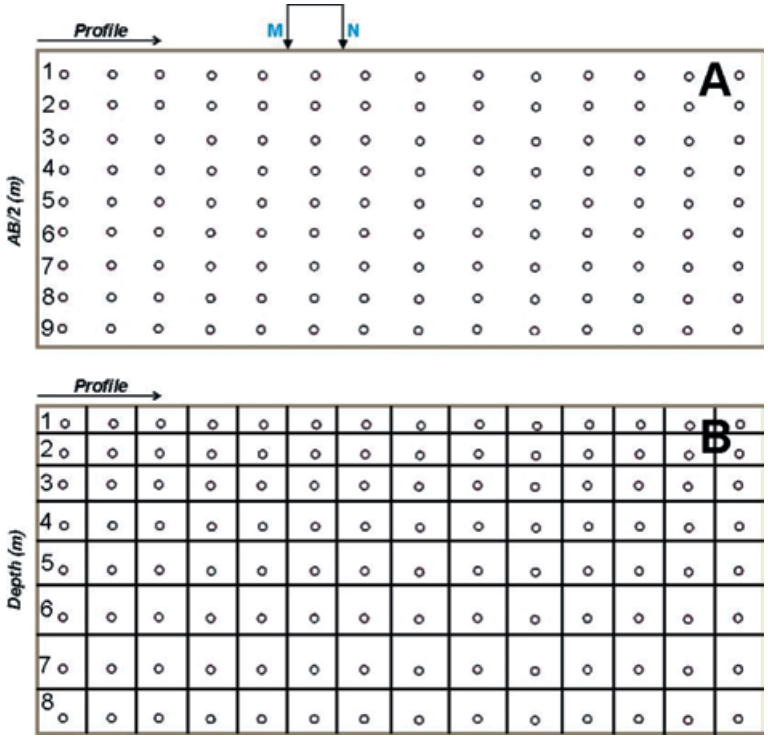

Figure 1. Presentation of measured and interpreted resistivity values for an ERT profile. (A) Cross-section of measured values (r_a). Numbers on vertical axis of the cross-section (A) indicate the current electrodes spacing numbers. (B) Interpreted resistivity (r) cross-section after inversion using software RES2DINV. Numbers on vertical axis of the cross-section (B) show the interpreted layers.

value of its porosity, so the model of the mixture consists of two types of capillaries with different radii (Shevnin *et al.*, 2007).

The capillaries of sand and clay can be connected in series, parallel or a combination of both connections. In nature, the combination of both parallel and series capillaries is generally observed, because some part of the clay is usually smeared on pore walls of the sand fraction, and some clay exists in the sand pores as plugs. The parallel and series connections of the conductive component were considered in the resistivity models developed by Wyllie and Southwick (1954) and Bussian (1983). To include the influence of the pore microstructure in the model, we have taken into account the tortuosity of the sand pores as a function of the content of solid sand grains in the mixture. Therefore considering this model it is possible to generate theoretical curves of electrical resistivity behavior from any soil consisting of sand and clay (in any proportion), according to the pore water salinity, based on the variation of the petrophysical parameters: clay content, porosity, and CEC.

Based on the need to obtain resistivity measurements versus pore water mineralization, a methodology was developed to calculate the petrophysical parameters; including a procedure for preparation of unconsolidated sediment sample and another procedure for experimental electrical measurements in the lab.

Once the in-field sample is collected, it is subjected to a drying and homogenization process, stirring well the soil sample. Afterwards, five resistivity boxes are filled with this homogenized sample, where salinized water is added (different for each resistivity box in the interval 0.1 to 80 gl^{-1}) until the sample is fully saturated. These resistivity boxes are connected to any resistivity equipment (ERA, Saris, SYSCAL, etc.). Two potential measuring electrodes (M and N) are placed along one of the long sides for obtaining voltage measurements, which are recorded in the resistivity meter (Figure 2). A current electrode (A and B, Figure 2) is placed in each of the shorter side to inject current to soil sample.

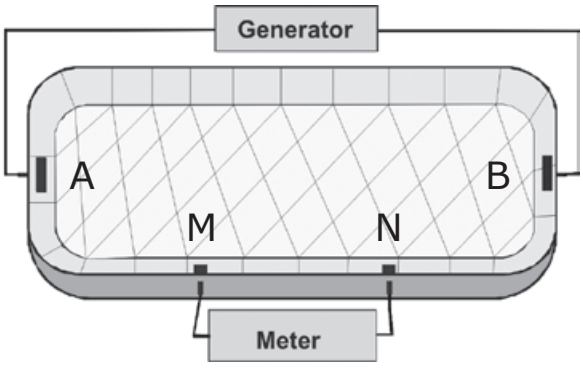

Figure 2. Resistivity box used to apply the SRM technique.

Potential electrodes M and N are connected to the meter, and electrodes A and B are connected to the generator. The current (I) is injected to the resistivity box through electrodes A and B (Figure 2). The meter shows a value corresponding to the potential difference (ΔU) between electrodes M and N.

The electrical resistivity value is determined by:

$$\rho_s(T) = K * \Delta U / I \qquad (4)$$

Where:

K = calibration coefficient of the resistivity box (m)

ΔU = potential difference value (mV)

I = electric current injected by generator (mA)

$\rho_s(T)$ = resistivity (Ohm.m) of the soil sample at room temperature T.

To calculate the calibration coefficient (K), each resistivity box is filled with water of known salinity (and resistivity) and electrical resistivity measurements (ΔU and I values) at controlled temperature are performed. Using the equation (4), K value is determined.

The soil resistivity value obtained in this way depends on temperature, so it is necessary to measure the temperature of the sample in each resistivity box in order to determine its correction. To correct the measurements to a reference temperature of 20°C the expression (2) is used.

At the end of this procedure five values of soil electrical resistivity (ρ_s) are obtained for each resistivity box depending on the pore water salinity (C), creating a database which is used in an iterative inversion process, to estimate the petrophysical parameters. Iterative inversion is a process of minimizing the error among the electric resistivity values, obtained by using the theoretical model described above, and the experimental data measured in the lab. The reduction of the error is performed by using the software *PetroWin* developed by A. Ryjov (Ryjov and Sudoplatov, 1990; Ryjov and Shevnin, 2002). Using software *PetroWin,* the modification

of different petrophysical parameters, such as the CEC of the clay, capillary radius of sand and clay, porosity of clay and sand, from the theoretical model is performed, resulting in the theoretical resistivity function. Software *Petrowin* works is several steps: first, calculation of water resistivity, taking into account types of ions in solution (cations and anions), their mobility and concentration, then, calculation of conductivity in electrical double layer (between water and solid phase) taking into account properties of solution and solid phase (CEC value is zero for sand and maximal for clay), after, calculation of rock resistivity taking into account rock porosity, pore size, humidity and clay content and, after that, software can calculate resistivity for different positions of clay in pores (as corks in capillary paths and as thin layers at capillary wall). Finally, calculation of clay content, porosity and CEC values for the soil sample (Shevnin *et al.*, 2007).

Estimation of the petrophysical parameters from resistivity measurements obtained by ERT and WRM.

If we use the interpreted soil resistivity values obtained by ERT and groundwater salinity values calculated by WRM, instead of a curve of resistivity versus salinity for a soil sample from electrical measurements made in laboratory, it is then possible to determine, for each ERT profile, petrophysical parameter sections for clay content, porosity and CEC. This procedure uses the same petrophysical modeling algorithm and can convert resistivity maps (for any geoelectrical layer) into petrophysical maps (Delgado-Rodríguez *et al.*, 2006). It is necessary to have an initial model based on the results of the SRM method obtained for some soil samples collected at the site.

Textural analysis of Bouyoucos

The knowledge of soil texture is important because it affects the soil fertility and determines the rate of consumption and storage of water in soil. The relative proportion of sand, silt and clay in a soil may be used to determine a textural type following the Bouyoucos procedure (Bouyoucos, 1936).

The determination is fast and approximate, separating aggregates, and analyzing particles. A measured time is chosen for the separation of larger particles and another one for small ones. As a general rule, after 40 s the sand particles (diameter greater than 0.005 mm) settle at the bottom of the hydrometer, while silt particles (diameter greater than 0.002 mm) need 2 h. In the case of the clay, it requires up to 24 h for a precise calculation of settled particles. Knowing the length of the hydrometer we can calculate the velocity of the particles and their diameters and, thus, determine the sand, silt and clay contents.

Results and discussion

Practical example

The site is located in the plain of the Atoyac River, on the outskirts of the Oaxaca City, Oax., sothern Mexico, showing a dry and sandy-loam soil.

Through in-field application of ERT and WRM methods, a section of the clay content, porosity and CEC is obtained for each profile. On this same transect, samples at different depths are taken to obtain in the lab the petrophysical parameters using the SRM method. The clay content estimation obtained through both ways is compared among them, and also checked against the values of the petrophysical parameters obtained in the laboratory for the same soil samples by using Bouyoucos technique.

Application of WRM

A groundwater sample was collected from a well located a few meters away from the site. Using a portable resistivimeter Hanna HI98130 and applying equation (1), a groundwater resistivity value of 3.2 Ohm.m was obtained, corresponding, according to the equation (3), to a salinity value of 1.9 gl^{-1}. The depth of the water table was 10.3 m, which, along with the sandy texture of the soil (high permeability), explains its low moisture. The calculated salinity value was used in the petrophysical modeling process (software *PetroWin*) for determining the soil petrophysical parameters.

Application of ERT

ERT measurements were carried out along four profiles (P1 to P4), each 50 m long. At each ERT survey, five measurements were performed for spacings of the current electrodes AB/2 = 0.5, 1, 1.5, 2, 2.5 and 3 m, assuring a study depth of 1.5 m. The distance between the VES survey was 5 m. The distance between the profiles P2, P3 and P4 was 5 m, while between profiles P1 and P2 the separation started around 5 m at X = 0 m and reached a maximal separation of 7.5 m at X = 50 m. Each profile has 11 VES points, so the total number of measurement points was 44.

The ERT profiles were subjected to a two-dimensional inversion process using software Res2DInv (Loke and Barker, 1996a). Figure 3 shows the inverted sections for profiles P1 and P2. In general, there are high values of resistivity (ρ > 100 Ohm.m) in two sections (Figure 3) indicating not only the low soil moisture in situ,

but also it a low clay content. Probably the clay content is higher in the relatively conductive layer observed in both sections between 0.7 m and 1.2 m of depth.

Application of SRM

Fourteen soil samples were collected at different depths (Table 1) along profiles P1 and P2 taking into account the geoelectric sections (Figure 3). Soil samples were analyzed in lab applying respectively Bouyoucos and SRM methods.

The content of sand, clay and silt was determined for each soil sample through the application of Bouyoucos method. The obtained results were placed in the textural triangle (Figure 4), noting the predominance of the sandy loam and loamy sand soils in the study area.

Table 1 shows the clay content determined by both methods, showing a strong similarity between them.

The graph in Figure 5 shows the good correspondence between clay content quantity estimated by both techniques (Bouyoucos and SRM) based on linear regression analysis. The linear equation is close to the identity function (Y = X), with a low dispersion (coefficient of determination, R^2, equal to 0.93).

Sample	Clay content (%) Bouyoucos	Clay content (%) SRM	Sampling depth (m)
1	10	10	0.25
2	13	11	1.00
3	4	4	0.25
4	11	11	1.00
5	6	6	0.25
6	14	13	1.00
7	6	6	0.25
8	13	13	1.00
9	5	5	0.25
10	14	13	1.00
11	4	4	0.25
12	15	14	1.00
13	6	6	0.20
14	17	12	1.00

Table 1. Clay content values obtained by Bouyoucos and SRM techniques.

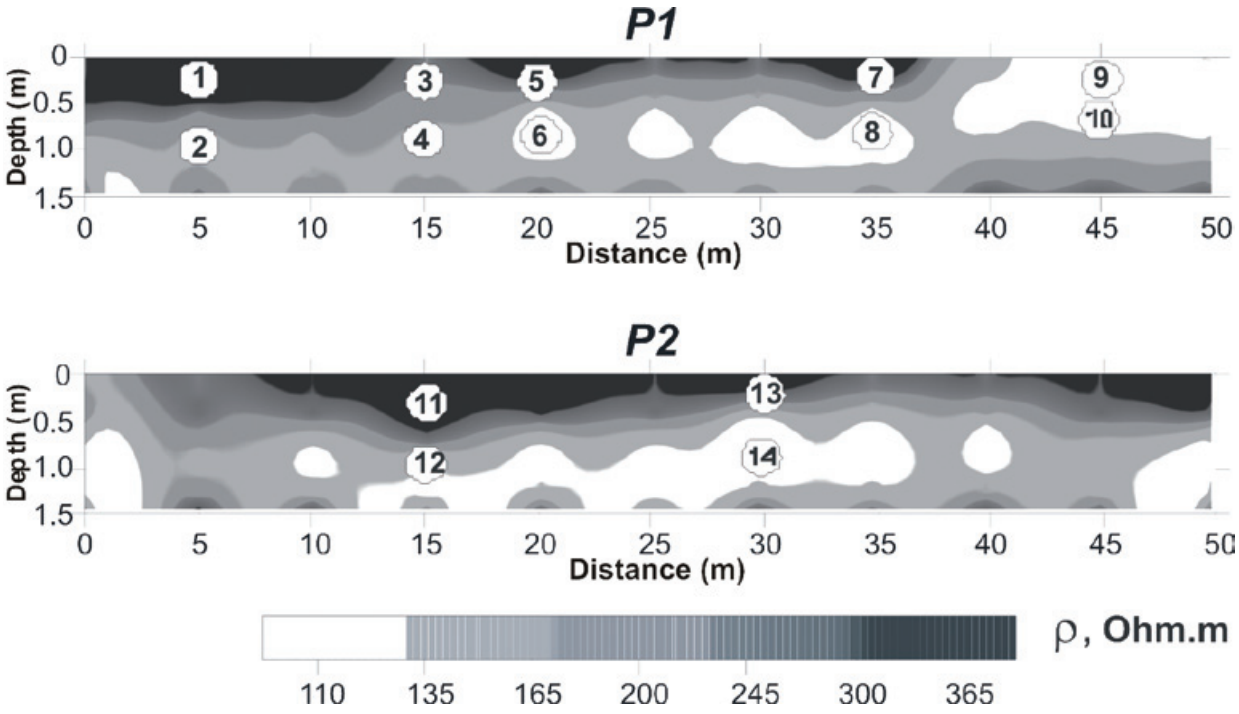

Figure 3. Resistivity sections obtained for P1 and P2 profiles. White circles indicate the location of the 14 soil samples.

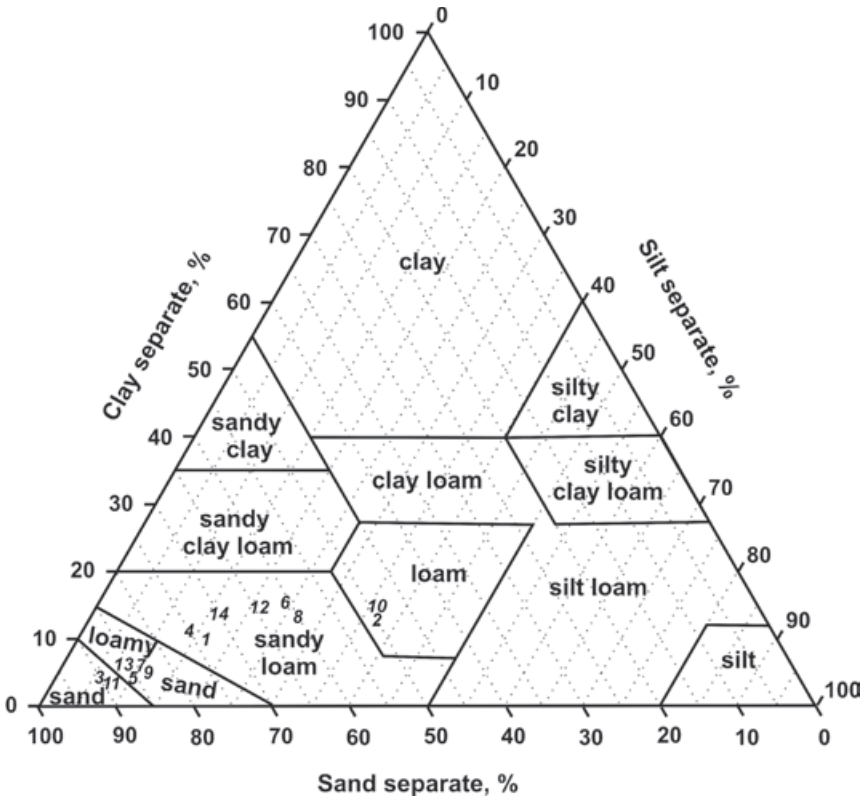

Figure 4. Triangle with the textural classification of the 14 soil samples, noting the prevalence (10 samples) of sandy-loam and loamy-sand soils in the study area.

Determination of petrophysical sections

Geoelectrical sections were converted to petrophysical parameters sections using software *PetroWin*, taking into account the salinity of groundwater and estimating a soil moisture percent down to a depth of 1.5 m.

Figure 6 shows sections of clay content for profiles P1 and P2, with a notable increase of clay content in profile P2 in an intermediate layer between 0.5 m and 1.2 m. For the sake of comparison, the estimated values of clay content at the same soil sampling points are used, whose values are shown in Table 2.

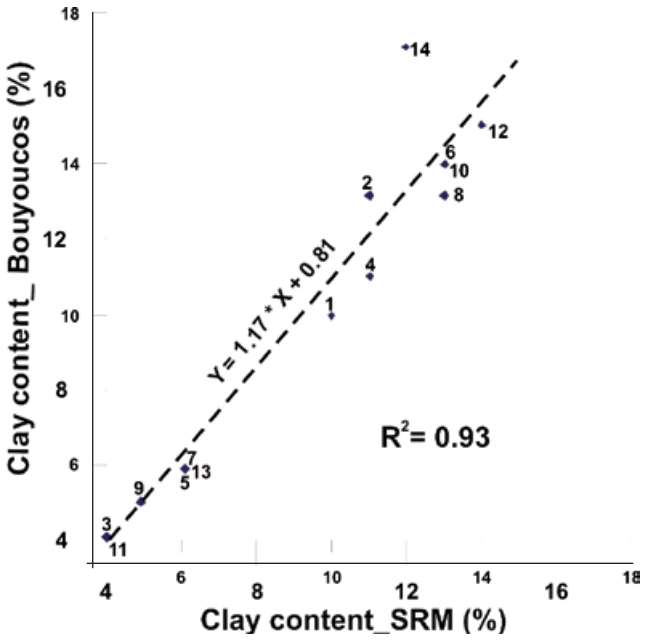

Figure 5. Correlation between clay content values estimated by Bouyoucos and SRM techniques.

Table 2. Clay content values obtained by Bouyoucos and ERT&WRM techniques.

Sample	Clay content (%) Bouyoucos	Clay content (%) ERT&WRM
1	10	6
2	13	9
3	4	7
4	11	11
5	6	7
6	14	11
7	6	10
8	13	15
9	5	6
10	14	15
11	4	4
12	15	15
13	6	5
14	17	14

Among the values determined by ERT&WRM and Bouyoucos techniques (Table 2), notable differences were observed in samples 1, 2 and 7. Regression analysis (Figure 7) shows that, although there is a line of best fit very close to the identity function Y = X, the dispersion of the values (R^2= 0.7) is higher than in the case of the correlation between Bouyoucos and SRM techniques. This is due to ignoring the soil moisture at the time of measurements with ERT, leading to a source of error in clay content estimation. In the case of the SRM technique, the total saturation of the soil sample in the lab, as a requirement before making electrical measurements, eliminates this source of error.

Determination of petrophysical maps

Taking into account the resistivity behavior in sections of the Figure 3, two maps were drawn for depths 0.5 m and 1 m (Figure 8), showing that at depth 0.5 m (Figure 8A) there are values of resistivity higher than at 1 m of depth (Figure 8B).

This result confirms the likely increase in clay content with depth, which is reflected in the decreasing of resistivity values in the central part of the study site (Figure 8B).

Maps of clay content, porosity and CEC are shown in Figure 9 for depths 0.5 m and 1 m. For both depths, an increase of clay content (Figure 9 A and D) apparently yields a decrease in porosity (Figure 9 B and E). This is because when the clay fraction is less than the sand porosity, the clay particles (which have an average radius much smaller than that of the sand grains) will fit within the sand pores and will not change the

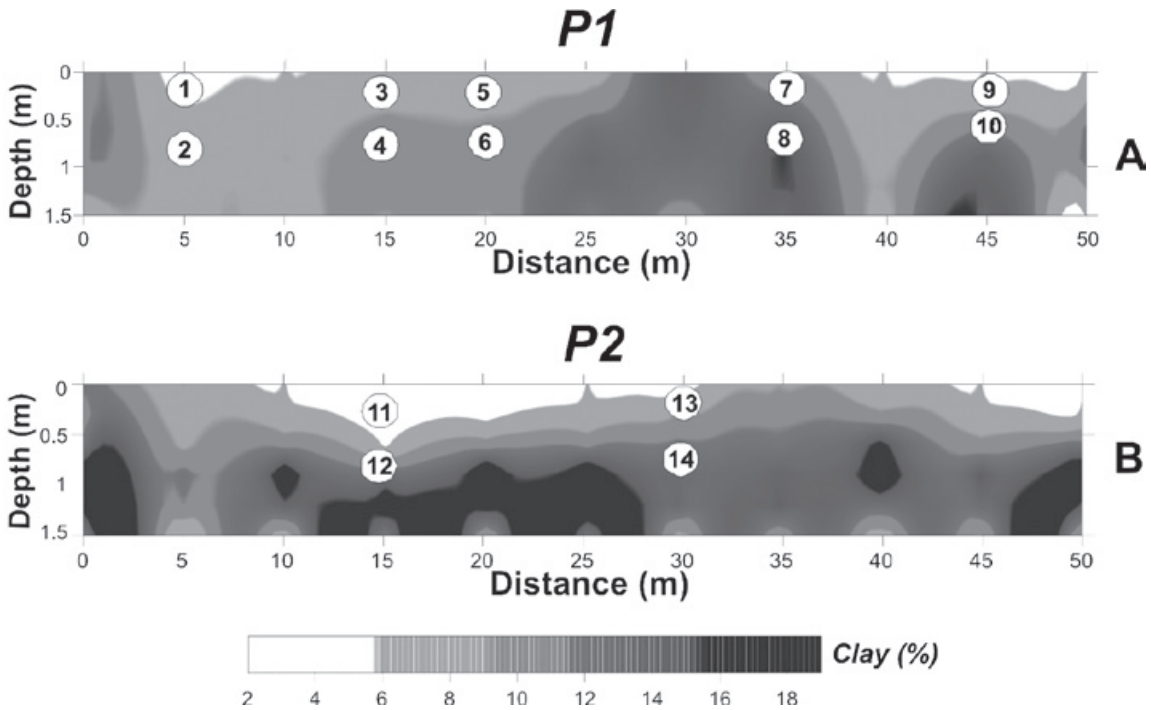

Figure 6. Clay content sections for P1 and P2 profiles obtained by ERT&WRM technique. White circles indicate the location of the 14 soil samples.

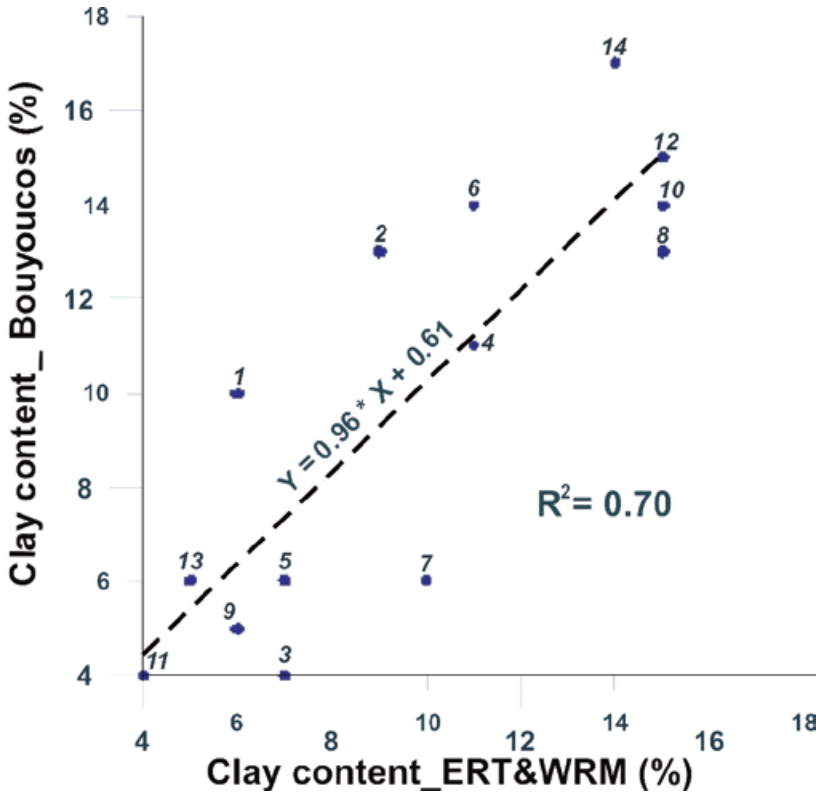

Figure 7. Correlation between clay content values estimated using ERT&WRM and Bouyoucos techniques.

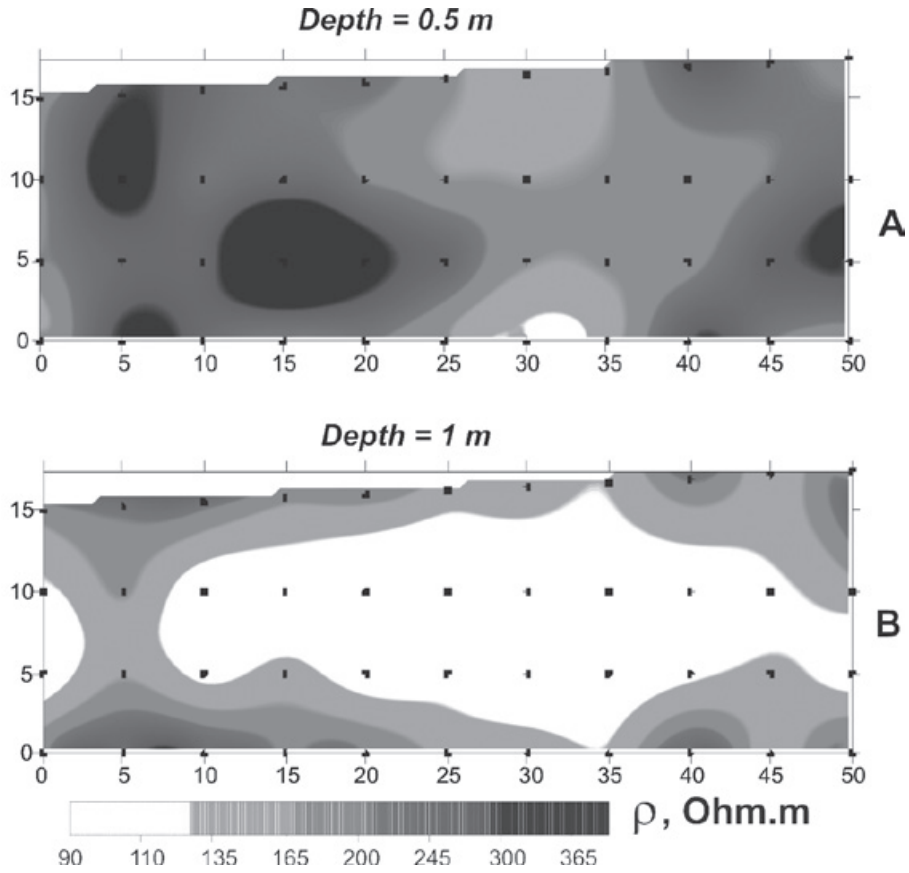

Figure 8. Resistivity maps obtained by ERT&WRM technique. A) Resistivity map for 0.5 m depth. B) Resistivity map for 1 m depth. Black dots indicate the location of ERT measurement points.

sand structure. When the clay fraction exceeds the sand porosity, the sand grains become suspended in the clay host (Shevnin *et al.*, 2007).

The behavior of the CEC (Figure 9 C and F) is also controlled by the behavior of clay content: higher clay content yields higher CEC, both reaching their highest values at a depth of 1 m (Figure 9F).

Conclusions

An estimation of clay content, porosity and CEC can be obtained by applying geoelectrical techniques and subsequent petrophysical modeling process, and their values are comparable to those determined by traditional techniques of texture analysis (Bouyoucos).

The results obtained in the sandy-loam site demonstrated that both ERT&WRM and SRM techniques are efficient for obtaining the petrophysical parameters, showing the SRM technique a higher accuracy.

The ERT&WRM technique has higher productivity than the SRM technique, allowing the estimation of clay content, porosity and CEC in large tracts of land, with low cost, in a short time. Given this goal, we recommend the use of ERT to ensure the detailed study of the range of 0 to 0.5 m deep, or use the faster electromagnetic profiling method for studying at a maximum depth of 0.75 m (e.g., Geonics EM38 equipment).

These results define a new application of geoelectrical methods for PF studies: The determination of clay content, porosity and CEC in an accurate, quick and inexpensive way.

Bibliography

Beklemishev A.V., 1963, Measures and units of physical values. Fizmatgiz, 296 pp. (In Russian).

Bouyoucos G.J., 1936, Directions for Making Mechanical Analysis of Soils by the Hydrometer Method. Soil Science, 42, 3, 225-228.

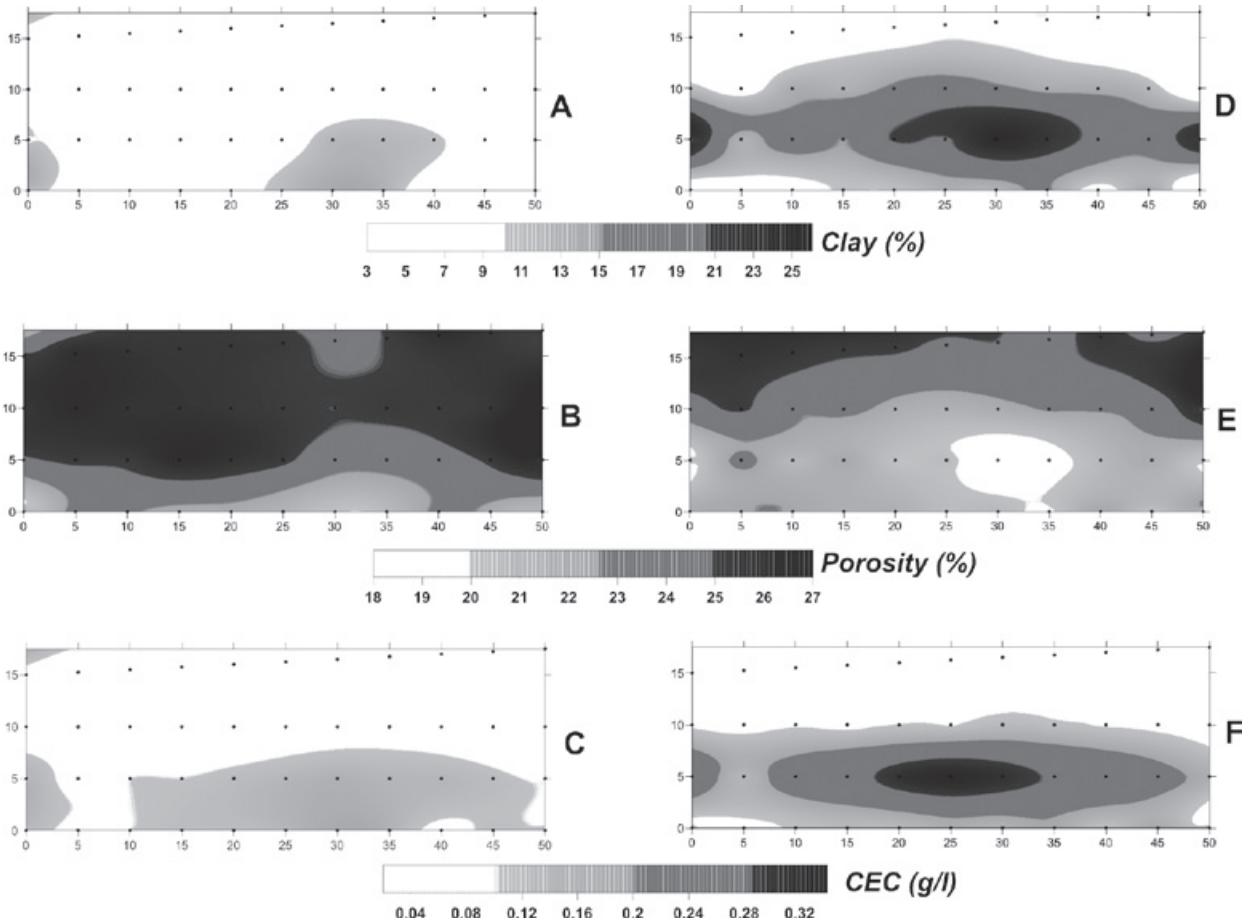

Figure 9. Petrophysical maps: clay content (A), porosity (B) and CEC (C) for 0.5 m depth; and clay content (D), porosity (E) and CEC (F) for 1 m depth.

Bussian A.E., 1983, Electrical conductance in a porous medium. Geophysics, 48, 1258–1268.

Delgado-Rodríguez O., Shevnin V., Ochoa-Valdés J., Ryjov A., 2006, Geoelectrical characterization of a site with hydrocarbon contamination caused by pipeline leakage. Geofísica Internacional, 45, 1, 63-72.

Keller G., Frischknecht F., 1966, Electrical Methods in Geophysical Prospecting, Pergamon Press Inc., Oxford.

Loke M.H., Barker R.D., 1996a, Rapid least-squares inversion of apparent resistivity pseudosections by a quasi-Newton method. Geophysical Prospecting, 44, 131-152.

Loke M.H., Barker R.D., 1996b, Practical techniques for 3D resistivity surveys and data inversion. Geophysical Prospecting, 44, 499-523.

McKenzie R.C., Chomistek W., Clark N.F., 1989, Conversion of electromagnetic induction readings to saturated paste extract values in soils for different temperature, texture, and moisture conditions. Canadian Journal of Soil Science, 69, 25-32.

Pascual A, Delgado O, Fuentes N (1995) Determinación de la conductividad eléctrica equivalente de los suelos de la República de Cuba, Geofísica Internacional, 34, 2, 233-237.

Robert P.C., 2002, Precision agriculture: a challenge for crop nutrition management, Plant and Soil, 247, 143-149.

Ryjov A., Shevnin V., 2002, Theoretical calculation of rocks electrical resistivity and some examples of algorithm's application. SAGEEP proceedings, P2, 10 pp.

Ryjov A., Sudoplatov A.D., 1990, The calculation of specific electrical conductivity for sandy - clayed rocks and the usage of functional cross-plots for the decision of hydro-geological problems. // In "Scientific and technical achievements and advanced experience in the field of geology and mineral deposits research, Moscow, 27-41. (In Russian).

Sudduth K.A., Drummond S.T., Kitchen N.R., 2000, Measuring and interpreting soil electrical conductivity for precision agriculture. Second International Geospatial Information in Agriculture and Forestry Conference, Lake Buena Vista, Florida.

Shevnin V., Delgado-Rodríguez O., Mousatov A., Flores-Hernández D., Zegarra-Martínez H., Ryjov A., 2006, Estimation of soil petrophysical parameters from resistivity data: their application for oil contaminated sites characterization. Geofísica Internacional, 45, 3, 179-193.

Shevnin V., Mousatov A., Ryjov A., Delgado-Rodríguez O., 2007, Estimation of clay content in soil based on resistivity modeling and laboratory measurements. Geophysical Prospecting, 55, 265-275.

Sorensen J.A., Glass G.E., 1987, Ion and Temperature Dependence of Electrical Conductance for Natural Waters. Anal. Chem., 59, 1594-1597.

Williams B.G., Baker G.C., 1982, An electromagnetic induction technique for reconnaissance surveys of soil salinity hazards. Australian Journal of Soil Research, 20,107-118.

Wyllie M.R.J., Southwick P.F., 1954, An experimental investigation of the SP and resistivity phenomena in dirty sands. Journal of Petroleum Technology, 6, 44–57.

Abridged Title: Soil petrophysical parameters based on electrical resistivity

Geofísica Internacional (2012) 51-1: 17-37

Original paper

Structure of the Guaraní aquifer in the surroundings of the Uruguay river from magnetotelluric soundings

Fernando Corbo, Jorge Arzate and Alejandro Oleaga

Received: June 3, 2010; accepted: October 13, 2011; published on line: December 16, 2011

Resumen

Este trabajo se enfoca en obtener un modelo geológico del Sistema Acuífero Guaraní (SAG) en una de las zonas de mayor explotación, mediante sondeos magnetotelúricos de espectro amplio. La región analizada comprende ambos flancos del Río Uruguay entre las latitudes 30º 30' y 31º 52' Sur y las longitudes 57º y 58º 22' Oeste. Como parte de este estudio se realizaron un total de 31 sondeos AMT y MT los cuales fueron calibrados con 14 pozos profundos con información del subsuelo. Previo a la interpretación cuantitativa de los datos, se llevó a cabo un análisis de distorsión de los datos para determinar la dimensionalidad del medio geológico de la región. Los resultados indican que a frecuencias mayores de 1 Hz el subsuelo se comporta como un semi-espacio estratificado (1D) a excepción de algunos sitios en donde existe distorsión asociada a estructuras geológicas locales. A partir de la inversión unidimensional del conjunto de sondeos, se estimó la distribución de las principales unidades litológicas que constituyen el relleno de la cuenca Chaco-Paranense en esta zona, incluyendo al SAG. La calibración de los modelos obtenidos y la asignación de rangos de resistividad de las principales unidades litológicas se llevó a cabo utilizando siete registros de perforaciones profundas disponibles en la zona. Los resultados muestran que el basamento precámbrico se hace más profundo en dirección Oeste, alcanzando profundidades mayores a los 4 km en el lado Argentino del área de estudio. Como parte de los resultados se destaca la presencia de una estructura próxima y paralela al Río Uruguay que parece corresponder a una falla regional que sugiere desplazamientos verticales mayores a los 2 km, con el bloque caído hacia el poniente. Según esta interpretación, el Río Uruguay es en sí mismo una expresión superficial de dicha estructura ya que tiene aproximadamente su misma dirección. A frecuencias inferiores a 1 Hz el subsuelo se comporta como un medio bidimensional con un azimuth de la estructura regional de aproximadamente 0º, el cual es consistente con la orientación aproximada NS del río Uruguay. Usando esta información se llevó a cabo una inversión bidimensional a lo largo de cuatro perfiles transversales a la dirección del río con el objeto de contrastar los modelos obtenidos con aquellos que resultan del tratamiento 1D. Los modelos 2D obtenidos arrojan resultados consistentes, mostrando rasgos y estructuras semejantes a los obtenidos a partir de la inversión 1D del invariante de la impedancia.

Palabras clave: sistema acuífero Guaraní, sondeos magnetotelúricos, modelo unidimensional, modelo bidimensional.

F. Corbo
Posgrado en Ciencias de la Tierra
Centro de Geociencias
Campus UNAM - Juriquilla
Blvd. Juriquilla 3001, 76230
Querétaro, México
*Corresponding author: fcorbo@geociencias.unam.mx

J. Arzate
Centro de Geociencias
Campus UNAM - Juriquilla
Blvd. Juriquilla 3001, 76230
Querétaro, México
Email: arzatej@geociencias.unam.mx

A. Oleaga
INGESUR SRL
Requena 1062/302
Montevideo, 11200
Montevideo, Uruguay

Abstract

We use wide band magnetotelluric soundings to infer the geological and structural surrounding of the Guarani Aquifer System (SAG) in an area of major exploitation. The studied region comprises both sides of the Uruguay river, between latitudes 30º 30' and 31º 52' South and longitudes 57º 00' and 58º 22' West. A total of 31 AMT and MT soundings were used for the geological interpretation, which were calibrated with 14 deep wells with lithologic information. Prior to a quantitative interpretation of the data, a distortion analysis of the impedance was carried out to define the dimensionality of the predominant geological structures in the zone. The results show that at high frequencies, larger than 1 Hz, the earth behaves as a stratified ground or one-dimensional (1D) earth, excepts at some of the sites where the observed distortion is associated to local geological structures. From the one-dimensional inversion of the impedance determinant of the data set we estimate the distribution of the main lithological units that conform the sedimentary filling in the zone of the Chaco-Paranense basin, including the SAG. The calibration of the obtained models and the assignation of the resistivity ranges of the main geological units were done using seven resistivity logs from deep wells available in the area. The results show that the Precambrian basement becomes deeper towards the west, reaching depths larger than 4 km in the Argentinian side of the studied area. The results also show the existence of a structure near and parallel to Uruguay river, that seems to correspond with a major regional fault, suggesting vertical displacements larger that 2 km. According to this interpretation the Uruguay river is a superficial expression of the deep regional fault having roughly the same azimuth. At frequencies below 1 Hz the ground turns out to be bi-dimensional with a regional strike angle of around 0º, which is consistent with the NS trend of the Uruguay river. Using this information a 2D inversion was performed along four profiles perpendicular to the river to contrast the results obtained using the more simple 1D approach. The 2D models obtained yield consistent results showing similar features and structure for the SAG obtained from the 1D inversion of the invariant of the impedance.

Key words: Guarani aquifer system, magneto-telluric soundings, one-dimensional models, two-dimensional models.

Introduction

The Guaraní Aquifer System (SAG) is one of the largest groundwater reservoirs known on earth. It has an extension of about 1,195,500 km^2 (Araujo *et al*., 1999), of which 840,000 km^2 are in Brazilian territory, 225,000 km^2 are in Argentina, 71,700 km^2 in Paraguay and 50,000 km^2 in Uruguay. The Guaraní aquifer is located in southestern South America approximately between the 12º and 35º of southern latitude and 47º and 65º of longitude west (Figure 1). The aquifer is known to be hosted in Triasic to Jurasic (245 to 144 My) sedimentary rocks of variable thickness, sometimes outcropping in the periphery of the SAG and sometimes located at depths of more than 1.5 km below an early Cretaceous thick basaltic layer. Its annual recharge is estimated in 166 km^3 (Da Cunha-Reboucas and Amore, 2002). According to the actual limits, the inhabitants over the SAG amount nearly 15 million people. In some regions, it represents the only available source of water supply for urban, agricultural and industrial uses. Despite the relative large number of water wells drilled for this purpose, the limits of the SAG at the south-west of basin are poorly defined compared to other regions (Costa-Ribeiro, 2008). In the surroundings of the Uruguay river, the furthest southwestern region of the SAG, the aquifer has been explored for thermal water supplies used mainly by the tourist industry. In this region, water wells (in some cases) reach depths of 1.3 km, with yields that reach 120 l/s and temperatures up to 51 ºC. The wide band magnetotelluric survey carried out in this zone, that cover a total area of nearly 12,000 km^2, is aimed to obtain a geological model of the SAG and how is affected by the presence of the Uruguay river.

The SAG in the area

The studied area is located in the Uruguay-Argentina border centered in the Salto-Concordia thermal area covering the northeast of the Entre-Rios province of Argentina and the northwest sector of Uruguay. This area is regarded as the southernmost part of the Paraná basin. The basement in this region consists of Precambrian granites at the bottom of the sequence. Overlying discordantly are a series of sedimentary deposits of Devonian age that range from fluvial to neritic depth marine environments. This sequence marks a transgressive-regressive tectonic cycle that apparently reversed during the early to middle Permian, where neritic marine sediments appear again in the sequence (Figure 2). From the middle Permian to the Upper Jurassic a new period of shallow sea, lacustrine and eolic sedimentation was emplaced discordantly upon Lower Permian marine deposits. The upper part of this sedimentary sequence corresponds to

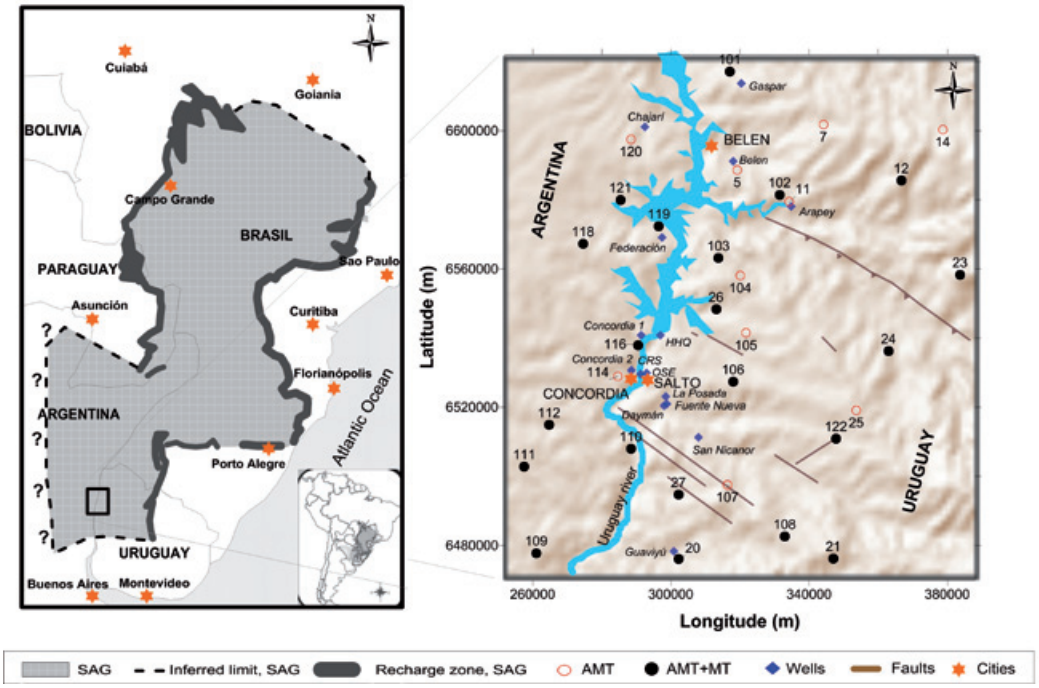

Figure 1. Limits of the outcropping sandstones and potential recharge zone of the Guaraní Aquifer (shaded zone to the left). Dashed lines are inferred or unknown limits (REF). The study area is located at the southern partion of the SAG, centered in the Uruguay river (small rectangle). In the amplified frame, the location of the audio-magnetotelluric (AMT) and wide band magnetotelluric (AMT+MT) soundings is shown by black circles and triangles respectively. Diamonds represent wells where parametric soundings were carried out for model extrapolation. The Uruguay river is shown in gray (modified from Costa-Ribeiro, 2008).

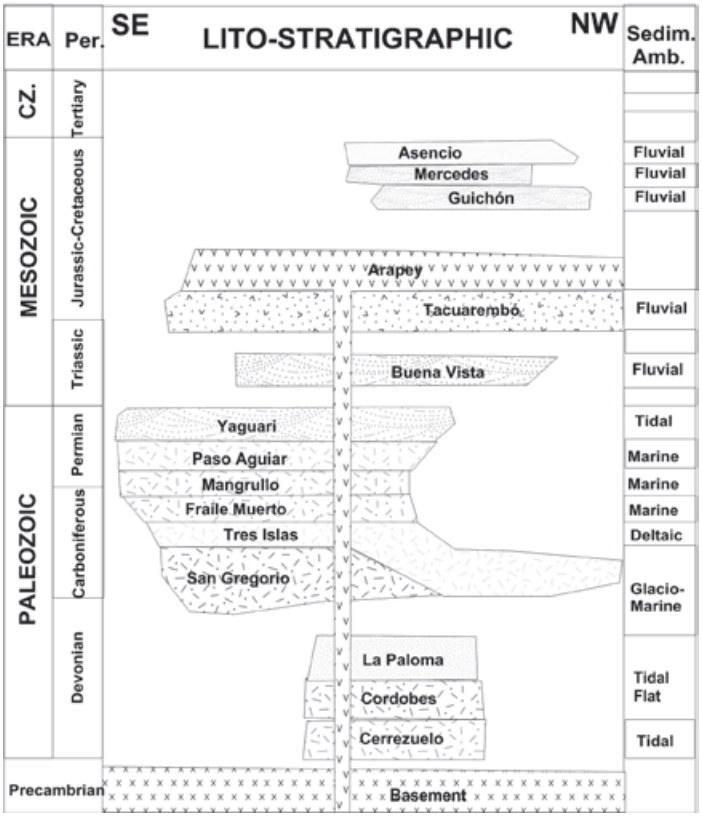

Figure 2. Stratigraphic column (modified from De Santa Ana and Ucha, 1994) of the studied area showing the names of the main formations, age, environment of deposition.

the eolic, fluvial, and lacustrine rock package of Triassic-Jurassic age that conform the SAG (De Santa Ana *et al*., 1994). The estimated thickness from available wells is 300 to 800 m at depths ranging between 400 and 1000 m below the surface, although the thickness is around 300 m at Salto city. The lower part of the Permian-Jurassic deposits, conformed by a rock package of marine and glacial deposits, has lower hydraulic permeability than the Triassic – Jurassic package, but its shallow marine origin is often conditioning the water quality. Towards the Jurassic-Cretaceous limit an important effusive volcanic event started in the Pangea continent associated to the rifting of the south Atlantic, and started a slow subsidence of the northern basin (Soares and Landim, 1976, *cited in* Sprechmann *et al*., 1981). During the Lower Cretaceous, successive fissure basalts flows were laid over the Permian-Jurassic sedimentary sequence reaching exceeding thicknesses of 1 km in the area (Bossi and Schipilov, 1998; Corbo Camargo, 2006; Oleaga Batzerrica, 2002), burying and confining the Triassic-Jurassic deposits. A sedimentary cover of variable thickness (0 to 200 m) is at the top of the basalts that some authors consider as more than 26 different magmatic pulses (Montaño *et al*., 2004). From the geological point of view, the SAG is constituted by sedimentary rocks of the Jurassic Tacuarembó Formation (Bossi *et al*., 1975 *cited in* Veroslavsky *et al*., 2003), and by the Triassic Formation Buena Vista (Ferrando and Andreis, 1986). In general, the SAG is formed by a progression of continental sandstones (Tacuarembó Fm.) deposited in fluvial and lacustrine environments with intercalated eolic deposits, and sedimentary rocks from a transitional - continental environment (Buena Vista Fm.). Underlying the SAG, Permian-Carboniferous sedimentary rocks are conformed by tidal and marine environment (Yaguarí Fm, Paso Aguiar Fm, Mangrullo Fm, Fraile Muerto Fm, Tres Islas Fm. and San Gregorio Fm; De Santa Ana and Ucha, 1994). The bottom of basins are conformed by Devonian transgressive-regressive sequence (La Paloma Fm, Cordobés Fm and Cerrezuelo Fm; De Santa Ana and Ucha, 1994).

Magnetotelluric soundings

In general, the audio-magnetotelluric (AMT) and magnetotelluric (MT) soundings are used for different purposes. The AMT soundings are used for prospecting targets located at depths <1000 m, whereas the MT soundings are generally used for upper and middle crustal studies. In this work, we have used coincident AMT+MT soundings that combined cover a wide frequency range of naturally occurring electromagnetic fields from 10^4 to 10^{-3} hz. The acquisition time of sounding ranges from 16 to 24 hours, about 2 hours for the high frequency (AMT) record and the rest of the time for the intermediate and low frequency (MT) data. A wide spectrum frequency sounding produce apparent resistivity and phase curves that provide information from shallow surface deposits to deep regional basement structure. The measured horizontal electric and magnetic vector fields are related through the second rank frequency dependent impedance tensor Z through:

$$\begin{bmatrix} E_x \\ E_y \end{bmatrix} = \begin{bmatrix} Z_{xx} & Z_{xy} \\ Z_{yx} & Z_{yy} \end{bmatrix} \begin{bmatrix} H_x \\ H_y \end{bmatrix} \quad (1)$$

The estimation of the impedance elements from the horizontal electric and magnetic field components measured as time series is the first step in the processing scheme that leads to the estimation of the complex impedance elements (e.g., Jones *et al*., 1989).

From the impedance elements Z_{ij}, that together provide the response function of the ground, it is possible to define the apparent resitivities and phase differences between the electric and magnetic conjugated fields E_i and H_j. Strictly speaking, the four complex elements of the tensor define an equal number of apparent resistivities and phase differences for a structurally complicated ground. However, the prevailing geology often allows to simplify **Z** in the event of a two-dimensional (2D) or one-dimensional (1D) ground. A regional geological contact or another elongated structural feature would correspond to the first case, while a stratified or thick uniform ground (stable craton or a marine platform) could represent the later. In both such cases, the diagonal elements of **Z** are nil whereas $Z_{xy} \neq Z_{yx}$ for the 2D case, and $Z_{xy} = Z_{yx}$ for the stratified/uniform 1D ground. This means that for the two-dimensional case two orthogonal resistivities and two phases are defined, when one of the reference coordinate axis is coincident and the other perpendicular to the strike direction of the regional structure, in which case (Vozoff, 1989):

$$\rho_{xy}(\omega) = \frac{C_1}{\omega\mu_0}\left|Z_{xy}(\omega)\right|^2$$

$$\varphi_{xy}(\omega) = \tan^{-1}\left[\frac{\mathrm{Im}\, Z_{xy}(\omega)}{\mathrm{Re}\, Z_{xy}(\omega)}\right] \quad (2a)$$

$$\rho_{yx}(\omega) = \frac{C_2}{\omega\mu_0}\left|Z_{yx}(\omega)\right|^2$$

$$\varphi_{yx}(\omega) = \tan^{-1}\left[\frac{\mathrm{Im}\, Z_{yx}(\omega)}{\mathrm{Re}\, Z_{yx}(\omega)}\right] \qquad (2b)$$

where C_1 y C_2 are constant quantities representing the static shift of the resistivity curves produced by the effect of electrical charge building across local heterogeneities. The units of apparent resistivity ρ_{ij} and phase ϕ_{ij} are Ohm-m and degrees (º) respectively. In these equations $\omega = 2\pi f$ with f the prospecting frequency given in hertz, and μ_0 is the magnetic permeability of vacuum equals to $4\pi \times 10^{-7}$ H/m. In the case that a predominantly stratified ground with little or not structural complexity, the apparent resistivity as well as the phase are the same in any horizontal direction for a given frequency and, in principle, can be estimated using any pair of the above equations. However, it is more accurate to use the determinant average expression that account for possible lateral variations such as (Berchichevsky and Dmitriev, 1976):

$$\rho_{\det}(\omega) = \frac{C}{\omega\mu_0}\cdot\left|Z_D\right|^2 \qquad (3)$$

where $Z_D = Z_{xx}Z_{yy} - Z_{xy}Z_{yx}$. This expression is a geometric means respectively of Z_{xy} and Z_{yx}, and has the additional advantage that Z_D is rotationally invariant, that means that its value do not depend on the rotation of the coordinate system. The determinant mode reduces the distortion effects caused shallow heterogeneities and non-finite lateral structures, and the phase is not affected by galvanic distortions (Berchichevsky and Dmitriev, 1976). The inversion, generally allows a good data fit while at the same time resolving reasonably well both resistive and conductive structures along any profile.

In total we measured 31 sites of which 21 where wide band (AMT+MT) soundings and 10 where just high frequency (AMT) soundings (Figure 1), seven of them where parametric soundings measured in the vicinity of wells with known lithology. Four of those wells have also available electric logs that allowed us to calibrate our models.

Apparent resistivity maps

The distribution of apparent resistivity at specific frequencies in the studied area is a useful representation of raw data to acquire a first insight of the underground geology and its complexity. Previous to the elaborated an interpolated map the resistivity curves were analyzed for static shift and corrected by correlation using the available geological map as well as neighboring sites to fix the correct resistivity level. Figure 3 shows the distribution of apparent resistivities, calculated from the impedance determinant, in the zone, for frequencies of 100, 10, 1, and 0.1 Hz, which correspond to shallower to deeper depths respectively accordingly to the depth-frequency dependence given by (e.g. Vozoff, 1989):

$$\delta(f) \propto \sqrt{\frac{\rho_{avg}}{f}} \qquad (4)$$

being d, the (skin) depth, ρ_{avg}, the average resistivity and f the testing frequency, in this case 100, 10, 1 and 0.1 Hz. As observed from this equation, the lower the frequency, the deeper the penetration depth and conversely. Hence, at 100 hz and 10 Hz low (less than 80 Ohm-m) and intermediate (from 80 to 400 Ohm-m) resistivities are characteristic at shallow depths (Figures 3a and 3b); the lower resistivities are distributed in the west and south of the studied area, whereas the intermediate resistivities are located mainly in the central and northeast regions. At 1 Hz (Figure 3c) the distribution of intermediate resistivities (80-400 Ohm-m) cover almost entirely the area except some isolated spots. In both cases, the intermediate resistivities are associated to the spatial distribution of the fissure basalts, known to be widespread distributed in the area at depths above 1 to 1.5 km. At frequencies lower than 0.1 (Figure 3d), representing deeper depths, a zone a higher resistivities (> 400 Ohm-m) becomes apparent mainly to the east of the Uruguay river, that suggest a shallower resistive basement in this region in contact with more conductive deposits that extend towards the west.

Dimensionality of the ground

There are different techniques to establish the dimensionality of the ground from the measured impedance tensor **Z** (i.e. Swift, 1967; Groom and Bailey, 1989, 1991; Bahr, 1988, 1991; Lilley, 1998a,b; Weaver *et al*., 2000). From the distortion parameters estimated, particularly the skew, it is possible to define the complexity of the ground at different frequencies in terms of the geological structures that modify the flow of the natural electromagnetic fields propagating below the ground that are measured at the surface. From the distortion analysis of the data it is possible to make a decision on the appropriate treatment required by them. If the tensor do not has a distortion, then it is not necessary 2D or a 3D data treatment to adequately interpret

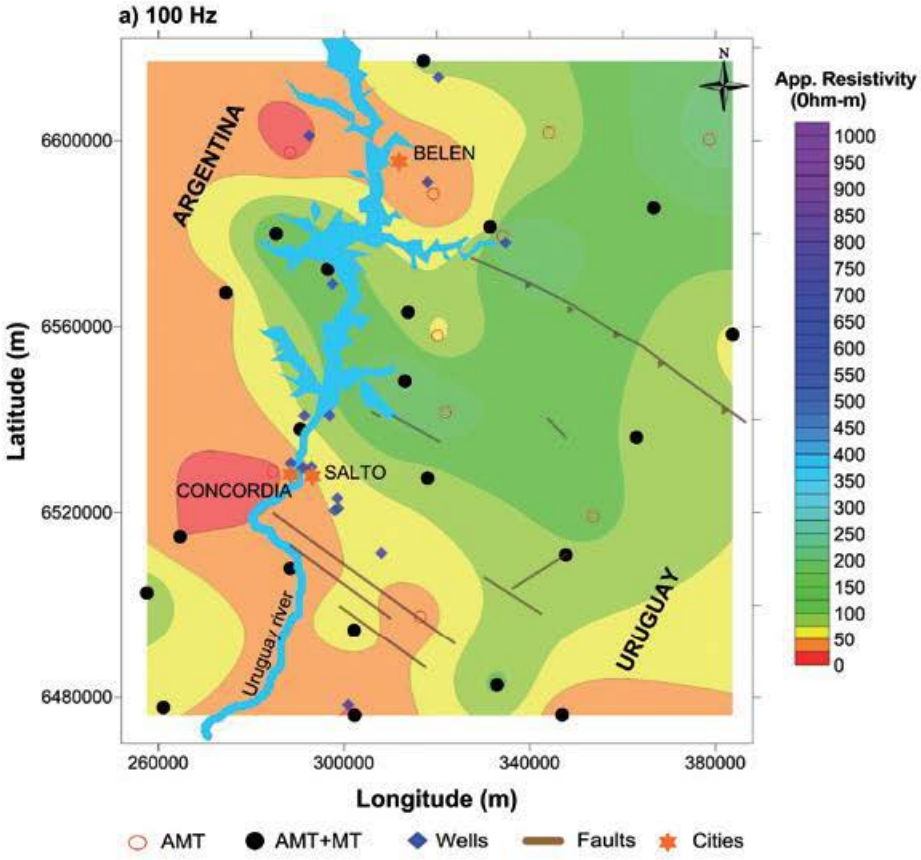
a) 100 Hz
ARGENTINA
BELEN
SALTO
CONCORDIA
URUGUAY
Uruguay river
N
App. Resistivity (Ohm-m)
1000
950
900
850
800
750
700
650
600
550
500
450
400
350
300
250
200
150
100
50
0
Latitude (m)
6600000
6560000
6520000
6480000
260000
300000
340000
380000
Longitude (m)
AMT
AMT+MT
Wells
Faults
Cities

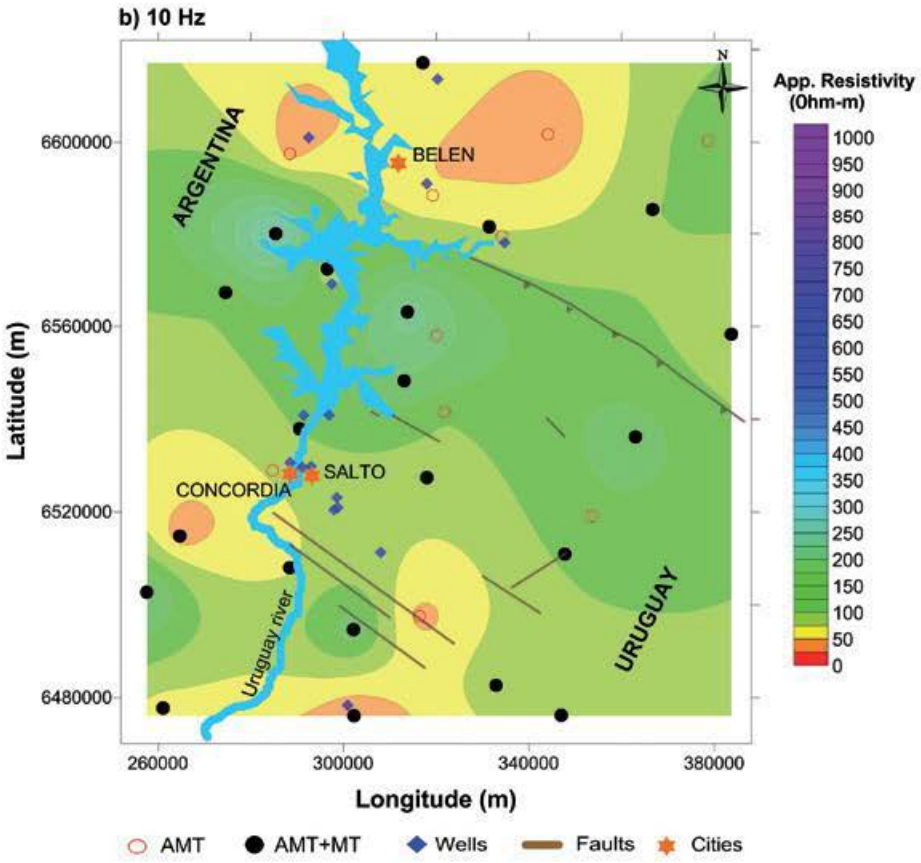
b) 10 Hz
ARGENTINA
BELEN
SALTO
CONCORDIA
URUGUAY
Uruguay river
N
App. Resistivity (Ohm-m)
1000
950
900
850
800
750
700
650
600
550
500
450
400
350
300
250
200
150
100
50
0
Latitude (m)
6600000
6560000
6520000
6480000
260000
300000
340000
380000
Longitude (m)
AMT
AMT+MT
Wells
Faults
Cities

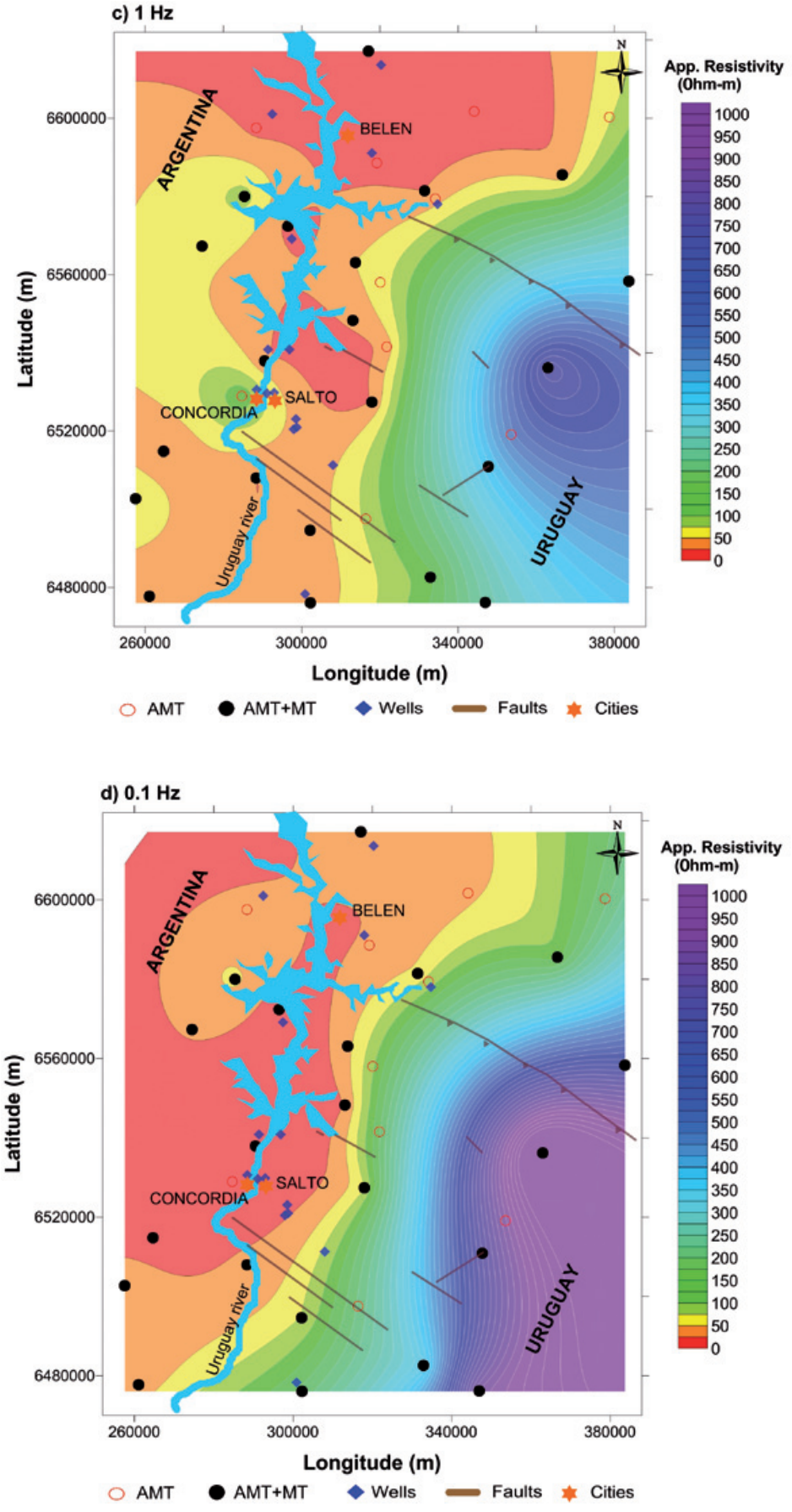

Figure 3. Apparent resistivity maps at 100 Hz (a), 10 Hz (b), 1 Hz (c) and 0.1 Hz (d). The Uruguay river is shown in blue and the black circles indicate the location of the magnetotelluric soundings. Explanation is in the text.

the correct structure of the ground because the absence of distortion is telling us is that the earth behaves as a stratified ground. However, often happens that the impedance has different degrees of distortion for different frequency bands and therefore a single sounding can detect different dimensionality at different depths. A situation like this would indicate different degrees of geological complexity as a function of depth.

We have applied the dimensionality techniques of Swift (1967) and Bahr (1991) for every frequency of all 31 soundings in order to define the more appropriate treatment required by the data. The numerical criteria given by the authors were used to establish the dimensionality of the impedance **Z**, although the additional distortion parameters m and h of Bahr's criteria were also used, which provides a more robust estimation of dimensionality. Figure 4 represents the results applying both methods of dimensionality to all soundings. The results of this soundings suggest that the ground in the studied area can be regarded one-dimensional down to a frequency of 1 Hz approximately (light gray tone in Figure 4), except for sites where distortion occur associated to local structural complexity. About 80% of the analyzed soundings indicate a prevailing 1D ground for frequencies above 1 Hz and predominantly 2D for frequencies lower than this, with some sites showing a 3D behavior in limited band widths.

Parametric soundings

Seven of the AMT+MT soundings were carried out in the surroundings of equal number of water wells an which have lithology available; four of them had also electric logs. The wells where the parametric soundings were done are named Gaspar, Belén, Arapey, Guaviyú, Chajarí, Concordia and Federación, the first three located in Uruguay and the later four in Argentina (Figure 1). Their depths range from 800 to more than 2,500 m. The correlation of the lithology and the associated electrical well logs allowed us to assign ranges of formation resistivity values to the geological units along the column and extrapolate these values through the modeled resistivity at parametric soundings to the rest of the studied area. The resistivity ranges associated to the main geological units identified in the area from the available wells aresummarized in Table 1. These results show that the electrical resistivity of the Lower Cretaceous basalt layer is quite variable, the reason is that according to drilled samples there are alteration zones within this formation, but particularly at the top of the unit. The alteration zones decrease towards the base of the layer and the resistivity becomes larger and more stable. The electric logs show that the altered sectors have resistivities of around 50 Ohm-m whereas in sectors without alteration it takes values around 650 Ohm-m. On the other hand, the Jurassic-Triassic sedimentary

Table 1. Typical resistivity values of the main geological units in the studied area deduced from the correlation of electric well logs and observed lithology along them. Extrapolation of resistivity values was done using the parametric AMT soundings (Oleaga-Bazterrica, 2002).

		Electric resistivity (Ohm - m)	
Lithology	**Period**	**Variation interval**	**More frequent value**
Sediments	Upper Crestaceous	11 to 15 and 100 to 200	12 and 150
Basalts	Lower Crestaceous	50 to 650	200
Sedimentary rocks	Jurassic - Triassic	17 to 70	30
Diabases	Triassic or Lower Crestaceous	450 to 700	500
Sedimentary rocks	Devonian - Permian	3 to 14	9
Basement	Precambrian	400 to 100	600

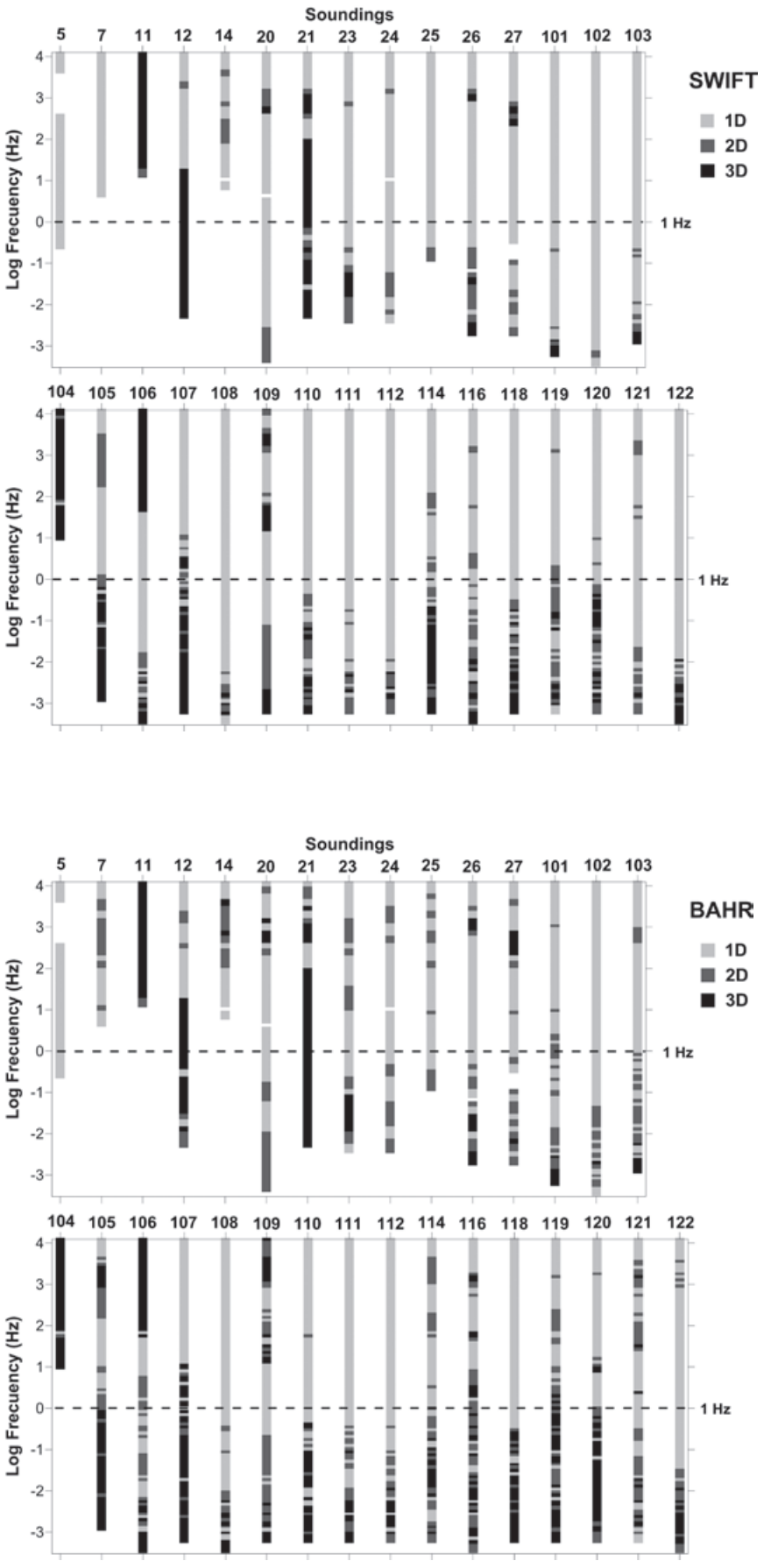

Figure 4. Results of the distortion analysis performed to the data. Here we present the results from all soundings analyzed using Bahr´s distortion approach and Swift´s skew. The black tones indicate a three-dimensional ground, the grey ones a two-dimensional earth and light gray indicate a stratified one-dimensional ground, that in 76% poresent show a 1D behavior up to 1 hz.

unit, associated to saturated sandstones of the SAG underlying the basalt layer, shows a smaller range of variation from 17 to 70 ohm-m. In some areas, exist the presence of individual diabase intrusions, thin layers within the aquifer body, have observed resitivities ranging from 450 to 700 Ohm-m, however their thickness compared to that of the SAG (more that 200 m in the zone) represent only a fraction.

The Devonian-Permian package of sedimentary rocks underlying the SAG also shows a range of small resistivity variations, from 3 to 14 Ohm-m, suggesting a reasonable stratigraphic homogeneity for this unit, although is more probable that the brackish water content of this predominantly marine unit plays a major role in either its homogeneity and the lower values of resistivity observed. The low resistivity character of this layer makes relatively easy to identify it in the resistivity curves obtained from the magnetotelluric soundings, however because of the relatively small resistivity contrast with the SAG it often becomes uncertain to separate them from each other giving rise to ambiguity in the estimation of the aquifer thickness. At the bottom of the sequence is located the more resistive member, the Precambrian granitic basement, that shows a range of resistivity variation between 400 and 1000 ohm-m. The lower resistivity values correspond to the upper few meters of the basement where alteration occurs by effect of the chemical interchange with the overlying marine rock package. Deeper into the basement is expected to have larger and more homogeneous values as suggested by several measured resistivity curves.

One-dimensional inversions

According to the previous dimensionality results, the behavior of the ground for frequencies larger than 1 Hz, which corresponds to the SAG, can be regarded as one-dimensional. Likewise, the distortion analysis yielded unstable values for the strike of the regional structure for most of the frequency band above this 1 Hz, which is also an indication of an stratified earth. With few exceptions that seem to correspond to the presence of local fault structures besides the measuring sites, most of the analyzed soundings present characteristics of a 1D ground in the mentioned range. In addition, the induction vectors for the same range of frequencies provide consistent results with the distortion analysis. In a homogeneous or stratified ground, this means, in the absence of a structurally complex ground, the vertical field component is null.

The Geomagnetic Transfer Function (Tipper) is defined as the relation between the vertical with the corresponding horizontal components of the magnetic field *Hz*, given by the expression (e.g. Vozoff, *et al*., 1989; Lilley *et al.*, 1982):

$$Hz = A.Hx + B\cdot Hy, \qquad (5)$$

In this equation A and B are complex numbers. The Tipper can be decomposed into two real vectors in the xy plane, corresponding to its real and imaginary parts; these real vectors are called induction vectors. The expressions for the magnitude (I) and phase (β) of the induction vectors can be estimated through the expressions (Vozoff, 1991):

$$I_{\mathrm{Re,Im}} = \left(\mathrm{Re,Im}(A)^2 + \mathrm{Re,Im}(B)^2\right)^{1/2}$$

$$\beta_{\mathrm{Re,Im}} = \tan^{-1}\left(\frac{\mathrm{Re,Im}(B)}{\mathrm{Re,Im}(A)}\right) \qquad (6)$$

Both magnitude and phase of the real induction vectors are related to the presence of lateral changes in conductivity at specific ranges of frequencies. The vectors point towards the conducting structures, and their magnitude increases with their proximity as well as with their size with respect to the sounding location. If no lateral conductors exist in a range of frequencies, then the magnitude of Hz approaches to zero at that specific range frequencies, which is an indication that the ground is one-dimensional. Figure 5 shows examples of the real part of induction vectors at frequencies of 100, 1.0 and 0.01 Hz, where it is observed that their value at 1Hz (case b) is in general very small for most of the sites, and that for the other cases (a) and c) the values are in general considerably larger.

Depth charts

Base upon the previous distortion analysis and induction vector results, we carried out one-dimensional inversions of the resistivity and phase curves of the rotationally invariant, using an Occam algorithm. Several models were worked out but the depth maps were obtained from the extrapolation of the one-dimensional layered models of all the interpreted soundings. The results are shown in Figure 6 in form of depth maps to the bottom and tops of the main formation units related to the SAG and discussed above. Figure 6a represents the estimated depth to the top of the basalt unit, where the darker tones indicate the zones of larger depths. As observed, to the east of the Uruguay river the basalts are outcropping in most of the area, whereas to the west the sedimentary layer covering this unit reaches thickness of 90 m. Figure 6b represents the depth to the bottom

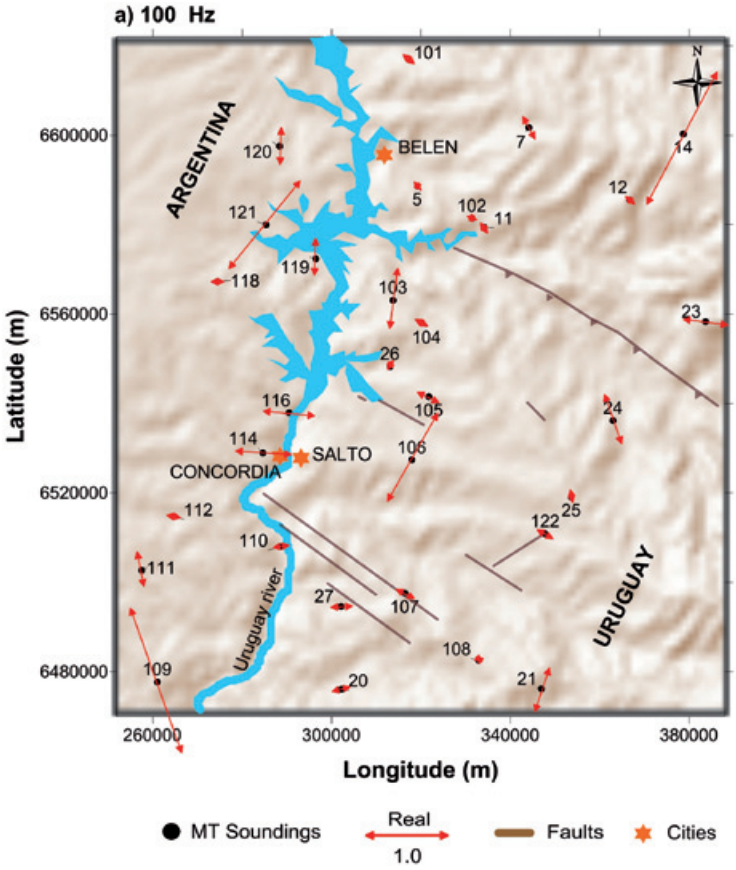

Figure 5a.

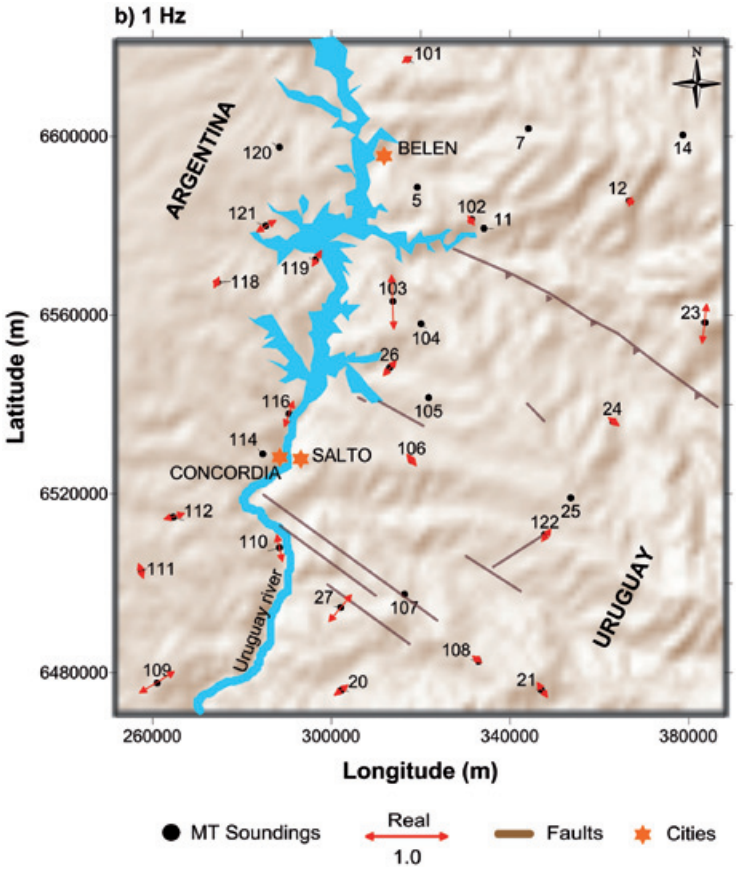

Figure 5b.

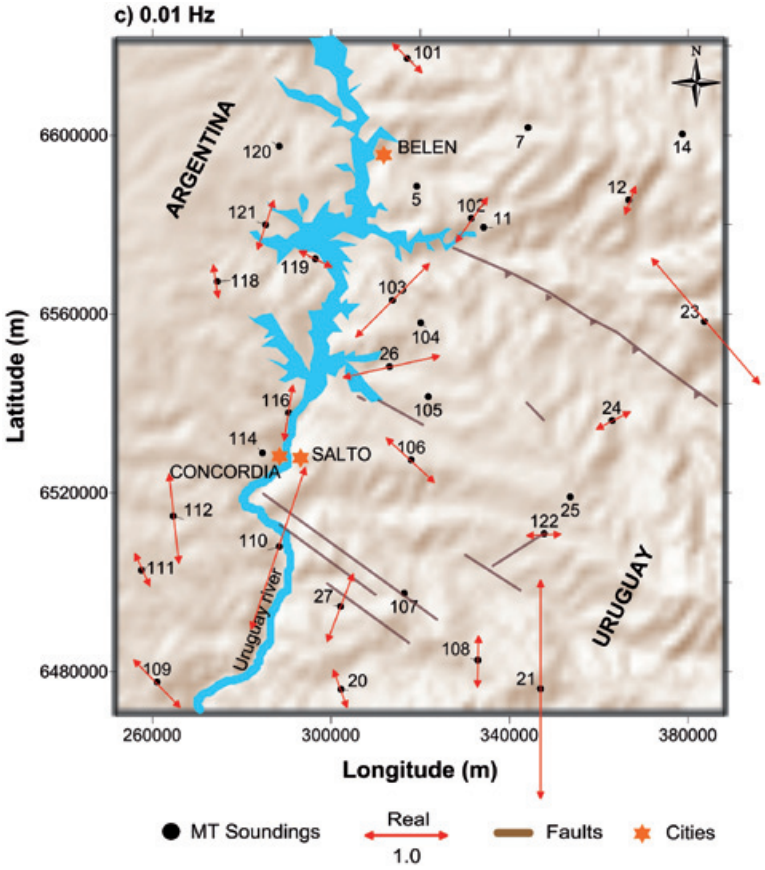

Figure 5c.

Figure 5. Induction vector maps for 100 Hz (a), 1 Hz (b) and 0.01 Hz (c) that show net differences in magnitude. The reduced size of induction arrows in the first case indicates a 1D ground, whereas the larger size in the second case suggests a more complex structure of the ground at lower frequencies.

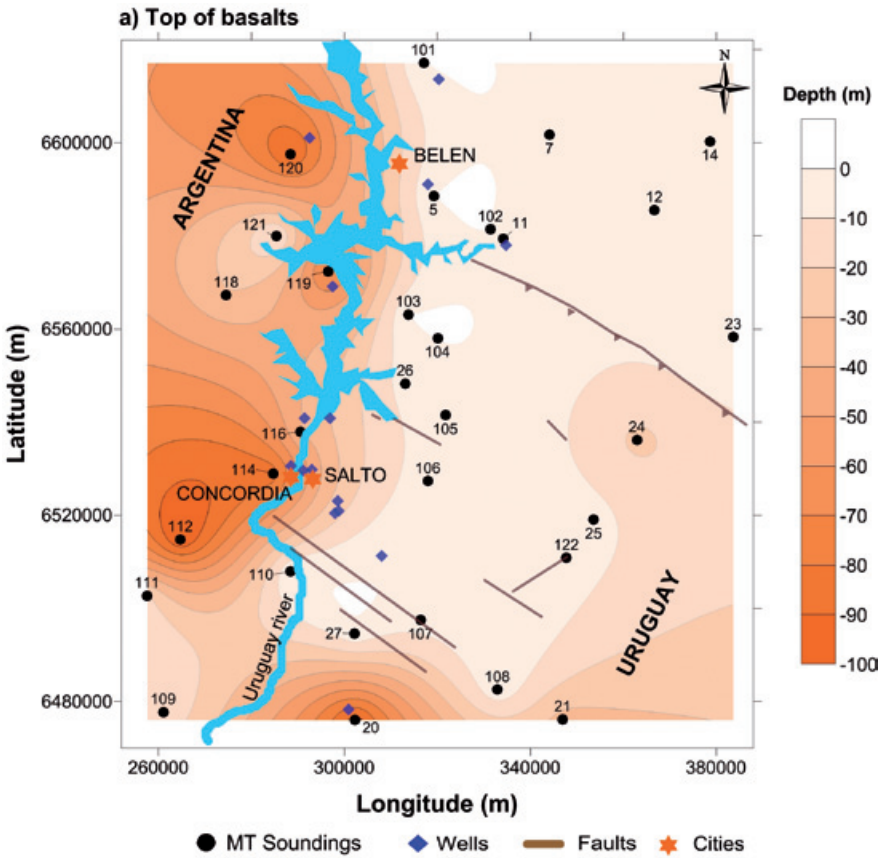

Figure 6a.

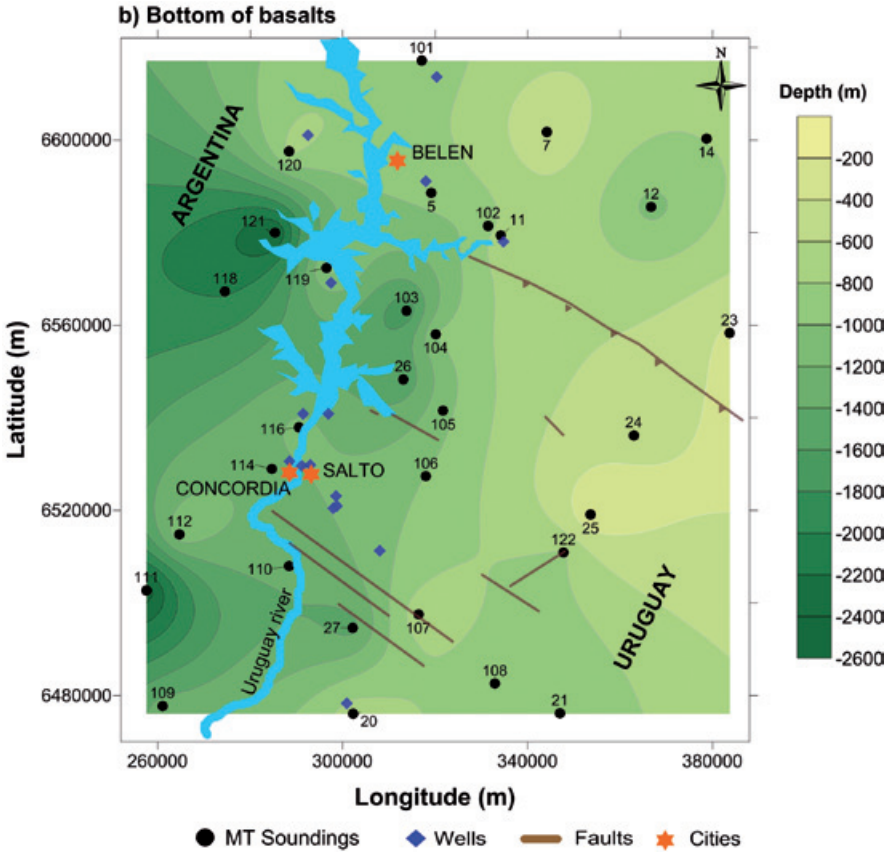

Figure 6b.

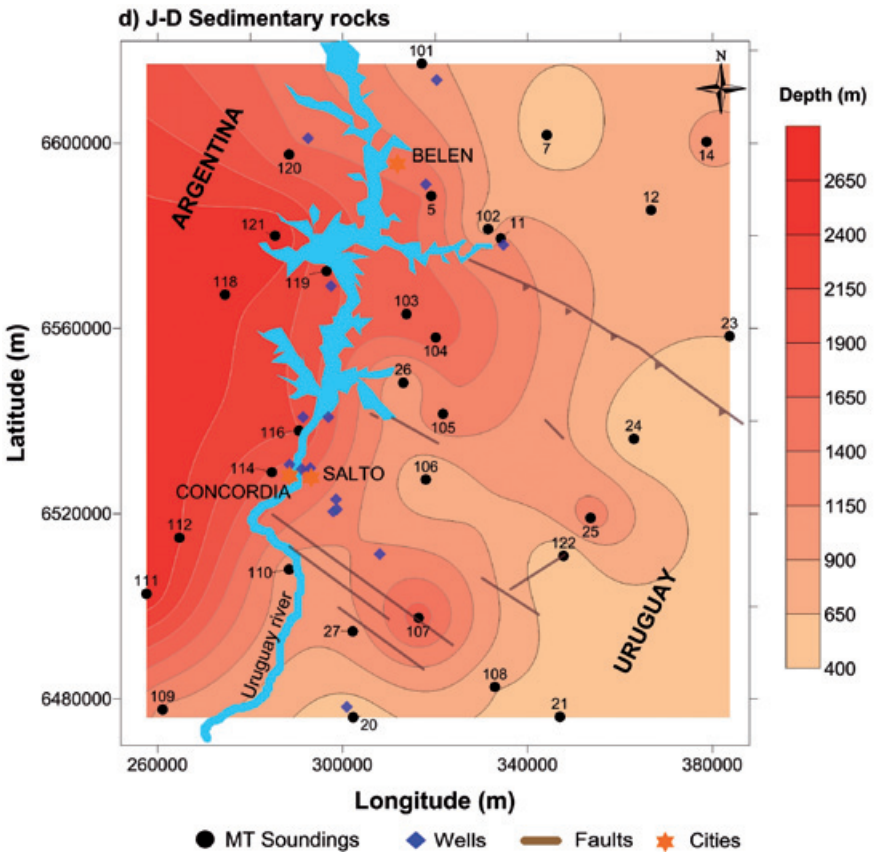

Figure 6c.

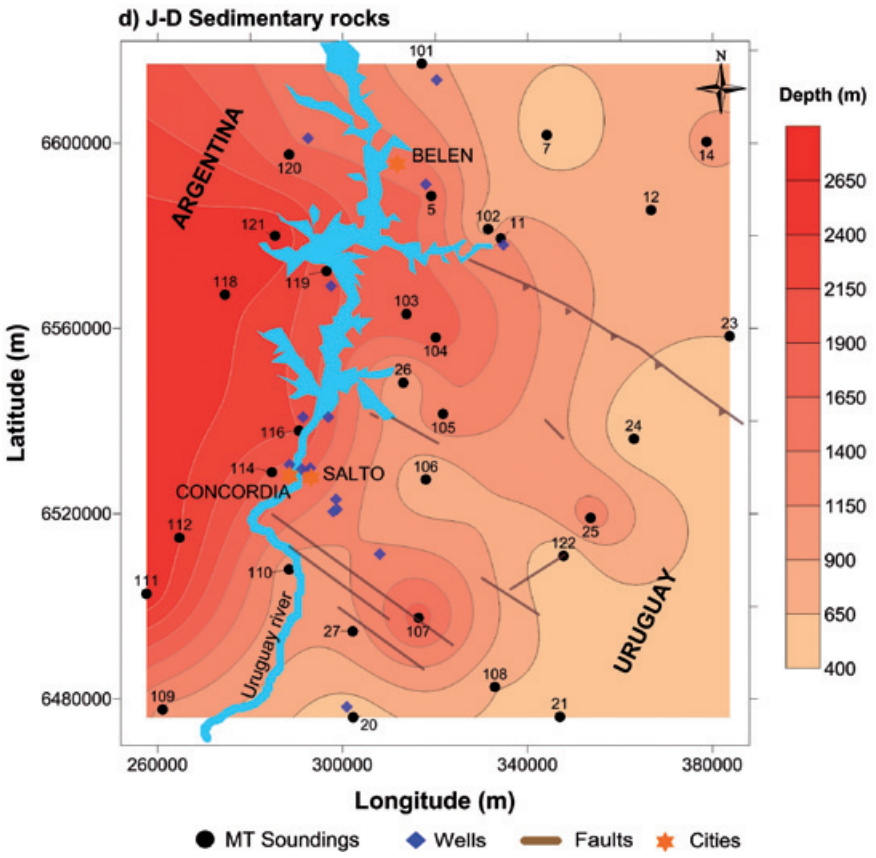

Figure 6d.

Figure 6. Interpolated depth maps to the top of basalts (a), to the base of the basalts (b), and to the base of the basin (c). The interpreted thickness distribution of the Jurassic-Devonian sedimentary rocks is also shown (d).

of the Cretaceous basalts, that varies from few hundred of meters to more than 2,000 m in some sectors, in particular towards the west of the studied zone. The base of this unit, correspond to the top of the Jurassic sedimentary rocks that contain the Guaraní aquifer. To the east of the river, the interface of the basalt layer with the sandstones unit is well defined, but to the west of the river there are some intercalations of diabases in the top of sandstone that makes difficult to trace a clear limit between them. In Figure 6c the depth to the bottom of the Devonian sedimentary sequence is shown, which is regarded as the base of the Chaco-Paraná basin in the area. These results indicate that the Precambrian basement of the basin is dipping towards the west where it can reach depths of 4,500 m or more, whereas to the east of the river estimated maximum depths are around 800 m. Actually, there is an apparent sudden change in the basement depth suggested by the closing of the contour lines about 30 km east of the river and nearly parallel to its trace. The thickness of the Jurassic-Devonian sedimentary package (Figure 6d), obtained from the difference between the base of the basalt unit and the top of the basement, also suggest an important change of volume of sediments occurring at about the same location. Figure 7 shows the extrapolated one-dimensional interpretation summarized in a simplified geological model. It can be appreciated that there is a vertical displacement of several hundred of meters of the basement east of the Uruguay river and parallel to it. Also, the interpreted model suggests another vertical displacement just under the Uruguay river, implying that its trace at the surface is a manifestation of such regional buried structure. According to this interpretation, the major faulting of the Precambrian basement occurred previous or may be contemporary to the emplacement of the Cretaceous basalts.

Two-dimensional models

According to the distortion analysis carried out to the data set, the SAG is within a predominantly one-dimensional stratified earth. However, for frequencies larger than 1 hz, several soundings reveal a more complicated behavior. An indication of this become apparent from the results of the one-dimensional extrapolated model (Figure 7) that suggests the existence of regional faults corresponding to depths of the basement. In order to find out if such structures have a two-dimensional or a more complex distribution, we applied Swift (1967) and Bahr (1988, 1991) methods to analyze the azimuthal strike angle at

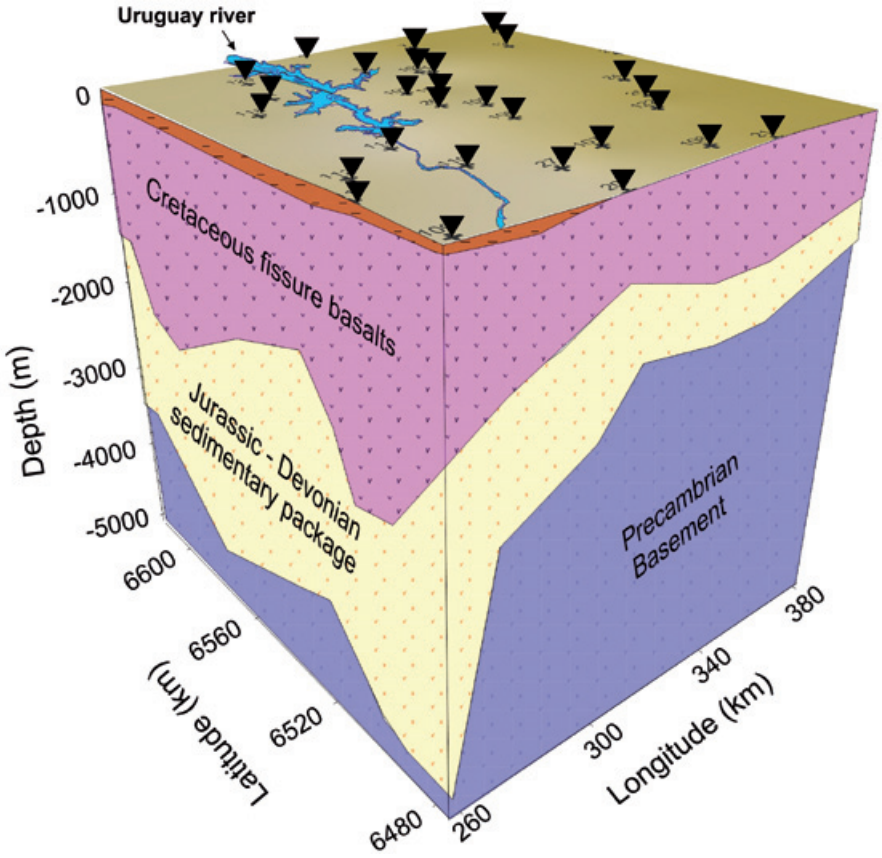

Figure 7. Geologic model of the Guaraní Aquifer System obtained from the extrapolation of the 1D inversions of the invariant of the resistivity and phase curves from the 31 magnetotelluric soundings. It can be observed that the Precambrian basement becomes deeper to the west. Also, it appears that bellow the Uruguay river there is an important structural discontinuity to the west, which probable has a regional character.

every sounding for frequencies below 1 Hz and frequencies where the dimensionality was 2D or 3D. Figure 8 shows the results obtained, that suggest a consistent mainly two-dimensional behavior at low frequencies with values for the strike angle around 0º. This result implies the existence of a deep regional structure with a predominant North-South orientation that can be regarded as the direction of the principal structure in this zone. The little dispersion of estimated azimuth indicates a well defined two-dimensional feature.

Using the azimuth value of 0º we carried out the 2D inversion of 4 profiles approximately perpendicular to the regional structure, which approximately coincide with the Uruguay river, and 2 profiles parallel to it (Figure 9) using the Winglink7 program. There was not need to rotate the impedance tensor to the regional strike as the measurement X axis of the soundings coincided systematically with the north-south direction and the Y axis with the east-west direction. Under this conditions, the transverse magnetic or TM mode is defined by the resistivities $\rho_{xy}(\omega) = \rho_{TM}(\omega)$ and phases $\phi_{xy}(\omega) = \phi_{TM}(\omega)$ and correspondingly, the transverse electric or TE mode is defined by $\rho_{yx}(\omega) = \rho_{TE}(\omega)$ and $\phi_{yx}(\omega) = \phi_{TE}(\omega)$. Both modes were inverted simultaneously using 50 iterations and a fix variance of 2.5%. We used the Rodi and Mackie's (2001) inversion code, which makes a regularization of the Tikhonov equation using the method of non-linear conjugate gradients. We have made several attempts to find out the optimal number of necessary iterations for the inversion in order to obtain the minimum RMS error with the best regularization parameter. The regularization parameter τ controls the balance between the measured MT data and the model of resistivity; high values of τ produce a resistivity model with a poor fit with the measured data but spatially smoothed, while small values of τ produce a better fit of the measured data but the model can be coarse and containing artifacts (Unsworth *et al*., 2005). Figure 10 shows the resulting resistivity models (upper half) obtained after 50 iterations using a regularization parameter $\tau = 4$, and the interpreted geology profiles (lower half) using the available lithology from wells. The mean quadratic error associated with the models fit, using a floor standard deviation error for resistivity and phase for both polarization modes and tipper was: RMS=3.1, profile 1; RMS=1.9, profile 2; RMS=2.4, profile 3; RMS=2.4, profile 4; RMS=1.91, profile 5; and RMS=2.84, profile 6. Profiles 1, 3, 5, and 6 cross approximately perpendicular the Uruguay river. They show a consistently dipping basement and

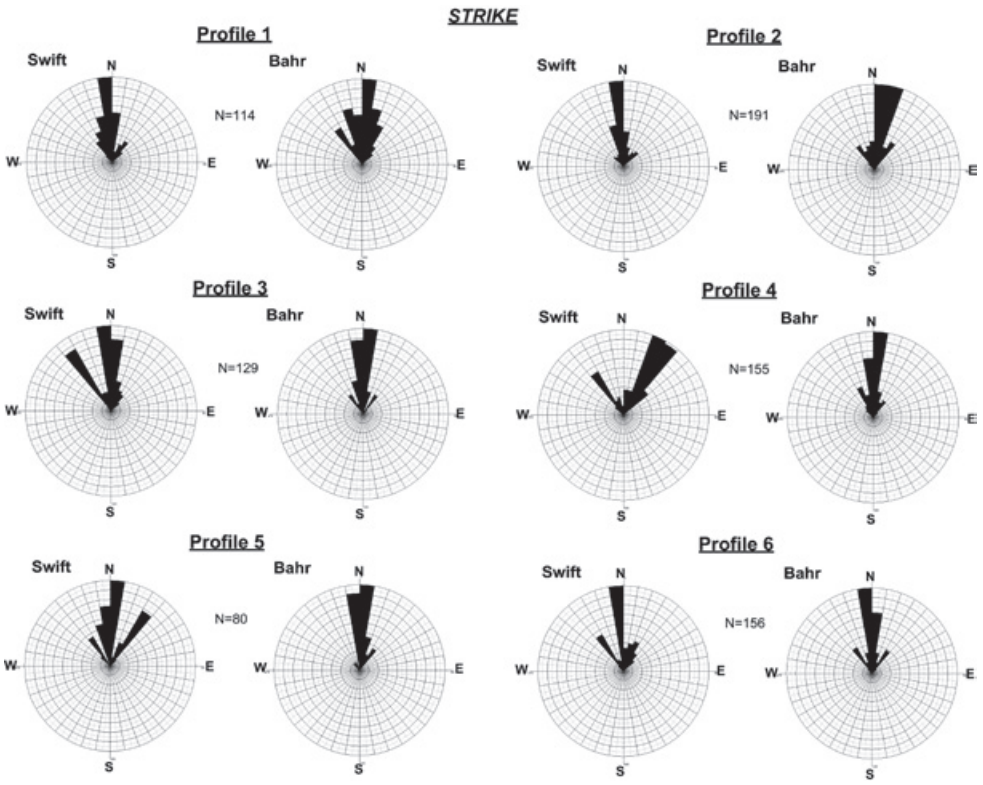

Figure 8. Azimuth of the regional strike, corresponding to the direction of the main structure in the zone, obtained from the dimensionality analysis using the methods of Swift (a) and Bahr (b). Both methods provide azimuth close to 0°.

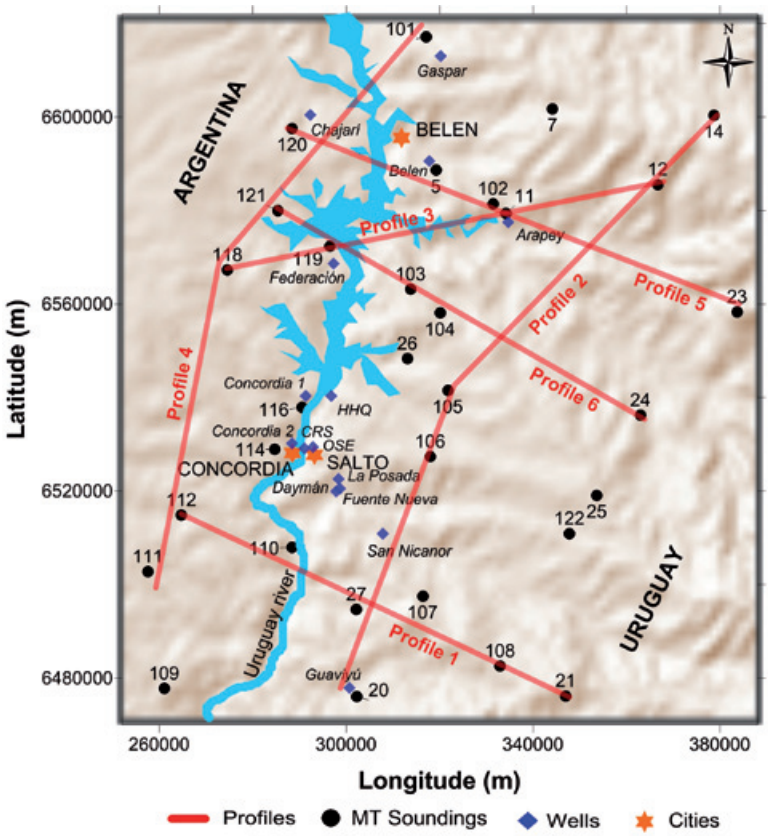

Figure 9. Location of the modeled profiles using a 2D algorithm.

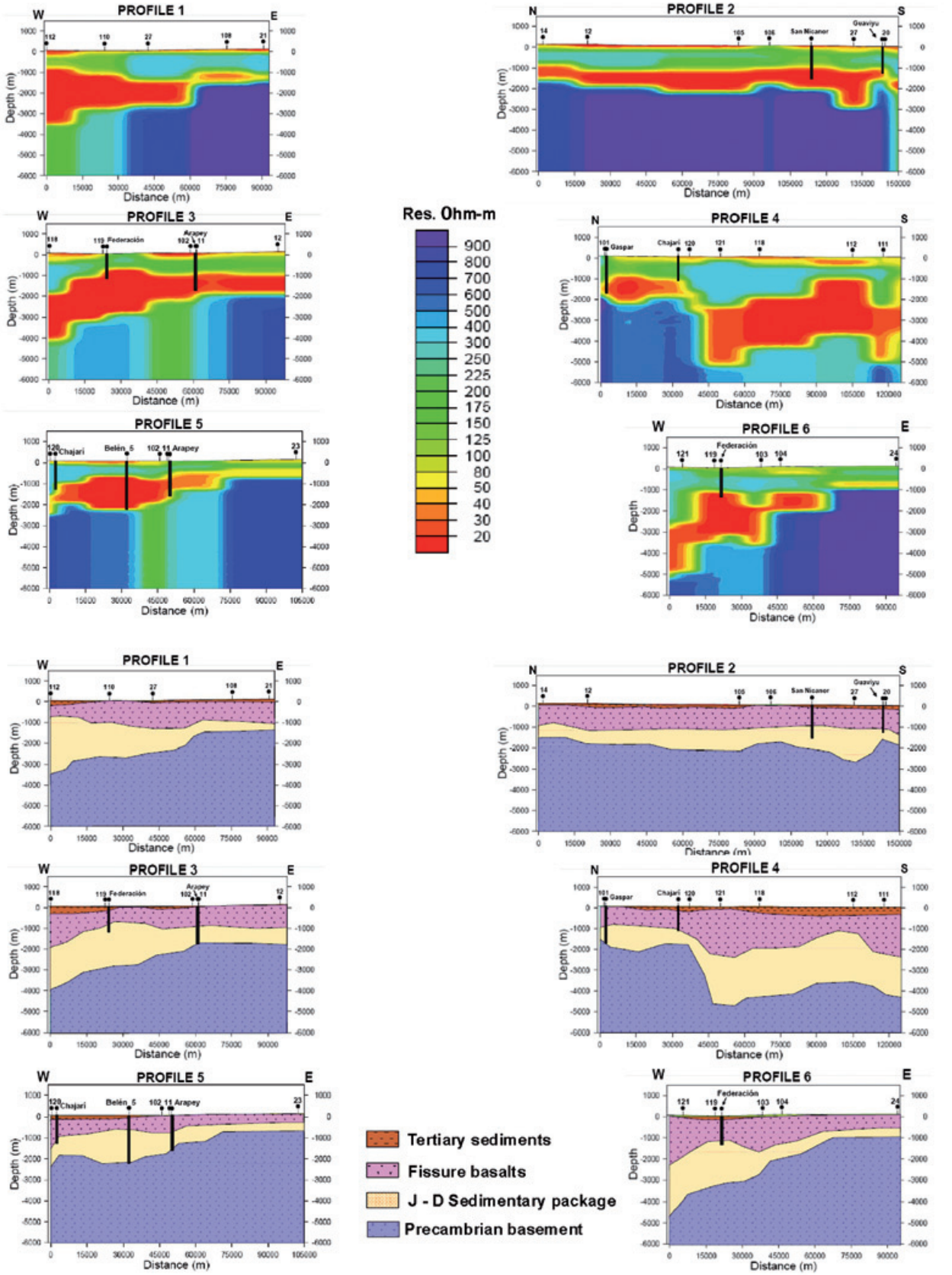

Figure 10. Two-dimensional models of resistivity (upper half) and corresponding geologic interpretation (lower half) obtained from the correlation of resistivities deduced from parametric soundings (see Table 1).

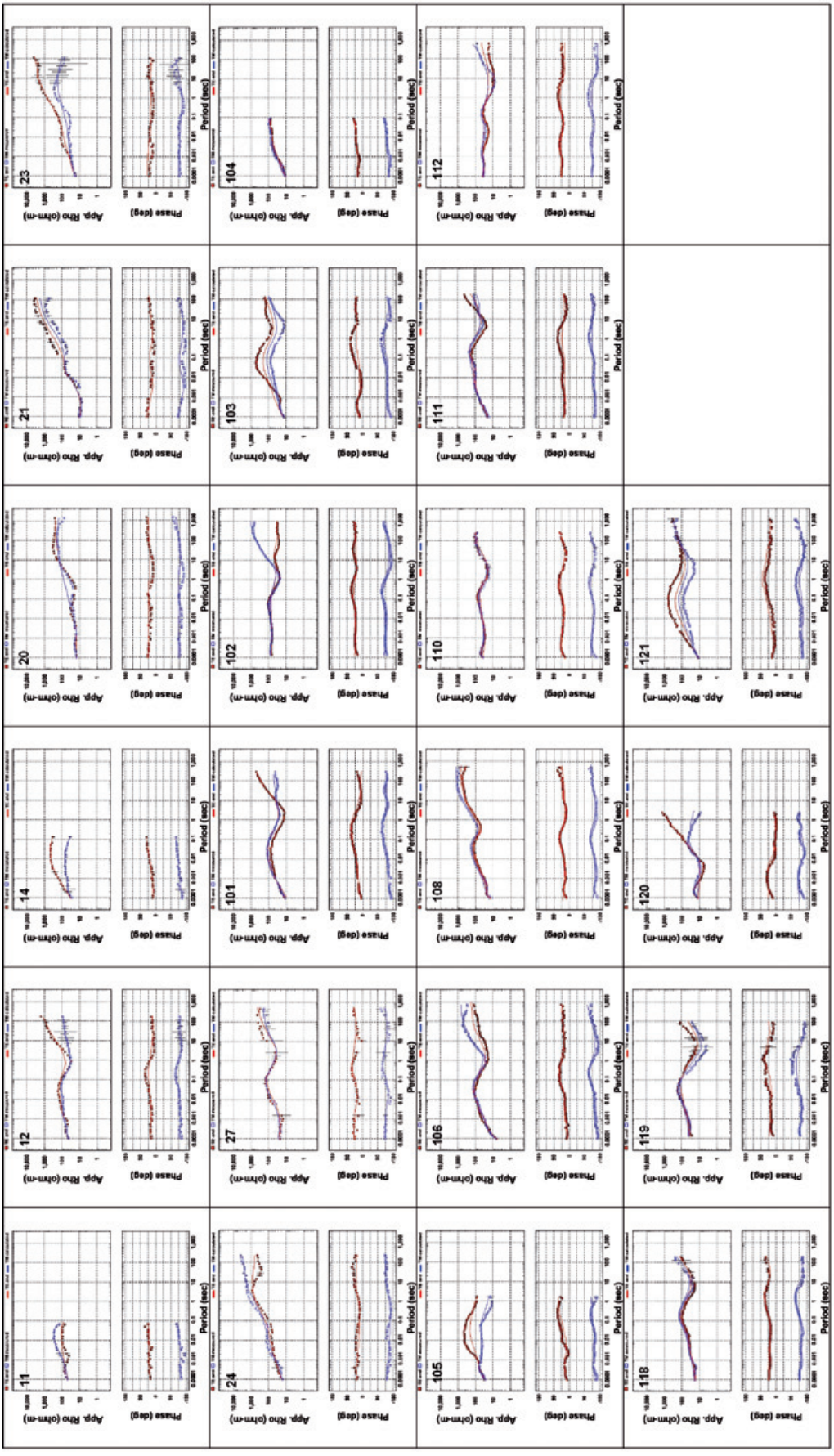

Figure 11. Plots of the resistivity and phase field curves, with the fitting curves from the 2D inversion.

thickening of the sedimentary Jurassic-Devonian package to the west, towards Argentina. To the east of the river, Profile 2 suggests a tectonically stable basement except for perceptible variations around Site 27, where it becomes deeper. It appears that the observed feature is related to the fault system mapped at the surface, which seems to be affecting the basement as well. The induction arrows at Sites 27 and 110 at 0.01 Hz (Figure 5c) support the existence of a nearby discontinuity at basal depths. This Profile 2, running parallel to the Uruguay river but crossing it to the north, shows a clear basement discontinuity that may be related to the westward continuation of the NE-SW fault mapped to the east. However, such fault does not have a significant vertical displacement to the east of the Uruguay river, although it is possible to observe a noticeable variation around Site 105. Figure 11 shows the resistivity and phase field curves, with the fitting curves obtained from the 2D data inversion.

Conclusions

Given the good contrast between the confining bottom and top resistive geological units with the more conductive sedimentary rock package that contains Jurassic and Devonian rocks, the magnetotelluric soundings of wide spectrum constitute an adequate tool to investigating the SAG as well as the Chaco-Paranense basin in this region. The 31 measured sites represent an important advance for the geological knowledge of the basin. The interpretation of this information produced a previously inexistent model of the distribution of the main geological units present in the area. However, despite the good lithologic control and the well defined electric contact between the Jurassic sandstones and the Cretaceous basalts, the presence of intercalations of thin sandstones reduces accuracy in the determination of the depth to this interface, in this cases we detect the boundary of the basalts at the midpoint of collations. Also, because of the poor resistivity contrast between the Jurassic-Triassic SAG and the Permian-Devonian sedimentary rocks, both relatively conductive, is not possible to separate them individually, thus we only estimate their combined thickness.

The applied distortion and dimensionality criteria to the data suggest that the ground can be regarded as stratified, without major lateral discontinuities, to depths larger than 2 km. Using these results we obtained a model of the distribution of the sedimentary Jurassic-Devonian package from the interpolation of the 1D inversion of the invariant of the 31 soundings. A complementary two-dimensional inversion along six selected profiles across and along the Uruguay river, show consistent results with the 1D interpolated block model. These results support the existence of a NS basement discontinuity below the river, which could be interpreted as a regional normal fault with the down block to the west. The deduced orientation of the structure appears to have a tectonic relation with the trace of the Uruguay river that also bears an approximately NS direction.

According to these results, the vertical displacements of basement rocks across the fault could be as large as 2 km or more. The Jurassic-Devonian sedimentary package west to the river is thicker than to the east and the basalts also appear to have larger thicknesses than to the east of the river. In addition, one of the 2D profiles (profile 4) suggests the existence of another possible vertical discontinuity in the basement at the NW quadrant of the study area. It appears that such basal discontinuity is related to the westwards prolongation across the river of the Arapey fault.

Acknowledgments:

The authors wish to acknowledge the financing of the Guaraní Aquifer System Project (PSAG) for the Sustainable Development and Environmental Protection. We also wish to thank the group of Groundwater Hydrology of the Faculty of Engineering of the *Universidad de la República* in Montevideo, the support we receive for the field work activities. Most of the data of this research work are from the master thesis of Fernando Corbo of the Earth Sciences program of the National University of Mexico. The postgraduate studies of Fernando Corbo were financed by the *Dirección General de Estudios de Posgrado* of the Universidad Nacional Autónoma de México *(DGEP-UNAM).*

Bibliography

Araujo L.M., Franca A.B., Potter P.E., 1999, Hydrogeology of the Mercosul aquifer system in the Paraná and Chaco-Paraná Basins, South America, and comparison with the Navajo-Nugget aquifer system, USA. *Hydrogeology Journal*, Springer, v 7(3), pp 317-336.

Bahr K., 1988, Interpretation of the magneto-telluric impedance tensor: regional induction and local telluric distortion. *Journal of Geophysics*, v 62, pp 119-127.

Bahr K., 1991, Geological noise in magneto-tellurical data a classification of distortion types. *Phys. Earth Planet Interiors*, v 66, pp 24-38.

Berdichevsky M.N., Dmitriev V.I., 1976, Distortion of magnetic and electric fields by near surface lateral inhomogeneities, Acta Geod. Geophys. Montan. Acad. Sci. Hung. 11, pp. 447–483.

Bossi J., Schipilov A., 1998, The Arapey Group: confining basalts of the Guaraní Aquifer in Uruguay, Revista Agrociencia, Facultad de Agronomía, Universidad de la República Oriental del Uruguay, v II (1), pp 12-25.

Bossi J., Ferrando L., Fernandez A., Elizalde G., Morales H., Ledesma J., Carballo E., Medina E., Ford I., Montaña J., 1975, Carta geológica del Uruguay. Departamento de Publicaciones. Universidad de la República. Montevideo. Uruguay.

Corbo Camargo, F., 2006, Modelo geofísico del Acuífero Guaraní: zona comprendida entre Uruguay y Argentina. Master Thesis. Universidad Nacional Autónoma de México

Costa-Ribeiro W., 2008, Aqüífero Guarani: Gestão compartilhada e soberania. Estudos Avançados, v 22 (64), pp 227-238, Brazil.

Da Cunha-Reboucas A., Amore L., 2002, O Sistema Aquifero Guaraní – SAG; Rev. Águas Subterrâneas, 16, pp 135-143, Brazil

De Santa Ana H., Ucha N., 1994, Exploration perspectives and hydrocarbon potential of the Uruguayan sedimentary basins. Administración Nacional de Combustibles, Alcohol y Pórtland (ANCAP). Internal report, pp 100.

Ferrando L.A., Andreis R.R., 1986, Nueva estratigrafía en el Gondwana del Uruguay. Actas I Congreso Latinoamericano de Hidrocarburos. ARPEL. Buenos Aires, Argentina. I: 295-323.

Groom R.W., Bailey R.C., 1989, Decomposition of magnetotelluric impedance tensor in the presence of local three-dimensional galvanic distorsion. *Journal Geophysics Research*, v 94, pp 1913-1925.

Groom R.W., Bailey R.C., 1991, Analytical investigations of the effects of near surface three dimensional galvanic scatterers on MT tensor descomposition. *Geophysics*, v 56, pp 496-518.

Jones A.G., Chave A.D., Auld D., Bahr K., Egbert G., 1989, A comparison of techniques for magnetotelluric response function estimation. *Journal of Geophysical Research*, 94, pp. 14,201-14,213.

Lilley F.E.M., Arora B.R., The Sign Convention for Quadrature Parkinson Arrows in Geomagnetic Induction Studies. Reviews of Geophysics and Space Physics, 20, 3, p 513-518.

Lilley F.E.M., 1998a, Magnetotelluric tensor decomposition 1. Theory for a basic procedure, *Geophysics*, 63, 1884-1897.

Lilley F.E.M., 1998b, Magnetotelluric tensor decomposition 2. Examples of a basic procedure, *Geophysics*, 63, 1898-1907.

Montaño, J., Da Rosa, E., and Hernández, M., 2004. Características hidrogeológicas del acuífero transfronterizo Guaraní. Asociación Latinoamericana de Hidrología Subterránea para el Desarrollo. *http://www.alhsud.com/castellano/resultats.asp?results=articulos.*

Oleaga-Bazterrica A., 2002, Contribución a la hidrogeología del acuífero Guaraní en el sector Uruguay. Un enfoque integral. Master Thesis. Universidad Nacional Autónoma de México.

Rodi W., Mackie R., 2001, Nonlinear conjugate gradients algorithm for 2-D magnetotelluric inversion. Geophysics, v 66, (1), pp 174–187.

Soares P.C., Landim P.M.B., 1976, Comparison between the tectonic evolution of the intracratonic and marginal basins in south Brazil. Anais da Academia brasileira de Ciencias, 48, p 313-324.

Sprechmann P., Bossi J., Da Silva J., 1981, Cuencas del Jurásico y Cretácico del Uruguay. *In* Volkheimer, W. y Mussachio (Eds.) Cuencas sedimentarias del Jurásico y Cretácico de América del Sur. Comité Sudamericano del Jurásico y Cretácico. Buenos Aires, Argentina, v 1, pp 239-270.

Swift C.M., 1967, A magnetotelluric investigation of an electrical conductivity anomaly in the southewesteern United State. Doctoral thesis, M. I. T.

Unsworth M., Soyer W., Tuncer V., 2005, Magnetotelluric measurements for determining the subsurface salinity and porosity structure of Amchitka Island, Alaska. Draft Report prepared for CRESP, Department of Physics and Institute for Geophysical Research University of Alberta, Edmonton, Alberta, T6G 0B9, Canada.

Veroslavsky G., Daners G., De Santa Ana H., 2003, Rocas sedimentarias pérmicas en la plataforma continental uruguaya: el prerift de la Cuenca de Punta del Este. Geogaceta, 34: 203-206. España.

Vozoff K., 1989, The magnetotelluric method, *in* Electromagnetic methods in applied geophysics, Nabigian M.N. (Ed.). Soc, Expl. Geophys.

Vozoff K, 1991, *in* Electromagnetic Methods in Applied Geophysics, Vol. 2, Application, pp. 641-711, Society of Exploration Geophysicists, Tulsa.

Weaver J.T., Agarwal A.K., Lilley F.E.M., 2000, Characterization of the magnetotelluric tensor in terms of its invariants. *Geophys. J. Int.*, 141, 321-336.

Geofísica Internacional (2012) 51-1: 39-49

Original paper

New $^{40}Ar/^{39}Ar$ ages from the Central Part of the Chiapanecan Volcanic Arc, Chiapas, México

Juan Carlos Mora*, Paul W. Layer and María del Carmen Jaimes-Viera

Received: June 4, 2010; accepted: August 31, 2011; published on line: December 16, 2011

Resumen

El Arco Volcánico Chiapaneco (AVC; CVA = siglas en inglés) se localiza en la porción central del estado de Chiapas, es una cadena de estructuras volcánicas alineadas en dirección NO-SE de aproximadamente 150 km de longitud.
En su parte central el AVC está compuesto de al menos 10 estructuras volcánicas alineadas al Noreste y concentradas en fallas con rumbo NNO-SSE asociadas al Sistema de Fallas Motagua-Polochic.
Las estructuras son siete Domos Volcánicos (Huitepec, Amahuitz, La Iglesia, Mispía, La Lanza, Venustiano Carranza y Santotón), un Cráter de Explosión (Navenchauc), una Estructura de Colapso (Apas), y un Complejo de Domos Volcánico (Tzontehuitz).
En este trabajo, reportamos 13 nuevas edades $^{40}Ar/^{39}Ar$ de rocas de los siete domos que incrementan las dataciones disponibles para la actividad volcánica durante el Cuaternario, en la parte central del Arco Volcánico Chiapaneco. Con las nuevas dataciones y las reportadas en bibliografía se tiene al Complejo de Domos Tzontehuitz como la estructura más antigua 2.1 Ma y al Domo Volcánico Venustiano Carranza como el de actividad más reciente de 0.225 Ma.

Palabras clave: Arco Volcánico Chiapaneco, domos volcánicos, edades $^{40}Ar/^{39}Ar$.

Abstract

The Chiapanecan Volcanic Arc (CVA), located in the central portion of the State of Chiapas, is a 150 km long chain of volcanic structures aligned in a NW-SE direction.
The central part of the CVA is composed of an irregular northeast-trending alignment of more than 10 volcanic structures, generally centered along NNW-SSE trending faults splayed from the Motagua-Polochic Fault System. Among these structures are seven volcanic domes (Huitepec, Amahuitz, La Iglesia, Mispía, La Lanza, Venustiano Carranza, and Santotón), one explosion crater (Navenchauc), one collapse structure (Apas), and one dome complex (Tzontehuitz).
In this work, we report thirteen new $^{40}Ar/^{39}Ar$ ages of rocks from seven domes that increase the available geochronometric data on Quaternary volcanic activity in the central part of Chiapanecan Volcanic Arc. From the new and previous data, we identified the Tzontehuitz Dome Complex as the oldest volcanic center in the CVA, yielding an age of 2.1 Ma, and the Venustiano Carranza Volcanic Dome as exhibiting the most recent activity in the zone, with an age of 0.225 Ma.

Key words: Chiapanecan Volcanic Arc, volcanic domes, ages $^{40}Ar/^{39}Ar$.

J. C. Mora
Departamento de Vulcanología
Instituto de Geofísica
Universidad Nacional Autónoma de México
Ciudad Universitaria
Delegación Coyoacán, 04510
México D.F., México
*Corresponding author: jcmora@geofisica.unam.mx

P. W. Layer
Geophysical Institute
University of Alaska Fairbanks
Fairbanks, AK, 99775, USA

M. C. Jaimes-Viera
Posgrado de Ciencias de la Tierra
Instituto de Geofísica
Universidad Nacional Autónoma de México
Ciudad Universitaria
Delegación Coyoacán, 04510
México D.F., México

Introduction

The Chiapanecan Volcanic Arc (CVA), located in the central portion of the State of Chiapas, is a 150 km long chain of volcanoes irregularly aligned in a northwestly direction between two more prominent volcanic features: the Trans-Mexican Volcanic Belt (TMVB) to the northwest and the Central American Volcanic Arc (CAVA) to the southeast. While both the TMVB and the CAVA have been the focus of numerous geological and geochronological studies (Demant, 1976, 1978; Nixon, 1982; Siebe *et al*., 1995; Suter *et al*., 1995; Aguirre *et al*., 1998; Aguirre *et al*., 1998; Ferrari, *et al*., 1999; Wallace *et al*., 1999; Aguirre and Carranza, 2000), the CVA has been relatively unmapped and poorly described until recently (Jaimes-Viera *et al*. 2004; Jaimes-Viera, 2006; Mora *et al*., 2007). These authors have identified eight volcanic domes (Navenchauc, Huitepec, Amahuitz, La Iglesia, Mispía, La Lanza, Venustiano Carranza and Santotón), one explosion crater (Navenchauc), one collapse structure (Apas), and one dome complex (Tzontehuitz) within the CVA, and have documented changes in the eruptive style and chemical composition of the eruptive products of these volcanic centers.

The CVA lies in a tectonically complex region where three tectonic plates interact: the North American Plate, the Caribbean Plate, and the Cocos Plate (Figure 1). A zone of lateral displacement and a zone of convergence define the boundaries between these plates. The first is characterized by a regional system of left-lateral strike-slip faults known as the Motagua-Polochic Fault System, formed by the eastward migration of the Caribbean Plate relative to the North American Plate, and the second is formed by the subduction of the Cocos plate under the North American and Caribbean Plates (Mora *et al*., 2007).

Because of its geographic location, the CVA has a very important role in the geological evolution of the region. The purpose of this study is to demonstrate that the CVA volcanic activity is continuous from 2 Ma to the present and it is related to both the TMVB and CAVA.

Geologic setting and previous work.

The CVA was first described by Damon and Montesinos (1978) who named it "Modern Chiapanecan Volcanic Arc". These authors described it as a 150 km- long volcanic structure aligned NW-SE. Damon and Montesinos (1978) concluded that the CVA was formed as a result of a readjustment of the direction of plate motion of the Cocos Plate at 2.79 Ma; they believed it to be essentially continuous with the TMVB. Capaul (1987) renamed this arc the "Chiapanecan Volcanic Arc" (CVA), and described it as composed of Quaternary volcanoes, including El Chichón volcano, characterized by low eruptive

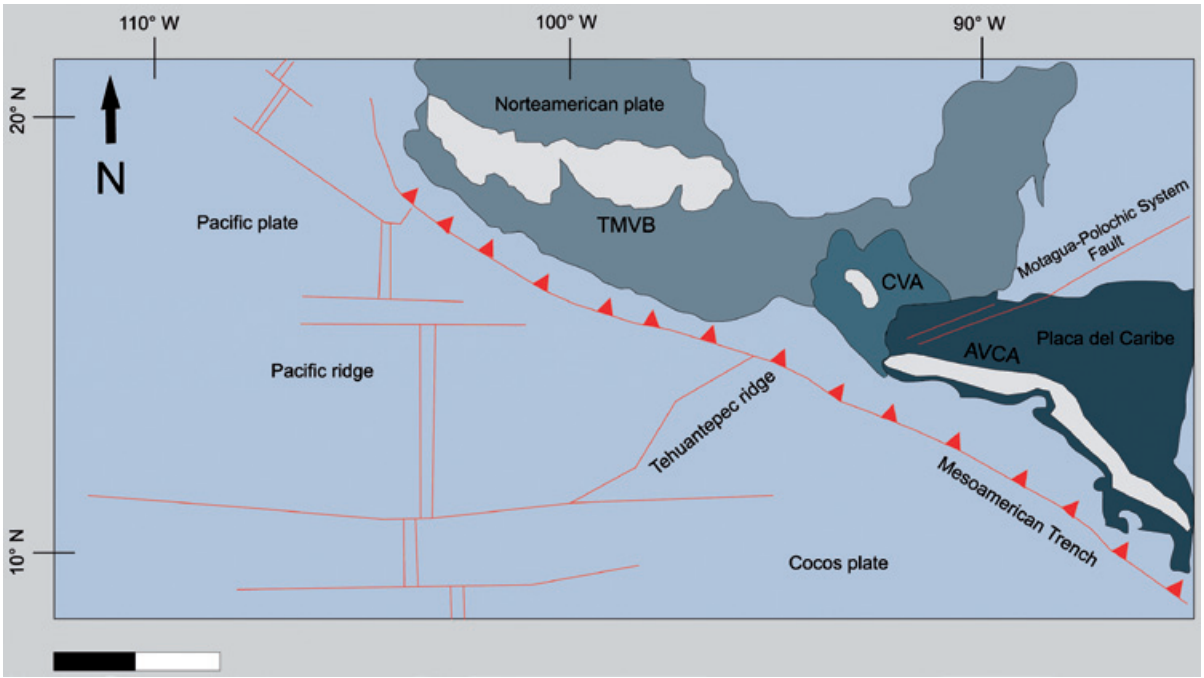

Figure 1. Location map and tectonic setting of the Chiapanecan Volcanic Arc (CVA), Trans-Mexican Volcanic Belt (TMVB) and Central American Volcanic Arc (CAVA).

volume and that were formed in a tectonically complex region of Chiapas. All eruptive products of the CVA have intermediate, calc-alkaline compositions except El Chichón which has some basic alkaline affinity (trachybasalts) (Capaul, 1987). Jaimes-Viera *et al*. (2004) conducted preliminary mapping of the central part of the CVA and showed 11 volcanic structures with deposits of pyroclastic flows and associated fall deposits (Figure 2; Damon and Montesinos, 1978; Capaul, 1987; Macias *et al*., 2003; Jaimes-Viera, *et al*., 2004).

The volcanic activity in the CVA was mainly effusive, accompanied by less frequent explosive and phreatomagmatic events and is characterized by volcanic domes accompanied by block-and-ash flows, ash flows with accretionary lapilli, falls, and pumice flows. The volcanic structures and deposits are calcalkaline in composition with a medium to high content of potassium. CVA volcanic rocks vary from basaltic andesite to dacite with SiO2 between 55 and 66 wt.% (Mora *et al*., 2007).

Jaimes-Viera (2006) and Mora *et al*. (2007) divided the study area into three groups, according with their location. The first group is represented by the Tzontehuitz Dome Complex; located at the northern part. The second group is composed of the Apas, Navenchauc, Huitepec and Amahuitz volcanic structures; they were emplaced between 2 faults: Chicoasén-Malpaso-Huixtlán to the north and Bajucú to the south. The last group consists of the Mispía, La Iglesia, Santotón and Venustiano Carranza domes. This group is characterized by a N-S alignment (Figure 2).

$^{40}Ar/^{39}Ar$ geochronologic study

For $^{40}Ar/^{39}Ar$ analysis, we sampled lava domes and juvenile blocks from pyroclastic flow deposits of 9 of the 11 volcanic structures in the CVA. Thirteen crushed and sieved (to ~0.3 mm) whole- rock samples (pheoncryst-free groundmass separates) were dated in the Geochronology Laboratory at University of Alaska Fairbanks (Layer, 2000). The monitor mineral

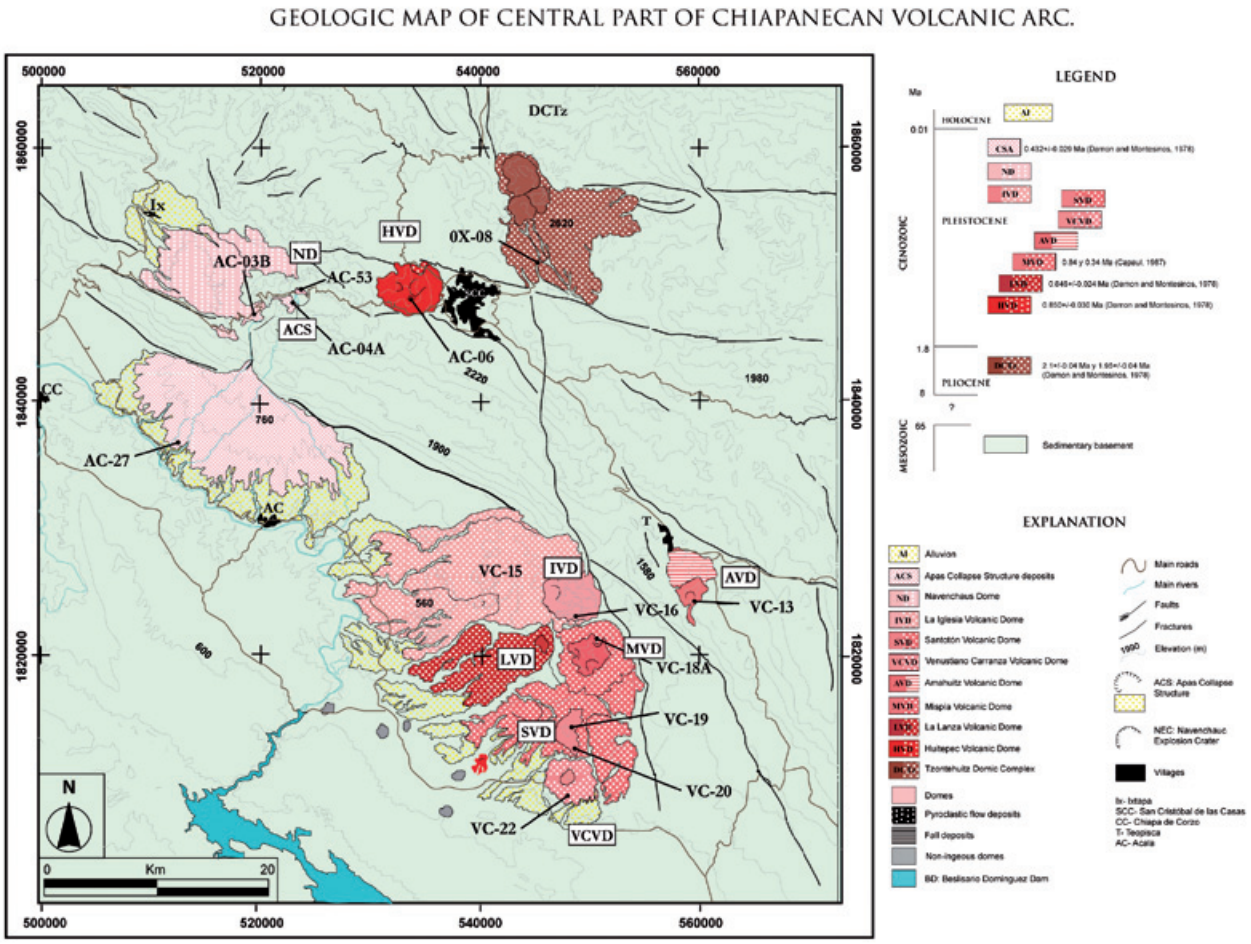

Figure 2. Geologic map of the central part of the Chiapanecan Volcanic Arc (Jaimes-Viera, 2006) showing the samples from this studio.

TCR-2 with an age of 27.87 Ma (Lanphere and Dalrymple, 2000) was used to monitor neutron flux (and calculate the irradiation parameter, J). The samples and standards were wrapped in aluminum foil and loaded into aluminum cans of 2.5 cm diameter and 6 cm height. The samples were irradiated in position 5c of the uranium-enriched research reactor of McMaster University in Hamilton, Ontario, Canada for 0.5 megawatt-hours. Two different irradiations were done in 2005 and 2006.

Upon their return from the reactor, ~10 chips of the samples and monitors were loaded into 2 mm-diameter holes in a copper tray that was then loaded in an ultra-high vacuum extraction line. The monitors were fused, and samples heated, using a 6-watt argon-ion laser following the technique described in York *et al*. (1981), Layer *et al*. (1987), and Layer (2000). Argon purification was achieved using a liquid nitrogen cold trap and a SAES Zr-Al getter at 400°C for 10 minutes. The samples were analyzed in a VG-3600 mass spectrometer. The argon isotopes measured were corrected for system blank and mass discrimination, as well as calcium, potassium and chlorine interference reactions following procedures outlined in McDougall and Harrison (1999). System blanks generally were $2x10^{-16}$ mol ^{40}Ar and $2x10^{-18}$ mol ^{36}Ar, which are 10 to 50 times smaller than fraction volumes. Mass discrimination was monitored by running both calibrated air shots and a zero-age glass sample. These measurements were made on a weekly to monthly basis to check for changes in mass discrimination. Table 1 show the ages obtained for the CVA samples along with previously published K-Ar ages from Damon and Montesinos (1978). All ages are reported at the 1-sigma level. For each run, plateau and isochron ages were calculated. For most samples, there was agreement between the two ages, and only the plateau ages are reported (the exceptions being those samples that had significant argon loss). Criteria for a plateau are that the step heating contain three or more contiguous fractions constituting at least 50% of gas release, and the agreement in age between the fractions is significant at the 95% confidence level (as seen by an MSWD < ~2.5). All samples except VC-13C have significant plateaus. For some samples, two runs were done. Plateau ages from these samples were averaged together to get a 'best' plateau age (Table 1). Analytical data are reported in Appendix 1.

Tzontehuitz Dome Complex.

This volcanic structure was first studied by Damon and Montesinos (1978) who referred to it as "Tzontehuitz Volcano". Capaul (1987) observed that the volcanic structure is a volcanic complex. Mora *et al*. (2007) considered this structure to be composed of at least three domes (El Calvario, Tzontehuitz 1 and 2) aligned in a north-south orientation with associated pyroclastic flow deposits (Figure 2). Because it appears to be a multi-phase structure, it was described as a dome complex, rather than as a single dome. The area covered by the TzDC is approximately 16 km^2 (Mora *et al*., 2007). The first geochronological data were reported by Damon and Montesinos (1978), who obtained two K-Ar whole-rock ages: 2.14 ± 0.04, and 1.95 ± 0.04 Ma. Afterward, Capaul (1987) dated by fission- track technique three new samples and the data obtained are: (a) 1.360 ± 0.142 Ma (pumice); (b) 1.758 ± 0.190 Ma (pumice); and (c) 1.776 ± 0.168 Ma (dome). In this work, we dated one sample from Tzontehuitz 1 Dome (OX-08, Figure 2), which was classified as andesite. Our $^{40}Ar/^{39}Ar$ plateau age for this sample is 2.132 ± 0.022 Ma (Figure 3), similar to the oldest K-Ar age.

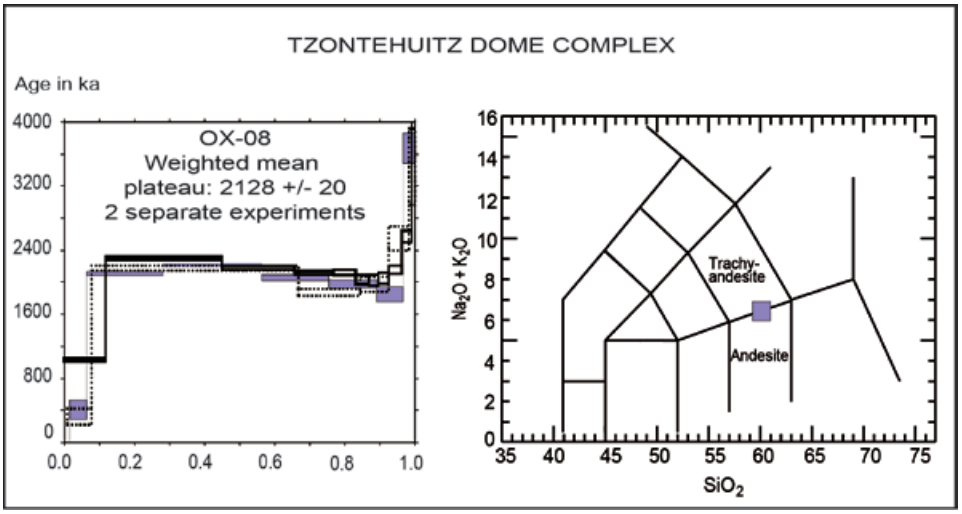

Figure 3. Age spectra plots for $^{40}Ar/^{39}Ar$ data and block chemical classification from Tzontehuitz Dome Complex.

Table 1. Summary of data on dated rocks from Chiapanecan Volcanic Arc.

Volcanic Source	Sample	% SiO2	Rock Type	Integrated Age (Ma)	Plateau or K-Ar Age (Ma)	Plateau Information
VCVD	VC-22	62.78	Trachydacite	0.384 ± 0.051	0.225 ± 0.030	4 fractions, 83% ^{39}Ar release, MSWD = 0.7
ND	AC-53	63.21	Dacite	0.266 ± 0.007	0.277 ± 0.005	7 fractions, 88% ^{39}Ar released, MSWD = 0.7
NEC	AC-03B	63.72	Dacite		0.369 ± 0.018	2-run weighted average, MSWD = 0.2
	run 1			0.391 ± 0.037	0.378 ± 0.028	5 fractions, 78% ^{39}Ar release, MSWD = 1.4
	run 2			0.166 ± 0.059	0.363 ± 0.024	6 fractions, 87% ^{39}Ar release, MSWD = 1.1
ACS	AC-04A	61.37	Andesite		0.316 ± 0.009	2-run weighted plateau age, MSWD = 1.2
	run 1			0.336 ± 0.029	0.344 ± 0.027	5 fractions, 99% ^{39}Ar release, MSWD = 0.4
	run 2			0.334 ± 0.009	0.313 ± 0.009	6 fractions, 75% ^{39}Ar release, MSWD = 1.4
ACS*	10*	---	Dacite		0.432 ± 0.029	K-Ar Hornblende
ACS	AC-27	62.54	Dacite		0.447 ± 0.011	2-run weighted plateau age MSWD = 1.3
	run 1			0.392 ± 0.030	0.423 ± 0.023	3 fractions, 92% ^{39}Ar release, MSWD = 1.3
	run 2			0.429 ± 0.012	0.452 ± 0.010	3 fractions, 71% ^{39}Ar release, MSWD = 0.04
IVD	VC-15	63.47	Dacite		0.676 ± 0.005	2-run weighted plateau age, MSWD = 0.6
	run 1			0.695 ± 0.019	0.689 ± 0.017	5 fractions, 99% ^{39}Ar release, MSWD = 0.3
	run 2			0.682 ± 0.008	0.675 ± 0.005	5 fractions, 91% ^{39}Ar release, MSWD = 1.0
IVD	VC-16	61.15	Andesite		0.689 ± 0.033	2-run weighted plateau age MSWD = 0.01
	run 1			0.598 ± 0.105	0.692 ± 0.041	4 fractions, 59% ^{39}Ar release, MSWD = 0.4
	run 2			0.537 ± 0.103	0.685 ± 0.054	6 fractions, 96% ^{39}Ar release, MSWD = 1.7

Table 1. Summary of data on dated rocks from Chiapanecan Volcanic Arc.

Volcanic Source	Sample	% SiO2	Rock Type	Integrated	Plateau or K-Ar	Plateau
AVD	VC-13C	60.80	Andesite	0.581 ± 0.058	0.739 ± 0.110	3 fractions, 77% ^{39}Ar release, MSWD = 9.4
LVD*	9*	---	Dacite		0.846 ± 0.024	K-Ar Hornblende
HVD	AC-06	60.17	Andesite	0.295 ± 0.015	0.289 ± 0.014	6 fractions, 99% ^{39}Ar release, MSWD = 0.2
HVD* MVD	8* VC-18a	--- 57.10	Andesite Andesite	0.982 ± 0.014	0.850 ± 0.030 0.975 ± 0.011	K-Ar Hornblende 5 fractions, 89% ^{39}Ar release, MSWD = 0.7
SVD	VC-20	58.67	Andesite	1.027 ± 0.010	0.995 ± 0.009	4 fractions, 70% ^{39}Ar release, MSWD = 1.1
SVD	VC-19	56.75	Trachyandesite	0.875 ± 0.076	1.042 ± 0.051	5 fractions, 74% ^{39}Ar release, MSWD = 0.3
TzDC*	7*	---	Dacite		1.95 ± 0.04	K-Ar Hornblende
TzDC	OX-08	59.66	Trachyandesite	2.107 ± 0.012	2.132 ± 0.022	7 fractions, 51% ^{39}Ar release, MSWD = 2.2
TzDC*	6*	---	Andesite		2.14 ± 0.04	K-Ar Hornblende

Ages reported at ± 1 sigma. Abbreviations: VCVD: Venustiano Carranza Volcanic Dome; ND: Navenchauc Dome; NEC: Navenchauc Explosion Crater; ACS: Apas Collapse Structure; IVD: La Iglesia Volcanic Dome; AVD: Amahuitz Volcanic Dome; LVD: La Lanza Volcanic Dome; HVD: Huitepec Volcanic Dome; MVD: Mispía Volcanic Dome; SDV: Santotón Volcanic Dome; TzDC: Tzontehuitz Dome Complex., Plateau: 3+ consecutive fractions, MSWD (mean square weighted deviates) < ~2.5, more than 50% 39Ar release. Note that VC-13C age is not a true plateau age, but represents a weighted average age of three plateau-like fractions. For samples with two runs, a weighted average of the two plateau ages is reported. Bold: Best age for the sample. * K-Ar sample number, source and age data from Damon and Montesinos, 1978.

Apas collapse structure

This structure is located in the "Sierra de los Altos de Chiapas" (Jaimes-Viera, 2006; Mora *et al*., 2007). It is 2.87 km in diameter and associated with it is a sequence of pyroclastic flows (block-and-ash flows, ash flows, and pumice flows), with two directions of emplacement: to SW and NW (Jaimes-Viera, 2006; Mora *et al*., 2007). Damon and Montesinos (1978) reported a K-Ar age from this structure of 0.432 ± 0.029 Ma. They dated a hornblende from a dacite, which was collected from the deposit emplaced to the SW. We sampled two kinds of blocks with andesitic composition. The first sample was taken from pyroclastic flow to the SW (AC-27, Figure 2). The second sample was taken from the contact between the basement and pyroclastic flow (AC-04A). We obtained two different plateau ages, the oldest is 0.447 ± 0.010 Ma (AC-27) and the youngest is 0.316 ± 0.009 Ma (AC-04A) (Figure 4a). The oldest age that we obtained is comparable to that from Damon and Montesinos (1978).

Navenchauc Explotion Crater (NEC).

The Navenchauc crater (approximately 1.3 km in diameter) is also located in the "Sierra de los Altos de Chiapas", close to Apas. Associated with this structure is one dome and associated

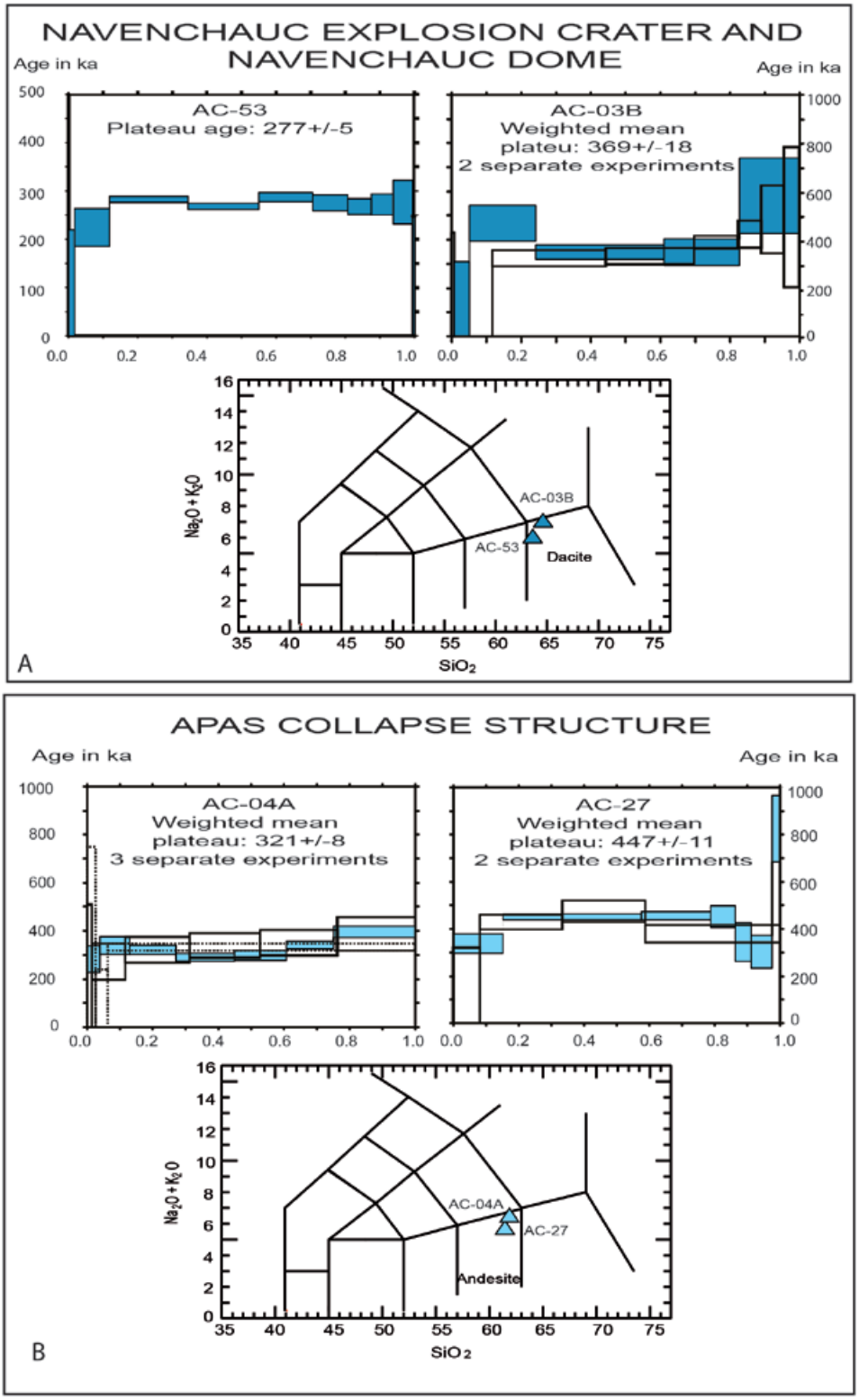

Figure 4. Age spectra plots for $^{40}Ar/^{39}Ar$ data and chemical blocks classification. (a) Navenchauc crater explosion; (b) Apas Collapse structure.

pyroclastic flow deposits. The Navenchauc Dome is found at the kilometer 64 milepost of Federal Highway 90 (Tuxtla Gutiérrez-San Cristóblal de las Casas). This dome has a maximum height of 100 m and a mean diameter of 575 m (Mora *et al*., 2007). We obtained two $^{40}Ar/^{39}Ar$ ages for two samples. The first was collected from a pyroclastic flow (AC-03B, Figure 2) and its age was 0.369 ± 0.018 Ma, making it the oldest unit from this eruptive center. The second sample

dated was taken from the dome (sample AC-53, Figure 2) with an age of 0.277 ± 0.005 Ma (Figure 4b). The chemical composition of both blocks is dacitic.

Huitepec Volcanic Dome (HVD)

The Huitepec Volcanic Dome is located 1 km west of San Cristóbal de las Casas (Figure 2). It has a mean diameter at its base of 5.2 km, covers an area of ~ 21.2 km^2, and an approximate height of 520 m. Associated with this dome is an ash flow deposit of (Mora *et al*., 2007). This structure has been studied by Damon and Montesinos (1978), who called it an andesitic dome; a hornblende they dated from the dome gave a K-Ar age of 0.85 ± 0.03 Ma. In this study, we analyzed an andesite sample (AC-06), which was collected from the dome. The $^{40}Ar/^{39}Ar$ whole-rock plateau age we obtained is 0.289 ± 0.014 Ma (Figure 5a), significantly younger than the previously reported K-Ar age. This could imply at least 2 eruptive periods in the formation of the structure.

Amahuitz Volcanic Dome (AVD)

According to Mora *et al.* (2007), the Amahuitz Volcanic Dome is located in the most eastern part of the study area, ~ 33 km southeast of San Cristobal de las Casas (Figure 2). This volcanic structure is ~ 400 m in height, has a diameter of ~ 2.5 km, and covers an area of ~ 4.4 km^2. It consists of massive, very compact, light gray andesitic rocks with a porphyritic texture and abundant plagioclase, amphibole, and pyroxene (Mora *et al*., 2007). Also, an avalanche deposit and an outcrop of fall deposits appear to be associated with this structure, based on their proximity (Jaimes-Viera, 2006; Mora *et al*., 2007). We sampled a block from the avalanche deposit (VC-13, Figure 2) and we obtained an $^{40}Ar/^{39}Ar$ whole rock age of 0.739 ± 0.110 Ma (Figure 5b).

La Iglesia Volcanic Dome (IVD)

The IVD has been studied by Jaimes-Viera (2006) and Mora *et al*. (2007). It is a circular structure with a diameter of ~ 5 km and a height of 600 m, and covers an area of ~ 18.1 km^2 (Figure 2). It consists of massive rock and associated deposits of block-and-ash-flows that were emplaced principally to the southwest (Mora *et al*., 2007). The samples dated were taken from the dome and we obtain two identical ages, of 0.689 ± 0.033 Ma (VC-16, Figure 2) and 0.676 ± 0.005 Ma (VC-15, Figure 6A). However, the first sample analyzed has an andesitic composition (61.15wt% SiO_2), whereas the second dated sample is dacite (63.47wt% SiO_2).

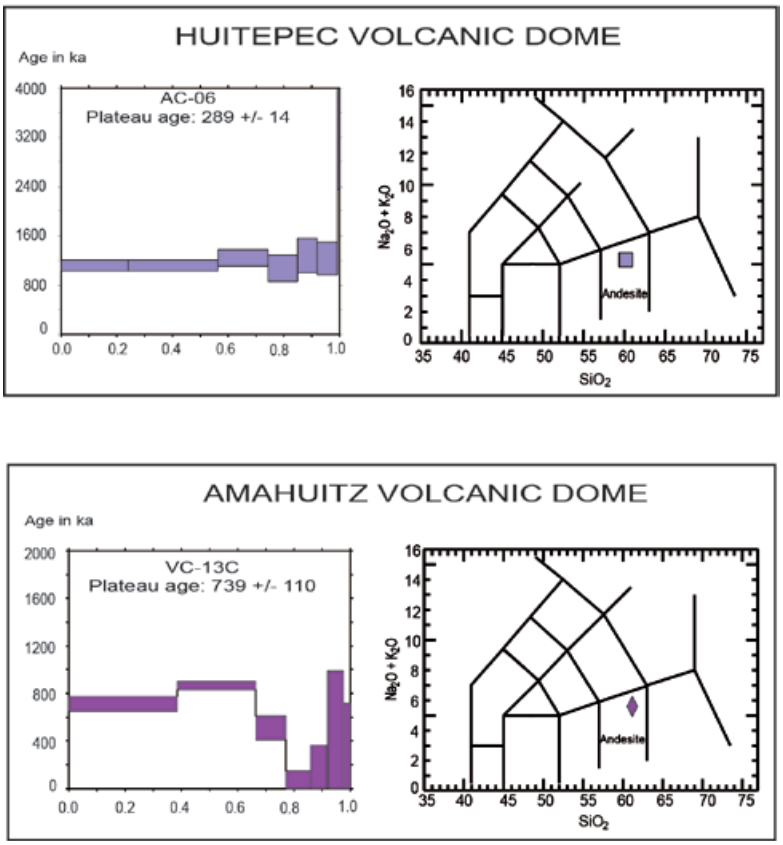

Figure 5. Age spectra plots for $^{40}Ar/^{39}Ar$ data and dome blocks chemical classification from. (a) Huitepec Volcanic Dome and (b) Amahuitz Volcanic Dome.

Mispía Volcanic Dome (MVD).

The MVD is located 5 km southeast of the IVD, has a mean diameter of ~ 3.6 km., a height of 600 m, and covers an area of ~ 8 km^2 (Figure 2). The rocks from this dome are basaltic andesite. Associated with this structure are some block-and-ash-flow deposits that were emplaced principally to the southeast (Mora *et al*., 2007). This structure was identified by Capaul (1987) as Nicolás Ruiz Volcano, for which he reported fission track ages of 0.341 ± 0.044; 0.403 ± 0.062 and 0.670 ± 0.104 Ma. In this study, we obtained a plateau age of 0.975 ± 0.011 Ma (Figure 6B) from the dome sample VC-18A.

La Lanza Volcanic Dome (LVD).

The LVD is located 2 km east of the MVD. Damon and Montesinos (1978) described this structure as a hornblende dacite volcanic neck with vertical banded-like appearance of "pelean" type, with a K–Ar age of 0.846 ± 0.024 Ma. This volcanic dome is composed of a main spine-like structure surrounded by deposits of pyroclastic flows. The spine is semi-circular with a mean diameter of 1.5 km, covering an area of ~1.2 km^2, and a height of 140 m. Pyroclastic flow deposits have a principal direction of emplacement toward the southeast, with a maximum range of 9.5 km., a mean thickness of 4 m, and cover an area of ~ 50 km^2.

Santontón Volcanic Dome (SVD).

The first studies in this dome were done by Jaimes-Viera *et al*. (2004), Jaimes-Viera (2006), and Mora *et al*. (2007). The SVD is located 4 km south of the MVD. According to these authors, it has a height of ~ 400 m, an elongated shape (major axis of 3.6 km and minor axis of 2 km), and covers an area of ~ 6.5 km2. It is also surrounded by deposits of associated pyroclastic flows (Figure 2). In this structure we sampled 2 blocks from the dome, and we obtained a precise age of 0.995 ± 0.009 Ma (VC-20) and a less precise age of 1.042 ± 0.051 Ma (VC-19, Figure 2, Figure 6C). These ages are not significantly different from one another. However, these samples are chemically different, one being as andesite (VC-20; 58.67% SiO2) and the other is a basaltic andesite (56.75% SiO2).

Venustiano Carranza Volcanic Dome (VCVD)

This structure is an andesitic dome with block-and-ash-flow, fall and lahars deposits located 4 km to the south of the SVD (Jaimes-Viera, 2006; Mora *et al*., 2007). Pyroclastic flow deposits are found surrounding the volcano with a mean radius of 2 km and an estimated area of 13.7 km^2

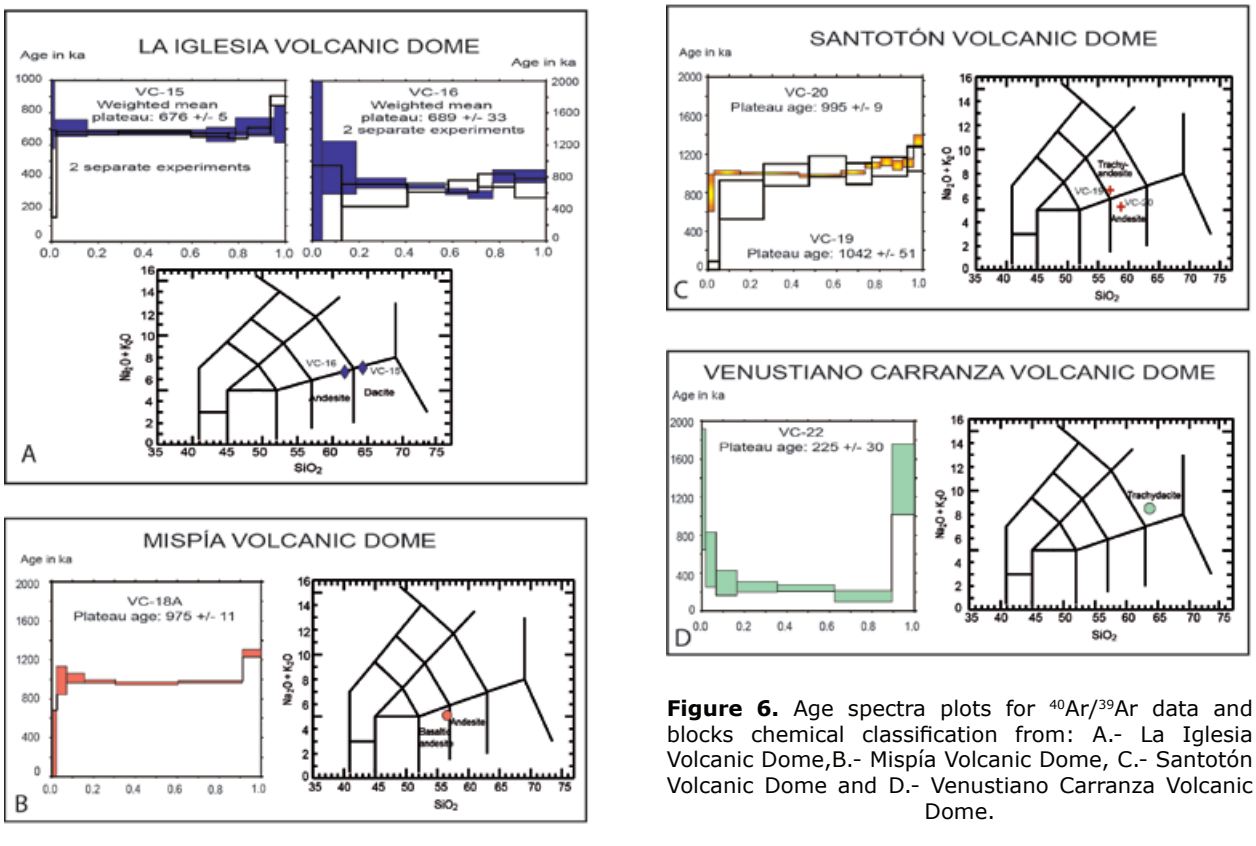

Figure 6. Age spectra plots for $^{40}Ar/^{39}Ar$ data and blocks chemical classification from: A.- La Iglesia Volcanic Dome,B.- Mispía Volcanic Dome, C.- Santotón Volcanic Dome and D.- Venustiano Carranza Volcanic Dome.

(Mora *et al*, 2007). The sample (VC-22, Figure 2) is a juvenile block taken from the pyroclastic flow deposit, and our analysis constrains the age for its emplacement is 0.225 ± 0.030 Ma (Figure 6D).

Discussion.

According to the available data, magmatic activity began at the Tzontehuitz Dome Complex at 2.128 ± 0.020 Ma (or 2.14 Ma, reported by Damos and Montesinos, 1978). Volcanic activity at this structure reactivated at 1.95 ± 0.04 Ma (Table 1). Magmatic activity occurred to south in the Santotón structure, involving two events, one at 0.995 ± 0.009 Ma and the other at 1.042 ± 0.051 Ma. The Mispia unit recorded magmatic activity at 0.975 ± 0.011 Ma. The peak of magmatic activity apparently took place at 0.85 ± 0.03 and 0.846 ± 0.024 Ma, as represented by the Huitepec and La Lanza volcanic structures, respectively, and the Amahuitz at 0.739 ± 0.110 Ma. The Iglesia Volcánic structure manifested magmatic activity at 0.689 ± 0.033 to 0.676 ± 0.005 Ma. The Apas structure had two periods of magmatic activity, one at 0.447 ± 0.011 Ma and the other at 0.321 ± 0.008 Ma. The Navenchauc structure was formed by phreatomagmatic activity at 0.369 ± 0.018, and an effusive dome-building episode occurred at 0.277 ± 0.005 Ma. The Huitepec structure developed around 0.289 ± 0.014. The most recent magmatic activity of the central part of the CVA was at 0.225 ± 0.030 Ma and resulted in the Venustiano Carranza structure.

Overall, sixteen magmatic events have been recorded in eleven units. Moreover, some structures manifested more than one magmatic episode (e.g., Tzontehutz, Santotón, Huitepec, Apas, and Navenchauc). These CVA structures have elongate forms, extending up to 3.5 km in length. In the CVA, there is no evidence of large stratovolcanoes as is common in the TMBV and CAVA, probably because of the fact that the CVA was developed in a tectonic complex zone with both compression and transform processes.

Conclusions

Magmatic activity in the CVA has been characterized by the emission of volcanic products of trachyandesitic, andesitic, trachydacite and dacitic composition. These products were emplaced during different eruptive events, both effusive and explosive. A main feature of the CVA is the lack of development of large stratovolcanoes, as is common in the TMVB and CAVA. This observation can be explained by magma not being erupted for a long time via the same conduits, such that the magma arrives at the surface in different zones of weakness. This kind of activity does not permit the vertical growth of the structures giving origin to a lateral or lineal growth, following the zone of weakness.

The oldest volcanic center is represented by Tzontehuitz Domic Complex with an age of 2.1 Ma, where as the youngest volcanic structure is Venustiano Carranza Volcanic Dome with an age of ~ 0.225 Ma. In the interval of time from ~ 1 Ma to ~ 0.7 Ma, magma sources feeding the volcanism migrated from south to north. From ~ 0.45 Ma to 0.28 Ma, the volcanic activity was concentrated in the west part of the study area. Here the manifestation was more explosive than the other parts with phreatomagmatic activity. The last volcanic activity (225 ka) in the central part of the CVA was in the south (VCVD), and the most recent volcanic activity was to the eruption sequence at El Chichón volcano (Espindola *et al*., 2000; Layer *et al*., 2009) in 1982.

Bibliography

Aguirre-Díaz G., Ferrari L., Nelson S., Carrasco-Núñez G., López-Martínez M., Urrutia-Fucugauchi J., 1998, El Cinturón Volcánico Mexicano: Un proyecto multidisciplinario, GEOS, Unión Geofísica Mexicana, A.C., pp. 131–138.

Aguirre-Díaz G.J., Carranza-Castañeda O., 2000, Oligo-Miocene basins of central-northern Mexico and the misinterpretation of their sedimentary fill as Quaternary alluvium. 60the Annual Meeting of the Society of Vertebrate Paleontology. Abstracts of Papers 25A.

Capaul W.A., 1987, Volcanoes of the Chiapas Volcanic Belt, Mexico. Michigan, Michigan Technological University: 93p.

Damon P., Montesinos E., 1978, "Late Cenozoic volcanism and metallogenesis over an active Benioff Zone in Chiapas, Mexico". Arizona Geological Society Digest 11: 155-168p.

Demant A., 1978, Características del eje neovolcánico transmexicano y sus problemas de interpretación. UNAM, Inst. Geol. Rev., vol. 2, pp. 172–187.

Espíndola J.M., Macías J.L., Tilling R.I., Sheridan M.F., 2000, Volcanic history of El Chichón Volcano (Chiapas, Mexico) during the Holocene, and its impact on human activity. *Bull. of Volc.*, 62, 90–104.

Ferrari L., López-Martínez M., Aguirre-Díaz G., Carrasco-Nuñez G., 1999, Space-time patterns of Cenozoic arc volcanism in Central Mexico: from Sierra Madre Occidental to Mexican Volcanic Belt. Geology, 27, 91–105.

Jaimes-Viera M.C., 2006, Petrología y Geoquímica del Arco Volcánico Chiapaneco. Tesis de Maestría, posgrado de Ciencias de la Tierra, UNAM.

Jaimes-Viera M.C., Mora J.C., Layer P., Rueda A., Sánchez S., 2004, Geología y Petrología del Arco Volcánico Chiapaneco. IV Reunión Nacional de Ciencias de la Tierra, Resúmenes, pp.242.

Jaimes-Viera M.C., Mora J.C., Santo A.P., Vaselli O., 2008, The Tzontehuitz Dome Complex, Chiapanecan Volcanic Arc (Chiapas, Mexico): geochemical and petrological insights. 1st SIMP-AIC Joint Meeting, Book of abstracts, pp 64.

Lanphere M.A., Dalrymple G.B., 2000, First-principles calibration of ^{38}Ar tracers: Implications for the ages of $^{40}Ar/^{39}Ar$ fluence monitors, U.S. Geological Survey Professional Paper 1621, 10p.

Layer P.W., 2000, Argon-^{40}/argon-^{39} age of the El'gygytgyn impact event, Chukotka, Russia, Meteroitics and Planatary Science, v. 35, 591-599.

Layer P.W., García-Palomo A., Jones D., Macías J.L., Arce J.L., Mora J.C., 2009, El Chichón volcanic complex, Chiapas, México: Stages of evolution based on field mapping and $^{40}Ar/^{39}Ar$ geochronology. Geofísica Internacional, 48, 33-54.

Layer P.W., Hall C.M., York D., 1987, The derivation of 40Ar/39Ar age spectra of single grains of hornblende and biotite by laser step heating, *Geophys. Res. Lett.,* 14, 757- 760.

Macías J.L., Arce J.L., Mora J.C., Espíndola J.M., Saucedo R., Manetti P., 2003, A 550- year-old Plinian eruption of el Chichón volcano, Chiapas, Mexico: Explosive volcanism linked to reheating of a magma reservoir. *J. Geophys. Res*., 108 (B12), pp. 2569.

McDougall I., Harrison T.M., 1999, Geochronology and Thermochronology by the $^{40}Ar/^{39}Ar$ method-2nd ed, Oxford University Press, New York, 269pp.

Mora J.C., Jaimes-Viera M.C., Garduño-Monroy V.H., Layer P., Pompa-Mera V., Godinez L., 2007, Geology and geochemistry characteristics of the Chiapanecan Volcanic Arc (Central Area), Chiapas Mexico. Journal of Volcanology and Geothermal Research, 162, 43–72.

Nixon G.T., 1982, The relationship between Quaternary volcanism in central Mexico and the seismicity and structure of the subducted ocean lithosphere. Geological Society of America Bulletin, 93, 514–523.

Siebe C., Macías J.L., Abrams M., Elizarras R.S., Delgado H., 1995, Quaternary explosive volcanism and pyroclastic deposits in east Central Mexico: implications for future hazards. Geological Society of Annual Meeting 1995, New Orleans, Louisiana Field trip guide book, vol. 1, p. 47.

Suter M., Quintero-Legorreta O., López-Martínez M., Aguirre-Díaz G., Farrar E., 1995, The Acambay graben: active intraarc extension in the Trans Mexican Volcanic Belt, Mexico. Tectonics, 14 (5), 1,245–1,262.

Wallace, P.J., Carmichael, I.S.E., 1999, Quaternary volcanism near the Valley of Mexico: implications for subduction zone magmatism and the effects of crustal thickness variation on primitive magma compositions. Contributions to Mineralogy and Petrology, 135, 291–314.

York D., Hall C.M., Yanase Y., Hanes J.A., Kenyon W.J., 1981, $^{40}Ar/^{39}Ar$ dating of terrestrial minerals with a continuous laser, *Geophys. Res. Lett.,* 8, 1,136-1,138.

Geofísica Internacional (2012) 51-1: 51-61

Original paper

Structures and petroleum prospects of the Saramaguacán basin, Cuba, from 3D inversion of gravimetric data

José Batista Rodríguez*, Jesús Blanco Moreno, Marco Pérez-Flores and Alina Rodríguez Infante

Received: October 5, 2010; accepted: October 10, 2011; published on line: DEcember 16, 2011

Resumen

Se presentan nuevas particularidades estructurales de la cuenca Saramaguacán, Cuba, a partir de la inversión 3D de datos gravimétricos, constreñidos por información de pozos y geología de superficie. Esas particularidades muestran una tectónica compleja de procesos de cabalgamiento, revelando el esquema estructural más probable dentro de la cuenca, el cual indica estructuras en formas de rampa y plataforma, así como la ubicación y geometría de la cuenca y varias sub-cuencas. También se conocen las ubicaciones y comportamiento en profundidad de las principales fallas, y se sugieren posibles nuevas fallas. A las diferentes formaciones rocosas se le determinaron las variaciones de su geometría, profundidad y espesor. Esta determinación posee particular importancia para las rocas sedimentarias (rocas colectoras) y las rocas del paleomargen (rocas madres) porque constituye la base para futuras investigaciones orientadas a seleccionar los mejores sitios para ubicar las perforaciones petroleras y calcular el volumen de hidrocarburo que pueden almacenar las rocas colectoras. Ambos grupos de rocas son potenciales para la prospección petrolera. A 4 km de profundidad se localizaron las rocas madres del sistema petrolero cubano, asociadas a las rocas carbonatadas del paleomargen. Las rocas colectoras alcanzan 10 km de profundidad. El modelo 3D obtenido apoya la hipótesis de un emplazamiento tectónico de sur a norte de las ofiolitas y las rocas volcánicas cretácicas, sobre las secuencias terrigenous-carbonatadas del paleomargen de Bahamas. Las particularidades estructurales mostrada por el modelo constituyen indicadores de la tectónica compresiva que originó la cuenca Saramaguacán en el Mesozoico-Terciario. También indican que la cuenca Saramaguacán posee condiciones favorables para la preservación de petróleo.

Palabras clave: teoría inversa, anomalías gravimétricas y estructura de la Tierra.

Abstract

New structural details of the Saramaguacán basin in central Cuba are presented, based on 3D inversion of gravimetric data constrained by wells and surface geology information. The basin shows complex tectonics of the overthrust process. A probable structural analysis of the basin suggests structures of ramp and shelf, as well as the location and geometry of the basin and several sub-basins. Known location and behavior of fault depth suggests some possible new or unknown faults. Geometry variation, depth and thickness were determined for different rock formations. This has great importance for the sedimentary (oil-bearing) and paleomargin (oil-source) rocks, because it is the basis for future research to select the best sites for drilling, as well as a broad estimate calculation of hydrocarbon volume that can be stored in the oil-collector rocks. Both groups of rocks are potential targets for oil prospecting. The oil-source rocks of the Cuban system were found to be around 4 km depth. They are associated with carbonated rocks of the Paleomargin. The oil-bearing rocks reache a depth of 10 km. The 3D model obtained supports the hypothesis that the ophiolites and the Cretaceous volcanic arc rocks were tectonically emplaced from south to north, on top of carbonate-terrigenous sequences from the Bahamas paleomargin. The model shows elements of the compressive tectonics that originated the Saramaguacán basin in the Mesozoic-Tertiary. It also suggests that the Saramaguacán basin presents favorable geologic conditions for oil deposits.

Key words: inverse theory, gravity anomalies and Earth structure.

J. Batista Rodríguez*
College of Engineering
Universidad Autónoma de Coahuila
Blvd. Adolfo López Mateos S/N, Nueva Rosita
Coahuila, México

Department of Geophysics
Centro de Investigación Científica y de Educación Superior de Ensenada Baja California - CICESE
Baja California, México
*Corresponding author: jabatistar@yahoo.com

J. Blanco Moreno
Department of Geology
Instituto Superior Minero Metalúrgico de Moa - ISMMM
Las Coloradas Moa
Holguín, Cuba
Email: jblancoismm@edu.cu

M. Pérez-Flores
Department of Geophysics
Centro de Investigación Científica y de Educación Superior de Ensenada Baja California - CICESE
Baja California, México
Email: mperez@cicese.mx

A. Rodríguez Infante
Department of Geology
Instituto Superior Minero Metalúrgico de Moa - ISMMM
Las Coloradas Moa
Holguín, Cuba

Introduction

The Cuban territory is a folded belt, faulted and overthrusted on top of the North America passive paleomargin. This structure takes place at the contact between the North American and the Caribbean plate with oblique convergent motions (Mann *et al*., 1995), that allows the creation of a foreland basin system with a complex geometry, sedimentation and evolution from Late Campanian to Late Eocene, covered by less deformed Oligocene-Miocene sequences (Blanco and Proenza, 2000). These are favorable conditions for oil accumulation and storage (Blanco, 1999).

The Saramaguacán basin is located in Central Cuba (Figure 1), north of the granitoid belt of Camagüey County (Figure 2). It is bounded by ophiolitic rock sequences to the west. The basement consists of volcanic island arc rocks of Cretaceous age (Iturralde-Vinent and Thieke, 1986; Iturralde-Vinent *et al.,* 1981). According to geophysical data (gravimetric and seismic), the basin is 10 km deep (Martínez *et al*., 1998; Blanco *et al*., 2000). Several geologic and geophysical investigations have been carried out for oil prospecting without conclusive data about the characteristics of the geological structures underground.

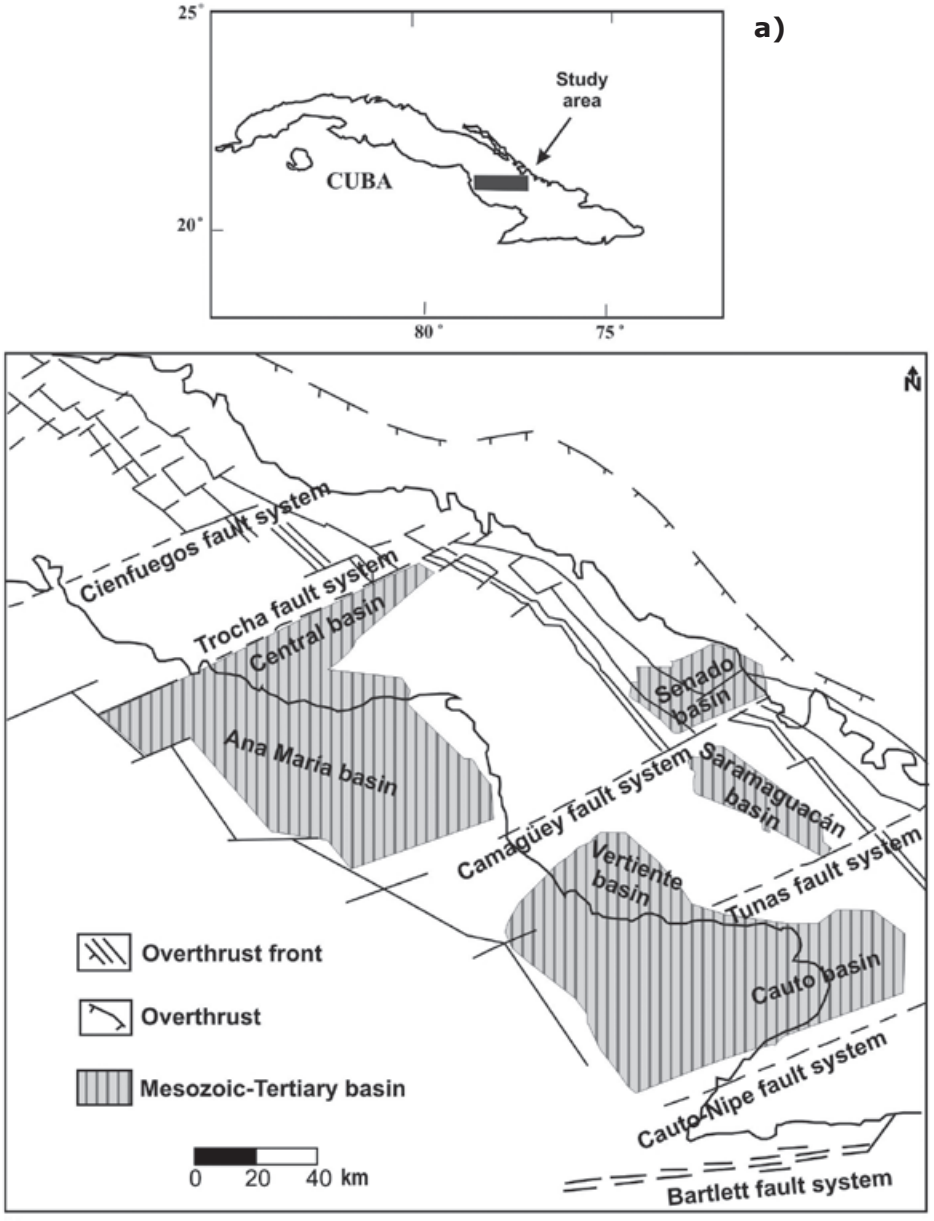

Figure 1. a) Geographical location of the study area; b) Location of the Saramaguacán basin in the tectonic set of the eastern center region of Cuba (Maximov *et al*., 1985).

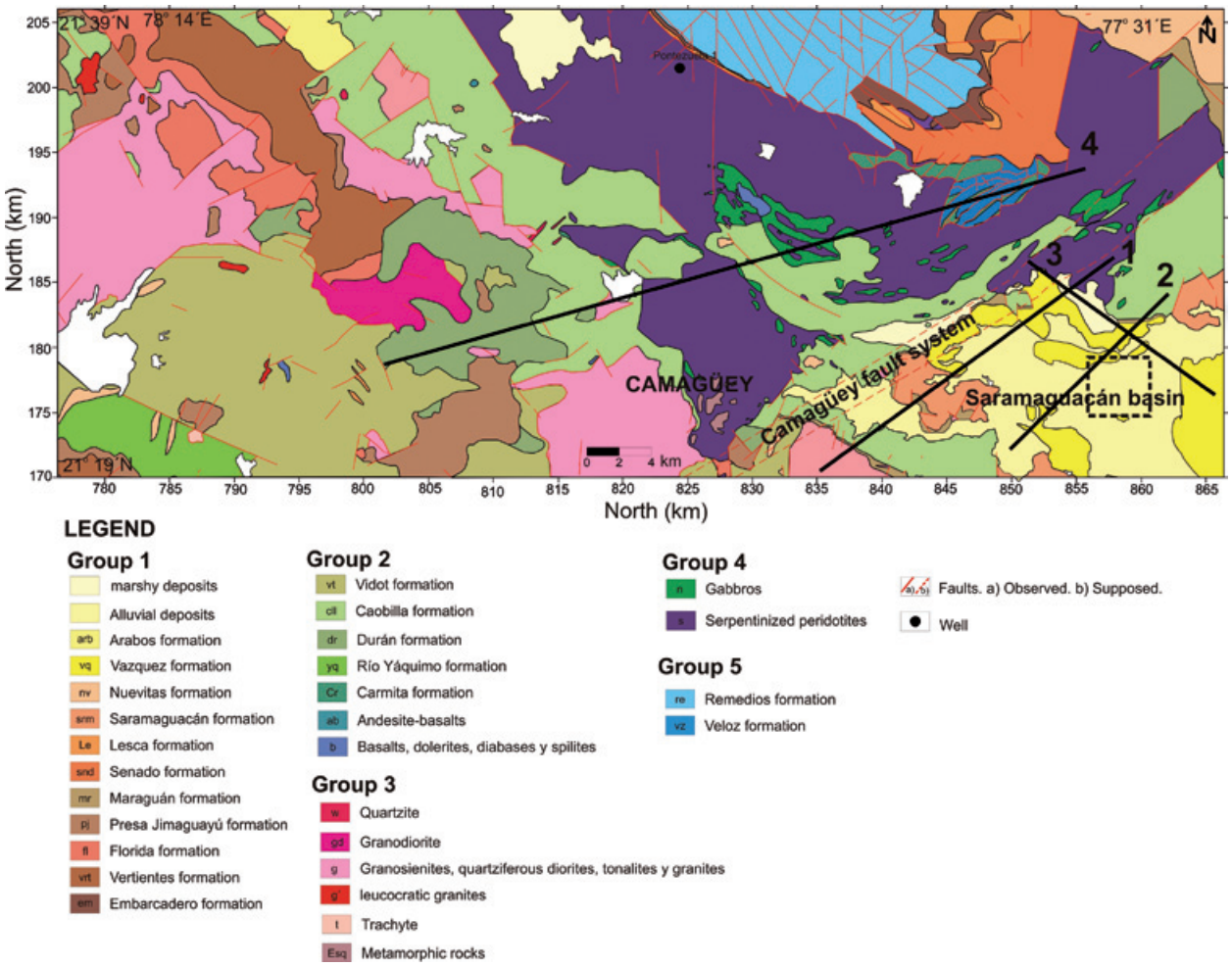

Figure 2. Geological map of the study region (taken from Albear *et al*., 1988). The geological formations are shown according to the chosen rock groups for the 3D inversion. The whole area of the geological map is included in the 3D inversion. Thick dashed line indicates location of the scheme of the Figure 4. Solid line 1, 2, 3 and 4 indicate the cross sections locations.

Using 3D inversion of gravimetric data it is possible to determine sedimentary basin shapes and limits, lithology depth and thickness as well as the location and extension of fault systems (Gallardo *et al*. 2003, 2005; Pérez-Flores *et al*., 2004; Batista *et al*., 2007). New structural features of the rock sequences in the Saramaguacán basin are obtained from 3D inversion of gravimetric data, with the method developed by Gallardo *et al*. (2003). The results yield information about deep structures, their link with oil-source and oil-collector rocks, and their distribution throughout the area. The results obtained by this technique should be very important to get relevant information about the Bahamas paleo-continental shelf, where the main oil-source rocks from the Cuban oil system are located (López-Rivera and López-Quintero, 2004; Magnier *et al*., 2004; Domínguez and López-Quintero, 2005).

Geologic setting

Two tectono-stratigraphic units constitute the Saramaguacán basin. The lower unit of Mesozoic-Early Tertiary age is characterized by a blanket-form folded structure, while the upper unit is a sedimentary sequence of Late Cenozoic age (Blanco, 1999). Both units have different tectonic characteristics (Figure 2).

Inside the Saramaguacán basin, Durán and Presa Jimaguayú Formations outcrop as a poly-mictic sand-gravel conglomerate of carmelite color with tuff clasts, volcanogenic rocks, serpentinites and gabbros. These rocks lay discordantly over Cretaceous vulcanites and granitoids belonging to the volcanic arc. The youngest rocks underlay discordantly Paleocene olistostrome sequences. Concerning the Eocene Formations, Saramaguacán and Maraguán units

discordantly cover the latest geological units, as shown in Figure 3. These rocks consist of a sand-sandstone polymictic sequence with sporadic oblique interbedding, including conglomerates and polymictic gravelites.

The Saramaguacán basin presents facies varying from conglomerate to flyschoid with sedimentary environment from marine to continental. Sediments originate mainly from erosion of the Cretaceous volcanic sequences and ophiolites (Iturralde-Vinent, 1996). To the north, northwest and west of Saramaguacán basin these are outcrops of Cretaceous volcanic and carbonated rocks, as well as ophiolites and acid intrusives. In general, the group of sedimentary rocks that overlies the Cretaceous volcanic rocks has potential to collect oil (oil-collector rocks; Blanco, 1999). The volcanic rocks overlie ophiolitic rocks overlying limestones and marls belonging to the Bahamas paleomargin of Upper Jurassic and Lower Cretaceous age. These latter rocks are considered the main oil-source rocks in the Cuban oil system.

Tectonics of the Saramaguacán basin

The Saramaguacán basin is a synform structure with an axis SE-NW direction similar to a hemigraben according to seismic data. It is limited by a regional deep fault in the northern and southern part (Figure 4; Martínez *et al.,* 1998).

The fault systems show SW-NE and SE-NW direction (Figures 1, 2 and 4), matching the Cuban tectonic pattern (Puscharovskiy *et al.,* 1989). Stretching faults appear as well as deep vertical and strike-slip faults belonging to the Camagüey fault zone. The Saramaguacán basin is defined as a tensional basin developed from the stress of the Camagüey strike-slip fault system, producing a block system at different depths and making a set of small sub-basins (Blanco, 1999).

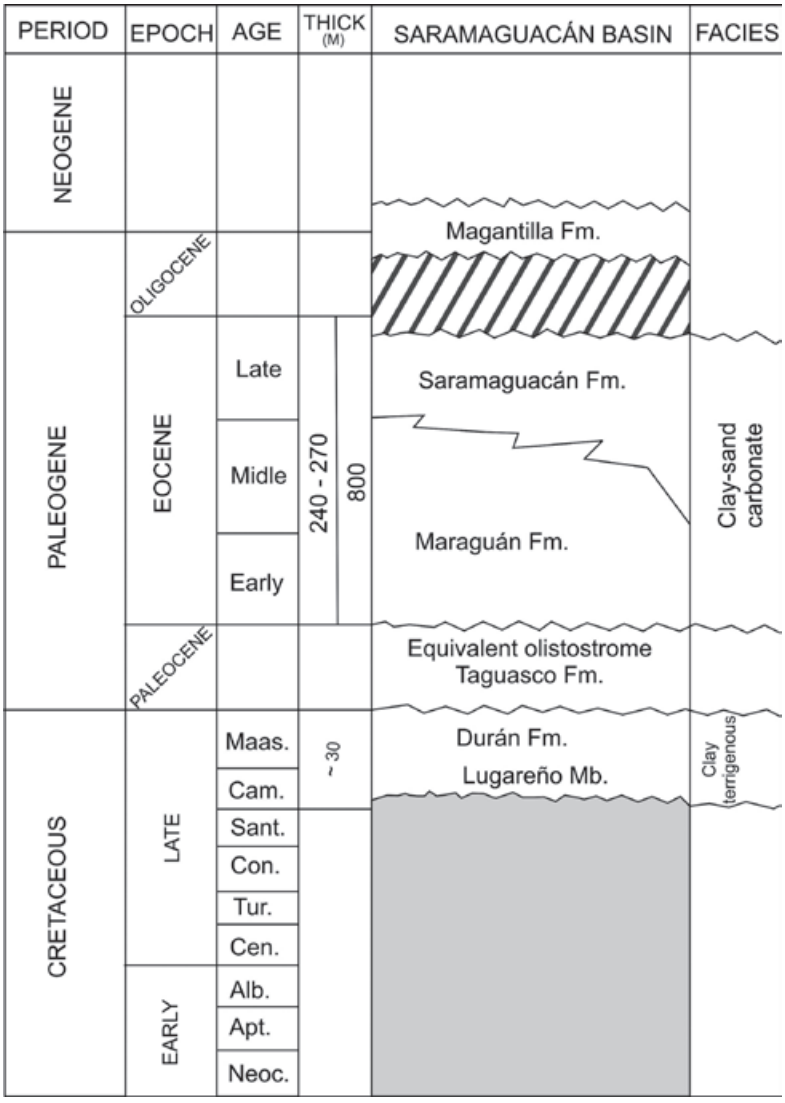

Figure 3. Generalized schematic geologic column (Blanco, 1999). Gray indicates Cretaceous volcanic rocks. Dimension is not to scale.

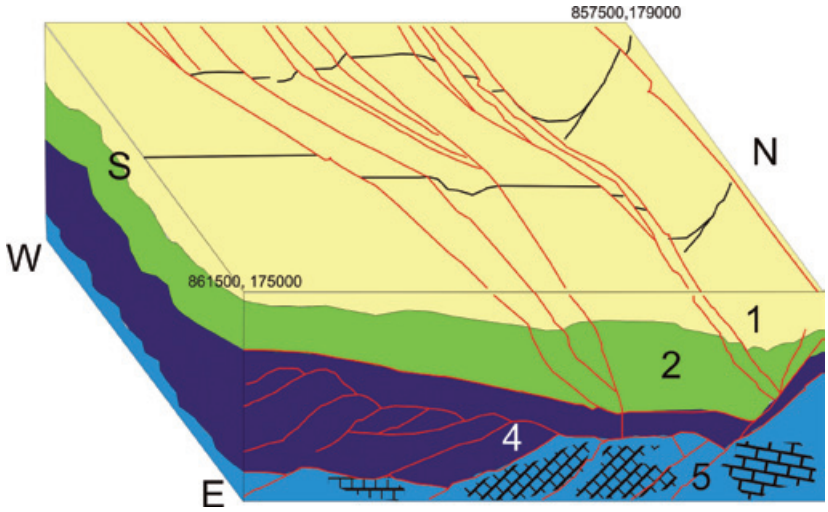

Figure 4. Structure of the Saramaguacán basin according to seismic data (size is not to scale). The number 1, 2, 4 and 5 indicate the group of rocks 1, 2, 4 and 5, respectively. Modified from Martínez *et al.* (1998).

Methodology and data

Bouguer gravity anomalies were obtained from a 1:50,000 scale survey with 5812 measuring points and 0.051 mGal accuracy measured in a geologic cartography campaign in the CAME III Camagüey polygon (Iturralde-Vinent and Thieke, 1986). These data cover an area of approximately 1,600 km^2 in central and northern Camagüey county. The Bouguer reduction was performed assuming a density of 2.6 g/cm^3.

The 3D inverse process used the surface geology as constraints (Albear *et al.,* 1988), plus the Pontezuela 1 well data (Álvarez-Castro *et al.,* 1995). Topography correction was not necessary because the area is almost flat and near sea level. The well was associated with a prism, and the thickness of the lithological groups traversed by the well during the inverse process remained unchanged. The surface geology, according to the geological map, was considered in the prisms of the first group and was not changed during inversion.

Details about the 3D inversion can be found in Gallardo-Delgado *et al.* (2003) and Gallardo *et al.* (2005). The ground is discretized in layers of rectangular prisms. Every layer is a rectangular conglomerate of prisms, simulating one rock formation; density or density contrast remain constant in the whole set of layer prisms. The horizontal section of every prism could be rectangular and the shape is maintained constant at all the prisms. In that way, it is possible to compute which prism is on the left side or the bottom of each. The top depth of every prism fits the top topography of such a layer. The bottom of every prism is the corresponding bottom topography of that layer. In this research, we needed five layers with five different densities or density contrasts. Every layer is constituted of a set of rectangular prisms. The inverse process computes the top and bottom tridimensional topography for every rock formation through the calculation of the top and bottom depth for every single prism in every layer: a huge amount of calculations. The process is non-linear and converges iteratively. After convergence criteria are fulfilled we get the top and bottom depth for every prism. A smoothing parameter is added to the objective function: it works with the spatial derivatives of the prism depths. A large value yields a very smooth topography for every layer; small parameters yield very rough layers. We tried several parameters but we selected a smooth solution, so that large topography deflections will be avoided. The actual deflection could be seen only if the data are sensible to them. Those deflections could be caused by faults.

A smoother parameter gives us some confidence that such deflections exist and that the faults also exist. The use of quadratic programming (Gill *et al*., 1986) allows us to add constraints to the prism depth estimation. Surface geology is introduced in the algorithm through those constraints. For example, if one part of the third layer prisms outcrops, we force the first and second layer prisms to collapse to zero thickness in order to allow such an outcropping. Well log information can be easily added. The more additional information we add, the easier and faster is the inversion process to find the optimal solution.

First we analyzed densities (ρ) for the different lithologies in the survey area (Iturralde-Vinent and Thieke, 1986). After the density analysis and considering the stratigraphic position of these lithologies, we selected five groups of rocks (Figure 2) with average values of densities

according their lithologies. Group 1: sedimentary rocks (ρ =2.35 g/cm^3), Group 2: volcanic rocks (ρ =2.61 g/cm^3), Group 3: acid rocks intrusive complex (ρ =2.7 g/cm^3), Group 4: ophiolitic rocks (ρ =2.46 g/cm^3), Group 5: paleomargin rocks (ρ =2.5 g/cm^3).

We assigned an average density values to each lithology representing the five groups of rocks used at this research. Group 1 is dominated by limestone, marl, calcareous sandstone, as well as breccias and polymictic conglomerates. Group 2 or volcanic rocks, consists mainly of basalts, andesites and diabases. Group 3 or acid rocks are represented by quartzite and granodiorite. Group 4 or ophiolites are gabbros and peridotites, the latter with a high serpentinization degree, which leads to low density values. Group 5 presents mainly limestone, dolomite, dolomitized and clayed limestone.

The study area was gridded into 360 prisms. Every prism area was 3x3 km^2. Minimum and maximum thicknesses for every prism were established according to previous geological and geophysical studies (Iturralde-Vinent *et al.,* 1981; Iturralde-Vinent and Thieke, 1986). These geological and geophysical studies suggest thickness up 10 km for the group 1, likewise, 5 km for group 2, 4 km for group 3 and 4.

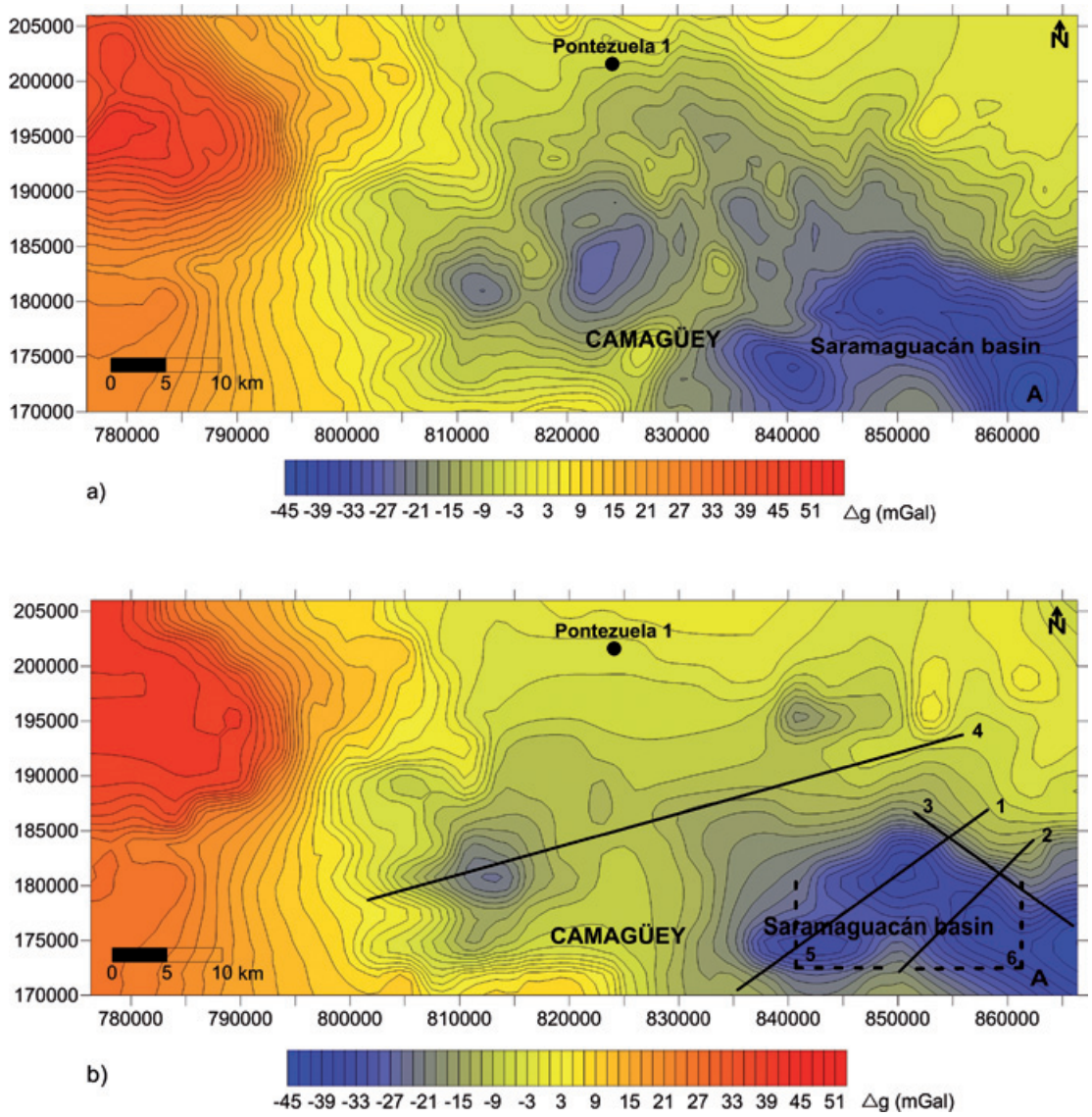

Figure 5. Saramaguacán basin's gravimetric map (modified from Iturralde-Vinent & Thieke 1986). a) Observed. b) Response data. Solid line 1, 2, 3 and 4 indicate the cross sections locations. Dashed lines shows the corners 5 and 6 indicating the location of the 3D drawings.

After running the 3D iterative inversion program, a comparison between gravity data and response was done. For a better understanding of the 3D model, we made several cross-sections.

Results

Some minimums separated by relative highs are observed on the gravimetric map, suggesting sub-basin locations inside the main basin (Figure 5a). Toward the SE of the basin, a minimum of -45 mGal (Letter A) is located indicating the largest thickness of the sedimentary rocks (oil-collector rocks) and also the depocenter of the Saramaguacán basin. The latter was also suggested by seismic surveys (Martínez *et al.,* 1998).

After 20 iterations during 80 minutes the following model was obtained, with a misfit of 3.2% suggesting an excellent fit to the data (Figure 5b).

The most important oil-source rocks in Cuba are related to the Bahamas paleomargin (López-Rivera and López-Quintero, 2004; Magnier *et al.,* 2004; Domínguez and López-Quintero, 2005) that outcrops northward of the Saramaguacán basin (Figure 2) and reach 10 km depth within the Saramaguacán basin, according to 3D model obtained (Figure 6). Ramp and shelf is the typical morphology (Figure 7), getting closer to the surface northeastward (< 4 km). Paleomargin and the ophiolites rocks show large variations at depth. These structural variations match with the deep drilling oil holes in Varadero (Cuba oil producing area) and northward Camagüey (Blanco, 1999).

Analyzing the thickness map for the sedimentary rocks (Figure 6a), the cross sections (Figure 7) and the 3D drawing (Figure 8), we can infer that the potential oil-collector rocks (group 1: sedimentary rocks) reach 10 km of depth.

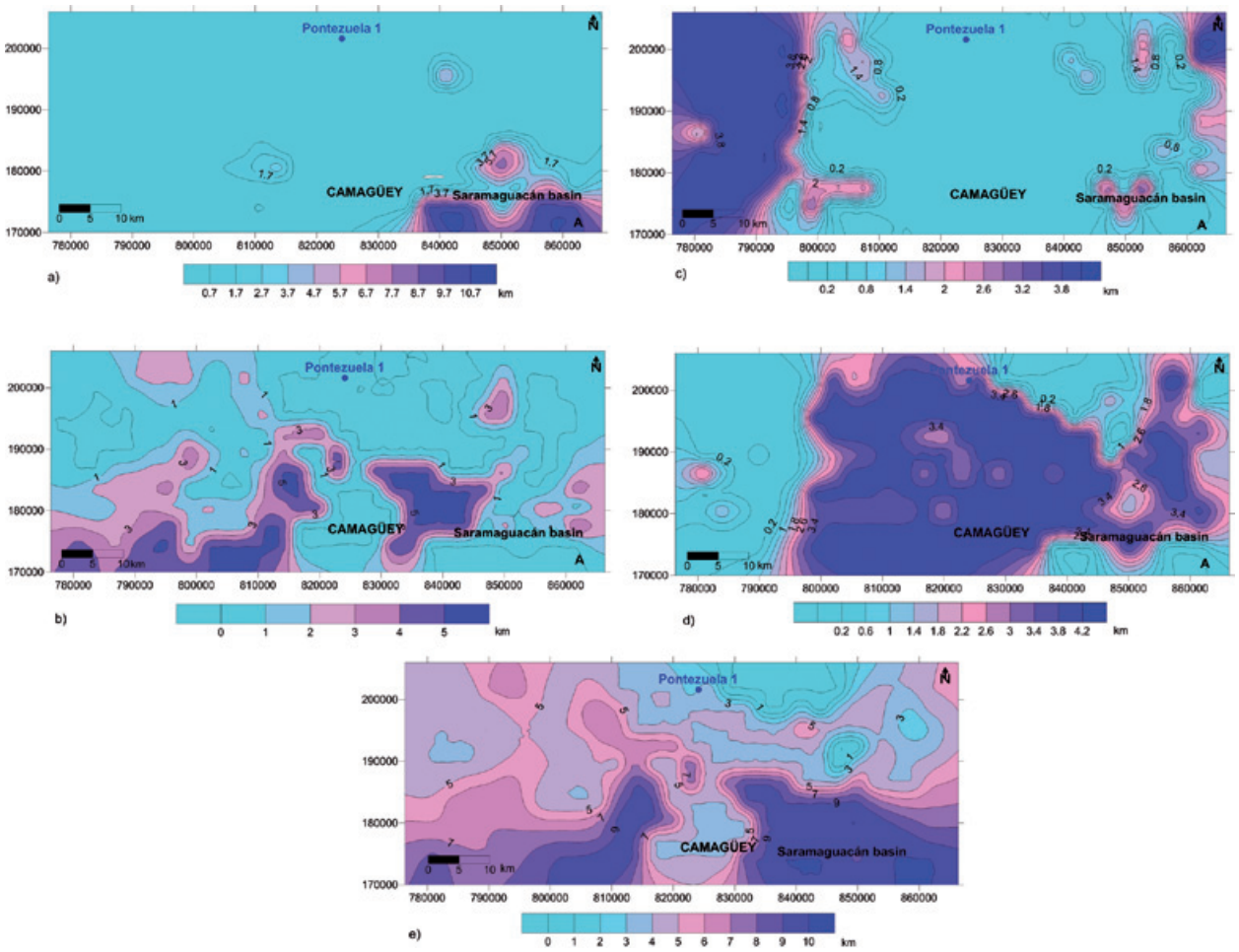

Figure 6. Thickness maps for the different rock groups. a) Sedimentary. b) Volcanic. c) Acid intrusive. d) Ophiolitic. e) Depth map of the Paleomargin rocks.

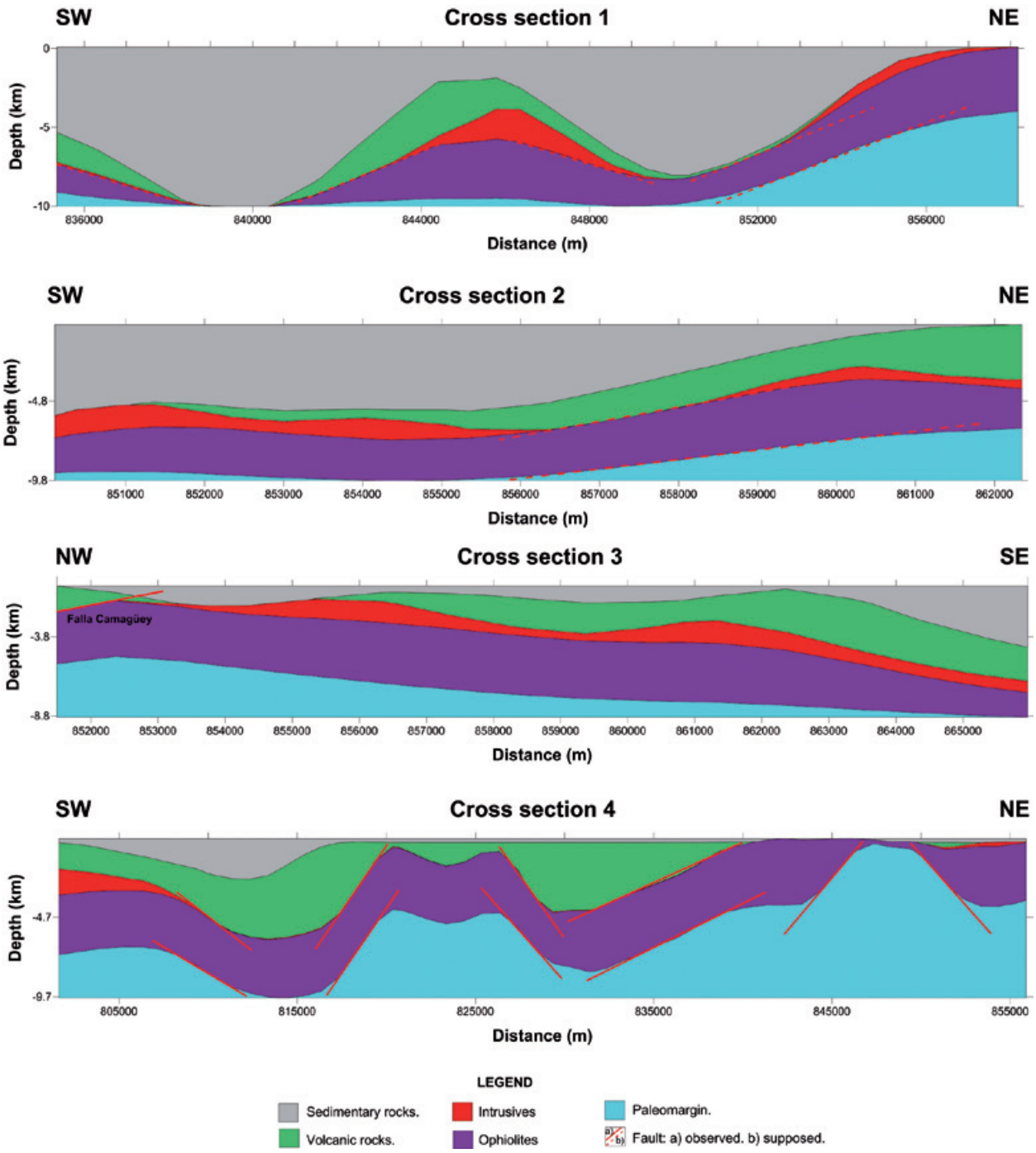

Figure 7. Cross-sections to the 3D model.

Their, thickness was not reached by previous drill holes in the Saramaguacán and Maraguán formations (Martínez *et al.,* 1998). This 10 km thickness is in agreement with seismic (Martínez *et al.,* 1998) and gravimetric profiles (Blanco *et al.,* 2000).

Cross-sections show ophiolites and paleomargin rocks at the crests (Figure 7; cross-section 4), excepting volcanic rocks for cross-section 1 (Figures 7 and 8). Cross-sections show that structural crests of volcanic rocks, limiting the sub-basins, are in discordant contact with the Cretaceous-Tertiary sedimentary sequences. Other basins present similar features and tectonic development (e.g., the Central Basin of Cuba) and are considered as potential oil targets for drilling (Blanco, 1999).

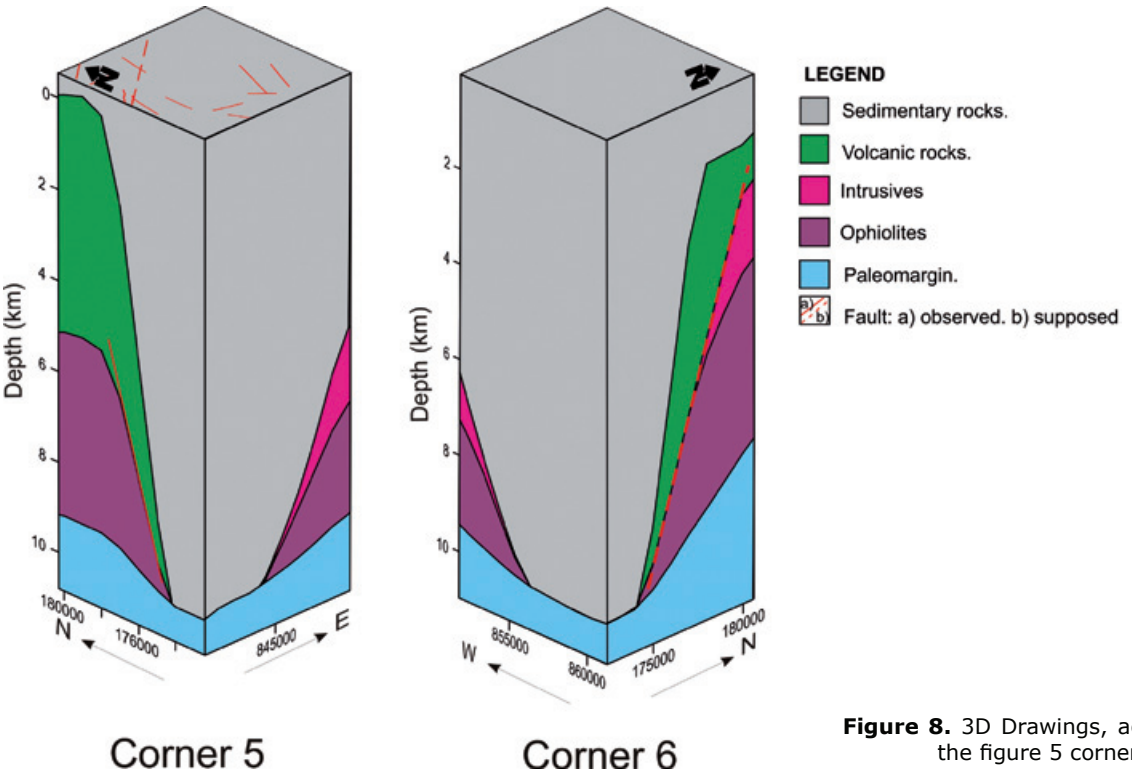

Figure 8. 3D Drawings, according to the figure 5 corners.

Knowledge of the lateral variations of the depth and thickness of oil-source and oil-collector rocks allows us to decide the best sites for future oil drilling and to conduct a preliminary estimation of the hydrocarbon volume that can be stored by the oil-collector (considering that this has favorable characteristics as; porosity and permeability for the whole thickness).

The cross-sections in the 3D model were done in SW-NE and SE-NW direction (Figure 7), trying to cut the faults perpendicularly. This fault behavior is due to the oblique collision and strike-slip faulting that began in the Maastrichtian (Late Cretaceous) time (Mann *et al.,* 1995; Iturralde-Vinent, 1996). The geometry of the rock groups show slope changes that can be related with the observed faults on the surface. Other faults are inferred as new or not reported previously (Figures 7 and 8).

Ophiolites outcrop NE of cross-section 4 (Figure 7) and reach 9.7 km depth at southwards with 4 km as maximum thickness. Ophiolites are

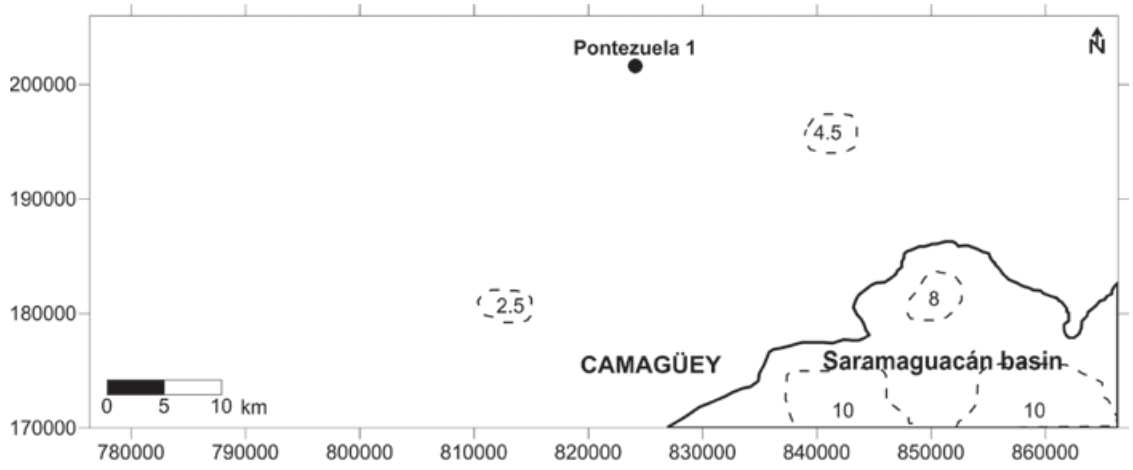

Figure 9. Interpretation Scheme. Solid and dashed lines indicate the limits of the basin and sub-basin, respectively. Numbers indicate the sub-basins depth in km.

shown over the passive paleomargin, thanks to the inverse paleo-faults producing overthrusting (Pindell *et al.,* 2006). Therefore, the shape of the ophiolites bodies are related with this process.

The structural relations between the different rock groups are inferred from the cross-sections analysis, confirming a compressive tectonic process that produced the south to north emplacement of the ophiolites and Cretaceous volcanic arc rocks over the passive paleomargin during the Mesozoic-Tertiary time.

The main results obtained from the analysis of the 3D model include the limits of the Saramaguacán basin, the sub-basins location and their maximum depths as shown in Figure 9.

Conclusions

New structural features of the Saramaguacán basin were obtained based from 3D inversion of gravimetric data. The depocenter depth and thickness for the different rock groups were also determined. The cross-sections show the tectonic complexity of the overthrust process, revealing structures of ramp and shelf, as well as the location and geometry of the sub-basins and depths of the probable oil-collector rocks. It is very important to know the lateral variation with depth of the oil-source (Paleomargin rocks) and oil-collector (sedimentary rocks) rock, for the later one, it will be important to know the thickness to support future research to locate oil drilling and oil volume to calculate that could be stored by the oil-collector rocks. Evidence was obtained for the compressive tectonics that originated the Saramaguacán basin in the Mesozoic-Tertiary. The 3D model supports the hypothesis concerning south to north tectonic emplacement of the ophiolites and Cretaceous rocks over the carbonate-terrigenous sequences from the Bahamas paleomargin. The basin limits, its structural scheme and the more probable inside stratigraphy were determined. The contact relations between volcanic, intrusive, ophiolites and paleomargin rocks obey the faulting originated along the push, tectonic transport, and isostatic equilibrium process. In cross sections and isometric diagrams indicate the location and behavior of the fault depth and the possible presence of new or unknown faults. It is important to identify the source rocks (carbonates from paleomargin) at depths lower than 4 km. The Saramaguacán basin exhibits favorable geologic conditions for oil preservations.

Acknowledgments

We thank Esthenis Martínez Rojas for the well records and geophysical data used in this research. Financial support was granted to the principal author through a scholarship from CONACYT.

Bibliography

Albear J., Boyanov I., Brezsnyanszky K., Cabrera R., Chejovich V., Echevarría B., Flores R., Formell F., Franco G., Haydutov I., Iturralde-Vinent M., Kantchev I., Kartashov I., Kostadinov V., Millán G., Myczynski R., Nagy E., Oro J., Peñalver L., Piotrowska K., Pszczolkowski A., Radoczj J., Rudnicki J., Somin M.L., 1988, Geological map of Cuba, Scale 1:250 000, Cuba Academy of Sciences and Institute of Geology and Paleontology.

Alvarez-Castro J., Otero R., Valladares S., García R., López J.O., Cruz R., Villavicencio B., Sánchez-Arango J., 1995, Geological Characterization Block 14-15. CEINPET file, Havana, Cuba.

Batista J., Pérez-Flores M.A., Quiroga-Goode G., Gallardo L.A., 2007, Geometry of ophiolites in Eastern Cuba from 3D inversion of aeromagnetic data, constrained by surface geology. *Geophysics,* 72, (3), May-June, B81-B91.

Blanco J., 1999, Stratigraphy and paleogeography of piggyback basins eastern Cuba Center. PhD. Thesis, Dept. of Geol., Instituto Superior Minero Metalúrgico de Moa, Cuba.

Blanco J., Batista J., Riverón B., 2000, Structure of the foreland basin in the suture zone in the region Esmeralda, Minas, Camaguey province according to gravity data. Paper presented at 1st. Cuban Congress of Geophysics. Cuban Society of Geology.

Blanco J., Proenza J., 2000, Tectonostratigraphic Systematization of central-eastern Cuba. Minería y Geología, 3, (1), 35-45.

Domínguez Z., López-Quintero J.O., 2005, Geochemical characterization of crude Cubans: classification based on saturated biomarkers. Paper presented at III Brazilian Congress P&D in Oil and Gas.

Gallardo L.A., Pérez-Flores M.A., Gómez-Treviño E., 2005, Refinement of three-dimensional multilayer models of basins and crustal environments by inversion of gravity and magnetic data. *Tectonophysics*, 397, 37-54.

Gallardo-Delgado L.A., Pérez-Flores M.A., Gómez-Treviño E., 2003, A versatile algorithm for joint 3- D inversion of gravity and magnetic data. *Geophysics*, 3, (68), 1-11.

Gill P., Hammarling S., Murray W., Saunders M., Wright M., 1986, User's guide for LSSOL: A package for constrained linear least-square and quadratic programming: Stanford Univ. Tech. Report SOL-886-1.

Iturralde-Vinent M., Tchounev D., Cabrera R., 1981, Geology of the territory Ciego-Camagüey-Las Tunas: the results of scientific research and geological mapping at 1:250 000. Technical Report. Academy of Sciences of Cuba and Bulgaria. ONRM. Havana.

Iturralde-Vinent M., Thieke H., 1986, Final report on the results of complex geological survey and accompanying search at 1:50 000 in the polygon CAME III, Camagüey. Technical Report. Havana.

Iturralde-Vinent M., 1996, Introduction to Cuban geology and geophysics. In: Ophiolites and volcanic arcs of Cuba. Iturralde-Vinent, M. (ed.) Miami. Florida: 83-120.

López-Rivera J.G., López-Quintero J.O., 2004, The Main Scenarios for Petroleum Exploration in the Southeastern Part of the Gulf of Mexico. Paper presented at AAPG International Conference. Mexico.

Magnier C., Moretti A.I., López-Quintero J.O., Gaumet F., López J.G., Letouzey J., 2004, Geochemical characterization of source rocks, crude oils and gases of Northwest Cuba. Marine and Petroleum Geology, 21, (2), 195-214.

Mann P., Taylor F., Lawrence E., Ku T., 1995, Actively evolving microplate formation by oblique collision and sideway motion along strike-slip faults: An example from the northeastern Caribbean plate margin. *Tectonophysics,* 246, 1-69.

Martínez E., Sorá A., García R., 1998, The geological-structural portion of the Basin Western Central California according to geophysical data. Paper presented at Geology and Mining '98. Volume 1. CNIG. Institute of Geology and Palaeontology (ed.). Cuba: 404-407.

Maximov S.P., Shein V.S., Furrazola-Vermúdez G., 1985, Tectonic map of Cuba. 1:500 000. 4 sheet (ed.) ICGC. Cuba.

Pérez-Flores M.A., Suárez-Vidal F., Gallardo L.A., González A., Vázquez R., 2004, Structural pattern of the Todos Santos Coastal Plain, based on geophysical data. *Ciencias Marinas*, 30(2), 349-364.

Pindell J., Kennan L., Stanek K.P., Maresch W.V., Draper G., 2006, Foundations of Gulf of Mexico and Caribbean evolution: eight controversies resolved. *Geologica Acta*, 4(1-2), 303-341.

Puscharovskiy Y.M., Mossakovskiy A.A., Suárez J., 1989, Tectonic map of Cuba at 1:500 000 (4 sheets): Academy of Sciences of Cuba, Institute of Geology and Paleontology and Academy of Sciences of the USSR, Moscow.

Geofísica Internacional (2012) 51-1: 63-72

Original paper

A case of study for Pseudorange multipath estimation and analysis: TAMDEF GPS network

Guadalupe Esteban Vázquez B.* and Dorota A. Grejner-Brzeziska

Received: January 31, 2011; accepted: June 7, 2011; published on line: December 16, 2011

Resumen

Un estudio de investigación se llevó a cabo para evaluar la cantidad del efecto de multiruta en pseudo-distancias a partir de observaciones GPS (Sistemas de Posicionamiento Global) en la red TAMDEF (Montañas Trans Antárticas), situadas en la región de Victoria en la Antártica y que consta de 33 estaciones GPS. Es bien sabido que, a pesar de la selección cuidadosa de los lugares para el establecimiento de estaciones GPS, éstas son en cierta medida afectadas por el efecto de multiruta. El efecto de multiruta para mediciones GPS de pseudo-distancias puede ser entonces una contribución potencial que podría tener un impacto en el posicionamiento de las estaciones TAMDEF. De tal manera que, las variaciones de los errores medios cuadráticos (MP1-RMS y MP2-RMS) fueron estimadas y analizadas a fin de identificar las estaciones con mayor y menor índice de afectación, considerando datos GPS desde el año 1996 hasta el año 2006. La estación McMurdo (MCM4) del IGS fue incluida como parte de la red TAMDEF, tomando en cuenta que ésta es considerada el punto principal de acceso al ITRF (Marco de Referencia Terrestre Internacional) para esta parte de la Antártica.

Palabras clave: pseudo-distancia, multiruta, GPS, TAMDEF, Antártica.

Abstract

A research study was conducted to evaluate the amount of pseudorange multipath from GPS (Global Positioning System) observables at TAMDEF (Trans Antarctic Mountain Deformation) network, located in Victoria Land, Antarctica consisting of 33 GPS stations. It is well known that, despite carefully selected locations, the GPS stations are to some extent, affected by the presence of multipath. Pseudorange multipath effect for GPS measurements could be a potential contributor that might have an impact on the TAMDEF stations positioning. Thus, the root mean squared error variations (MP1-RMS and MP2-RMS) were estimated and analyzed in order to identify the most and least affected sites, considering GPS data span from year 1996 to year 2006. McMurdo (MCM4) IGS (The International GNSS Service for Geodynamics, formerly the International GPS Service) site, was adopted as part of the TAMDEF network, since MCM4 is the primary ITRF (International Terrestrial Reference Frame) access point for this part of Antarctica.

Key words: Pseudorange, multipath, GPS, TAMDEF, Antarctica.

G. Esteban Vázquez B.
Escuela de Ciencias de la Tierra de la Universidad Autónoma de Sinaloa
Culiacán, México
*Corresponding author: estebanv_99@yahoo.com

Dorota A. Grejner-Brzeziska
Satellite Positioning and Inertial Navigation
SPIN Laboratory
The Ohio State University

Introduction

The TAMDEF Network is a GPS array deployed on bedrock, consisting of 25-campaign sites, 6-quasi-continuous sites and 2-continuous sites (see Figure 1), located in the Trans Antarctic Mountains of the southern Victoria Land and on the islands in the adjacent Ross Sea. TAMDEF is the OSU (Ohio State University) and USGS (United States Geological Survey) joint project sponsored by the NSF (National Science Foundation), initiated in 1996 with the primary objective to measure vertical and horizontal crustal deformation (http://www.geology.ohio-state.edu/TerryWilson/research_gps.htm). At the present time, some of the TAMDEF sites are part of the related POLar Earth observing NETwork (POLENET) which is expected to be an ambitious international project to understand geophysical aspects at very remote high-latitude such as the Antarctic continent (http://www.polenet.org/).

Despite their careful selection, the TAMDEF GPS sites are, to some extent, affected by the presence of local multipath effects. This effect may vary slowly on a seasonal basis, or abruptly due to such natural events as snowfall. Studies of multipath effects and suitable processing

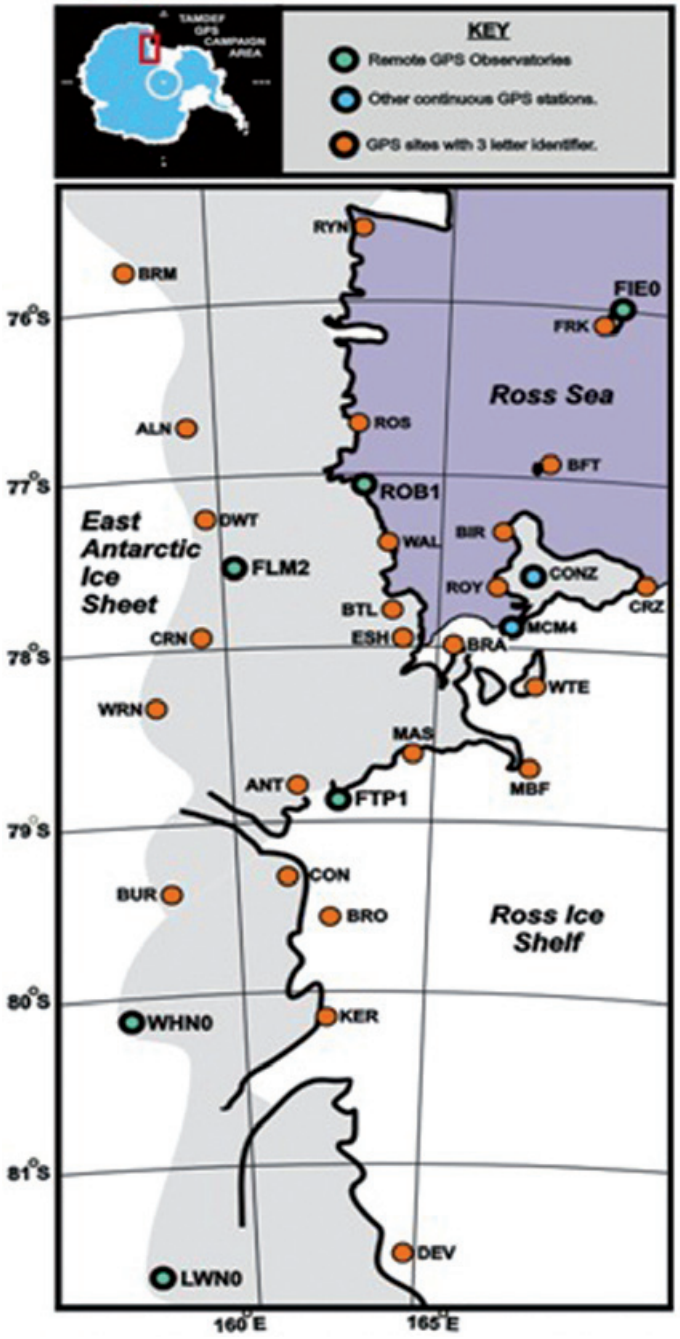

Figure 1. TAMDEF GPS network, located in the Trans Antarctic Mountains of the southern Victoria Land and on the islands in the adjacent Ross Sea.

techniques are given, for example, by Han and Rizos (1997), Rizos (1999), Meertens (2000), Ge *et al*. (2000), Dodson *et al*. (2001), Roberts *et al*. (2002), Ge *et al*. (2002) and Satirapod *et al*. (2003). It is important to indicate here that all of the methods cited above have their advantages and limitations; however, it is been shown in the above-cited literature that the multipath error in the pseudoranges is significantly larger (up to several meters) than for carrier phases (usually, millimeter to centimeter level).

Since the multipath effect depends on the satellite geometry and the surrounding environment of the GPS antenna (as well as the antenna type), it is practically the same after one sidereal day under similar atmospheric conditions. In other words, with the current GPS orbit design, the entire satellite configuration normally advances about 4 minutes between two consecutive days. Thus, the positioning solution of data derived from the repetition of the GPS satellite constellation between two sidereal days ought to be affected by "systematic" multipath. This effect can be used to extract the multipath signature from the positioning time-series (Ge *et al*., 2000, Roberts *et al*., 2002). Hilla and Cline (2002) pointed out that the significance of analyzing pseudorange multipath is that the accuracy of any GPS application relies to a large extent on pseudorange measurements (e.g., differential pseudorange, kinematic and rapid static surveying, and ionospheric monitoring). Therefore, in order to identify the effective level of multipath, the daily MP1-RMS and MP2-RMS variations were estimated and analyzed at each TAMDEF site.

TAMDEF GPS instrumentation

TAMDEF hardware consists of a wide variety of dual-frequency, 12-20 channel, geodetic-grade GPS receivers, kept in insulated boxes and powered from 60W solar panels and 80 amp-hours gel-cell batteries. The GPS receivers used in the TAMDEF network are: Trimble 5700/R7, Ashtech Z-Surveyors, DL4-NovAtel, Leica RS500, Javad Legacy and Javad Euro-80. The GPS receivers, supplied through cooperation with USGS, OSU and UNAVCO (University NAVstar COnsortium), are usually set to record data every 30 seconds in the field without any replacement of their memory cards. To allow for consistency, the TAMDEF team places the same antenna type at each site each year. TAMDEF almost exclusively uses Ashtech/Thales Dorne-Margolin (D&M) choke-ring antenna designed to reduce L1 multipath. This type of antenna is used because it accepts a wide range of input voltages, and it has also been tested to be consistent for possible phase center variations when using the antenna calibration parameters provided by NGS (National Geodetic Survey) (http://www.grdl.noaa.gov/ANTCAL/).

GPS data availability and data processing

When TAMDEF network was first established, only GPS data for a short of time period (1 or 2 weeks) was available. However, this has improved over the past few years and data from some permanent quasi-continuous (with 1 to 3 months of data) and also continuous trackers (with almost the entire year of data) are now accessible for further processing. Figure 2 illustrates TAMDEF station data availability for those sites (FLM2: Mount Fleming 2; FTP1: Fishtail Point 1; LWN0: Lonewolf Nunatak; MCM4: McMurdo; ROB1: Cape Roberts; WHN0: Westhaven Nunatak) with longer GPS data span from 1996 to 2005, hereinafter called "tested" sites.

The TAMDEF GPS data were converted and archived to the RINEX (Receiver INdependent EXchange) format (ftp://igscb.jpl.nasa.gov/igscb/data/format/rinex210.txt). The TEQC software (Test of Quality Check) provided by UNAVCO, which is also available for public use at (http://www.unavco.org/facility/software/teqc/teqc.html), was used to verify the quality and integrity of the RINEX files and to estimate the daily root mean squared variations for each analyzed TAMDEF site. The main specifications for the GPS data processing included the use of a 30-sec sampling rate and 10° cut-off angle.

Pseudorange multipath estimation

It is important to point out, that in the one-way observation equations used for the multipath estimation, the inter-channel bias and the non-integer initial phase terms for the satellite and the receiver were neglected. This research follows the pseudorange multipath approach proposed by Estey and Meertens (1999); Hilla and Cline (2002); http://www.unavco.org QC V3 Users Guide, UNAVCO 1994. The pseudorange and carrier phase measurements on L1 and L2 for a satellite (κ) and a receiver (i) are given by:

$$P_{L1} = R + c(\quad t^k - \quad t_i) + I_{L1} + T + MP_{P1} \tag{1}$$

$$P_{L2} = R + c(\quad t^k - \quad t_i) + I_{L2} + T + MP_{P2} \tag{2}$$

$$\Phi_{L1} = R + c(\quad t^k - \quad t_i) + \lambda_{L1} N_{L1} - I_{L1} + T + MP_{\Phi_{L1}} \tag{3}$$

$$\Phi_{L2} = R + c(\quad t^k - \quad t_i) + \lambda_{L2} N_{L2} - I_{L2} + T + MP_{\Phi_{L2}} \tag{4}$$

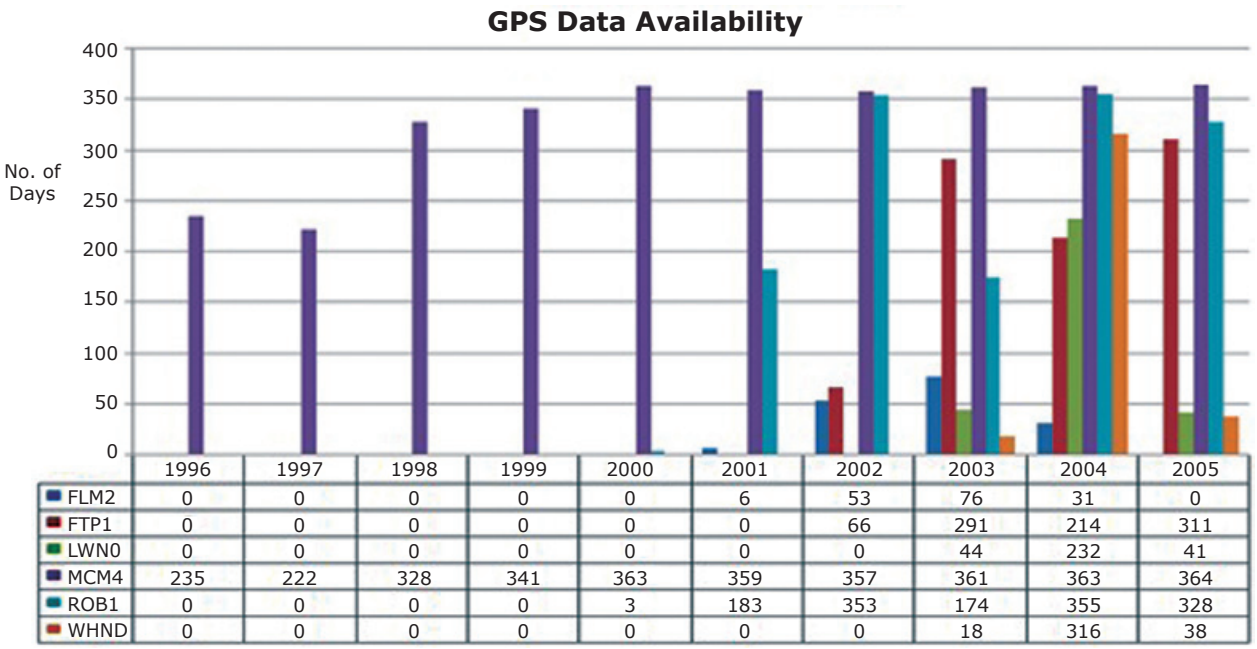

	1996	1997	1998	1999	2000	2001	2002	2003	2004	2005
FLM2	0	0	0	0	0	6	53	76	31	0
FTP1	0	0	0	0	0	0	66	291	214	311
LWN0	0	0	0	0	0	0	0	44	232	41
MCM4	235	222	328	341	363	359	357	361	363	364
ROB1	0	0	0	0	3	183	353	174	355	328
WHND	0	0	0	0	0	0	0	18	316	38

Figure 2. GPS data availability for "tested" (with longer GPS data span) TAMDEF sites.

where: P_{L1} and P_{L2} are the pseudorange observations (in meters), ϕ_{L1} and ϕ_{L2} are the corresponding carrier phase observations on L1 and L2, respectively, R is the geometric distance between the satellite and the receiver (in m), c is the constant speed of light (in m/s), Δt_i is the satellite clock correction (in s), Δt^k is the receiver clock correction (in s), I_{L1} and I_{L2} are the ionospheric range errors (in m), T is the tropospheric range error (in m), N_{L1} and N_{L2} are the integer ambiguities (in cycles), MP_{P1}, MP_{P2}, $MP_{\phi L1}$ and $MP_{\phi L2}$ are the corresponding pseudorange and carrier phase multipath, respectively (including the observational noise), $\lambda_{L1} \approx 19$ cm and $\lambda_{L2} \approx 24$ cm are the wavelengths of the signals on L1 and L2, $f_1 \approx 1.5754\ GHz$ and $f_2 \approx 1.2276\ GHz$ are frequencies of signals L1 and L2, respectively.

Taking the advantage of the relationship that between the ionospheric delay for L1 and L2 leads to:

$$I_{L2} = \alpha \cdot I_{L1} \tag{5}$$

with:

$$\alpha = \left(\frac{f_1}{f_2} \right)^2 .$$

Subtracting Equation (4) from (3) gives:

$$\Phi_{L1} - \Phi_{L2} = \lambda_{L1} N_{L1} - I_{L1} + MP_{\Phi_{L1}} - \lambda_{L2} N_{L2} + I_{L2} - MP_{\Phi_{L2}} \tag{6}$$

Substituting Equation (5) into (6), grouping and simplifying yields:

$$\frac{(\Phi_{L1} - \Phi_{L2})}{(\alpha - 1)} = I_{L1} + \frac{(\lambda_{L1} N_{L1} - \lambda_{L2} N_{L2})}{(\alpha - 1)} + \frac{(MP_{\Phi_{L1}} - MP_{\Phi_{L2}})}{(\alpha - 1)} \tag{7}$$

Combining Equation (7) with (3) to eliminate I_{L1} term, results in:

$$\begin{aligned} \Phi_{L1} + \frac{(\Phi_{L1} - \Phi_{L2})}{(\alpha - 1)} &= R + c(\quad t^S - \quad t_R) + T + \lambda_{L1} N_{L1} + \\ &\frac{(\lambda_{L1} N_{L1} - \lambda_{L2} N_{L2})}{(\alpha - 1)} + MP_{\Phi_{L1}} + \frac{(MP_{\Phi_{L1}} - MP_{\Phi_{L2}})}{(\alpha - 1)} \\ &= R + c(\quad t^S - \quad t_R) + T + b_1 + m_{\Phi_1} \end{aligned} \tag{8}$$

Equation (8) is a linear combination of observed L1 and L2 carrier phases, where the ambiguity bias term b_1 is introduced as:

$$b_1 = \lambda_{L1} N_{L1} + \frac{(\lambda_{L1} N_{L1} - \lambda_{L2} N_{L2})}{(\alpha - 1)} \tag{9}$$

While the phase multipath effect is now defined by:

$$m_{\Phi_1} = MP_{\Phi_{L1}} + \frac{(MP_{\Phi_{L1}} - MP_{\Phi_{L2}})}{(\alpha - 1)} \quad (10)$$

Combining Equations (3), (7) and (8) gives:

$$P_{L1} - \left[1 + \frac{2}{(\alpha-1)}\right]\Phi_{L1} + \left[\frac{2}{(\alpha-1)}\right]\Phi_{L2} = MP_{P1} - \frac{(\lambda_{L1}N_{L1} - \lambda_{L2}N_{L2})}{(\alpha-1)} - b_1 + MP_{\Phi_{L1}} - 2m_{\Phi_1} \quad (11)$$

The new ambiguity bias term is now defined by:

$$B_1 = -\frac{(\lambda_{L1}N_{L1} - \lambda_{L2}N_{L2})}{(\alpha-1)} - b_1 = -\left[1 + \frac{2}{(\alpha-1)}\right]\lambda_{L1}N_{L1} + \left[\frac{2}{(\alpha-1)}\right]\lambda_{L2}N_{L2} \quad (12)$$

And the new phase multipath effect is introduced as:

$$M_{\Phi 1} = -(MP_{\Phi_{L1}} - MP_{\Phi_{L2}}) - m_{\Phi_1} = -\left[1 + \frac{2}{(\alpha-1)}\right]MP_{\Phi_{L1}} + \left[\frac{2}{(\alpha-1)}\right]MP_{\Phi_{L2}} = MP_{\Phi_{L1}} - 2m_{\Phi_1} \quad (13)$$

The pseudorange multipath MP_1 is then expressed as the linear combination from (11), namely:

$$MP_1 = P_{L1} - \left[1 + \frac{2}{(\alpha-1)}\right]\Phi_{L1} + \left[\frac{2}{(\alpha-1)}\right]\Phi_{L2} = MP_{P1} + B_1 + M_{\Phi_1} \quad (14)$$

Similar derivations are performed to express MP_2 as a linear combination:

$$MP_2 = P_{L2} - \left[\frac{2\cdot\alpha}{(\alpha-1)}\right]\Phi_{L1} + \left[\frac{2\cdot\alpha}{(\alpha-1)} - 1\right]\Phi_{L2} = MP_{P2} + B_2 + M_{\Phi 2} \quad (15)$$

with: MP_{P2}, B_2, and $M_{\phi 2}$ are defined similarly to MP_{P1}, B_1, and $M_{\phi 1}$.

Based on the above derivations, the daily MP1-RMS and MP2-RMS variations were computed by means of Equations (14) and (15).

Results and analysis

Even though TAMDEF network consists of 33-stations, only the "tested" sites with longer GPS data span (FLM2, FTP1, LWN0, MCM4, ROB1 and WHN0) were considered for the analysis, and they are illustrated in Figures 3 and 4. There the daily MP1-RMS (with scatter from 0 to 1 meter) and MP2-RMS (with scatter from 0 to 3 meters) variations are presented in terms of

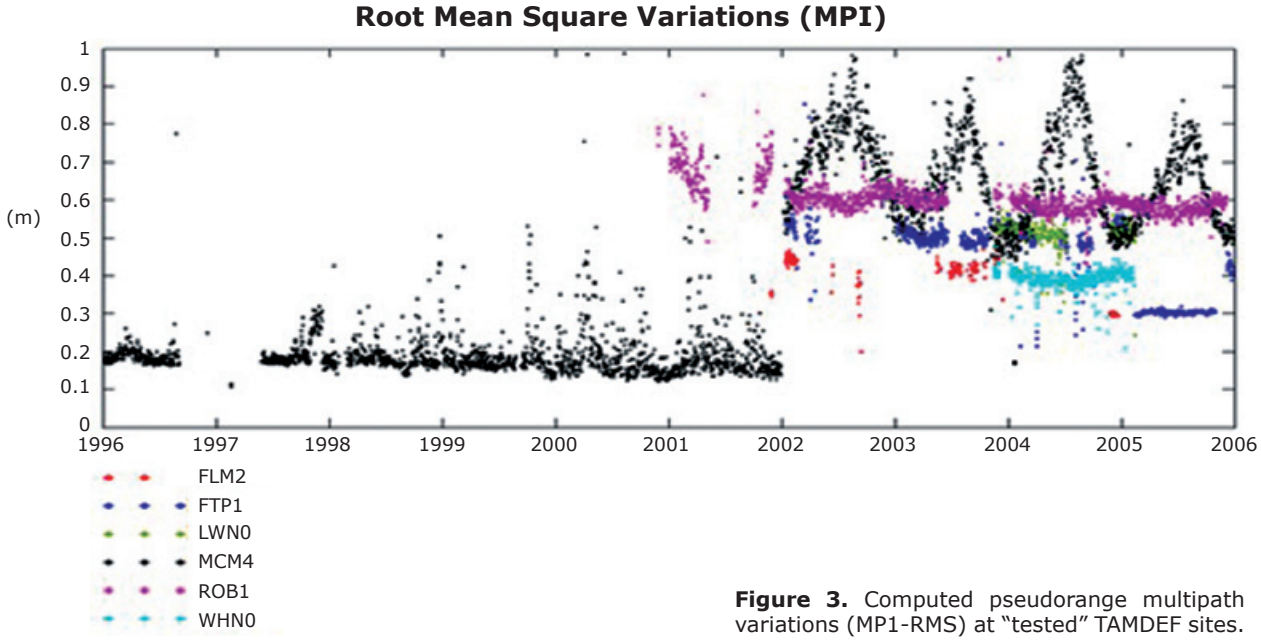

Figure 3. Computed pseudorange multipath variations (MP1-RMS) at "tested" TAMDEF sites.

time-series (1996-2006). As can be seen in these figures, MCM4 is the site with almost 10-years of continuous data. In other words, roughly 3300 days of GPS data were available for this site. However, there is a gap from September 1996 to May 1997; after that date, the MCM4 station recorded data almost for the entire next years. A jump on the MP1-RMS and MP2-RMS results can be observed at the MCM4 site at the beginning of year 2002. This fact could be attributed to the hardware change when the AOA SNR-12 ACT replaced the ROGUE SNR-8000 GPS receiver on January 3, 2002.

It is very important to point out, that there was no antenna replacement since the installation of the MCM4 site and this is illustrated in Figure 5. Also note that seasonal moisture condensation can be seen inside the radome. Furthermore, for the period between 2002 and 2006 (after the receiver replacement issue), the MP1-RMS and MP2-RMS results for MCM4 behave the same way (i.e., annual variations) getting the highest values in the middle of every year. Prior to 2002, the results look much more comparable among them at MCM4.

The MP1-RMS and the MP2-RMS represent the pseudorange multipath variability, for instance, often track the annual variations of heights. Thus, according to Ray (2006) annual heights and MP1-RMS and MP2-RMS variations are sometimes found to be correlated with changes in station tracking hardware, and this is illustrated in Figure 6. Annual signals begin with GPS receiver swap (3 Jan 2002), Turbo Rogue SNR-8000 changed to AOA SNR-12. Scale and units (millimeter) for the height (dU) are shown in the left hand side, while the scale and units (meter level) for the MP1-RMS and MP2-RMS are presented on the right hand side of the figure.

Results for the FLM2, LWN0 and WHN0 sites fluctuate within 20 to 65 centimeters for MP1-RMS and within 0.3 to 1.3 meters for MP2-RMS, respectively; with no significant variations

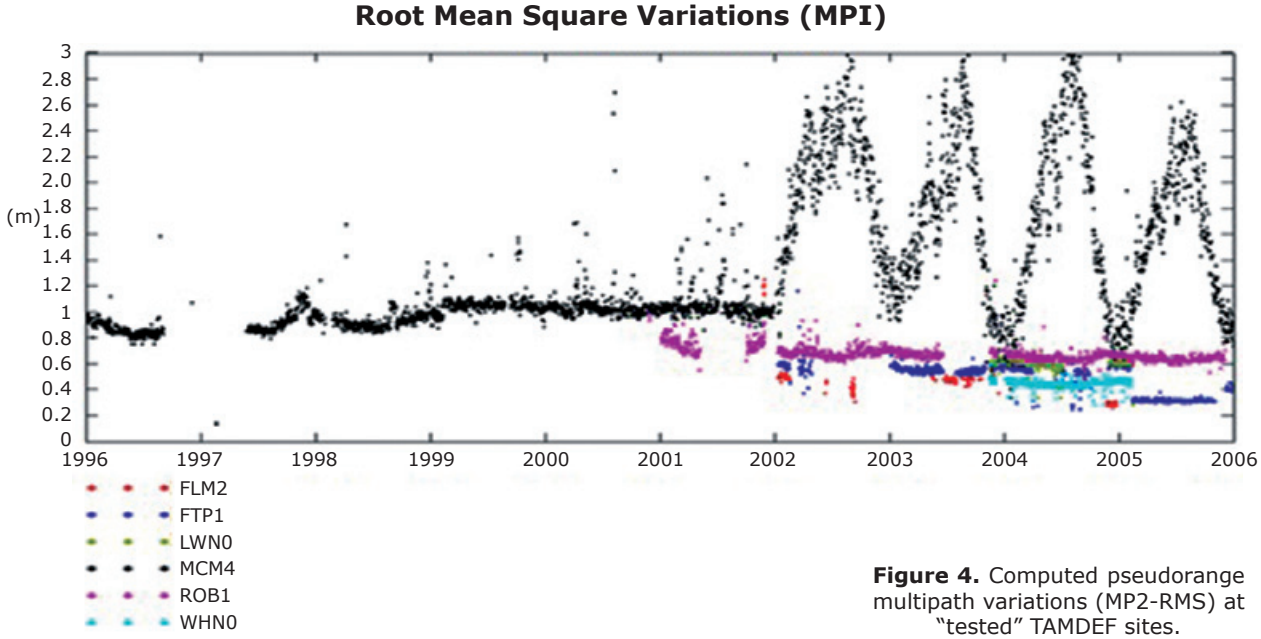

Figure 4. Computed pseudorange multipath variations (MP2-RMS) at "tested" TAMDEF sites.

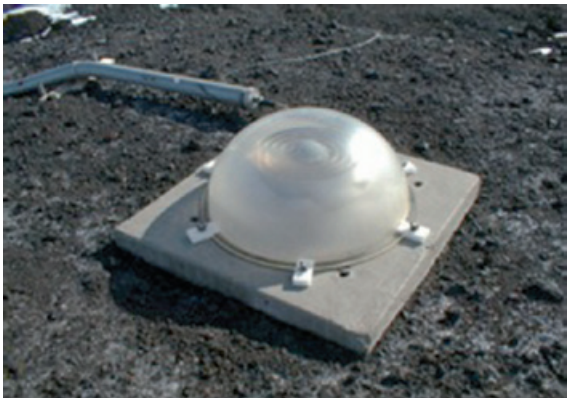

Figure 5. McMurdo (MCM4) IGS and TAMDEF site, primary ITRF access point for this part of Antarctica.

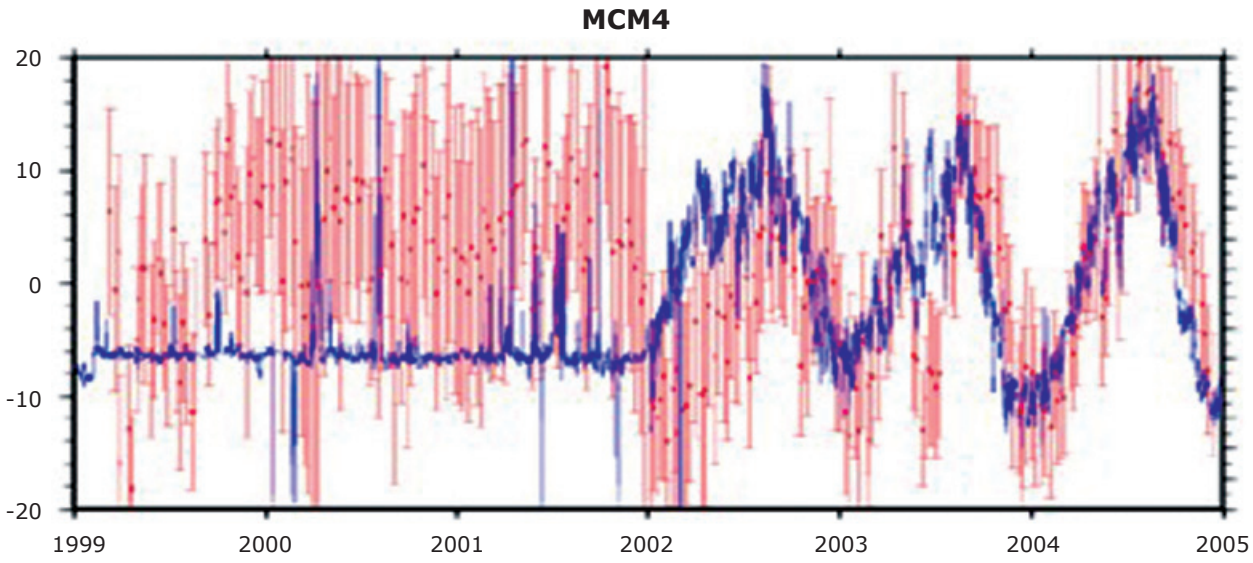

Figure 6. Annual heights vs. MP1-RMS and MP2-RMS at MCM4 site.

in their behavior. However, it is difficult to comment on how these stations performed, since not enough data is available for a better interpretation; except for the WHN0 that shows almost a complete year (316 days) of consistent results for the analysis. Results for the FTP1 site oscillate from 20 to 90 centimeters for MP1-RMS and from 0.25 to 1.15 meters for MP2-RMS, respectively. In addition, FTP1 station presents a discontinuity in the results that can be observed after year 2005. This fact definitely cannot be attributed to any change in the hardware, since no replacement in the antenna or receiver had occurred since the installation of the site. On the other hand, the MP1-RMS variations for ROB1 site ranges from 0.4 to 1 meter, while the scatter for the MP2-RMS is within 0.4 to 1.25 meters and both graphs seem to follow a pattern that also could be considered as sinusoidal, but in a short scale as compared to the MCM4 station. A gap can be observed as well for the ROB1 station for mid 2003 to beginning of year 2004.

Photographs obtained for some of the tested GPS sites (FLM2, FTP1 and ROB1) verified the presence of rocks, solar panels and other reflectors in close proximity to the GPS antennas that could be a potential source of the multipath effect (see Figures 7, 8 and 9). In addition, with knowledge from these photographs and from analyzing pseudorange multipath for TAMDEF network it can be determined which sites were severely affected; thus, with other *in-situ* carrier phase calibration techniques one can experiment to infer how well they perform at these selected tested TAMDEF sites.

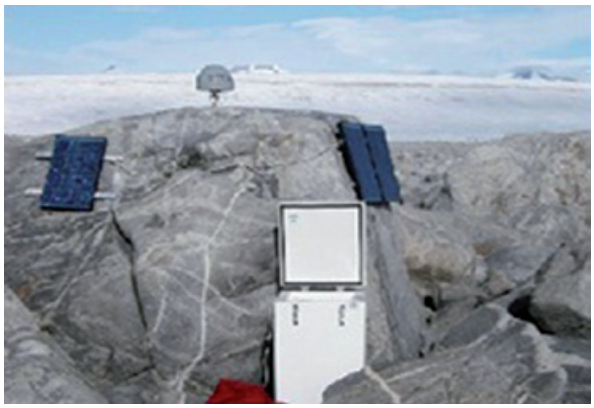

Figure 7. Mount Fleming (FLM2) site, located at the East Antarctic Ice Sheet.

Figure 8. Fishtail Point 1 (FTP1) site, located at the adjacent Ross Sea.

Figure 9. Cape Roberts (ROB1) site, located at the Ross Ice Shelf.

Table 1 and 2 shows the statistics of the MP1-RMS and MP2-RMS variations for all the TAMDEF sites. Here, the maximum, minimum, mean and standard deviations values are presented in units of meters.

In Tables 1 and 2 are sumarized the IGS designator for the hardware used (i.e., GPS receiver and antenna type) as well as the number of available days of data for each TAMDEF. FTP1, MCM4 and ROB1 were the sites with higher levels (meter range) of pseudorange multipath (MP1-RMS), ranking first, second and third as shown in Table 1. Hypothetically, these three stations are within the most affected tested sites with longer data span, even though they rank twenty

Table 1. Statistics of the MP1-RMS for the entire TAMDEF network.

Rank (Order)	Site	No. of Days	Max (m)	Min (m)	St. Dev. ±(m)	Mean (m)	Receiver Type	Antenna Type
1	MCM4	3293	1.76	0.11	0.25	0.40	AOA SNR-12 ACT	AOAD/M_T
2	ROB1	1406	0.97	0.43	0.04	0.60	TPS HE_GD	ASH700936E
3	FTP1	882	0.89	0.21	0.10	0.45	TPS HE_GD	ASH700936D_M
4	WTE0	69	0.85	0.01	0.21	0.54	ASHTECH Z-XII3	TRM29659.00
5	FIE0	266	0.83	0.24	0.05	0.43	TPS HE_GGD	ASH701945B_M
6	KER0	81	0.75	0.22	0.09	0.36	DL4-NovAtel	ASH700936E
7	BRM0	30	0.73	0.23	0.09	0.45	TRIMBLE_5700	ASH701945E_M
8	LWN0	317	0.64	0.24	0.04	0.51	TPS HE_GGD	ASH701945B_M
9	ROY0	69	0.59	0.08	0.12	0.22	TRIMBLE 4000SSI	TRM29659.00
10	BRO0	80	0.57	0.24	0.05	0.33	DL4-NovAtel	ASH700936E
11	WAL0	74	0.55	0.02	0.14	0.20	TRIMBLE 4000SSE	TRM 29659.00
12	BRA0	42	0.52	0.33	0.06	0.47	TRIMBLE 4000SSI	ASH700936E
13	ROS0	33	0.51	0.26	0.05	0.34	DL4-NovAtel	ASH701945D_M
14	MAS0	30	0.51	0.37	0.04	0.42	TRIMBLE 4000SSE	TRM29659.00
15	BIR0	31	0.51	0.08	0.16	0.29	TRIMBLE 4000SSI	ASH700936E
16	CRZ0	19	0.50	0.19	0.09	0.43	TRIMBLE 5700	ASH701945C_M
17	CON0	49	0.49	0.22	0.05	0.28	DL4-NovAtel	ASH700936E
18	WHN0	372	0.48	0.21	0.03	0.39	TPS HE_GGD	ASH701945B_M
19	ALN0	58	0.47	0.19	0.07	0.31	ASHTECH Z-12	ASH700936E
20	FLM2	166	0.47	0.20	0.06	0.39	TPS HE_GD	ASH700936E
21	BUR0	60	0.46	0.24	0.04	0.31	DL4-NovAtel	ASH700936E
22	BFT0	38	0.45	0.23	0.09	0.36	TPS LEGACY	ASH701945E_M
23	WRN0	124	0.43	0.17	0.05	0.27	DL4-NovAtel	ASH700936E
24	ANT0	46	0.40	0.20	0.05	0.29	TRIMBLE 4000SSE	ASH700936E
25	MBF0	74	0.38	0.18	0.06	0.27	TRIMBLE 5700	ASH701945E_M
26	BTL0	29	0.38	0.17	0.05	0.30	ASHTECH Z-12	TRM41249.00
27	ESH0	40	0.37	0.17	0.04	0.24	DL4-NovAtel	NOV702_2.02
28	RYN0	44	0.36	0.27	0.02	0.32	TRIMBLE 5700	ASH701945E_M
29	DWT0	21	0.36	0.21	0.04	0.29	ASHTECH Z-12	ASH700936E
30	VAN0	10	0.35	0.32	0.01	0.33	TRIMBLE 4000SSI	TRM22020.00+GP
31	FRK0	29	0.35	0.20	0.06	0.39	ASHTECH Z-12	ASH700936E
32	FLM0	18	0.31	0.27	0.01	0.29	TPS HE_GD	ASH700936E
33	CRN0	16	0.30	0.27	0.01	0.29	TRIMBLE 4000SSE	ASH700936E

Table 2. Statistics of the MP2-RMS for the entire TAMDEF network.

Rank (Order)	Site	No. of Days	Max (m)	Min (m)	St. Dev. ±(m)	Mean (m)	Receiver Type	Antenna Type
1	MCM4	3293	3.38	0.13	0.56	1.33	AOA SNR-12 ACT	AOAD/M_T
2	ROS0	33	1.59	0.37	0.41	1.10	DL4-NovAtel	ASH701945D_M
3	BTL0	29	1.54	0.26	0.45	0.78	ASHTECH Z-12	TRM41249.00
4	WAL0	74	1.53	0.04	0.36	0.36	TRIMBLE 4000SSE	TRM 29659.00
5	RYN0	44	1.53	0.88	0.15	1.31	TRIMBLE 5700	ASH701945E_M
6	BIR0	31	1.52	0.12	0.51	0.66	TRIMBLE 4000SSI	ASH700936E
7	ESH0	40	1.50	0.24	0.46	0.75	DL4-NovAtel	NOV702_2.02
8	WTE0	69	1.46	0.01	0.30	0.86	ASHTECH Z-XII3	TRM29659.00
9	CRZ0	19	1.46	0.38	0.29	1.12	TRIMBLE 5700	ASH701945C_M
10	MBF0	74	1.45	0.27	0.43	0.70	TRIMBLE 5700	ASH701945E_M
11	BRA0	42	1.45	0.43	0.32	0.76	TRIMBLE 4000SSI	ASH700936E
12	ANT0	46	1.45	0.40	0.28	0.97	TRIMBLE 4000SSE	ASH700936E
13	DWT0	21	1.44	0.44	0.34	1.05	ASHTECH Z-12	ASH700936E
14	MAS0	30	1.43	0.84	0.24	1.17	TRIMBLE 4000SSE	TRM29659.00
15	FRK0	29	1.41	0.33	0.39	0.82	ASHTECH Z-12	ASH700936E
16	CRN0	16	1.40	1.15	0.07	1.30	TRIMBLE 4000SSE	ASH700936E
17	ALN0	58	1.39	0.30	0.40	0.69	ASHTECH Z-12	ASH700936E
18	WRN0	124	1.39	0.35	0.33	0.70	DL4-NovAtel	ASH700936E
19	BRM0	30	1.38	0.51	0.24	1.16	TRIMBLE_5700	ASH701945E_M
20	FLM0	18	1.36	0.38	0.24	1.07	TPS HE_GD	ASH700936E
21	FIE0	266	1.32	0.25	0.08	0.52	TPS HE_GGD	ASH701945B_M
22	FLM2	166	1.25	0.27	0.16	0.47	TPS HE_GD	ASH700936E
23	ROB1	1406	1.24	0.41	0.06	0.68	TPS HE_GD	ASH700936E
24	BFT0	38	1.21	0.49	0.25	0.71	TPS LEGACY	ASH701945E_M
25	FTP1	882	1.16	0.25	0.12	0.48	TPS HE_GD	ASH700936D_M
26	ROY0	69	1.14	0.15	0.24	0.35	TRIMBLE 4000SSI	TRM29659.00
27	KER0	81	0.98	0.54	0.10	0.71	DL4-NovAtel	ASH700936E
28	LWN0	317	0.71	0.28	0.05	0.60	TPS HE_GGD	ASH701945B_M
29	BUR0	60	0.69	0.55	0.03	0.61	DL4-NovAtel	ASH700936E
30	BRO0	80	0.69	0.33	0.06	0.45	DL4-NovAtel	ASH700936E
31	WHN0	372	0.60	0.28	0.03	0.45	TPS HE_GGD	ASH701945B_M
32	VAN0	10	0.58	0.44	0.04	0.53	TRIMBLE 4000SSI	TRM22020.00+GP
33	CON0	49	0.56	0.30	0.05	0.38	DL4-NovAtel	ASH700936E

first, one and twenty third, respectively for MP2-RMS (see Table 2). It is very important to point out here that, following the recommendation provided by Hilla and Cline (2002) the GPS data used to compute the pseudorange multipath results, which are presented in Tables 1 and 2 were not smoothed. In other words, it was ensure that the TEQC software used to generate the MP1-RMS and MP2-RMS variations had turned off the smoothing option; otherwise results tend to look overly optimistic.

Conclusions

Definitely, TAMDEF stations were mostly affected in MP2. This issue could be attributed to the presence of rocks, solar panels and other reflectors nearby to the GPS antennas that could be a potential source of the multipath effect. Other potential issues might be how the GPS antennas were mounted, the antenna type used and its surrounding environment. However, the antenna calibration issue could be another source for having high levels of multipath. Thus, overall it can be concluded that MCM4 was found to be the site with highest multipath (between 1 to 3 meters) for the MP1-RMS and MP2-RMS variations, respectively. This fact is not good at all, since MCM4 is the primary ITRF access point for this part of Antarctica. The reason for high multipath (with seasonal effect) at MCM4 might be due to the receiver itself, the location environment and the existence of the antenna radome. Also recall that MCM4 antenna never has

been calibrated since this was initially installed in 1995. Higher levels of pseudorange multipath were also found for FTP1 and ROB1 sites, which seem not to have a problem with the GPS hardware but perhaps for the antenna environment (rocks and solar panels). Additionally, results from the pseudorange multipath (MP1-RMS and MP2-RMS variations) should be considered for further research to improve positioning results and GPS data cleaning for TAMDEF network.

Bibliography

Dodson A.H., Meng X., Roberts G.W., 2001, Adaptive Method for Multipath Mitigation and Its Applications for Structural Deflection Monitoring. *Proceedings of International Symposium on Kinematic Systems in Geodesy, Geomatics and Navigation*, Banff Alberta, Canada 101-110.

Estey L.H., Meertens C.M., 1999, TEQC: the multi-purpose toolkit for GPS/GLONASS data. GPS Solutions (3)1:42–49.

Ge L., Han S., Rizos C., 2000, Multipath Mitigation of Continuous GPS Measurements Using an Adaptive Filter. *GPS Solutions*, 4(2), 19-30.

Ge L., Han S., Rizos C., 2002, GPS Multipath Change Detection in Permanent GPS Stations. *Survey Review*, 36(283), 306-322.

Han S., Rizos C., 1997, Multipath Effects on GPS in mine environments. *X International Congress of the International Society for Mine Surveying, Fremantle, Australia,* 447-457.

Hilla S., Cline M., 2002, Evaluating Pseudorange Multipath Effects at Stations in the National CORS Network. *Proceedings of the Weiko A. Heiskanen Symposium in Geodesy*, Department of Geodetic Science and Surveying The Ohio State University, Columbus, Ohio, on CD.

Meertens C., 2000, The Antenna and Multipath Calibration System website: http://www.unavco.ucar.edu/projects/active_projects/amcs.

Ray Jim, 2006, Systematic errors in GPS position estimates, *IGS Workshop 2006*, 8-11 May 2006.

Rizos C., 1999, Quality Issues in Real-time GPS Positioning. IUGG Congress, Birmingham, U.K.

Roberts G.W., Meng X., Dodson A.H., Cosser E., 2002, Multipath Mitigation for Bridge Deformation Monitoring. *Journal of Global Positioning System* 1(1), 25-33.

Satirapod C., Khoonphool R., Rizos C., 2003, Multipath Mitigation of Permanent GPS Stations Using Wavelets. *Proceedings of 2003 International Symposium on GPS/GNSS*, Tokyo, Japan, 133-139.

http://www.geology.ohio-state.edu/TerryWilson/research_gps.htm

http://www.polenet.org/

http://www.grdl.noaa.gov/ANTCAL/

ftp://igscb.jpl.nasa.gov/igscb/data/format/rinex210.txt

http://www.unavco.org/facility/software/teqc/teqc.html

http://www.unavco.org QC v3 User Guide, UNAVCO, Document Date: March 1994.

Geofísica Internacional (2012) 51-1: 73-86

Original paper

A source study of the October, 2007 earthquake sequence of Morelia, Mexico and ground-motion estimation from larger earthquakes in the region

Shri Krishna Singh*, Arturo Iglesias, Victor Hugo Garduño, Luis Quintanar, and Mario Ordaz

Received: February 28, 2011; accepted: June 7, 2011; published on line: December 16, 2011

Resumen

En este artículo se analiza una secuencia de siete sismos (2.5<Mw<3.0) ocurridos en la Ciudad de Morelia, México. Esta serie de temblores ocurrieron en un intervalo de 33 horas en el mes de octubre de 2007. Fueron registrados por dos estaciones locales ubicadas en esa Ciudad. Morelia se encuentra en la la parte central de la Faja Volcánica Trans-Mexicana (CTMVB, por sus siglas en inglés). Las formas de onda y los espectros de estos sismos son sorprendentemente similares, sugiriendo que sus localizaciones y mecanismos focales son casi idénticos. La inversión de forma de onda, restringida a partir de fallas descritas anteriormente en el área (rumbo ~E-O, buzando al norte), arroja un mecanismo focal definido por $\phi=265^0$, $\delta=75^0$ y $\lambda= -30^0$, lo cual es consistente con los mecanismos focales reportados previamente en la región. Dado que, para estos pequeños eventos, la señal se confunde con el ruido para frecuencias f<0.2Hz, se estimó el momento sísmico M_0 a partir del espectro de las ondas S en una banda de frecuencias definida en el intervalo $0.2 \leq f \leq 1$Hz. Sin embargo, en esta banda de frecuencias, existe una amplificación significativa de las ondas símicas debida a una capa de baja velocidad provocada por rocas volcánicas superficiales presentes en cualquier sitio localizado en el CTMVB. En la estimación del M_0 y en la interpretación de los espectros observados, se aproximó esta amplificación usando el cociente espectral H/Z. Asumiendo un modelo de fuente ω^2, los espectros observados pueden ser explicados con ternas ($\Delta\sigma$, t^*, f_m) (5MPa, 0.02s, 20Hz) y (20 MPa, 0.03 s, 20 Hz), donde $\Delta\sigma$ es la caída de esfuerzos asumiendo el modelo de Brune y t^* y f_m son los parámetros de atenuación. Con el fin de simular el movimiento fuerte del terreno, para un sismo postulado de M_w5, se usaron estas combinaciones de parámetros junto con las técnicas de Empirical Green Function (EGF) y Random Vibration Theory (RVT). Las aceleraciones horizontales PGA y velocidades PGV en los sitios de referencia están en el rango de 23 a 46 cm/s^2 y de 1.5 a 3.52 cm/s para una caída de esfuerzos de $\Delta\sigma$=5Mpa. Los valores pronosticados para una caída de esfuerzos $\Delta\sigma$=20Mpa son casi el doble (44-89 cm/s^2 and 2.5-6.1 cm/s). Las estimaciones obtenidas, especialmente para $\Delta\sigma$=5MPa, son considerablemente más pequeñas que las reportadas a partir de datos globales. Esta comparación sugiere que existe una alta atenuación en la región volcánica o una inadecuada estimación del efecto de t^* y f_m.

Palabras clave: Estimación de movimientos fuerte para la Ciudad de Morelia, efectos de sitio en la faja Volcánica Trans-Mexicana, atenuación.

S. K. Singh*
A. Iglesias
L. Quintanar
Instituto de Geofísica
Universidad Nacional Autónoma de México
Ciudad Universitaria
Delegación Coyoacán, 04510
México D.F., México
*Corresponding author: krishnamex@yahoo.com

V. H. Garduño
Departamento de Geología y Mineralogía
Universidad Michoacana de San Nicolás de Hidalgo
Morelia, Michoacán
México

M. Ordaz
Instituto de Ingeniería
Universidad Nacional Autónoma de México
Ciudad Universitaria
Delegación Coyoacán, 04510
México D.F., México

Abstract

We analyze an earthquake sequence of seven small events (2.5<Mw<3.0) which occurred in Morelia, Mexico during a 33-hour period in October, 2007 and was recorded by two local stations. Morelia lies in Central Trans-Mexican Volcanic Belt (CTMVB). The waveforms and spectra of the events are surprising similar, suggesting that their locations and focal mechanisms were nearly identical. Waveform inversion, with constraints imposed from mapped faults in the area (strike ~E-W, dipping to the north) yields a focal mechanism defined by $\phi=265^0$, $\delta=75^0$, and $\lambda= -30^0$, consistent with reported focal mechanisms in the region. For these small events, the signal is lost in the noise at f<0.2Hz. For this reason, we estimate seismic moment, M_0, from S-wave spectrum in the frequency band of $0.2\leq f\leq 1$Hz. Unfortunately, in this band significant amplification of seismic waves, caused by upper low-velocity volcanic rocks, is expected at all sites in the CTMVB. In the estimation of M_0 and interpretation of the observed spectra, we approximate the amplification by H/Z spectral ratio. Assuming an ω^2-source model, the observed spectra can be explained by the ($\Delta\sigma$, t^*, f_m) triplets of (5 MPa, 0.02 s, 20 Hz) and (20 MPa, 0.03 s, 20 Hz), where $\Delta\sigma$ is the Brune stress drop, and $t^*$and f_m are attenuation parameters. We use these parameters and EGF and RVT techniques to simulate ground motions for a postulated M_w5 earthquake. The estimated horizontal PGAs and PGVs at the two sites in Morelia with $\Delta\sigma$=5MPa range between 23 and 46 cm/s^2 and 1.5 and 3.52 cm/s, respectively. The predicted values are almost twice as large for $\Delta\sigma$=20MPa: 44-89 cm/s^2 and 2.5-6.1 cm/s. Our estimated PGAs, especially that for $\Delta\sigma$=5MPa, are significantly smaller than those predicted from regression of world-wide data, suggesting either higher attenuation in this volcanic region and/or inadequate estimation of the site effect, and the attenuation parameters $t^*$and f_m.

Key words: Strong motion estimation for Morelia city, Site effects in Central Trans-Mexican Volcanic Belt, Attenuation.

Introduction

The Trans-Mexican Volcanic Belt (TMVB) is an E-W, Miocene to Quaternary, calc-alkaline volcanic arc related to the subduction of oceanic Rivera and Cocos plates below Mexico along the Middle America trench. TMVB is traversed by networks of faults that are nearly parallel and orthogonal to its axis (Pasquaré *et al.*, 1987; Johnson and Harrison, 1990). The central part of the Trans-Mexican Volcanic Belt (CTMVB) is characterized by a 100-to-150 km-wide zone of Quaternary to active normal faults which are oriented E-W, with a left-lateral strike-slip component (e.g., Pasquaré *et al.*, 1987; Suter *et al.*, 1992, 1995a,b, 2001; Marquez *et al.*, 1999) (Figure 1). The estimated horizontal extensional

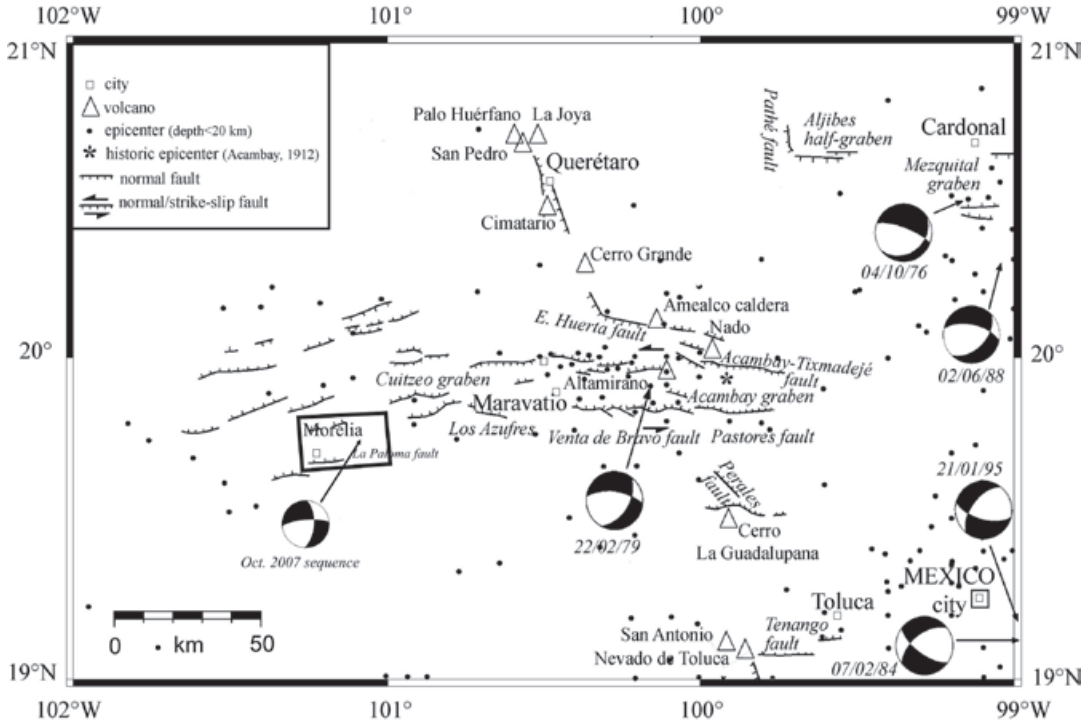

Figure 1. Tectonic map of Central Trans-Mexican Volcanic Belt showing faults, epicenters and focal mechanisms (modified from Ego and Ansan, 2002). Inset outlines the Morelia region covered in Figure 2.

and left-lateral slip rates across CTMVB along E–W-trending normal faults are 2 mm/year and less than 7 mm/year, respectively (Ego and Ansan, 2002). In the CTMVB, between 99^{0}W and 102^{0}W, Suter *et al.* (2001) report about 100 E-W-striking, normal faults which are >2 km in length. Of these faults, ~65 cut rocks <1.6 Ma old and ~22 are younger than 750 Ka. Although several for these faults have been studied in recent years, a detailed paleoseismological study is available only for the Acambay-Tixmadeje fault (Langridge *et al.*, 2000).

Seismicity in the CTMVB is moderate. Due to sparse seismic network and complex crustal structure of the region, the earthquake locations are inadequate to map active faults and reliable focal mechanisms are available only for a few earthquakes. Furthermore, the scarcity of data has severely limited our capability to estimate ground motions from future earthquakes. As a consequence, seismic hazard from earthquakes in the CTMVB is very poorly known. This is an unfortunate since large earthquakes are known to occur in the region. An example is the Acambay earthquake of 1912 (M7.0), which caused severe damage in the epicentral area (Urbina and Camacho, 1913). The problem is compounded by the fact that several highly-populated cities are located in the CTMVB (e.g., Mexico City, Toluca, Morelia, Puebla).

In this context, an analysis of an earthquake sequence, which occurred in Morelia in October, 2007, is important as it provides useful information on the characteristics of earthquake sources in the CTMVB. The earthquakes were recorded at two local stations (Figure 2). We also take advantage of these recordings to estimate ground motion from a postulated local M_w5 earthquake in Morelia. Recurrence period of such an event is not known. Suter *et al.* (2001) report ~10 faults with Quaternary activity in the Morelia region. Morelia fault (also called La Paloma fault, e.g., Garduño-Monroy *et al*., 2009), which is 13 km long, has been active in Holocene time. Rupture of a small segment of this fault could give rise an M_w5 earthquake.

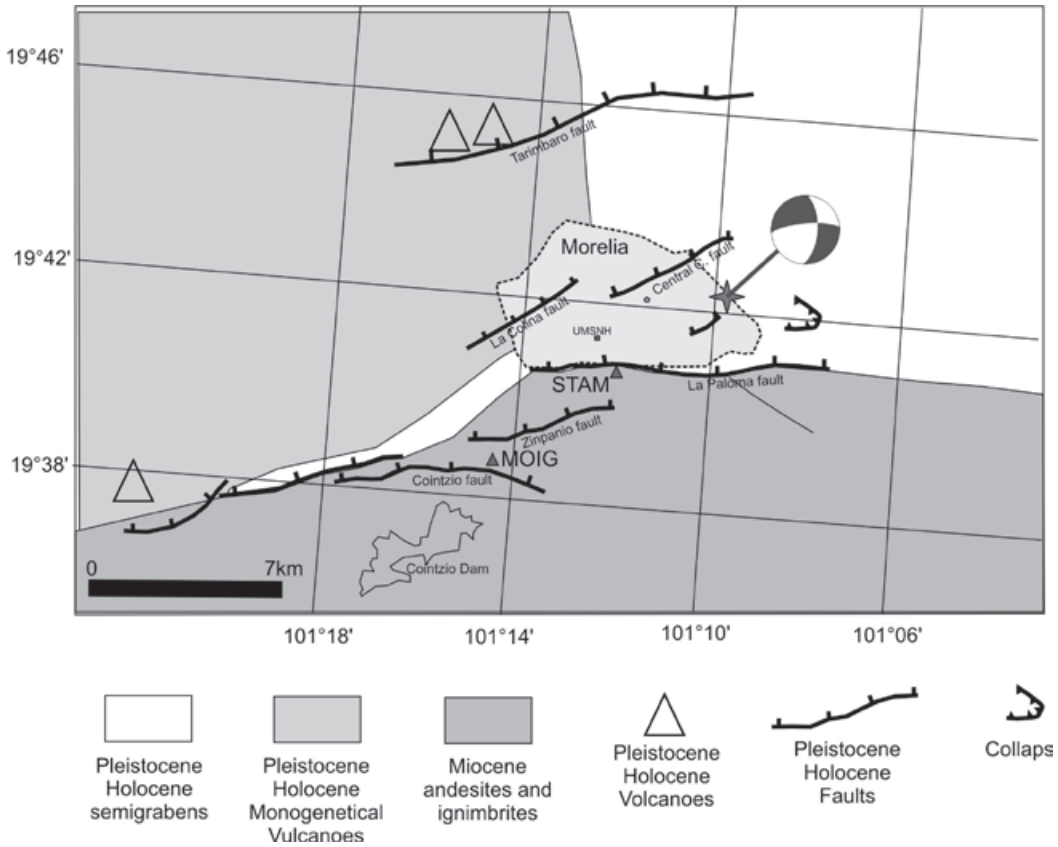

Figure 2. Map of Morelia region showing local faults. Locations of the 7 earthquakes, which occurred in October 2007, were nearly identical. They are shown by a single star. The focal mechanism of the earthquakes is also given. STAM is an accelerographic station. MOIG is equipped with a BB seismograph and an accelerograph.

The Earthquake Sequence

The earthquake sequence began on October 16, 2007 at 09:46. A broadband seismographic station, MOIG, situated in the Morelia campus of UNAM, recorded seven earthquakes in a 33-hour period (Figure 2, Table 1). MOIG is a permanent station of the Mexican National Seismological Service (Servicio Sismológico Nacional, SSN) network. It is equipped with a *Streckeisen STS-2* sensor and a *Quanterra Q330* data logger recording at 100 sps in a continuous mode. Four of the earthquakes (events 4 to 7 in Table 1) also triggered an accelerographic station, STAM, located in the city. STAM is a temporary station operated by Universidad Michoacana de San Nicolás de Hidalgo. It is equipped with *Kinemetrics K2* accelerograph. STAM recorded the earthquakes at 100 sps in a trigger mode.

MOIG and STAM are situated on ignimbrite which overlies severely fractured and altered andesite. The thickness of ignimbrite below STAM is ~180 m. This thickness below MOIG is not known. The waveforms of the earthquakes are remarkably similar to each other (Figure 3), as are their Fourier amplitude spectra (Figure 4). (S-P) times of the events at MOIG and STAM are 1.7 and 1.6 s, respectively. The waveform similarity and almost constant (S-P) time of the events imply that their locations and focal mechanisms are nearly identical. Iglesias *et al.* (in preparation) studied these common characteristics and, by using a multiplet coda-correlation technique, found that relative distances between events are between 50 to 350 m. For these reasons, we located only the event of October 17, 2007; 17:44. We estimated the seismic moment, M_0, and the focal mechanism

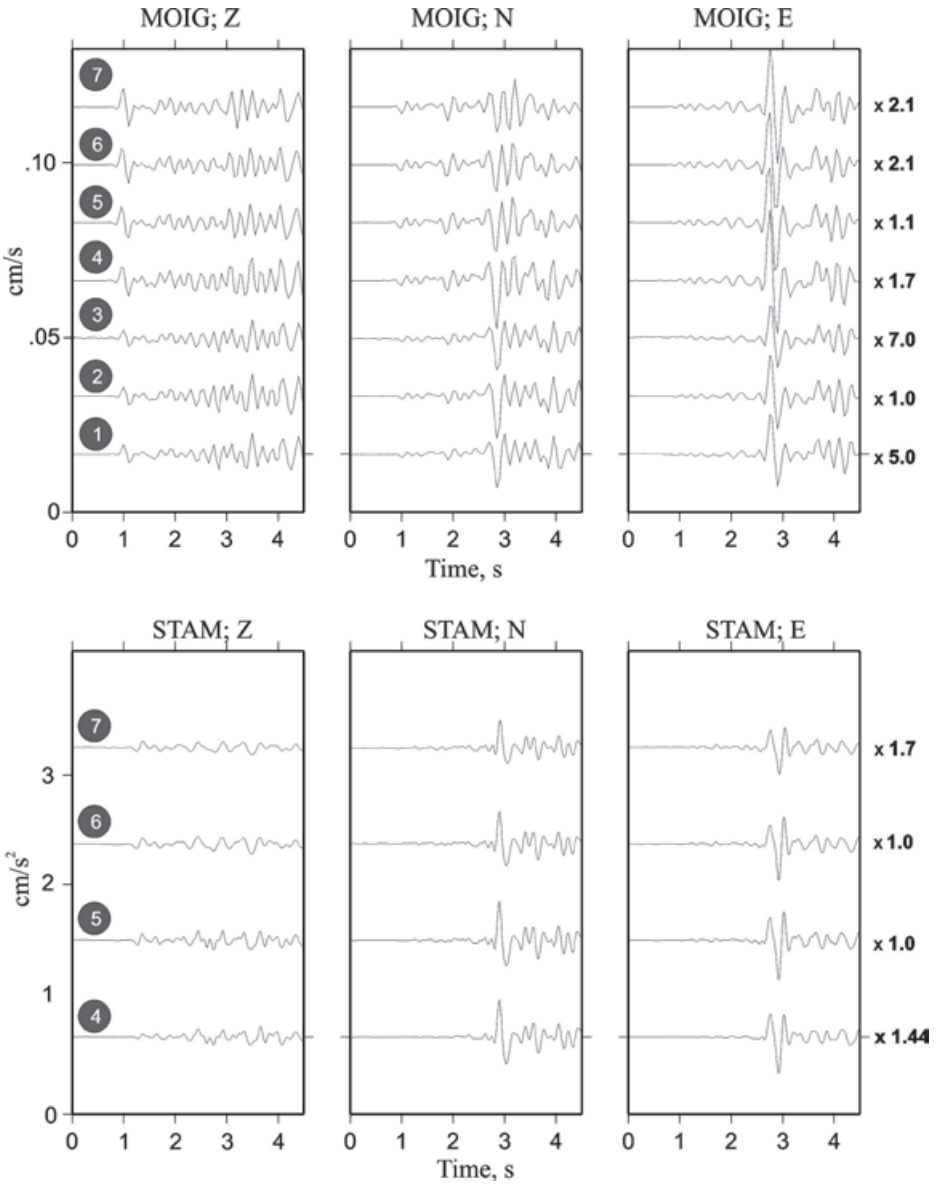

Figure 3. Top: Velocity waveforms of the earthquakes recorded at MOIG, and bottom: acceleration waveforms recorded at STAM. MOIG recorded 7 events while STAM was triggered by only 4 of these events. Gray circles show the number of each event in Table 1. Scaling factor to match the amplitude, for each event, is showed at the right of the figure. Note that the records are remarkably similar to each other, suggesting nearly the same location and focal mechanism.

Table 1. Source parameters and ground motions of events in the Morelia earthquake sequence of October, 2007. Location and focal mechanism of all events are nearly the same: 19.706^{0}N, 101.163^{0}W; H=11.4 km; ϕ=265^0, δ=75^0, λ=-30^0 (see text).

Event No.	Date	H: M: S	Stations	PGA, cm/s^2 NS	EW	Z	PGV, cm/s NS	EW	Z	M_0, N-m	Mw/Mc#
1	16/10/2007	09:47:01.7	MOIG	0.33	0.39	0.89	5.60e-3	6.08e-3	1.74e-2	7.9x10^{12}	2.53
2	16/10/2007	20:18:36.5	MOIG	1.63	1.69	1.93	3.00e-2	2.81e-2	3.40e-2	4.7x10^{13}	3.04
3	17/10/2007	12:59:09.2	MOIG	0.33	0.22	0.42	5.58e-3	3.69e-3	7.40e-3	7.9x10^{12}	2.53
4	17/10/2007	17:28:52.7	MOIG	1.09	0.79	1.00	2.00e-2	1.47e-2	1.96e-2	4.0x10^{13}	3.00/3.8
			STAM	1.06	0.74	0.47	3.45e-2	2.32e-2	1.19e-2		
5	17/10/2007*	17:44:09.9	MOIG	1.51	1.15	0.96	2.39e-2	2.51e-2	1.90e-2	4.0x10^{13}	3.00/3.6
			STAM	1.31	0.95	0.64	3.35e-2	2.81e-2	1.37e-2		
6	17/10/2007	17:46:28.5	MOIG	1.41	1.29	0.89	2.45e-2	2.56e-2	1.74e-2	3.2x10^{13}	2.94/3.5
			STAM	1.08	0.93	0.81	2.64e-2	2.53e-2	1.40e-2		
7	17/10/2007	18:18:47.2	MOIG	0.63	0.55	0.45	1.07e-2	1.42e-2	1.00e-2	1.6x10^{13}	2.73
			STAM	0.51	0.36	0.33	1.21e-2	1.22e-2	6.83e-3		

*Reference earthquake. Location, M_0, and focal mechanism of this event were determined in this study. M_0 of other events were estimated from their relative low-frequency spectral levels with respect to that of the reference event.
#Coda magnitude, Mc, was reported by SSN.

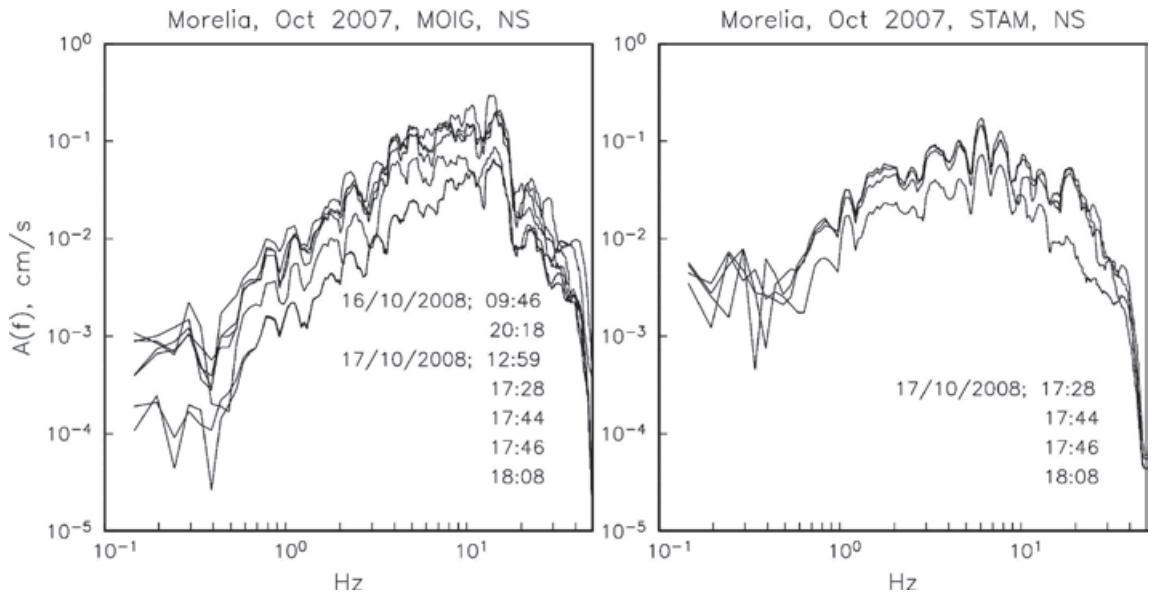

Figure 4. Fourier acceleration spectra (NS component) of the 7 earthquakes at MOIG and the 4 earthquakes at STAM. Note the similarity of the spectra.

of this event. The moment of other events in the sequence were obtained by scaling the low-frequency level of the spectra.

P and S arrival times at MOIG and STAM along with the azimuths of the source were used in the location using the SEISAN code (Haskov and Ottemoller, 2001) and its hypoinverse module (Fred, 2000).

The crustal structure below Morelia is not known. In locating the earthquake, we employed a crustal model reported by Campillo *et al.* (1996). It consists of a three-layer crust (layer 1: α=5.1 km/s, h=5 km; layer 2: α=5.9 km/s, h=12 km; layer 3: α=6.7 km/s, h=28 km). This 45-km-thick crust overlies a half space (α=7.95 km/s). We assumed a Poisson ratio of 1.78. We also tested a slightly modified model in which

layer 1 was split in two: layer 1a with α=2.9 km/s, h=2 km, and layer 1b with α=5.1 km/s, h=3 km. Layer 1a is consistent with a relatively low-velocity, 2-km-thick layer reported below the Valley of Mexico (Havskov and Singh, 1977-78). The locations obtained from the two models are almost identical: 19.706^{0}N, 101.163^{0}W; H=11.4 km. Computed distances from MOIG and STAM were ~ 9km and ~4 km, respectively. Table 1 gives a list of the seven events.

Cracks and faults, caused by subsidence due to extensive pumping of water, have been reported in Morelia. The depth of the earthquakes (11.4 km) suggests that they may not be related to the water depletion in the aquifer.

Focal mechanism

As mentioned earlier, the waveform similarity of the events at MOIG and STAM (Figure 3) suggests that the focal mechanisms of these earthquakes are almost the same. The first-motion data are available only at these two local stations. However, it is possible to obtain focal mechanism from waveform data at one or two local stations only (e.g., Kanamori *et al.*, 1990; Singh *et al.*, 2000). To determine the focal mechanism of the Morelia events, we performed waveform inversion of the displacements at MOIG and STAM for the 17 October, 17:44 event. In the inversion, we required that the solution be consistent with the first-motions and the reported fault orientation in the region (strike ~E-W, dipping towards north, Figure 1). For this reason, we restricted the azimuth, ϕ, and the dip, δ, of the fault to lie between 250^0 and 285^0 and 55^0 and 85^0, respectively. The inversion assumes that the event may be approximated by a point-source shear dislocation. Synthetic seismograms include near- and intermediate-field contributions (Singh *et al.,* 2000). The effect of the free surface is approximately taken into account by multiplying infinite-space synthetics by two. These approximations are reasonable, especially for S_H wave, if the epicentral distance, Δ, is smaller than the depth, H. In our case, H is 11.4 km and Δ is 5 and 9 km to STAM and MOIG, respectively. The inversion yields a nodal plane defined by ϕ=265^0, δ=75^0, and λ= -30^0, and a seismic moment, M_0 of 1.1x10^{14} N-m. This M_0 is likely to be an overestimation since no correction for local site effect has been made (see later discussion). The focal mechanism is similar to the mechanism of the 22 February, 1979, m_b=5.3, Maravatio earthquake (ϕ=280^0, δ=66^0, λ= -48^0) reported by Astiz (1980). Figure 5 shows the fit between the observed and synthetic seismograms. S waves on radial and transverse components at MOIG are well fit by the synthetics. However, P wave on Z component is nodal in the synthetic waveform, while it is clearly compressional on the observed seismogram. We attribute this discrepancy to possible error in the location of the earthquake. The synthetics at MOIG are more sensitive than those at STAM to small changes in the azimuth of the source. At STAM, S_H wave on transverse

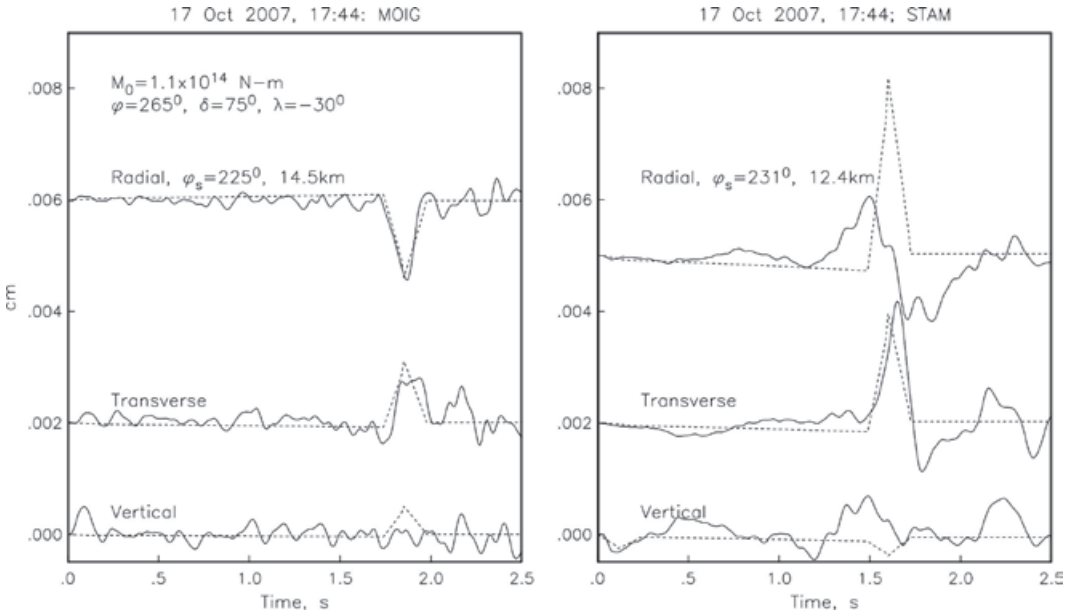

Figure 5. Observed (continuous curves) and synthetic displacements (dashed curves) at MOIG and STAM during the 17 October 2007, 17:44 earthquake. Synthetic displacements correspond to M_0=1.1x10^{14}N-m and focal mechanism given by: strike φ=225^0, dip δ=75^0, and rake λ=-30^0 (see text). Because of local site effect, M_0 is likely to be overestimated (see text).

component and P wave on Z component are well fit, but the fit to S_V wave on radial and Z components is poor. In fact, S_V pulses at STAM are not unipolar as would be expected from the simple infinite-space model. This underscores the inadequacy of the simple model used in generating the synthetics (Kanamori, 1990; Singh *et al.*, 2000). It will require a detailed knowledge of the crustal structure to better model the observed high-frequency displacement pulses. This, as mentioned earlier, is lacking at present. The focal mechanism given above, while not well constrained from the seismograms, is consistent with mapped faults in the region.

Spectral study of the Morelia Sequence

Fourier amplitude spectrum of S-wave group of small and moderate earthquakes is often used to estimate seismic moment, M_0, and stress drop, $\Delta\sigma$ (Brune, 1970). The observed spectrum of small earthquakes, however, is strongly affected by near-surface attenuation and local site effect. The corrections for these effects at high frequencies are very poorly known. As a consequence, for small earthquakes, the estimation of corner frequency, f_c, and, hence, $\Delta\sigma$, (which is computed from f_c) is very uncertain. Even the estimation of M_0 in the TMVB is problematic. For small earthquakes, low-frequency waves ($f \leq 0.1$ Hz), which may not be affected by local site effects, are dominated by ambient noise. Thus, one is forced to estimate M_0 from spectral amplitudes at $f \geq 0.2$ Hz. At these frequencies large amplification of seismic waves is expected in the TMVB due to low-velocity, recent volcanic materials which comprise the upper-most layers. This amplification is reasonably well documented in the hill-zone of the Valley of Mexico (e.g., Singh *et al.*, 1995). However, the information on local site effect is lacking in Morelia, as also in much of the TMVB. In the following, we will assume that ratio of spectrum of vertical component and horizontal component (H/Z) provides a first-order approximation to the site effect (Nakamura, 1989). Figure 6 illustrates H/Z spectral ratio at MOIG and STAM computed from the recordings of the October, 2007 sequence.

The Fourier acceleration spectral amplitude of the intense part of the ground motion at a station may be written as

$$A(f,R) = C\, f^2 \dot{M}_0(f)\, G(R)\, e^{-\pi fR/\beta Q(f)}\, e^{-\pi ft^*} B(f)\, Site(f) \quad (1)$$

where,

$$C = FPR_{\theta\varphi}(2\pi)^2/(4\pi\rho\beta^3)\ . \quad (2)$$

In equations above, $\dot{M}_0(f)$ is the moment rate spectrum so that $\dot{M}_0(f) \rightarrow M_0$ as $f \rightarrow 0$, R = hypocentral distance, $R_{\theta\phi}$ = average radiation pattern (0.55), F = free surface amplification (2.0), P takes into account the partitioning of energy in the two horizontal components ($1/\sqrt{2}$), β= shear-wave velocity at the source (taken here as 3.4 km/s), ρ= density in the focal region (assumed 2.85 g/cm^3), and Q(f) = quality factor, which includes both anelastic absorption and scattering. The attenuation in the near-surface layer and the finite bandwidth of the observed spectrum imposed by the sampling rate are accounted by the parameter t^* (Singh *et al.*, 1982; Anderson and Hough, 1984) and/or the Butterworth filter, B(f) (Boore, 1983). We take B(f)=(1.0+(f/f$_m$)**(8))**(-0.5). Site(f) in equation 3 is the local site effect. As mentioned above, we assume that it is given by H/Z spectral ratio shown in Figure 6. The geometrical spreading term, G(R), in equation (1) is taken as 1/R. Taking logarithm of equation (1) we obtain

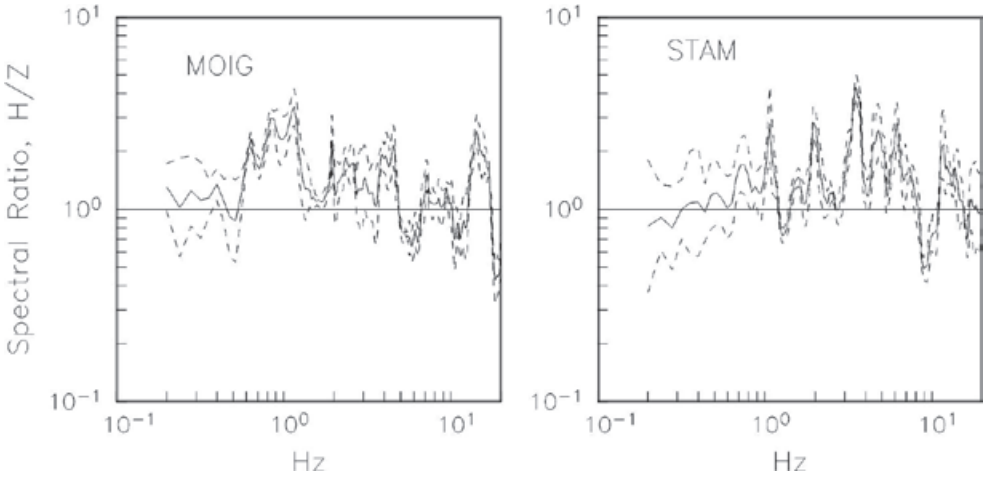

Figure 6. Horizontal to vertical (H/V) spectral ratio of S waves of the earthquakes at MOIG and STAM. The median and ± one standard deviation curves are shown.

$$\log [A(f,R)] = \log C + \log [G(R)] + \log [f^2 \dot{M}_0(f)] - 1.36 f [R/\beta Q(f) - t^*] - \log B(f) - \text{Site}(f) \quad (3)$$

The quality factor, Q(f), is not known for the Morelia region. For Central Mexican Volcanic Belt, along a profile passing through the Valley of Mexico, Singh *et al.* (2007) report $Q(f)=98f^{0.72}$. We assume the same Q(f) for the Morelia region.

We analyze the 17 October, 17:44 event in detail and invoke similarity of the waveforms and spectra (Figure 3 and 4) to determine the source parameters of other events listed in Table 1. Figure 7 illustrates observed median acceleration spectrum of the two horizontal components at MOIG and theoretical A(f) computed from equation 3. In the computation, we assume an ω^2-source and $\Delta\sigma$ values of 20 and 5 MPa. We tested many reasonable values of the (t^*, f_m) doublet. As Figure 7 shows, A(f) below 2 Hz is insensitive to the choice of ($\Delta\sigma$, t^*, f_m). The spectral level at f≤2 Hz requires M_0 of 4.0×10^{13}N-m (see left frames in Figure 7). If the site effect is well approximated by the H/Z spectral ratio, then this is the seismic moment

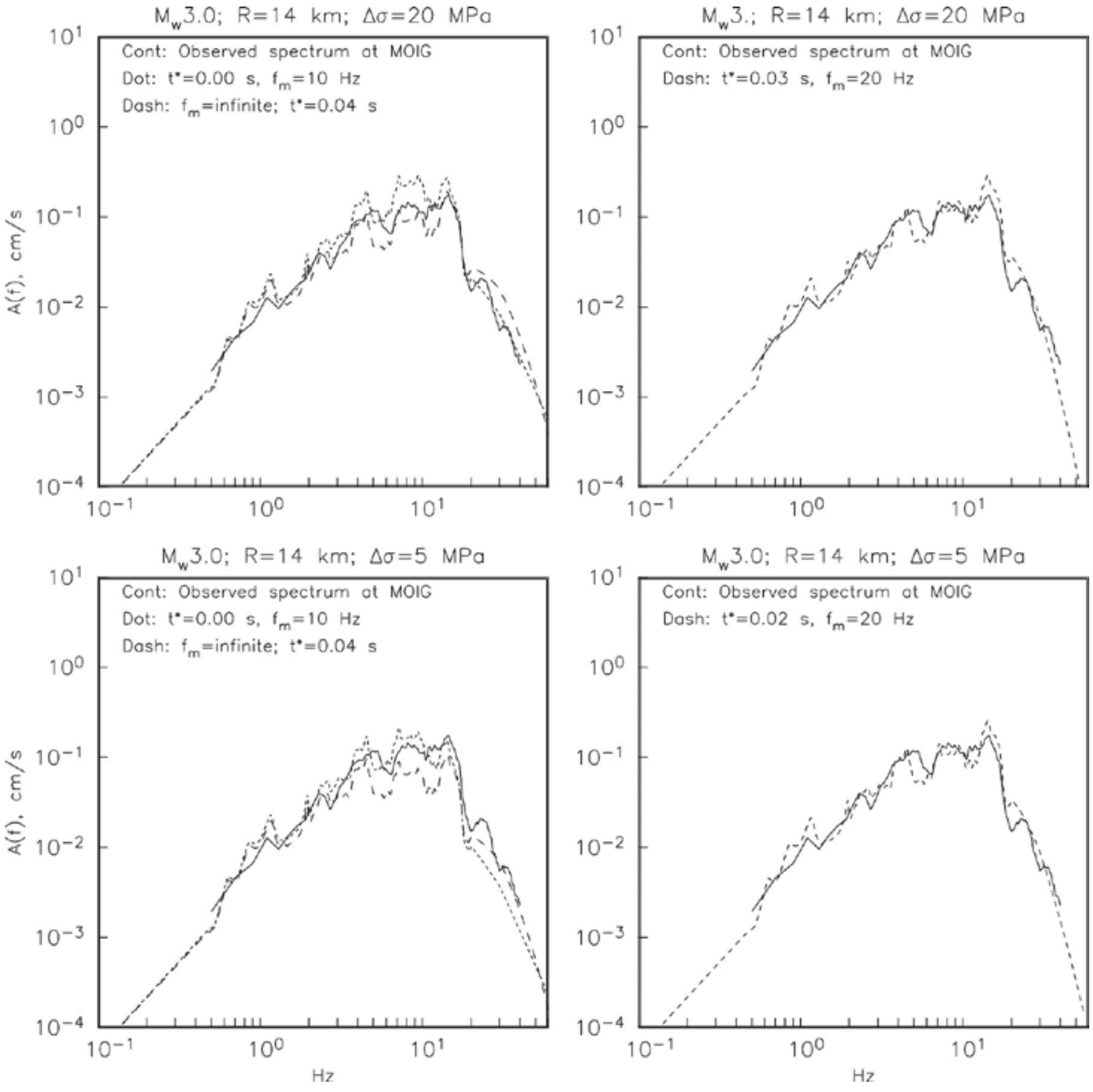

Figure 7. Median horizontal acceleration spectrum, A(f), of 17:44 earthquake at MOIG (continuous curves). Dotted and dashed curves are theoretically calculated from equation 1, assuming ω^2-source, accounting for local site effect, taking $M_0=4.0\times10^{13}$N-m (required to fit spectrum at 0.5<f<2Hz), and for $\Delta\sigma$=5MPa (bottom two frames) and 20MPa (top two frames). Theoretical curves in the left two frames are for (t^*, f_m) doublet of (0.0s, 10Hz) and (0.04s, ∞Hz). Right two frames demonstrate that the observed median spectrum can be equally-well be fit by ($\Delta\sigma$, t^*, f_m) triplets of (5MPa, 0.02s, 20Hz) and (20MPa, 0.03s, 20Hz). The figure confirms tradeoff among $\Delta\sigma$, t^*, and f_m.

of the 17:44 event. The seismic moments of the other 6 events, obtained from their relative low-frequency spectral levels with respect to that of the 17:44 event, are listed in Table 1. The moment magnitude, M_w, of the earthquakes listed in Table 1 ranges between 2.53 and 3.04.

The right hand frames in Figure 7 demonstrate that ($\Delta\sigma$, t^*, f_m) triplets of (20 MPa, 0.03 s, 20 Hz) and (5 MPa, 0.02 s, 20 Hz) reproduce equally well the observed A(f). Although the parameters of these triplets are reasonable, it is clearly possible to fit the observed spectrum with other values. Observed and computed A(f) at STAM are shown in Figure 8. Here M_0 and the two triplets ($\Delta\sigma$, t^*, f_m) used in the calculations are the same that fit the MOIG spectrum of the 17:44 event. The fit is, relatively, poor; the observed median spectrum is lower than the computed one between 3 and 20 Hz (especially between 10 and 20 Hz) and higher below 3 Hz. Clearly, the near-surface attenuation and local site effect at STAM differ from those at MOIG. From Figures 7 and 8, and in common with many previous studies, we conclude that a reliable estimate of stress drop of small earthquakes is not possible unless attenuation of seismic waves at high frequencies is well known.

Ground-Motion Estimation in Morelia from a Local Mw5.0 Earthquake

The earthquake sequence of 2007 provides elements to estimate ground motions from future, postulated earthquakes in the city of Morelia. Below we estimate ground motions in Morelia from a scenario local earthquake of M_w5.0. As mentioned earlier, recurrence period of such an earthquake is not known. Nevertheless, M_w5 earthquake is a reasonable scenario event in Morelia in view of 10 mapped faults in the region and 13-km-long La Paloma fault which has been active in the Holocene (Suter *et al.*, 2001). New building code of Mexico City also contemplates a local M5 earthquake (Rosenblueth *et al.*, 1989). In the synthesis of the ground motion in Morelia, we will use techniques based on empirical Green's function and random vibration theory.

If the entire length of La Paloma fault were to rupture in one event, it could give rise to an Mw6.3 earthquake (see, *e.g.,* Wells and Coppersmith, 1994). For such an earthquake, the far-field, point-source approximation would be grossly violated and alternative approaches would have to be employed for the synthesis of the ground motion.

(1) Empirical Green's Function (EGF) Technique

The recordings of the earthquake sequence may be used as EGFs to estimate ground motions in Morelia from local scenario earthquakes. We use the recordings of the 17 October 2007; 17:44 event (Table 1) as EGF to synthesize ground motions from a postulated Mw5.0 earthquake.

For the synthesis, we use a random summation scheme of EGF proposed by Ordaz *et al.* (1995). The method assumes that far-field and point-source approximations are valid. The summation

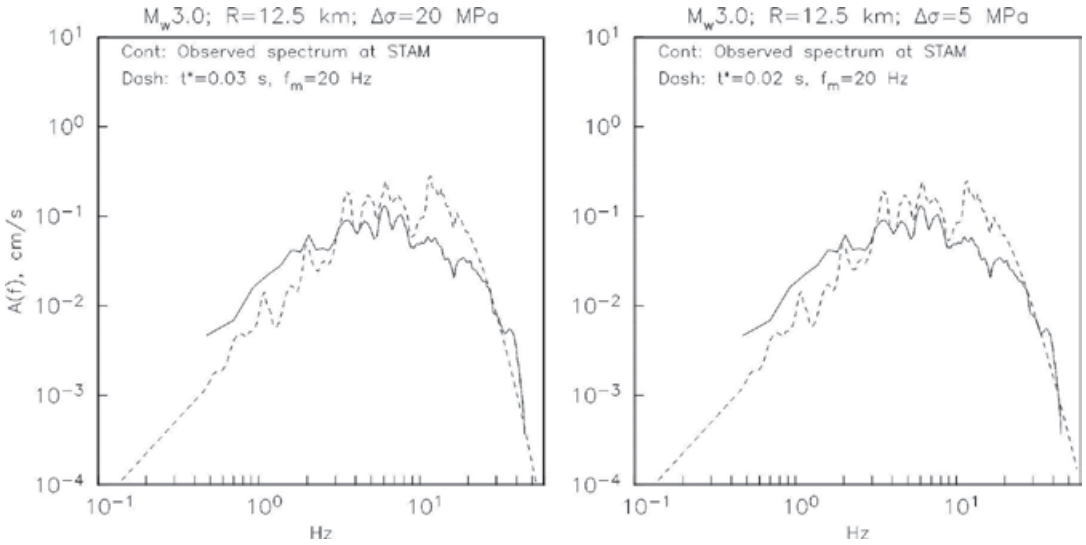

Figure 8. Median horizontal acceleration spectrum, A(f), of 17:44 earthquake at STAM (continuous curves). Dashed curves are theoretically calculated using equation 1, accounting for local site effect and taking the same parameters which fit the spectrum at MOIG (see the two right frames in Figure 7). Note that the theoretical dashed curves poorly fit the observed one.

scheme obeys the ω^2-source scaling law at all frequencies and produces realistic time histories. The method requires specification of only the seismic moments and the stress drops of the EGF and the target events. We assume the same stress drop for the target and the EGF event. We consider two values of stress drop: 5 and 20MPa. Figure 9 shows observed horizontal geometrical mean PGA and PGV during the sequence and the synthesized values for postulated Mw4 and Mw5 earthquakes. We note that the PGA and PGV values are roughly two times greater for $\Delta\sigma$=20MPa than for $\Delta\sigma$=5MPa.

(2) Technique Based on Random Vibration Theory (RVT)

A powerful method to estimate ground motion, which is especially useful in regions with sparse earthquake recordings, is based on the application of random vibration theory (RVT) (Hanks and McGuire, 1981; Boore, 1983). In this method, the spectrum of the ground motion is related to the root-mean-square (rms) amplitude in the time domain through Parseval's theorem. The expected peak amplitude is obtained from the rms amplitude using results from random vibration theory (Cartwright and Longuet-Higgins, 1956).

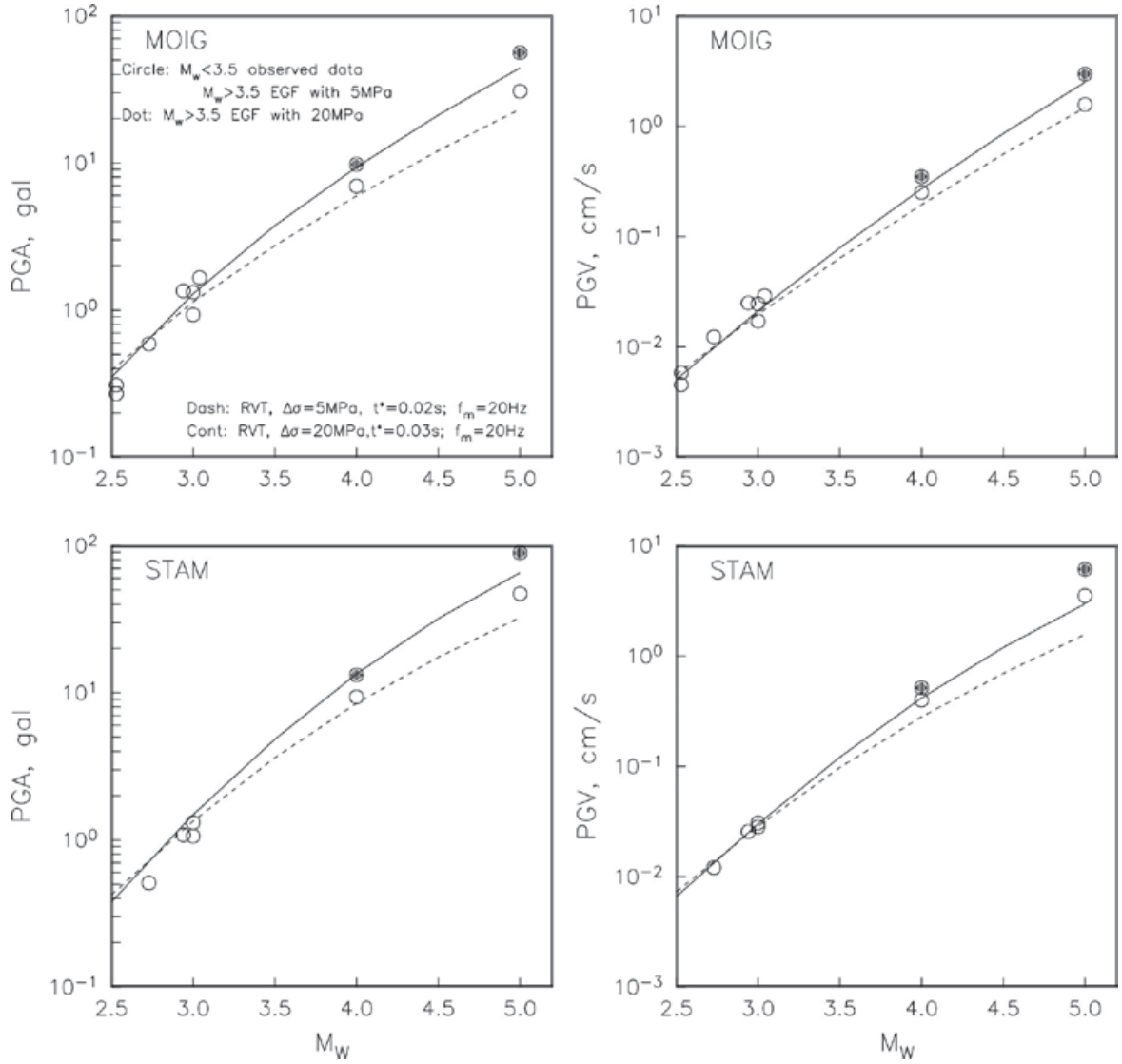

Figure 9. PGA and PGV as a function of M_w (top: MOIG; bottom: STAM). Circle: M_w<3.5 observed data; M_w>3.5 simulated using EGF technique with $\Delta\sigma$=5MPa. Dot: M_w>3.5 simulated using EGF technique with $\Delta\sigma$=20MPa. Continuous curve: RVT simulation with $\Delta\sigma$=20MPa, t^*=0.03s, and f_m=20Hz. Dashed curve: RVT simulation with $\Delta\sigma$=5MPa, t^*=0.02s, and f_m=20Hz.

As discussed earlier, the observed spectra during the Morelia sequence can be explained by an ω^2-source model, 1/R geometrical spreading, whole-path Q given by $Q(f)=98f^{0.72}$, local site effect shown in Figure 6 and ($\Delta\sigma$, t^*, f_m) triplet of (20MPa, 0.03s, 20Hz) or (5MPa, 0.02s, 20Hz) in equation 1. A further parameter needed is the effective duration of the ground motion, T_R. T_R is, often, taken as $T_R= f_c^{-1}+0.05R$ (Herrmann, 1985), where R is the hypocentral distance in km and f_c is the corner frequency (Brune, 1970). We find that this relation underestimates T_R for small earthquakes. For Morelia sequence, a more appropriate T_R is given by $T_R= 3.0+f_c^{-1}+0.05R$. Predicted horizontal PGA and PGV from RVT are shown by curves in Figure 9. As the computed spectrum with parameters listed above fits well the observed spectrum at MOIG of the 17:44 earthquake (and other earthquakes of the sequence as well), we expect the RVT predictions of PGA and PGV to be close to the observed ones at this station during the sequence. Figure 9 confirms this. For larger M_w, the RVT predictions from the two triplets differ. This is to be expected since the predicted spectra from the two sets of parameters also now differ. The results from EGF and RVT predictions are given in Table 2. We note that the predictions from the two techniques with the same $\Delta\sigma$ are in reasonable agreement with each other. An exception is the PGV at STAM where EGF prediction is nearly twice that from RVT. This is a consequence of higher observed A(f) than the theoretical one at f<3 Hz (Figure 8). From Figure 9 and Table 2, the expected geometrical mean horizontal PGA and PGV at MOIG from a local Mw5 earthquake are 23 to 56 cm/s^2 and 1.5 to 3.0 cm/s, respectively. The corresponding values at STAM are 32 to 89 cm/s^2 and 1.6-6.1 cm/s, respectively.

It is useful to compare our predicted PGA values with those of Spudich *et al.* (1999) who derive a ground motion prediction relation for extensional tectonic regime that is valid for M≥5.5. An extrapolation of this relation predicts horizontal geometrical mean PGA of about 90 and 120 cm/s^2 at MOIG and STAM, respectively for a M5 earthquake at the same focus as the 2007 sequence, assuming that these are hard rock sites. The corresponding values for soft sites are ~115 and 155 Gal. MOIG and STAM, which are situated above ignimbrite, would probably qualify as hard sites in Spudich *et al.*'s classification. Even for hard sites, our predictions are somewhat low. Low predictions from EGF technique may arise from the following causes: (1) Overestimation of M_0 of the 17:44 event. If so, then a smaller number of EGF records have been used in the random summation, giving rise to smaller expected ground motions. An overestimation of M_0 is possible because H/Z spectral ratio provides only a rough approximation to the local site effect. Furthermore, data from only two stations are available for the estimation of M_0 which may result in a biased, overestimation. (2) The earthquake sequence involved smaller than "normal" stress drop and, hence, relatively small ground motions. This possibility does not seem likely as our choice of Ds=20 MPa is on the high side. Low PGA from RVT may result if the site effect is underestimated in some critical frequency band. Of course, low PGA from both EGF and RVT techniques may be simply a consequence of higher attenuation in the TMVB.

Table 2. Simulated peak horizontal ground motions at sites MOIG and STAM in Morelia, Mexico from a postulated M_w5.0 local earthquake.

Technique	Stress Drop (MPa)	Simulated horizontal PGA (cm/s^2) MOIG	STAM	Simulated horizontal PGV (cm/s) MOIG	STAM
EGF#	5	30.7	45.5	1.57	3.52
	20	56.1	89.2	2.96	6.10
RVT##	5$	23.3	32.4	1.47	1.57
	20$$	44.2	65.6	2.52	2.96

#Stress drop of EGF and target events are taken to be equal. EGF event: Oct 17, 2007, 17:44 whose M_0 is taken as 4.0×10^{13}N-m. PGA and PGV are geometrical mean values.
##In the calculations local site effect is included.
$In the calculations, t^*=0.02s, f_m=20Hz.
$$In the calculations, t^*=0.03s, f_m=20Hz.

Discussion and Conclusions

Although a detailed knowledge of seismicity in the TMVB is critical to understand the seismotectonics and seismic hazard of the region, it is sorely lacking at present. This is because of few seismographs, relatively low seismicity, complex crustal structure, and significant local site effect in the region. As a result, reliable locations and focal mechanisms are available for only a handful of earthquakes. Furthermore, since $M_w \geq 5$ earthquakes are rare but important in seismic hazard estimation, the source characteristics of such earthquakes must be inferred from the study of small earthquakes in the region. Unfortunately, reliable estimation of source characteristics of small earthquakes in the TMVB still remains a challenging task. Morelia sequence of October 2007 provides an example of the difficulties faced in the analysis of small TMVB earthquakes.

The October 2007 earthquake sequence was recorded by two local stations. Hence, we could only confirm that the waveforms are consistent with known focal mechanisms in the region ($\phi=265^0$, $\delta=75^0$, and $\lambda= -30^0$). Amplification of seismic waves is expected in the TMVB due to low-velocity upper volcanic rocks. This amplification probably occurs at frequencies greater than about 0.2 Hz. Unfortunately, seismic moments of small TMVB events have to be determined at frequencies between about 0.2 and 1 Hz since the signal is lost in the noise at lower frequencies. Thus, unless the observed spectra are corrected for local site effect, the seismic moment is likely to be overestimated. This is true for all small earthquakes in the TMVB. For the Morelia sequence, we have assumed that Nakamura technique (i.e., H/Z spectral ratio) provides reasonable approximation of the local site effect. Based on this assumption, we have estimated the seismic moments of the events and, within the framework of ω^2-source model and two values of stress drops, the attenuation parameters t^* and f_m. The chosen stress drops are 5 and 20 MPa. Stress drop of 5 MPa, which may represent a reasonable average value, yields (t^* and f_m) doublet of (0.02s and 20Hz). The corresponding doublet is (0.03s and 20Hz) when the unusually large stress drop of 20 MPa is chosen. In order to estimate ground motions in the epicentral region of a postulated M_w5.0 earthquake in the focal region of the October 2007 sequence, we have used EGF and RVT techniques assuming stress drops of 5 and 20MPa. The estimated horizontal PGA and PGV at the two sites in Morelia, for the stress drop of 5MPa, range between 23 and 46 cm/s^2 and 1.5 and 3.52 cm/s, respectively. If we assume a stress drop of 20MPa, then the estimated values are almost twice as large: 44-89 cm/s^2 and 2.5-6.1 cm/s (Table 2). Our estimated range of PGA, especially that corresponding to the stress drop of 5MPa, is significantly smaller than the predicted value of 90-120 cm/s^2 at hard sites from world-wide, strong-motion, extensional-regime data (Spudich *et al.*, 1999). The two possible explanations are: (1) Anomalously high attenuation along wavepaths from the sources to the sites in Morelia during the sequence (and, possibly, along all similar source/site paths in the TMVB). (2) Error in the estimation of local site effect (thus resulting in an underestimation of the seismic moment), and the attenuation doublet (t^*, f_m). We think (1) above is more likely but we can not reject (2) as the cause. Much more data from local earthquakes in the TMBV is needed to resolve this issue and to better understand the seismotectonics of the region.

Acknowledgements

We are grateful to F. Ego for providing us with PDF of a figure. The research was partially supported by DGAPA UNAM projects IN111411 and IN112411.

Bibliography

Astiz L.M., 1980, Sismicidad en Acambay, Estado de México. El temblor de 22 de febrero de 1979. B. S. thesis, Universidad Nacional Autónoma de México, Mexico City, 130 pp.

Anderson J.G., Hough S.E., 1984, A model for the shape of the Fourier amplitude spectrum of acceleration at high frequencies. *Bull. Seism. Soc. Am.,74,* 1,969-1,993.

Boore D.M., 1983, Stochastic simulation of high-frequency ground motions based on seismological models of radiated spectra. *Bull. Seism. Soc. Am.,* 73, 1,865-1,884.

Brune J.N., 1970, Tectonic stress and the spectra of seismic shear waves from earthquakes. *J. Geophys. Res., 75*, 4,997-5,009.

Campillo M., Singh S.K., Shapiro N., Pacheco J., Herrmann R.B., 1996, Crustal structure south of the Mexican volcanic belt, based on group velocity dispersion. *Geofis. Intern., 35,* 361-370, 1996.

Cartwright D.E., Longuet-Higgins M.E., 1956, The statistical distribution of maxima of a random function. *Proc. Roy. Soc. London, Ser. A*., 237, 212-232.

Ego F., Ansan V., 2002, Why is the Central Trans-Mexican Volcanic Belt (102º - 99º W) in transtensive deformation? *Tectonophysics*, *359*, 189-208.

Fred W.K., 2000, User's guide to HYPOINVERSE-2000, a Fortran program to solve for earthquake locations and magnitudes. USGS Open File Rept, pp. 2–171.

Garduño-Monroy V.H., Pérez-Lopez R., Israde-Alcantara I., Rodríguez-Pascua M.A., Szynkaruk E., Hernández-Madrigal V.M., García-Zepeda M.L., Corona-Chávez P., Ostroumov M., Medina-Vega V.H., García-Estrada G., Carranza O., López-Granados E., Mora Chaparro J.C., 2009, Paleoseismology of the southwestern Morelia-Acambay fault system, central Mexico. *Geofis. Intern.*, 48, 319-335.

Hanks T.C., McGuire R.K., 1981, The character of high-frequency strong ground motion. *Bull. Seism. Soc. Am., 71*, 2,071-2,095.

Havskov J., Singh S.K., 1977-78, Shallow crustal structure below Mexico City. *Geofis. Intern., 17*, 223-229.

Haskov J., Ottemoller L., 2001, Seisan, the earthquake analysis software, University of Bergen, Norway, pp. 25–40.

Herrmann R.B., 1985, An extension of random vibration theory estimates of strong ground motion at large distances. *Bull. Seism. Soc. Am., 75*, 1,447-1,453.

Kanamori H., Mori J., Heaton T.H., 1990, The 3 December 1988, Pasadena earthquake (M_L=4.9) recorded with the very broadband system in Pasadena. *Bull. Seism. Soc. Am., 80,* 483-487.

Johnson C.A., Harrison C.G.A., 1990, Neotectonics in central Mexico. *Phys. Earth Planet. Int.*, *64*, 187–210.

Langridge R.M., Weldon R.J., Moya J.C., Suarez G., 2000, Paleoseismology of the Acambay earthquake and the Acambay-Tixmadejé fault, Trans-Mexican Volcanic Belt. *J. Geophys. Res.*, *105*, 3,019–3,037.

Marquez A., Verma S.P., Anguita F., Oyarzun R., Brandle J.L., 1999, Tectonics and volcanism of Sierra Chichinautzin: extension at the front of the central TMVB. *J. Volcanol. Geotherm. Res.*, 93, 125–150.

Nakamura Y., 1989, A method for dynamic characteristics estimation of subsurface using microtremor on ground surface. *QR-RTR1, 30,* 1, February.

Ordaz M., Arboleda J., Singh S.K., 1995, A scheme of random summation of an empirical Green´s function to estimate ground motions from future large earthquakes. *Bull. Seism. Soc. Am., 85*, 1,635-1,647.

Pasquaré G., Vezzoli L., Zanchi A., 1987, Morphological and structural model of Mexican Volcanic Belt. *Geofis. Int*., *26*, 159-176.

Rosenblueth E., Ordaz M., Sánchez-Sesma F.J., Singh S.K., 1989, Design spectra for Mexico's Federal District. *Earthquake Spectra, 5*, 258-272.

Singh S.K., Apsel R., Fried J., Brune J.N., 1982, Spectral attenuation of SH-wave along the Imperial fault. *Bull. Seism. Soc. Am., 72*, 2,003-2,016.

Singh S.K., Quaas R., Ordaz M., Mooser F., Almora D., Torres M., and R. Vásquez , 1995. Is there truly a "hard" site in the Valley of Mexico? *Geophys. Res. Lett., 22*, 481-484.

Singh, S.K., Ordaz M., Pacheco J.F., Courboulex F., 2000, A simple source inversion scheme for displacement seismograms recorded at short distances. *J. Seismology, 4,* 267-284.

Singh S.K., Iglesias A., García D., Pacheco J.F., Ordaz M., 2007, Q of Lg waves in the Central Mexican Volcanic Belt, *Bull. Seism. Soc. Am., 97*, 1,259-1,266, 2007.

Spudich P., Joyner W.B., Lindh A.G., Boore D.M., Margaris B.M., Fletcher J.B., 1999, SEA99: A revised ground motion prediction relation for use in extensional tectonic regime, *Bull. Seism. Soc. Am., 89,* 1,156-1,170.

Suter M., Quintero O., Johnson C.A., 1992, Active faults and state of stress in the central part of the TMVB, Mexico: 1. The Venta de Bravo fault. *J. Geophys. Res., 97,* 11,983-11,993.

Suter M., Quintero-Legorreta O., López-Martínez M., Aguirre-Díaz G., Farrar E., 1995a, The Acambay graben: active intra-arc extension in the TMVB, Mexico*. Tectonics, 14,* 1,245–1,262.

Suter M., Martínez M.C., López-Martínez M., Farrar E., 1995b, The Aljibes half-graben-active extension at the boundary between the TMVB and the Basin and Range province, Mexico. *GSA Bull., 107*, 627–641.

Suter M., López-Martínez M., Quintero Legorreta O., Carrillo-Martínez M., 2001, Quaternary intra-arc extension in the central Trans-Mexican Volcanic Belt. *GSA Bulletin*, *113*, 693–703.

Urbina F., Camacho H., 1913, La zona megaseísmica Acambay-Tixmadejé. Estado de México, conmovida el 19 noviembre 1912. *Bol. Inst. Geol. Méx., 32*, 125 pp.

Wells D.L., Coppersmith K.J., 1994, New empirical relationship among magnitude, rupture length, rupture width, rupture area, and surface displacement, *Bull. Seism. Soc. Am., 84*, 974-1,002.

Geofísica Internacional (2012) 51-1: 87-107

Review article

Precursors to eruptions of Popocatépetl Volcano, Mexico

Ana Lillian Martin-Del Pozzo

Received: November 28, 2011; accepted: December 2, 2011; published on line: December 16, 2011

Resumen

Las erupciones volcánicas pueden ser precedidas por cambios en la actividad sísmica y vulcanomagnética, en la composición química de los gases, del agua de manantiales y algunas veces por deformación. Para hacer un pronóstico volcánico adecuado es necesario reconocer estas señales indicativas de una erupción y su temporalidad. Las erupciones del Popocatépetl que comenzaron el 21 de Diciembre 1994, fueron precedidas por aumentos en los eventos sísmicos vulcanotectónicos (VTs), cambios en temperatura y concentración de sulfatos y cloruros en el lago del cráter y en la pCO_2 en los manantiales. También hubo un descenso en pH en algunos manantiales varios meses antes de la erupción. Los eventos sísmicos de periodo largo también aumentaron antes de algunas erupciones y los episodios de tremor armónico así como las anomalías magnéticas negativas antecedieron a la formación de domos y están ligadas al ascenso de magma. La energía sísmica cumulativa de los VTs muestra una aceleración en la tasa antes de las erupciones principales. Hubo precursores claros antes de las erupciones de diciembre–enero 2001, como son las anomalías magnéticas negativas correlacionadas con el incremento en la sismicidad, así como pequeños cambios en los manantiales. Estos cambios ocurrieron 2 meses antes de la erupción. Adicionalmente, unos días antes se presentaron episodios de tremor armónico de gran amplitud y aumento en el flujo de SO_2, esto, junto con el análisis de los datos del RSAM permitió hacer una evaluación y pronóstico adecuado de la erupción de 2000.

Palabras clave: precursores eruptivos, señales vulcanomagnéticas, sismicidad volcánica, precursores químicos, erupciones Vulcanianas, pronóstico.

Abstract

Volcanic eruptions can be preceded by changes in seismic and volcanomagnetic activity, chemical composition of the gases and spring water and sometimes deformation. Recognizing these signals of impending eruption and their timing is essential for adequate volcanic forecasting. The Popocatépetl eruptions that began on December 21, 1994, were preceded by increases in volcano-tectonic seismic events VTs, increasing temperature and sulfate and chloride concentrations in the crater lake, decreasing pH as well as rising pCO_2 in the spring water. Long period seismic events also increased before many of the eruptions and harmonic tremor episodes as well as negative magnetic anomalies precede dome formation and are linked to magma ascent. The VT cumulative seismic energy rose sharply preceding the main eruptions. Clear precursors were detected before the December-January 2001 eruptions. Two months before the eruption, negative magnetic anomalies correlated with increased seismicity, as well as small changes in the spring water were observed. Additionally, a few days before the eruption, episodes of high amplitude tremor and high SO_2 flux were detected and together with the analysis of the RSAM data were the bases for the adequate evaluation and forecasting of the 2000 eruption.

Key words: eruptive precursors, vulcanomagnetic signals, volcano seismicity, chemical precursors, Vulcanian eruptions, forecasting.

A. L. Martin-Del Pozzo
Instituto de Geofísica
Universidad Nacional Autónoma de México
Ciudad Universitaria
Delegación Coyoacán, 04510
México D.F., México
*Corresponding author: analil@geofisica.unam.mx

Introduction

Forecasting volcanic eruptions is a difficult task because of the complexity of volcanic processes and the varying structure and composition of the different volcanoes; nonetheless, advances have been made in recognizing precursory activity. This is especially important in decision making and hazard mitigation in areas with active volcanoes and dense population such as at Popocatépetl that has been erupting since 1994.

In this paper we review the eruptive precursors at Popocatépetl Volcano (19.02°N, 98.62°W, 5,454-m asl) leading up to the recent volcanic activity since 1994 (Figure 1). The volcano is located in central Mexico, in an area where more than 20% of the country population is concentrated as well as the most important economic and political activity (Figure 2). Popocatépetl reawakened after increased unrest on December 21 with a series of explosions. Current activity since 1994 has formed more than 27 small domes that have been destroyed explosively; ash from the largest of these eruptions covered areas more than 100 km away. Mexico City (20 million people) is 65 km to the west and the city of Puebla (2 million people) is 45 km to the east but there are also many small towns and cities on the flanks of the volcano and on the ravines nearby that are vulnerable not only to ashfall hazards but also to pyroclastic flows and lahars. The volcano in 1994 was still capped by glaciers on the northern and western flanks.

Some eruptions have been preceded by changes in the gas and spring water chemistry, deformation, volcanomagnetic signals and seismicity. Volcanic tremor increased in a matter of minutes before each lava fountaining episode began at Etna in Sicily during the 2000 activity**.** On the other hand, in a much larger eruption in the Philippines, the Pinatubo eruption in 1991 was preceded by precursors two months before the eruption and intense long period seismic event (LP) swarms escalated 10 days before (Wolfe and Hoblitt, 1996). Cumulative seismic energy can also be used to forecast some eruptions. Tokarev (1963) based his predictions of the 1959, 1961 and 1963 Bezymianny eruptions in Kamchatka, Russia on the hyperbolic extrapolation of the cumulative seismic energy release against time. Long period seismicity can be a useful precursor since it signals pressure induced disruption which may be lead to eruption (Chouet, 1996). Volcanomagnetic signals can also indicate that the volcano is heading towards eruption. Small short-term precursory magnetc signals occurred at Merapi Volcano before the 1992 eruption, where rapid signals were associated with changes in the stress field (Zlotnicki and Bof, 1998).

Chemical changes in the gases and spring water may also precede an impending eruption. Decreasing pH and increases in Radon and S/Cl may also be indicative of a oncoming eruption but can reflect changes in the hydrothermal system as well and do not necessarily end in eruption The ratio of HCl/SO_2 at Sakurajima in Japan

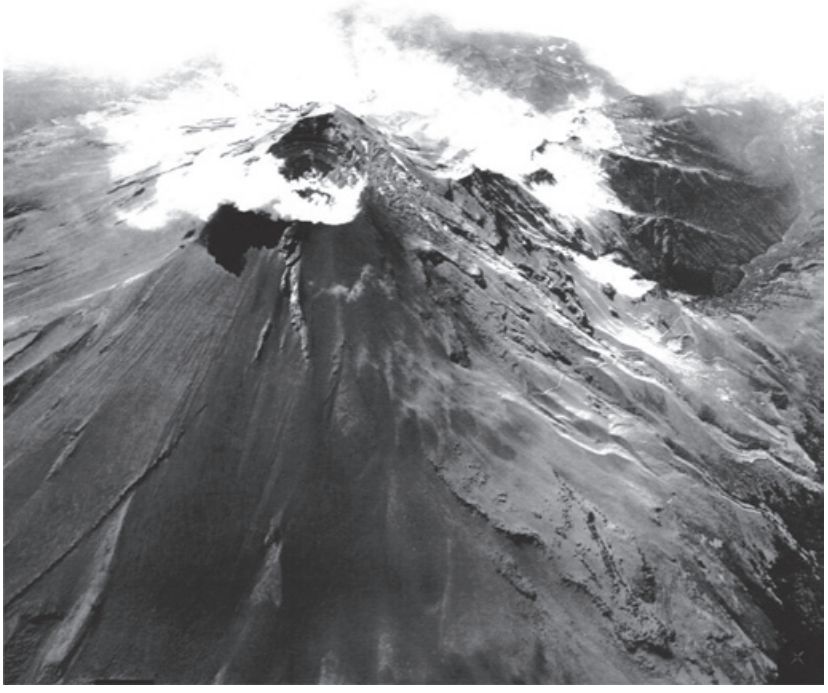

Figure 1. Popocatépetl Volcano covered by ash with a dome growing inside the crater.

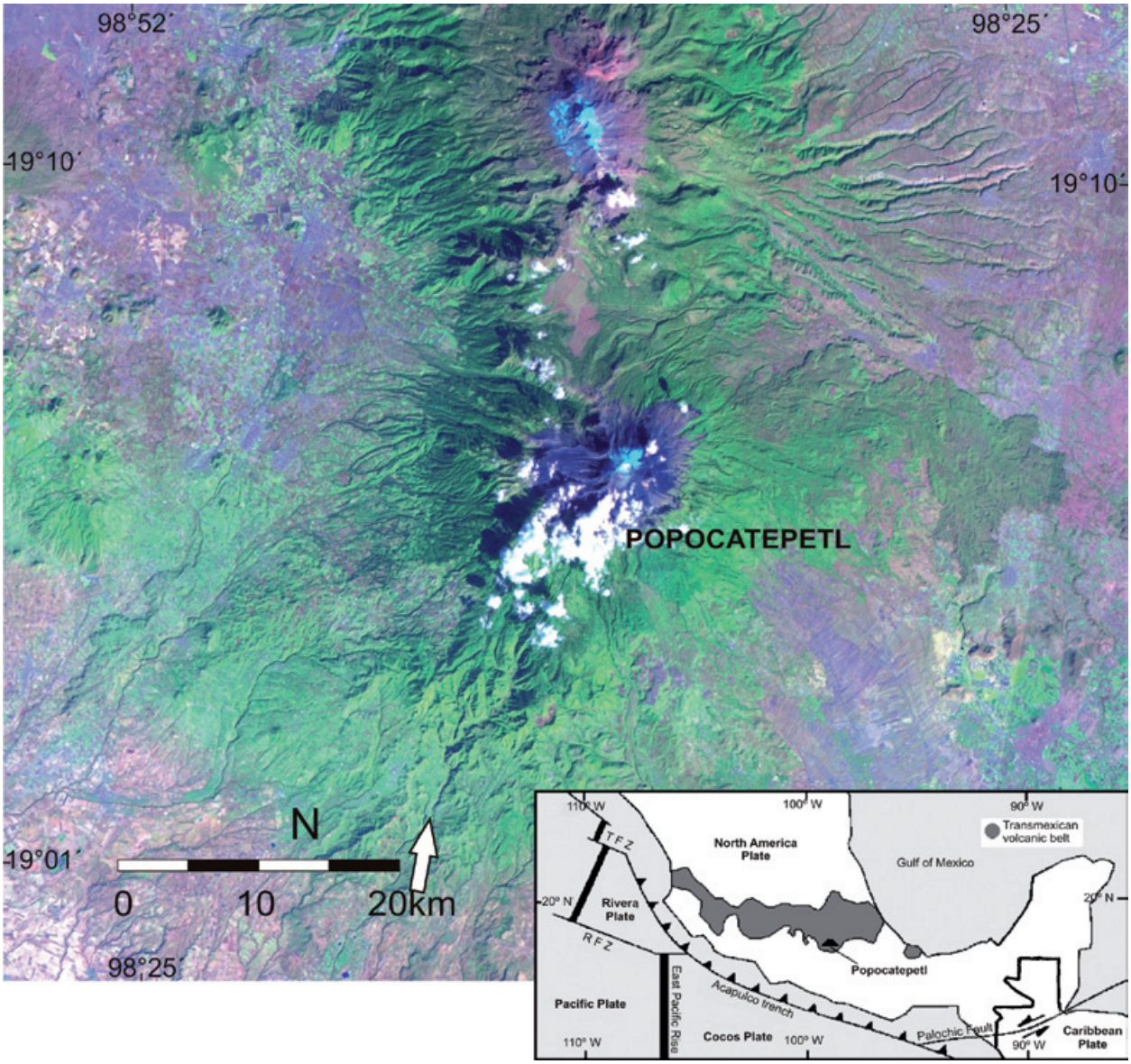

Figure 2. Landsat Thematic Mapper Satellite Image from January 11, 1995 showing Popocatépetl Volcano and its tectonic setting. A small plume can be seen issuing from the volcano and carried to the southwest.

increased prior to eruption in 1979 (Hirabashi *et al*., 1982). Fischer and others (1994) concluded that the shallow LPs at Galeras Colombia were produced by SO_2 accumulation under the crater. Rising temperature in fumaroles and crater lakes before eruptions has been documented at several volcanoes. The lake level at Taal volcano in the Philippines went down about one meter before and after the eruption of 1965, probably due to evaporation and temperature increased between 4°C and 17°C before the 1967 and 1968 eruptions (Alcaraz and Cardoso, 1969).

Eruptive History

Small Strombolian and Vulcanian eruptions with dome forming episodes occur at least once each century at Popocatépetl while Plinian eruptions take place on the order of 1,000-3,000 years (De la Cruz *et al*., 1995a; Macías *et al*., 1995; Martin Del Pozzo *et al*., 1997). Major collapse events have also occurred at least twice. The last sector collapse Mount. St. Helens-type event on which the present day Popocatépetl cone formed, was dated at about 23Ka by Siebe *et al.* (1995). This eruption produced the debris avalanche and its

hummocky topography found to the south of the volcano. One of these eruptions dated at 12,900 ±400 to 14,280±240 yr BP. by Mooser (1967) produced the 15 cm thick pumice and ash fall (PWA) found to the west, in Mexico City.

Figure 3. Vindobonensis Mexicanus 1 Codex, Popocatépetl Volcano with flames and ash plume issuing from the crater. Drawing from the XIII century (Anders, *et al*., 1992).

Fumarolic activity has been common even since pre-Columbian time as is clear from its name Popocatéptl which means Smoking Mountain in the Nahuatl language. Pre-Columbian settlements to the northeast of the volcano were covered by surges, pumice fall from Plinian eruptions and lahars on several occasions (Seele, 1973; Siebe *et al.,* 1996; Uruñuela and Plunket, 1998). Chimalpain (1612) referred to an eruption in 1347, when Popocatépetl smoked, before that, the volcano was called Xalliquehuac, flying ash. Among other eruptions, the one in 1363 was seen by the Aztecs and their neighbors (Chimalpain, 1612; Alvarado-Tezozómoc, 1609; Figure 3).

In the early fifteen-hundreds many small eruptions occurred, but Díaz del Castillo (1575) refers to a larger one in 1539. One year later, the smoke, noise and ash scared the people of Huejotzingo, Quetlaxcoapan, Tepelacac, Quauh-quecholla, Chololla, and Tlaxcallan; ash covered the fields and the cities and burnt the crops and the trees (López de Gomará, 1552). Ash fall was also reported in Atlixco, Tochimilco, Calpa, Puebla and Tlaxcala (Torquemada, 1615), and the Franciscan Codex (1889) mentions that ash fell much further away. The 1590 eruption was also explosive (Acosta, 1590). The ash from the 1663 eruption caused darkness in the area and activity continued in 1664 and 1665 when a strong explosion produced heavy ash and pumice fall on the city of Puebla causing roof collapse (Alcalá y Mendiola, 1664; Vetancurt, 1697; Figure 4). The volcano was also active in 1697, 1720 , 1792 and 1804 (Humboh, 1811; Figure 5).

Figure 4. Drawing of the 1665 eruption at Popocatéptl Volcano showing ballistcs (Gómez *et al*., 2000).

Figure 5. Map of Tochimilco, Puebla showing Popocatépetl erupting in 1792. (Archivo General de la Nación, Padrones, 12, 1792).

The last eruptions preceding the current eruptive activity occurred in the 1920s (Camacho, 1925). The eruptions produced ash fall for several years and at least one crater dome was formed. It was later partially destroyed and a small lake formed inside it. Murillo (1939) mentioned a 3 km ash plume in 1921 and 3 explosions in 1925 that produced ash fall to the south.

After increased fumarolic activity, in the early morning of December 21, 1994, Popocatépetl began erupting again. Ballistics were ejected several km from the crater and ash was carried eastward to the city of Puebla. These phreatic eruptions continued until December 31 and then became wider spaced until April 30, 1995. It was not until March 1996, that eruptions began again. The frequent plumes over 4 km high, that month, produced ash fall over cities to the east and southeast. The first crater dome was seen on April 20 and 10 days later it was partially destroyed by an explosion coincident with the formation of another new dome. This explosion killed several climbers that were in the area off limits. There were several eruptions months apart in late 1996 but the October and December eruptions were the largest. In 1997, Popocatépetl was very active. Eruptions in March and April escalated in May and June and on the 30, the ash plume which reached 13 km was carried to Mexico City causing visibility problems, traffic jams and flight cancellations. The new crater domes that were formed in August and December were destroyed explosively. The main eruptions in 1998 occurred on April 21 and 27, August 14, September 22 and 23, October 5, and increased in November and December when ejecta produced large impact craters up to 5 km from the crater.

During 1999, activity was relatively low, and was followed by dome formation in February-March and August-September 2000. Activity went up in October 2000 leading up to the larger eruptions in December 2000 and January 2001, which are related to several magma batches and can be considered belonging to the same eruptive sequence.

Changes in different monitoring parameters were detected several months before the main activity in December–January and will be discussed in the following sections in further detail. Seismicity and other precursors increased since October and again in mid December which resulted in the formation of a large dome that nearly filled the crater and several large ash eruptions from December 12 on.

The biggest eruption on January 22, 2001, formed a plume that reached 18 km and produced mixed pumice and ash fall hundreds of kilometers to the east and pyroclastic flows and associated mudflows that nearly reached the closest towns.

After the large eruption, activity declined with only small eruptions except for the one on July 3 when the ash plume reached 9 km asl. A new dome formed in March 2002 followed by small ash eruptions in April, May, June and July and larger explosions in November and December

2002 (Figure 6) and in February, June and July 2003. Activity in 2004 was low. Large eruptions occurred in July and December 2005, and July 2006, but the year was marked mostly by dome growth and small eruptions. In 2007, another small dome grew in the crater and only minor eruptions took place, but in 2008 larger ones occurred in January and February with small ash emissions in March, April, May, November, and December. Small emissions continued in 2009 and increased in October and November, but activity went down again afterwards and it was not until June 2010 that other ash emissions occurred. During 2011, small eruptions took place in January and March and larger ones in May and June followed by small eruptions again in August. A new dome formed in early September and was partially ejected on September 26 (Figure 7).

Risk Assesment

At the beginning of the eruptive period in December 1994, a scientific committee was set up to asses the eruptive activity and advice federal and local authorities on the state of the eruption. Daily meetings were programmed at the start of the eruption where the seismicity, COSPEC measurements (SO_2), deformation, spring water chemistry, ash distribution and components were discussed; meetings were frequent at the beginning and were more widely spaced when activity declined.

A seven color-coded volcanic alert system for Popocatépetl was implemented for Civil Protection agencies and simplified into a three color alert for the general public (De la Cruz and Tilling, 2008). The warning system is based on scientific data and its interpretation. The level of the Volcano Traffic Light Alert System indicates the most probable scenarios based on the volcano monitoring data and visible eruptive activity and sets recommendations for the Civil Protection authorities and population at risk. When the volcano is quiet and has only sporadic seismic events, the alert is classified as green phase 1 and is increased to phase 2 when there is fumarolic activity and low level seismicity. When low level seismicity increases, the level changes to yellow which is subdivided into three phases based on the level of activity and expected phenomena: moderate explosions with gas emission and light ash fall (phase 1), intermediate to high explosivity (phase 2), ash fall and small lahars, growth of lava domes (phase 3). The red alerts are issued when there is a possibility of large pyroclastic flows and lahars (phase 1) and large scale stratospheric plumes and/or massive sector collapse (phase 2). The National Civil Protection System carries out coordinated action for protection and prevention and participates in the risk management.

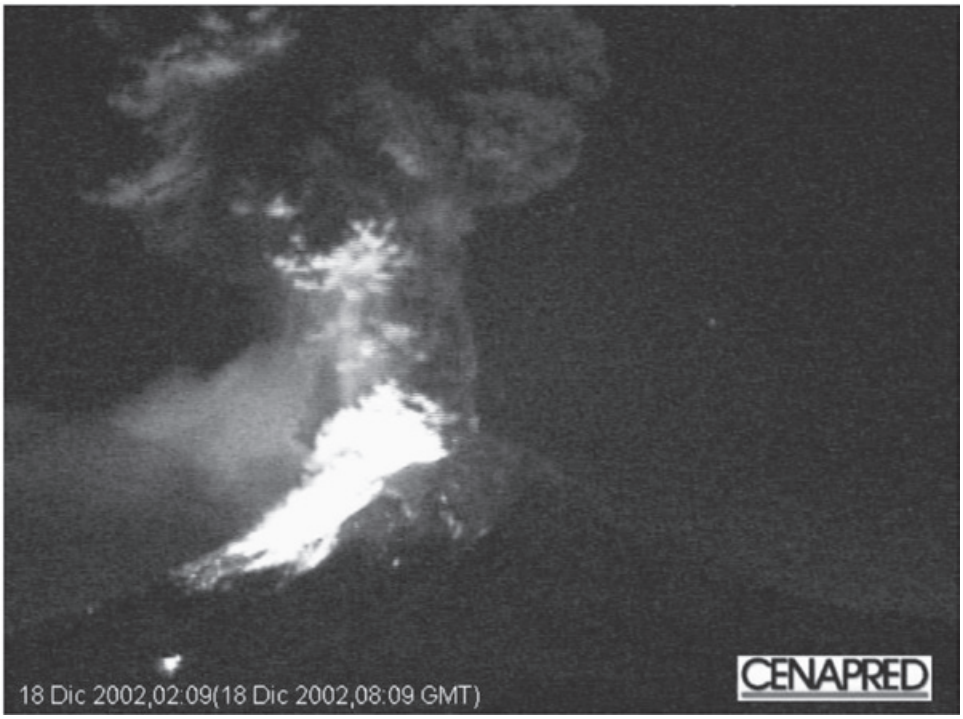

Figure 6. Explosion on December 18 2002, with ballistics and ash plume (Secretaria de Comunicaciones y Transportes -CENAPRED).

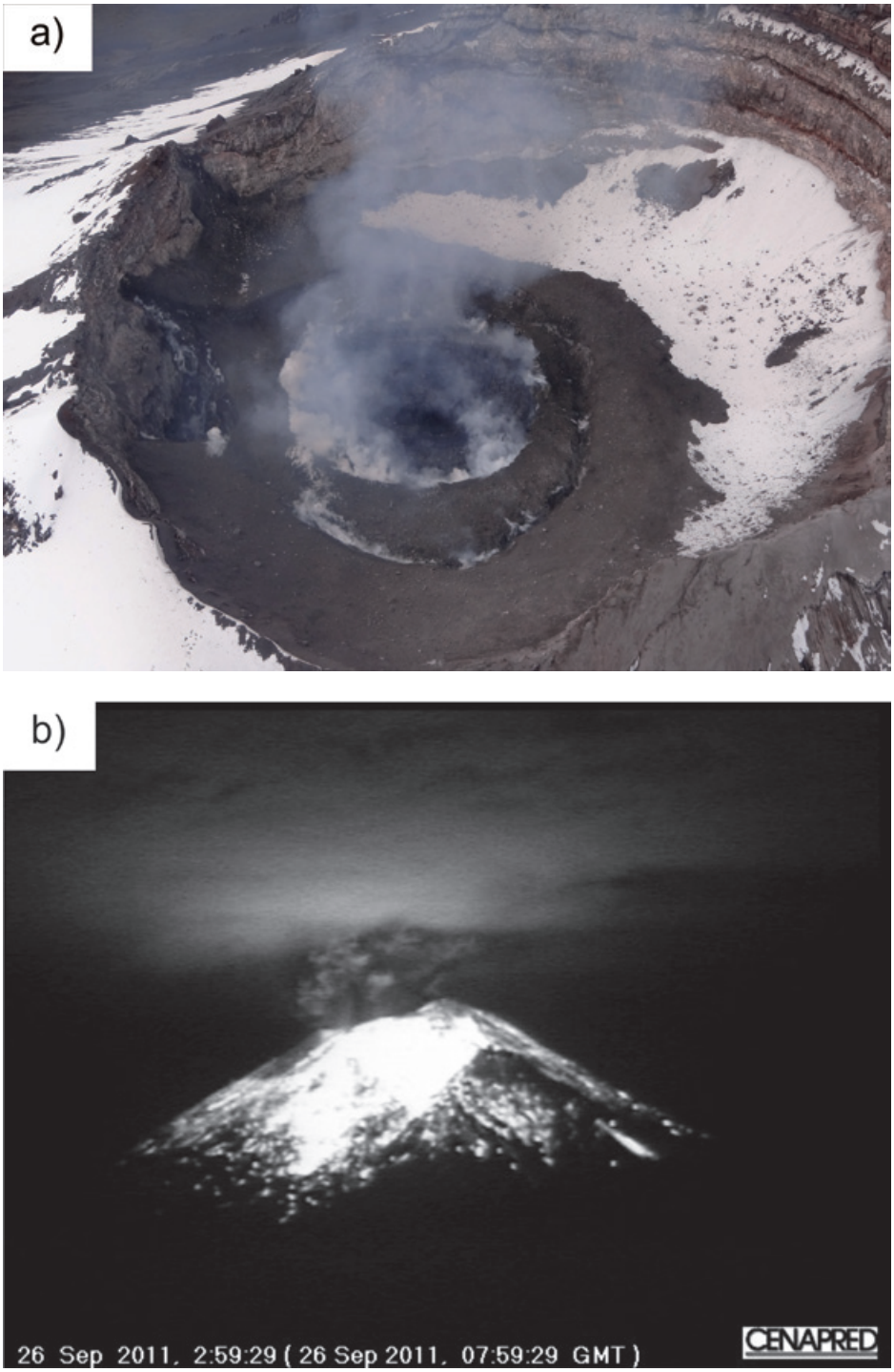

Figure 7. Volcanic activity in 2011. a) Dome growing in the crater on September 8, 2011. b) Explosion on September 26, 2011 following dome growth. (SCT-CENAPRED).

A hazard map was prepared with the existing geological information at the time. The hazard map shows fall deposits (Figure 8), pyroclastic flows and lahars (Figure 9) in three different colors (red, orange and yellow) depending on their hazard level, (Macías *et al*., 1995). The map has been the bases for planning and evacuation for federal, state and local authorities.

Risk perception may vary among scientists, authorities and the general public which makes decision making difficult, but adequate analyses of scientific information, consensus and good communication can result in an adequate response and reduce vulnerability.

Figure 8. Ash fall hazard from Popocatépetl indicating that main fall areas for the summer are to the west and the rest of the year to the east. The distribution of the PWA pumice is shown with diagonal lines (from Macías *et al*., 1995).

Figure 9. Close up of the Popocatépetl Hazard Map for flows. The red area can be affected by lava flows, pyroclastic flows, lahars and floods similar to the ones that have occurred twice in the last 1,000 years. The orange area can be affected by the same types of phenomena but on a larger scale, similar to the 10 eruptions that took place in the last 15,000 years and the yellow area is subject to the effects of much larger eruptions such as the ones that occurred twice in the last 40,000 years. Extended hazard from the flows in the gullies are shown with dashed lines (From Macías *et al*., 1995).

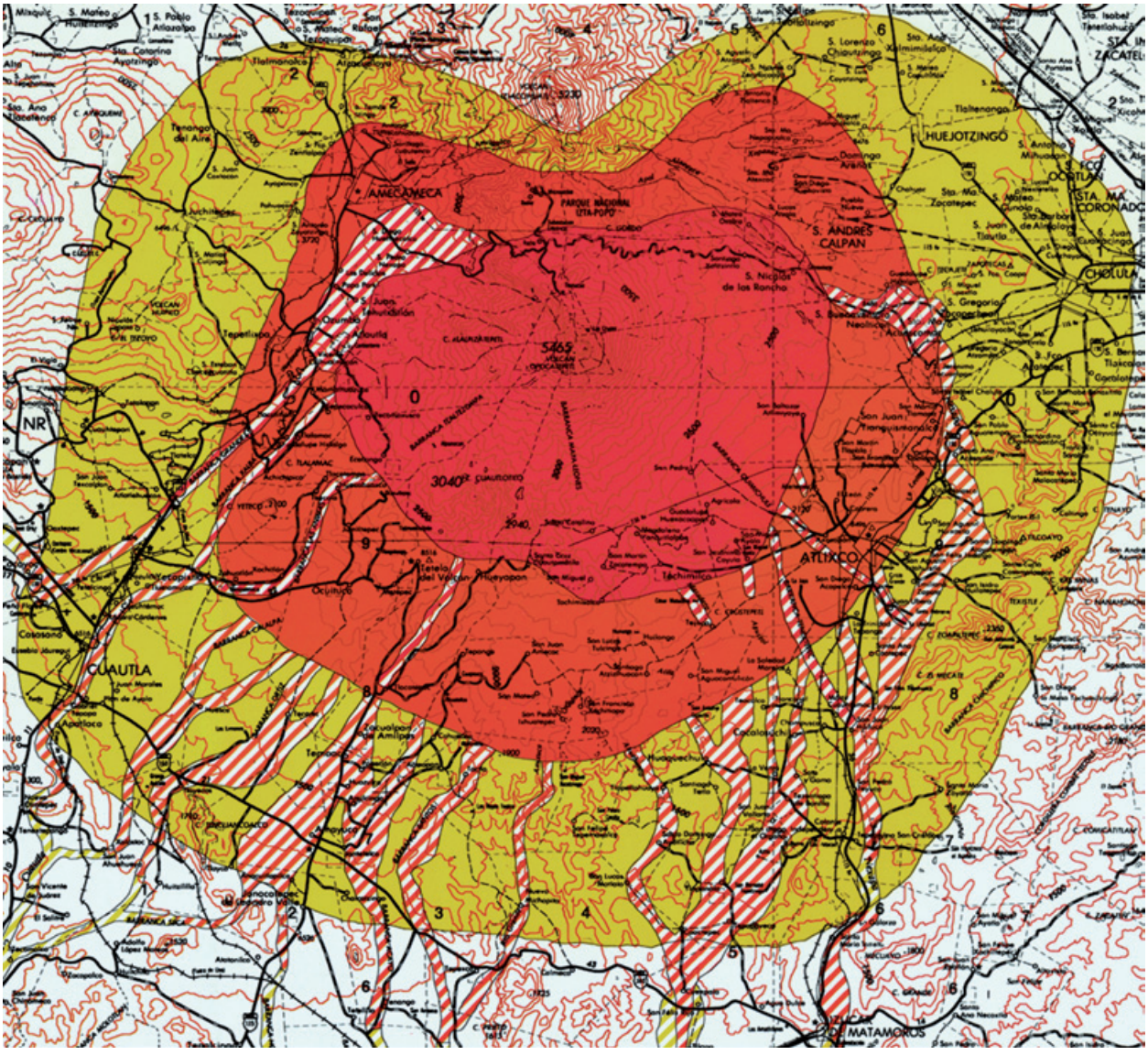

Surveillance

Permanent monitoring was set up at Popocatépetl several years before the current eruptions began in December 1994. A three–component short period telemetred seismic station was set up at Cerro Tlamacas (PPM), 4.8 km northeast of the crater, in 1989 by the Instituto de Geofísica of the Universidad Nacional Autónoma de México (UNAM) and another station was established at Altzomoni, 12 km to the north of the summit by the Engineering Institute of the same university, two years before. Shortly before the eruptions began in 1994, two more seismic stations at Chiquipixtle (PPX) about 4 km to the southwest and Colibri (PPC) 7 km to the southeast of the summit were installed by the Centro Nacional de Prevención de Desastres (CENAPRED) they also installed two more in January 1995 (PPB and PPP). Seismic signals are received in real time and processed at CENAPRED and the Institute of Geophysics in Mexico City. The stations are short-period 1 Hz stations that were operating on the flanks of the volcano between 3,200 and 4,200 m asl (Figure 10). Before this, only temporary portable networks were set up on the cone for short periods of time.

The first visual monitoring camera was installed at Alzomoni in January 1995 and since then, two more were, set up at Tlamacas and Tianguismanalco to the north and east of the summit.

A leveling line and three dry tilt stations on the north, northwest and northeastern flanks of Popocatéptl were measured periodically from 1988 to 1994 but no significant deformation was noted (Panohaya-Analco, 1991; Villareal, 1995). At the beginning of the eruptions, four tiltmeters were added to the seismic stations and geodetic measurements were also carried out with laser range finders on a small network on the northern flank since 1992 (De la Cruz *et al*., 1995b; De la Cruz and Tilling, 2008). Cabral *et al*. (2008) also installed a GPS network on the northern and southwestern flanks of the cone in 1994 at about 4,000 m asl.

Correlation spectrometry (COSPEC) airborne measurements of SO_2 emission were begun in February 1994 and later extended to measurements on tracts near the volcano. Chemical monitoring of the springs on the volcano began in 1988.

Vulcanomagnetic activity has also been monitored since 1997 when the TLA telemetred permanent total magnetic field Geometrics G-56 station was installed near Tlamacas on Popocatépetl's northern flank at Cruz Blanca. Several years later, in 2005, another Overhauser magnetic station was installed at Chiquipixtle (CHX). The magnetometers record the total magnetic field every minute and data is then transmitted by radiomodem to the Institute of Geophysics. This data is processed with data from the base station at the Teoloyucan Magnetic Observatory to eliminate magnetic effects that are not related to the volcano (Martin Del Pozzo *et al*., 2008a).

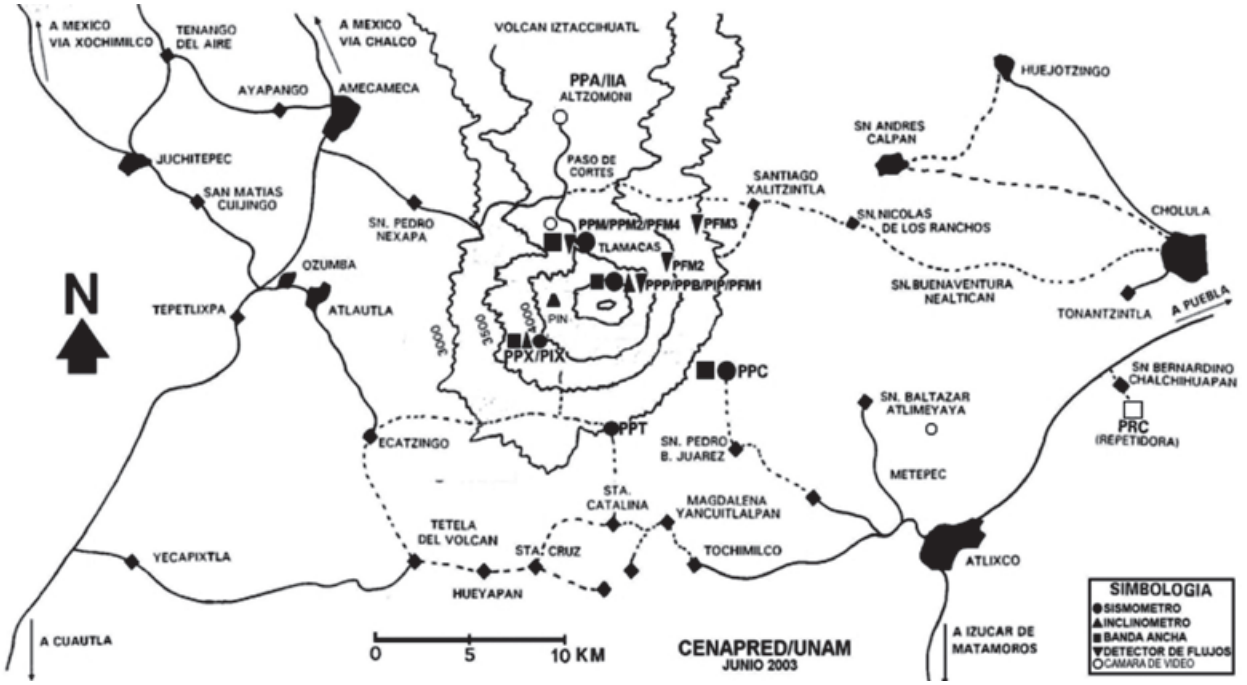

Figure 10. Map showing stations operated by CENAPRED.

Eruptive precursors at Popocatépetl

Popocatépetl showed several signs of volcano unrest leading up to the 1994 eruption, nonetheless due to their small magnitude, forecasting was inconclusive at the time. Since 1988, several volcano tectonic seismic events (VTs) were detected in a temporary portable network and after 1989 at the Tlamacas station at Popocatépetl, but it was not until 1993 that seismicity, water temperature in the crater lake and fumarolic activity rose significantly signaling the reawakening of the volcano. Spring water monitoring also showed increasing concentrations of chemical components such as pCO_2 and HCO_3 several months before the eruptions began. Probably the main precursors to eruptions are VTs characterized by high frequency and impulsive arrivals but long period seismic events (LPs) and harmonic tremor also precede certain eruptions.

Seismicity

De la Cruz *et al*. (2008) studied the seismicity recorded by the PPM station from January 1990 to December 21, 1994, when the eruptions began. They recognized several stages in the VTs leading up to the eruption associated with the thermal effects of a magmatic intrusion at depth, fracturing linked to opening of pathways, stress concentration accelerating the process and stress redistribution before the eruption. The cumulative seismic energy reflects the stress which leads to material failure and produces a logarithmic increase in the strain rate (Reyes-Davila and De la Cruz, 2002). The accelerating rates of strain and seismicity can be seen in Figure 11. The sharp increase is noted in 1993 and early 1994, several months before the eruption. The number of events and the acceleration rate of the cumulative energy decreased afterwards but increased again shortly before and again went down briefly before the eruption, reflecting fracturing and relaxation. The onset of the eruption on December 21, 1994 was marked by a swarm of VTs. Long period seismicity (LPs) increased from 7 events a day in October 1994 to 22 events in December 1994 and to 49 events on the day of the eruption on December 21. The frequency of the LPs and tremor suggest a shallow source 2.5 km beneath the crater and depths for VTs between 2.5 and 10 km (Arciniega *et al*., 2000; Figure 12). A day after the eruption started, volcanic tremor began (Valdés *et al*., 1995).

Volcano tectonic events (VTs) at Popocatépetl are located below the crater and to the southeast. Their fault plane solutions indicate that below the crater they have N70ºE pressure axes and normal fault mechanisms with some reverse

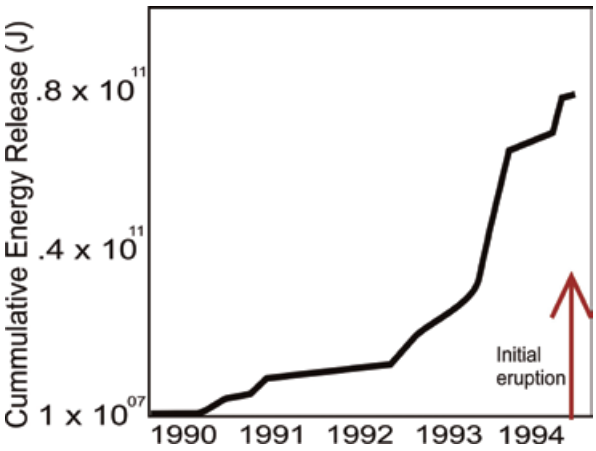

Figure 11. RSAM counts show accelerates rates in 1993 and early 1994 (Modified from De la Cruz *et al*., 2008).

events between 0 and -3 km asl. The tension axes are radial. On the other hand, VTs on the southeast flank have S–N and W–E pressure and tension axes and strike-slip solutions (Arámbula-Mendoza *et al*., 2010).

Espíndola *et al*. (2005) found three families of VTs (2< Mc< 2.5), two to four km deep at Popocatépetl which they considered to be stress related associated with magma movement through the conduit from September though December 1995, but no eruptions occurred until March 5, 1996. De la Rosa-Moreno *et al*. (2003) also classified the long period events into 7 families and distinguished that three of them were precursors to important eruptions at Popocatépetl. The June 30, 1997 eruption was preceded by VTs, double LPs and very long period LPs lasting several minutes and followed by tremor.

Tremor and LP swarms were associated with the formation of the dome from August to December 1997. Compression dominated (reverse solutions) events gave way to an extensional regime in the later stage (Arámbula-Mendoza *et al*., 2010). From December 25 to November 22, 1998 compression occurred at depth (-2.5 to -0.5 km asl) while there was extension at shallower levels and strike-slip solutions for the events on the southeast. In certain cases, changes in the stress field associated with tectonic earthquakes can trigger eruptions. De la Cruz *et al*. (2010) considered that precursory accelerating patterns after the M 7.0 tectonic earthquake, 143 km from Popocatépetl were associated with the first stage of material failure that triggered the June 15, 1999 activity at the volcano.

Arciniega *et al*. (2008) described 3 types of LP events with hypocenters less than 2 km below the crater floor when they carried out a broadband

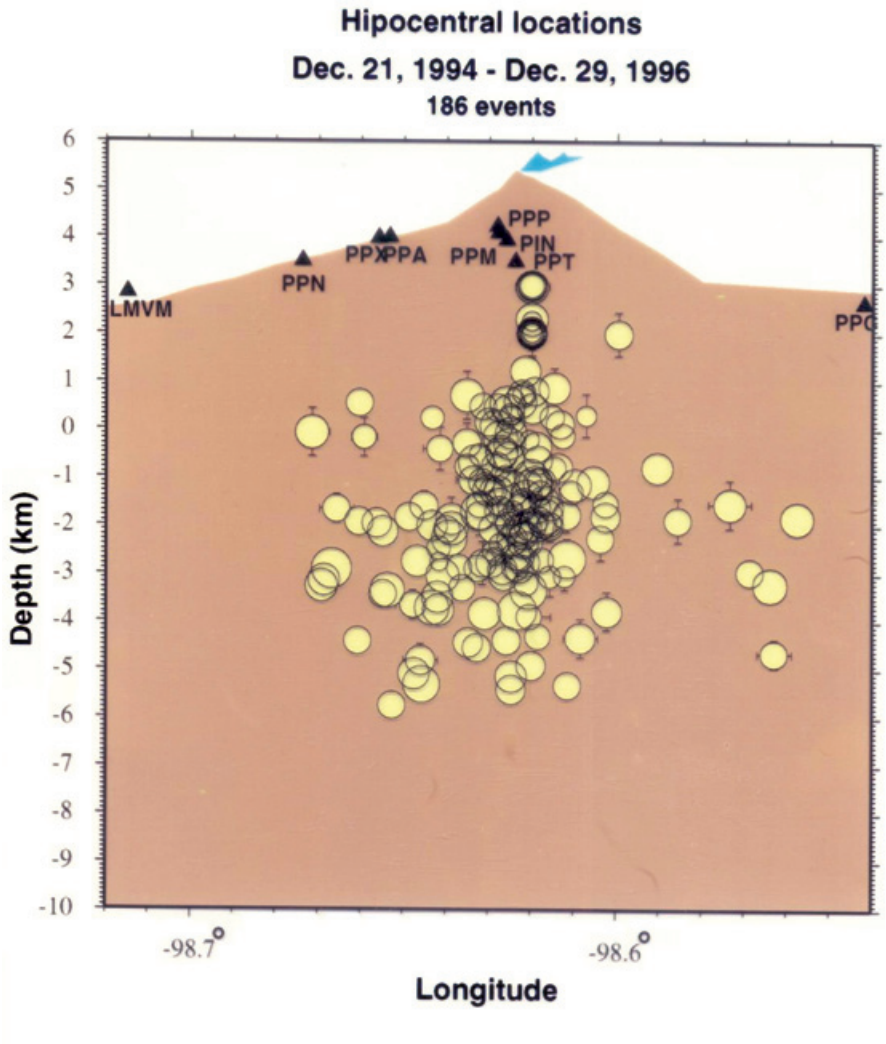

Figure 12. Section of Popocatépetl showing the seismicity from 1994 to 1996 indicating the location of the events (from Alicia Martínez Bringas personal communication).

seismic experiment at Popocatépetl from December 1999 to March 2000. Type 1 degassing events have impulsive first arrivals and a harmonic wave train with periods of 1.4-1.9 s related with a very long (30 s) wavelet. They are thought to be produced by expanding gas pockets coupled with acoustic resonance in the conduit (Chouet *et al*., 2005). Type 2 LPs are superimposed events with slowly emergent first arrivals made up of successive wavelets with a period of near 30 s and Type 3 LPs have emergent first arrivals and harmonic signature with a dominant period near 1.1 s and are associated with dome formation. In February and March 2000, they were linked to lava extrusion. Broadband signatures during the Vulcanian eruptions in April and May 2000 lasted 30-80 min.

After growth of the small lava domes in February-March as well as in August-September 2000, seismicity went up in October: VTs increased in magnitude and number and ash emissions grew larger. The December 2000-January 2001 activity at the volcano was preceded by important changes in seismic, chemical and magnetic parameters.

Periods of high amplitude volcanic tremor began on December 6 following a swarm of six VTs. Swarms of VTs occurred again on December 8 and 9 and on December 12, emissions increased considerably (De la Cruz and Tilling, 2008). Very high amplitude harmonic tremor began again on December 15 and rose to saturation level on all Popocatépetl seismic stations. The strong tremor lasted 10 hours and began again 16 hours later. Valdes *et al*. (2001) considered that these tremor episodes followed a time predictable loading-discharge process making it possible to forecast the next episode. The harmonic tremor on December 15, 16 and 17, 2000, and a sharp 200μrad deformation was associated with the tremor and a high effusion rate for the dome, ≈ 180-200m^3/s (De la Cruz and Tilling, 2008). The large dome reached 50 m from the eastern edge of the crater.

RSAM is a real time seismic amplitude measurement that provides information on the cumulative seismic energy. The RSAM plot clearly shows the June 30, 1997 and December 12, 2000 steps (De la Cruz and Tilling, 2008). Several other eruptions can also be recognized on the plot such as the ones on March 5, 1996, when eruptions began again after ceasing for about 10 months, the April 21, 1998 and the November 25, 1998 eruptions (Figure 13). Figure 14 also shows that the VT cumulative energy went up sharply associated with many of the eruptions such as the ones in March 21, 1997, June 30, 1997 and November 1998. The differences between Figure 13 and 14 are due to the seismic energy released by LPs and tremor, specially the large amplitude harmonic tremor from December 15–19.

The large explosion on January 22 was preceded by reverse and strike-slip events several weeks before and later on by a normal VT event (Arámbula-Mendoza *et al.*, 2010).

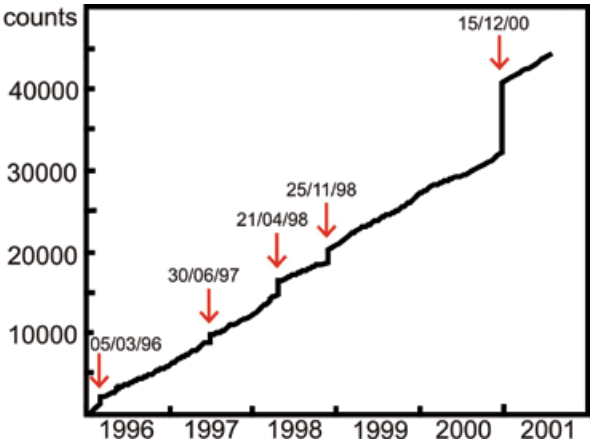

Figure 13. Real time Seismic Amplitude indicates steps for several of the eruptions (Modified from De la Cruz *et al*., 2008).

Novelo-Cassanova and Martínez-Bringas (2005) found a highly attenuating body 6-8 km below Popocatépetl which could be attributed to presence of magma. Berger *et al*. (2011) also report low velocity bodies, 4-7km to the north of the crater, 4-9 km to the southeast and 7 km bsl under the crater, as well as strong lateral heterogeneity in their 3D tomography of Popocatépetl.

Deformation

There was no significant deformation at Popocatépetl between 1988 and 1994 (measurements on the leveling line and dry tilt stations). Cabral *et al*. (2008) considered the volcano a minimally deforming system based on data from their GPS network and detected only small transients in early 1997 and late 2000 associated with higher dome effusion rates which formed the larger domes. The only deformation detected in the electronic tiltmeters was linked to the tremor in December 2000 showing tilt oscillations of up to 100– 200 μrad (Valdés *et al*., 2001).

We were able to visibly detect lateral deformation in the crater dome preceding the January 22, 2001 eruption from the aerial photographs taken by the Secretaria de Comunicaciones y Transportes by request of the Scientific Committee, although most of the magma from the 2001 eruption was probably already in place since there were relatively moderate changes in the activity in January (Martin-Del Pozzo *et al*., 2003).

Chemistry

Changes in gas and spring water chemistry as well as in soil degassing and ash leachates preceded the different eruptions as well. The SO_2 flux was lower in 1994 at the beginning of the phreatic phase (4.6 Kt/d) and increased when the eruption turned magmatic (10-13Kt/d) between

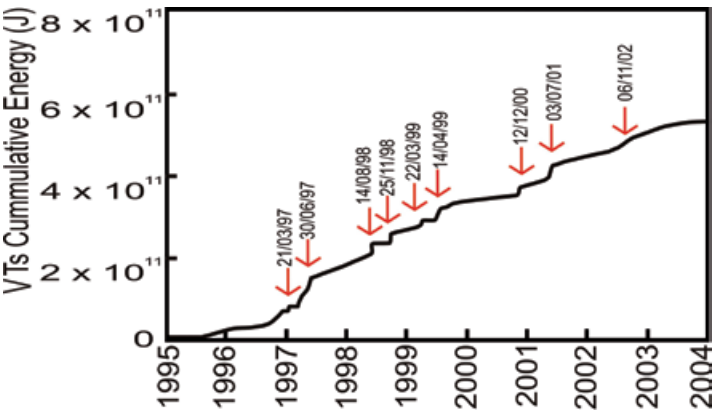

Figure 14. VT cumulative energy associated with eruptions (Modified from Arámbula *et al*., 2010).

1996 and 1997 (Delgado-Granados *et al*., 2001). The SO_2 flux rose drastically on December 13, 2000, reaching over 50Kt/d (Valdés *et al*., 2001). Before the eruptions began in December 1994, there was a small lake inside the crater which dried up before the formation of the new domes in 1996. The chemistry of the water in the crater lake changed significantly before the eruption. Between 1985 and 1994, the SO_4^{2-} content doubled and chlorides increased from 12,400 mg / l to 14,200 mg/l. Temperature also went up from 29° to 65 °C (Armienta *et al*., 2000).

Spring water monitoring since 1988 has shown that small peaks in HCO_3 concentration and PCO_2 are associated with incoming magmatic batches at Popocatépetl Volcano. Oxygen and hydrogen isotopic data indicate that the water system is controlled by magmatic recharge, but large amounts of CO_2 from the magma associated with degassing come into the system before eruptions (Martin Del Pozzo *et al*., 2002a; Martin-Del Pozzo *et al*., 2002b; Inguaggiato *et al*., 2004). Helium and carbon isotopic signatures are also consistent with magmatic gas input. The concentrations of SO_4, Cl^-, F^-, HCO_3^- and B, also increase before the main eruptions, Armienta *et al*. (2008) also noted some chloride and sulfate changes and the presence of boron preceding or coincident with increased volcanic activity.

Ash leachates can also indicate changes in the type of activity. The SO_4^{2-}concentration (19 550 ppm) in ash leachates from the initial eruption on December 21, 1994 decreased sharply afterwards and the same occurred the following year after a 10 month pause in the eruptive activity (Armienta *et al*., 1998). This could have been produced by accumulating gas and rock scavenging before these eruptions. An increase in F^- before the extrusion of the first lava dome was probably related to heating up of the system consistent with SO_4^{2-} and Cl^- concentration trends which reflected more of a magmatic signature in 1996 than during the phreatic phase the year before. This is also supported by the phreatic character of the ejecta in 1994-1995 and the first week in March 1996 which turned magmatic after March 11 and resulted in dome extrusion on March 20 (Martin-Del Pozzo *et al*., 2008a).

Ivanov *et al*. (1996) also detected that leachates from the first phase of the 1991 Avacha eruption in Kamchatka were phreatomagmatic and turned magmatic the next day. Sulphur isotopes for the first leachates reflected mixing of magmatic and hydrothermal components (δ^{34}=+11‰ CD) while the ones from the later date had magmatic signatures (δ^{34}= +7.5‰). At Mt. St Helens the ash leachates from March and April also had low SO_4^{2-} ~ 100 ppm and Cl^- ~ 600 ppm, reflecting their phreatic nature while concentrations went up to >3,000 ppm SO_4^{2} and > 1,000 Cl^- during the climatic eruption in May (Stoiber *et al*., 1980; Stoiber and Williams, 1990).

Armienta *et al*. (2010) considered the Popocatépetl ash leachates from September 1999 to October 2000 related to hydrothermal alteration, but from November to December 2000, preceding the eruptions, F^- increased suggesting renewed heating of the system linked to an intrusion at depth. The S/Cl ratios also increased during 2000.

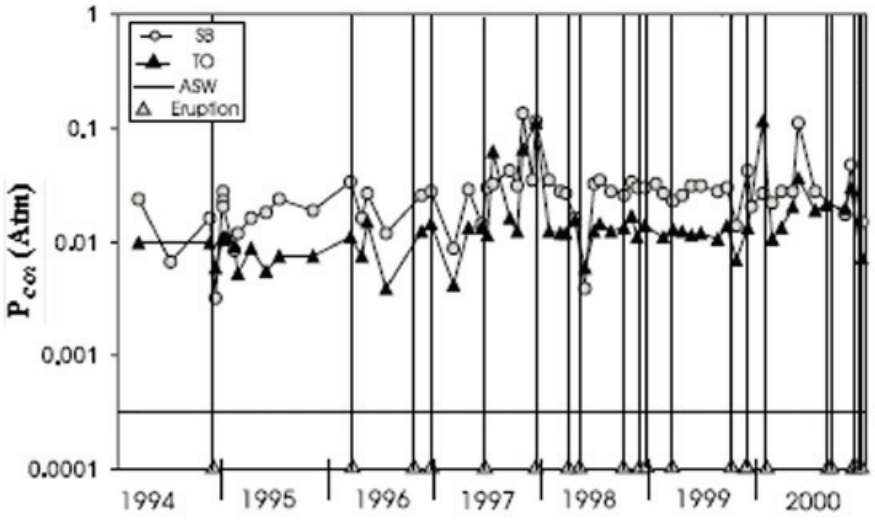

Figure 15. An example of PCO_2 in two of the springs at Popocatépetl shows increases before the beginning of the 1994 eruptions and then decreases, the same occurs before the eruptions in 1997 and early 1998. In 2000, two of these rising trends precede the eruptions (Modified from Martin Del Pozzo *et al*., 2002a).

Radon behavior can also indicate volcano unrest. The maximum soil radon peaks at Popocatépetl occurred in December 1994 and correspond to the onset of the eruptions. Higher ^{222}Rn values preceded the appearance of the December 1997 dome and eruption (Armienta *et al*., 2002) and a large soil radon peak at TLA (4,000 m asl) correlated with explosions that destroyed the lava dome. (Segovia *et al*., 2002, Segovia *et al*., 2005). A small increase in soil radon also occurred in November and December 1998 related with the eruptions. The December 2000 and January 2001 eruptions were also preceded by increasing soil radon at TLA several months before and peaked in December (Segovia *et al*., 2002). In February and April 2002 as well as in September and November 2002, radon also increased during dome formation and associated with the activity in February 2003.

Magnetics

Magnetic signals can also indicate periods of magma injection and gas pressure build-up; Negative magnetic anomalies during 1998-1999 were considered to be thermal caused by hot incoming magma while positive anomalies were related with dome cooling above the Curie point. Kotsarenko *et al*. (2008), also noted thermally induced changes in the geomagnetic record. Sharp positive anomalies are stress related as was seen in the correlation with a tectonic regional earthquake and explosions (Martin-Del Pozzo, 2002c). Negative magnetic anomalies 5 to 37 nT, were recorded from 1-8 days before eruptions.

The eruptions in December 2000 were preceded by an increase in VTs and in harmonic tremor episodes which resulted in several large ash plumes and a large dome that filled the crater up to 50 m from the rim. Ash eruptions followed the increase in the tremor amplitude on December 12 and 13, and on the 15, tremor amplitude rose again and remained high for 4 days associated with ash eruptions and dome effusion.

The largest eruption since 1994 occurred on January 22 with few precursors except for the VT event that day. The eruption was triggered by mixing of a mafic olivine-bearing melt with a more evolved magma (Martin-Del Pozzo, 2003). Magma probably started rising since October (5 nT) when seismicity first increased and the marked negative anomaly occurred and then continued with new rising magma batches reflected in the other anomalies shown in Figure 16.

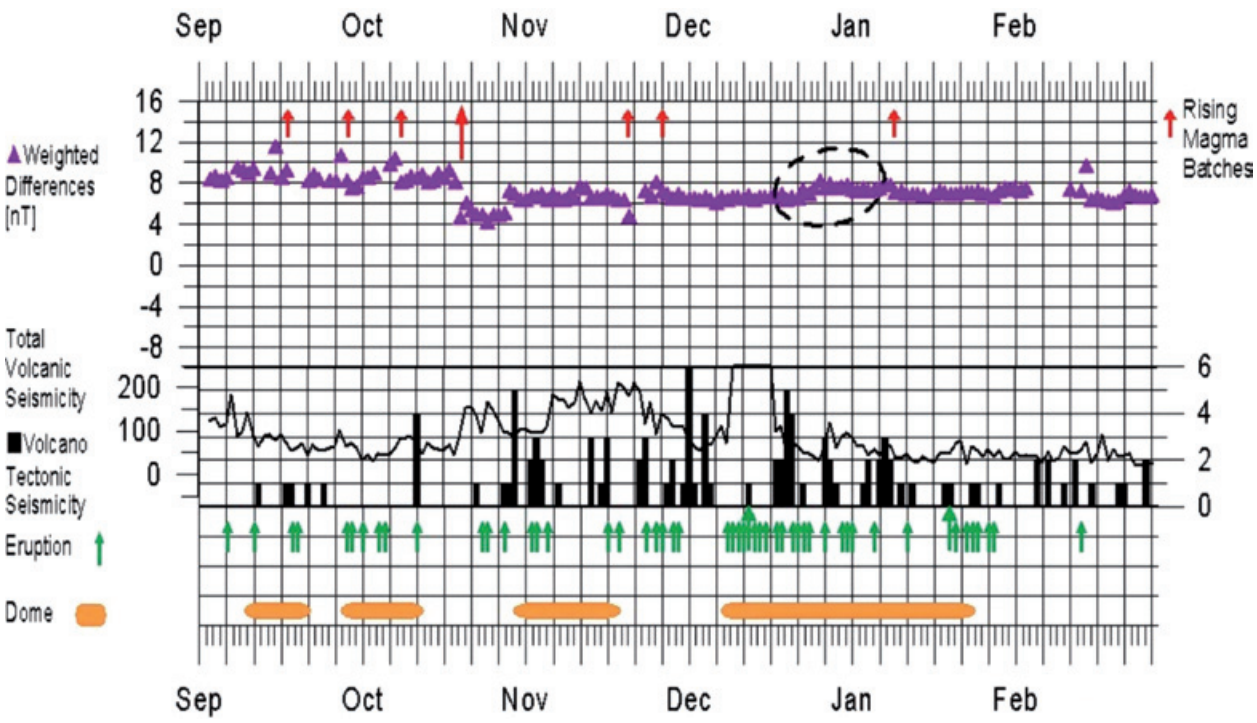

Figure 16. Vulcanomagnetic signals in 2000, seismicity and dome growth. Note the decreasing trend the last week in October correlates with the increase in seismicity and is considered to be related to the ascent of most of the magma of the December January eruptions. The dashed area is probably related to cooling of the dome (Modified from Martin-Del Pozzo *et al*., 2003).

During 2006 negative magnetic anomalies were again correlated with periods of harmonic tremor and interpreted as indicators of ascending magma and dome precursors (about 7 days) followed by increasing signals linked to cooling of the domes (Martin-Del Pozzo *et al*., 2008a).

Geologic

From 1994 to early 1996 ejecta consisted of non-juvenile material that gave way to juvenile ejecta with the formation of successive domes from April 1996 on. A glass component was first detected at Popocatépetl in the ash from March 11, a week before the appearance of a new crater dome (Martin-Del Pozzo *et al*., 2008b). There are at least two magmatic components at Popocatépetl, a mafic magma that crystallizes near the Moho and a more evolved component with which it mixes at depths of between 4 and 13 km (Straub and Martin-Del Pozzo, 2001).

Several months before the December 2000-January 2001 eruption, ash components changed. A large percentage of crystals, instead of lithics from the dome, reflected the changing conditions at the volcano.

Many of the Plinian eruptions at Popocatépetl were preceded by phreatomagmatic activity. These eruptions began with surges that underlie the Plinian pumice deposits. Espinasa and Martin-Del Pozzo (2006) and Arana-Salinas (2010) dated an orange pumice fall at 4650± 100 yr BP-4965±65 yr BP. This Plinian eruption began with a phreatomagmatic explosion and erupted about 2 km^2 (DRE) of magma (Arana-Salinas *et al.*, 2010) but other eruptions such as the PWA (≈14000 yr BP) were much larger.

Precursors at other Mexican Volcanoes

Eruptions at several volcanoes in Mexico have been preceded by increasing VTs, LPs and tremor, chemical changes in the fumaroles and some by deformation.

Colima

Colima is Mexico's most active volcano. Historical activity at Colima Volcano shows that Plinian eruptions occur about every 100 years, separated by repose periods several decades long followed by effusive activity which produces short viscous lava flows accompanied by dome growth and Merapi and Vulcanian eruptions with pyroclastic flows in the larger eruptions (Martin-Del Pozzo *et al*., 1995; Saucedo *et al*., 2002 and 2010). Conditions at the volcano now are similar to those that precede explosive eruptions. Fonseca and Martin-Del Pozzo (2010) proposed 7 scenarios for a Plinian eruption based on isopachs, daily radiosonde wind and socioeconomic data.

The situation now prevailing at the volcano is similar to the one preceding explosive eruptions, so Civil Protection agencies and scientists have been working closely with the population. Evacuation drills with towns such as Juan Barragán and Becerrera were frequent in 1998 and 1999, and some of the people living in the town of La Yerbabuena were relocated further from the volcano.

Seismic and chemical monitoring are carried out mainly by the University of Colima personnel, and a local scientific committee from the university meets with authorities when activity increases. Part of the volcano is in the state of Jalisco so joint meetings also are planned.

Short–term forecasting at Colima showed increases in seismicity and deformation in 1991 (Gonzalez-Pomposo *et al.*, 1993) and in 1997-1998 (Zobin *et al*., 2002). In 1991, dome growth occurred from March 1 to April 16, and before the partial collapse of the dome, the frequency of the volcanic tremor increased from 3.0 to 9.0 Hz and returned to lower frequencies sharply after the event (Gonzalez Pomposo *et al*., 1993). Distance measurement on the dome and summit cone of Colima Volcano showed accelerated expansion before the 1998 eruption (Murray and Ramírez-Ruiz, 2002). Steady inflation, increases in S/Cl and SO_2 (400 t/d- 1600 /d) in the fumaroles, and earthquake swarms 8 km beneath the summit which became shallower, were among the precursors which led up to the 1998 eruption (Zobin *et al*., 2002). Fumaroles at Colima showed a peak in the S/Cl and deuterium, one year before the activity in 1998 and SO^2 flux increased from 400T/d to 1600T/d before the eruption (Taran *et al*., 2002). Lopez-Loera and Urrutia-Fucugauchi (2003) also recognized vulcanomanetic precursors before the 1998-1999 eruption.

Chichón

Chichón Volcano has had an explosive history with periods of large dome formation (Espíndola *et al*., 2000). The last of these crater domes was destroyed in 1982. Three large Plinian eruptions and several small ones in between, took place on March 28 and April 3–4 1982, which destroyed the summit dome and covered eastern Mexico with ash and areas up to 6 km with surges and pyroclastic flows. The Chichón eruption resulted in about 2000 casualties and left 20,000 homeless (De la Cruz and Martin-Del Pozzo, 2009). The lack of coordinated action and the differing scientific opinions caused confusion in the authorities and population and were partly responsible for the disaster.

At least one month of shallow seismicity detected by the Comisión Federal de Electricidad at the dam nearby, preceded the Chichón eruption in 1982, but local inhabitants mentioned small quakes up to one year before. Episodes of LP swarms preceded the March 30 and April 3 eruption, and tremor intensity increased which was detected on a portable network with five MEQ-800 Sprengnether smoked-paper seismic stations set up on March, 29, 1982.

Parícutin

Parícutin was born in 1943 and erupted for 9 years producing heavy ash fall and lava flows that covered several villages nearby; Parícutin, Zirosto and San Juan Parangaricutiro had to be evacuated.

Precursory earthquakes at Parícutin Volcano occurred from January 7, 1943 until February 20, the outbreak of the eruption (Flores Covarrubias, 1945). Twenty-one volcanic earthquakes above magnitude 3 (3.2-4.5) were recorded mainly by the Weichert seismographs at the Tacubaya station in Mexico City, 320 km from the volcano. Maximum earthquake magnitudes increased before the eruption with the excerption of the first shock, and the cumulative precursory seismic energy release was very high, $2x10^{19,}$ ergs, consistent with the energy needed for the formation of a magma filled crack (Yokoyama and De la Cruz, 1990). Six months before, noises and heat marked the site where Parícutin would be born.

Discussion

The first eruptions at Popocatépetl were phreatic and turned magmatic a year later, after a 10 month cease in the eruptive activity. The first eruptions were preceded by increases in the seismicity and chemical changes in the crater lake and spring water, as well as in the fumarolic activity several years before, slowly leading up to the eruption. Shortly before the eruption began, these monitoring parameters went up again and decreased shortly before, associated with increased fracturing and degassing and later relaxation. From April 1996 on, dome formation and Vulcanian eruptions were also preceded by LP and VT events. Juvenile ejecta was detected one week before the appearance of the first dome and the rising F concentration in the leachates was attributed to a heating up of the system. The larger events such as the ones in 1997 and 2000-2001 were also preceded by an accelerated rate of seismic energy release. Especially high amplitude harmonic tremor preceded and accompanied the activity in December 2000 which resulted in the large crater dome and ash emission. Preceding this activity, increased seismicity was correlated with negative magnetic anomalies, rising SO_2 flux and radon in the soil, two months before, although seismicity escalated a few days before the eruptions. The largest eruption on January 22, 2001 produced pyroclastic flows and associated lahars that reached one km from the nearest town.

Before the eruption began, the stress induced by the ascending magma caused fracturing and opening of passageways which is reflected in VT behavior and resulted in eruption. The acceleration rate of the cumulative seismic energy release was slow possibly because of the successive magmatic batches that could not make their way through until December 1994. In andesitic volcanoes eruptions can occur when the cumulative seismic energy release is $\approx 10^{10\text{-}11}$ (Yokoyama, 1988). Pathways are obstructed and later cleared by increasing pressure from the degassing incoming magma. These explosions allow new lava to make its way up and form domes. The negative magnetic anomalies correlated with episodes of harmonic tremor that precede dome formation by several days are linked to ascent of magma batches.

Seismicity which precedes eruptions is of 3 basic types: long period events that are related to degassing-pressure induced disruption, vulcanotectonic events linked to brittle failure and fracturing and harmonic tremor which in many cases, as in Popocatépetl, is associated with underground movement magma. Decreasing pH can be due to dissolution of acid volcanic gases that mixes with the spring water.

Seismicity occurs in 2 areas below the crater and to the southeast. Low velocity zones and attenuation indicate there are pockets of magma at about 6-8 km bsl (Novelo-Casanova and Martínez Bringas, 2005; Berger *et al*., 2011). The Popocatépetl mafic magma crystallizes near the Moho and mixes with a more evolved component at depths of between 4 and 13 km (Straub and Martin-Del Pozzo, 2001). Espíndola *et al*. (2004) proposed a cylindrical magmatic body with a 3 km radius buried 11 km under the volcano. Chouet *et al*. (2005), found that the source of the mild Vulcanian eruptions at Popocatépetl in April and May 2000 was 1500 m below the crater and modeled it as a sill with a 10° easterly dip intersecting a northeast striking dike dipping 83°northwest, consistent with the opening of pathways and release of volcanic gases.

The real time seismic amplitude measurement (RSAM) analyses are the main forecasting tool, but understanding the different magmatic phenomenon and their timing is essential for the correct assessment of the situation. Some volcanic predictions have been based on the hyperbolic fits to the VT cumulative seismic

energy release (Tokarev, 1963; De la Cruz *et al*., 2008) and time predictable loading-discharge process for large tremor episodes (Valdes *et al*., 2001).Times of increased probability (TIPS) were estimated by Novelo- Casanova and Valdez-Gonzalez (2008) for seismicity from 1995-2005 who gave a retrospective predictions for the June 30 eruption, January 22, 2002 and September 4, 2002 eruptions. A seismic cluster occurred under their algorithm conditions a few days or weeks before the eruption.

Conclusions

Phreatic to magmatic, explosive and effusive dome activity throughout 17 years has given vulcanologists a chance to study the different processes and their precursors.

Considerable advances have been made in understanding how Popocatépetl works. Magma ascent and eruptive precursors are now recognized by harmonic tremor episodes, some LP events and negative magnetic anomalies, but there are still questions that need to be addressed such as constraining the timing of the different phenomena, quantifying the thresholds of specific types of activity such as for a Plinian eruption and especially how activity would escalate.

Multiparameter studies where the seismic, magnetic and chemical data are integrated and evaluated in real time is fundamental for adequate forecasting.

At Popocatépetl, several of the eruptions were expected beforehand because of the increasing VTs and LPs and changes in water and soil chemistry. Dome forming episodes were also detected due to the seismic, chemical and magnetic changes before the eruptions. Precursors occurred several months to a few days before the eruptions.

Volcano forecasting has been a success where people were saved because the eruption was predicted and they were evacuated in time. Precursors that lead to a clear assessment of the situation with a coordinated response can help mitigate a volcanic crisis, but is possible only if the monitoring network is well equipped and maintained and timely analyses are carried out.

Acknowlegements

The author would like to thank DGAPA-PAPIIT, Yuri Taran and Servando de la Cruz for their helpful suggestions and CENAPRED (Enrique Guevara, Carlos Gutierrez, Ramón Espinasa and Gilberto Castelan) for kindly helping with some of the figures. I am especially grateful to Alan Rodríguez who diligently helped classify the information as well as to Amiel Nieto and Andrés Salinas Omassi for redrafting. The Archivo General de la Nación allowed us to use unpublished documents.

Bibliography

Acosta J., 1590, Historia natural y moral de las Indias. Fondo de Cultura Económica, México-Buenos Aires, 247 pp.

Alcalá y Mendiola M., 1664, Descripción en bosquejo de la imperial cesárea, muy noble y muy leal ciudad de Puebla de los Ángeles. Benemérita Universidad Autónoma de Puebla, México, 299 pp.

Alcaraz A., Cardoso M.C.T., 1969, Lake Taal. *Comvol. Lett.*, 3, 4, 1-4.

Alvarado-Tezozómoc F., 1609, Crónica Mexicayotl. UNAM, México, 187 pp.

Anders F., Jansen M., Reyes García L., 1992, Origen e historia de los reyes mixtecos: libro explicativo del llamado Códice Vindobonensis. Fondo de Cultura Económica, México, 258 pp.

Arámbula-Mendoza R., Valdés González C., Martínez Bringas A., 2010, Temporal and spatial variation of the stress state of Popocatépetl Volcano, Mexico. *J. Volcanol. Geotherm. Res*., 196, 156-168.

Arana Salinas L., Siebe C., Macías J.L., 2010, Dynamics of the ca. 4965 yr ^{14}C BP "Ochre Pumice" Plinian eruption of Popocatépetl Volcano México. *J. Volcanol. Geotherm. Res.*, 192, 212-231.

Archivo General de la Nación, 1792. Padrones archives, 12.

Arciniega Ceballos A., Valdés González C., Dawson P., 2000, Temporal and spectral characteristics of seismicity observed at Popocatépetl Volcano, central Mexico. *J. Volcanol. Geotherm. Res*., 102, 207-216.

Arciniega Ceballos A., Chouet B., Dawson P., Asch G., 2008, Broadband seismic measurements of degassing activity associated with lava effusion at Popocatépetl Volcano, Mexico. *J. Volcanol. Geotherm. Res*., 170, 12-23.

Armienta M.A., Martin Del Pozzo A.L., Espinasa R., Cruz O., Ceniceros N., Aguayo A., Ramos E., Butron M.A., 1998, Geochemistry of ash leachates during the 1994–1996 activity of Popocatépetl Volcano. *Applied Geochemistry*, 13, 7, 841-850.

Armienta M.A., De la Cruz Reyna S., Macías J.L., 2000, Chemical Characteristics of the Crater Lakes of Popocatépetl, El Chichón and Nevado de Toluca Volcanoes, México. *J. Volcanol. Geotherm. Res*., 97, 105-125.

Armienta M.A., Varley N., Ramos E., 2002, Radon and chemical monitoring at Popocatépetl volcano. *Geofísica Internacional*, 41, 271-276.

Armienta M.A., De la Cruz Reyna S., Gómez A., Ramos E., Ceniceros N., Cruz O., Aguayo A., Martínez A., 2008, Hydrogeochemical indicators of the Popocatépetl Volcano activity. *J. Volcanol. Geotherm. Res.*, 170, 35-50.

Armienta M.A., De la Cruz Reyna S., Soler A., Cruz O., Ceniceros N., Aguayo A., 2010, Chemistry of Ash-Leachates to Monitor Volcanic Activity: An application to Popocatépetl Volcano, central Mexico. *Applied Geochemistry*, 25, 1198-1205.

Berger P., Got J.L., Valdés González C., Monteiller V., 2011, Seismic tomography at Popocatépetl volcano, Mexico. *J. Volcanol. Geotherm. Res*., 200, 234-244.

Cabral Cano E., Correa Mora F., Meertens C., 2008, Deformation of Popocatépetl Volcano using GPS: Regional geodynamic context and constraints on its magma chamber. *J. Volcanol. Geotherm. Res.,* 170, 24–34.

Camacho H., 1925, Apuntes acerca de la actividad actual del Popocatépetl en relación a la sismología. *Anales del Instituto Geológico de México*, 2, 1, 38-48.

Chimalpain C., 1612, Relaciones originales de Chalco Amaquemecan. Fondo de Cultura Económica, México, 363 pp.

Chouet B.A., 1996, Long-period volcano seismicity: its source and use in eruption forecasting. *Nature*, 380, 309-316.

Chouet B.A., Dawson P., Arcienega A., 2005, Source mechanism of Vulcanian degassing at Popocatépetl Volcano, Mexico, determined from waveform inversions of very long periods signals. *J. of Geoph. Res*., 110, 1-20.

Códice Franciscano, 1889, Siglo XVI. Nueva colección de documentos para la historia de México. Imprenta de Francisco Díaz de León, México, 307 pp.

De la Cruz Reyna, S., Quezada, J. L., Peña, C., Zepeda, O., Sánchez, T., 1995a, Historia de la actividad reciente del Popocatépetl (1354-1995). Volcán Popocatépetl, estudios realizados durante la crisis de 1994-1995, CENAPRED-UNAM, México, 3-22.

De la Cruz Reyna, S., Nolasco, H., Ramos, E., Degollado, J.L., Castillo, F.J., Velásquez, C., Medrano, A., González, H., Romero, H., Castellanos, D.A., 1995b, La Red Geodésica del Volcán Popocatepetl para el Monitoreo de la Actividad Volcánica. Volcán Popocatépetl, estudios realizados durante la crisis de 1994-1995, CENAPRED-UNAM, México, 167-192.

De la Cruz Reyna S., Tilling R.I., 2008, Scientific and public responses to the ongoing volcanic crisis at Popocatépetl Volcano, Mexico: Importance of an effective hazards-warning system. *J. Volcanol. Geotherm. Res.,* 170, 121–134.

De la Cruz Reyna S., Yokoyama I., Martínez Bringas A., Ramos E., 2008, Precursory seismicity of the 1994 eruption of Popocatépetl Volcano, Central Mexico. *Bull. Volcanol.*, 70, 753–767.

De la Cruz Reyna S., Martin Del Pozzo A.L., 2009, The 1982 eruption of El Chichón Volcano, Mexico: eye-witness perspectives of the disaster. *Geofísica Internacional*, 48, 1, 21-31.

De la Cruz Reyna S., Tárraga M., Ortiz R., Martínez Bringas A., 2010, Tectonic earthquakes triggering volcanic seismicity and eruptions: Case studies at Tungurahua and Popocatépetl volcanoes. *J. Volcanol. Geotherm., Res*., 193, 37-48.

De la Rosa-Moreno F., Valdéz González C. M., Gutierrez Martínez C. A., 2003, Análisis de patrones sísmicos asociados a algunas explosiones y emisiones de ceniza importantes del volcán Popocatépetl, México. *Revista Geofísica*, 58, 97-134.

Delgado Granados H., Cárdenas González L., Piedad Sánchez N., 2001, Sulfur dioxide emissions from Popocatépetl Volcano (Mexico): case study of high-emission rate, passively degassing erupting volcano. *J. Volcanol. Geotherm., Res.,* 108, 107–120.

Díaz del Castillo B., 1575, Historia verdadera de la conquista de la Nueva España, Porrúa, México, 700 pp.

Espinasa R., Martin Del Pozzo A.L., 2006, Morphostratigraphic Evolution of Popocatépetl Volcano. *Geol. Soc. America Special Paper*, 402, 115-137.

Espíndola J. M., Macías J. L., Tilling R. I., Sheridan M. F., 2000, Volcanic history of El Chichón Volcano (Chiapas, Mexico) during the

Holocene, and its impacts on human activity. *Bull. Volcanol.,* 62, 2, 90-104.

Espíndola J.M., Godinez M.L., Espíndola V.H., 2004, Models of Ground Deformation and Eruption Magnitude from a Deep Source at Popocatépetl Volcano, Central Mexico. *Natural Hazards*, 31, 191–207.

Espíndola J.M., Zamora Camacho A., Jiménez Z., 2005, Earthquake families in the seismicity of Popocatépetl Volcano. *Geofísica Internacional*, 44, 2, 169-176.

Fischer T.P., Morrissey M.M., Calvache V.M.L., Gómez M.D., Torres C.R., Stix J., Williams S.N., 1994, Correlations between SO_2 flux and long-period seismicity at Galeras volcano. *Nature,* 368, 135-137.

Flores Covarrubias, L., 1945, Interpretación del fenómeno volcánico a la luz de la sismología. *El Paricutín, Estado de Michoacán*, UNAM, Inst. de Geología, México, p. 41-58.

Fonseca R., Martin Del Pozzo A.L., 2010, Ash-fall hazard from a Plinian Eruption at Colima Volcano, Mexico. *Annals of Geophysics*, 53, 4, 1-15.

Gómez García L. E., Salazar Exaire C., Stefanón López M. E., 2000, Anales del barrio de San Juan del Río. Crónica indígena de la ciudad de Puebla, siglo XVII, Joaquín Alexo Meabe (transcription and translation XVIII). Instituto de Ciencias Sociales y Humanidades-Benemerita Universidad Autónoma de Puebla, México, 127 pp.

González Pomposo G., Martin Del Pozzo A.L., Panohaya Analco J., de Gante J., 1993, Estudio de la sismicidad y deformación del Volcán de Colima durante la crisis de Abril, 1991. *Geofísica Internacional,* 32, 4, 671-682.

Hirabashi J., Ossaka J., Ozawa T., 1982, Relationship between volcanic activity and chemical composition of volcanic gases: A case study on the Sakurajuma Volcano. *Geochemical Journal*, 16, 11-21.

Humboldt, A., 1811, Ensayo político sobre el reino de la Nueva España. Porrúa Ed.2004, México, 700 pp.

Inguaggiato S., Martin Del Pozzo A. L., Aguayo A., Capasso G., Favara R., 2004, Isotopic, chemical and disolved gas constraints on spring wáter from Popocatepet volcano (Mexico): evidence of gas-water interaction between magmatic component and shallow fluids. *J. Volcanol. Geotherm. Res*., 141, 91-108.

Ivanov B.V., Flrerov G.B., Masurenkov Y.P,, Kirianov V.Y., Melekestev I.V., Taran Y.A., Ovsyannikov A.A., 1996, The 1991 eruption of Avacha Volcano: Dynamics and the Composition of Eruptive Products. *Volc. Seis.*, 17, 369-394.

Kotsarenko A., Grimalsky V., Pérez E. R., Yutsis V., Koshevaya S., López C. J. A., Valdez-González C., Villegas C. R. A., 2008, Geomagnetic anomalies observed at volcano Popocatepetl, Mexico. *Adv. Geosci*, 14, 21-24.

López de Gomará F., 1552, Historia de las Indias y conquista de México. Condumex, México, 1,502 pp.

López Loera H., Urrutia-Fucugauchi J., 2003, Variaciones Vulcano-magnéticas en el volcán de Colima, México. *Revista Geofísica*, 58, 57-79.

Macias J.L., Carrasco G., Delgado H., Martin Del Pozzo A.L., Siebe C., 1995, Mapa de Peligros del Volcán Popocatépetl. *IGF-UNAM*.

Martin-Del Pozzo. A.L., Sheridan M., Barrera D., Lugo Hubp J., Vazquez L., 1995, Potential Hazards at Colima Volcano, Mexico. *Geofísica Internacional*, 34, 4, 363-376.

Martin-Del Pozzo A.L., Cordova C., Lopez J., 1997, Volcanic Impact on the Basin of Mexico during the Holocene. *Quatern. Intern*., 43, 181-224.

Martin-Del Pozzo A.L., Aceves F., Inguaggiato S, Saenz H., Aguayo A., 2002a, Spring Water and CO_2 interaction at Popocatepetl Volcano Mexico. *Geofísica Internacional*, 41, 3, 345-351.

Martin-Del Pozzo A.L., Aceves F., Espinasa R., Aguayo A., Butron M.A., Inguaggiato S., Morales, Cienfuegos E., 2002b, Influence of Volcanic Activity on Spring water at Popocatépetl Volcano, Mexico. *Chemical Geology*, 190, 207-229.

Martin-Del Pozzo A.L., Cabral E., Cifuentes G., Garcia E., Sanchez Rubio G., Reyes M., Arango C., 2002c, Volcanomagnetic signals during the Recent Popocatépetl eruptions and their correlation with eruptive activity. *J. Volcanol. Geotherm. Res.*, 113, 415-428.

Martin-Del Pozzo A.L., Cifuentes G., Cabral E., Bonifaz R., Correa F., Mendiola F., 2003, Timing Magma Ascent at Popocatépetl Volcano, México, 2000-2001. *J. Volcanol. Geotherm. Res*., 125, 107-120.

Martin-Del Pozzo A.L., Cifuentes G., Gonzalez E., Martínez A., Mendiola F., 2008a, Magnetic signatures associated with magma ascent and stagnation at Popocatépetl Volcano, Mexico during 2006. *Geological Society of London Bull.*, 304, 117-131.

Martin-Del Pozzo A.L., Gonzalez Moran T., Espinasa Pereña R., Butron M.A., 2008b, Characterization of the Recent Ash Emissions at Popocatépetl Volcano, Mexico. *J. Volcanol. Geotherm. Res.*, 170, 61-75.

Mooser F., 1967, Tefracronologia de la Cuenca de México para los úlltimos treinta mil años. *Boletín INAH*, 30, 12-15.

Murillo, G. (Dr. Atl), 1939, La actividad del Popocatépetl: Volcanes de México. Polis, México, 75 pp.

Murray J.B., Ramírez Ruiz J.J., 2002, Long-term predictions of the time of eruptions using remote distance measurement at Volcán de Colima, Mexico. *J. Volcanol. Geotherm. Res.,* 117, 79-89.

Novelo-Casanova D., Martínez Bringas A., 2005, A seismic attenuation zone below Popocatépetl volcano inferred from coda waves of local earthquakes. *Geofísica Internacional*, 44, 2, 177-186.

Novelo-Casanova D., Valdes-Gonzalez C., 2008, Seismic pattern recognition techniques to predict large eruptions at the Popocatepetl Mexico, volcano. *J. Volcanol. Geotherm. Res.*, 176, 583-590.

Panohaya-Analco J. 1991, Mediciones Geodésicas para detectar Deformaciones en el Popocatépetl. Facultad de Ingenieria. Benemérita Universidad Autónoma de Puebla. Tesis. 39pp.

Reyes-Davila G. A., De la Cruz-Reyna S., 2002, Experience in the short-term eruption forecasting at Volcán de Colima, México, and public response to forecasts. *J. Volcanol. Geotherm. Res.,* 117, 121-127.

Saucedo R., Macías J.L., Bursik M.L., 2002, Emplacement of pyroclastic flows during the 1998-1999 eruption of Volcán de Colima, México. *J. Volcanol. Geotherm. Res.*, 117, 1-2, 129-153.

Saucedo R., Macías J.L., Gavilanes J.C., Arce J.L., Komorawski C., Gardner J.E., Valdez-Moreno G., 2010, Eyewitness, stratigraphy, chemistry and eruptive dynamics of the 1913 Plinian eruption of Volcán de Colima, México. *J. Volcanol. Geotherm. Res.*, 191, 149-166.

Seele E., 1973, Restos de milpas y poblaciones prehispánicas cerca de San Buenaventura Nealtican, Puebla. *Comunicaciones,* 7, 77–86.

Segovia N., Armienta M.A., Seidel J.L., Monnin M., Peña P., López B., Mena M., Valdés C., Tamez E., López R.N., Aranda P., 2002, Radon in soil and chemical composition of spring water near the Popocatépetl Volcano. *Geofísica Internacional*, 41, 399-405.

Segovia N., Peña P., Valdés C., Armienta M.A., López M.B.E., Cisniega G., Mena M., 2005, Radon, water chemistry and pollution check by volatile organic compounds in springs around Popocatépetl Volcano, Mexico. *Annals of Geophysics*, 48, 1, 85-91.

Siebe, C., Abrams M., Macías, J. L., 1995, Derrumbes gigantes, depósitos de avalancha de escombros y edad actual del cono del Volcán Popocatépetl. Volcán Popocatépetl, estudios realizados durante la crisis de 1994-1995, CENAPRED-UNAM, México, 339 pp.

Siebe C., Abrams M., Macías J.L., Obenholzner J., 1996, Repeated volcanic disasters in Prehispanic time at Popocatépetl, central Mexico: Past key to the future?. *Geology*, 24, 5, 399-402.

Stoiber R.E., Williams S.N., Malinconico L.L., 1980, Mount St. Helens, Washington, 1980 volcanic eruption: magmatic gas component during the first 16 days. *Science*, 208, 1258-1259.

Stoiber R.E., Williams S.N., 1990, Monitoring active volcanoes and mitigating volcanic hazards: the case for including simple approaches. *J. Volcanol. Geotherm., Res*., 42, 129-149.

Straub S., Martin Del Pozzo A.L., 2001, The Significance of phenocryst diversity in tephra from recent eruptions at Popocatépetl Volcano. *Contrib. Min and Petrol.*, 140, 487-510.

Taran Y.A., Bernard A., Gavilanes J.C., Cortes A., 2002, Chemical and isotopic composition of fumarolic gases and the SO_2 flux from Volcán de Colima, México, between the 1994 and 1998 eruptions. *J. Volcanol. Geotherm. Res.*, 117, 105-119.

Torquemada, J., 1615, Monarquía indiana. De los veinte y un libros rituales y monarquía indiana, con el origen y guerras de los indios occidentales de sus poblazones, conversión y otras cosas maravillosas de la mesma tierras, UNAM, México, ed.1983, 442 p.

Tokarev P.I., 1963. On a possibility of forecasting Bezymianny volcano eruptions according to seismic data. *Bull. Volcanol.*, 26, 379–386.

Uruñuela G., Plunket P., 1998, Preclassic household patterns preserved under volcanic ash at Tetimpa, Puebla. *Latin American Antiquity,* 9, 4, 287–309.

Valdés C., González G., Arciniega A., Guzmán M., Nava E., Gutiérrez C., Santoyo M., 1995, Sismicidad del Volcán Popocatépetl a partir del 21 de diciembre de 1994 al 30 de marzo de 1995. Volcán Popocatépetl, estudios realizados durante la crisis de 1994-1995. CENAPRED-UNAM, México, 129-138.

Valdés, C., De la Cruz Reyna, S., Martínez, A., Quaas, R., Guevara, E., 2001, Resumen de la actividad del volcán Popocatépetl de diciembre 1994 a mayo 2001. Las cenizas volcánicas del Popocatépetl y sus efectos para la aeronavegación e infraestructura aeroportuaria. CENAPRED, México, D.F., 3-20.

Vetancurt, A., 1697, Teatro mexicano. Descripción breve de los sucesos ejemplares históricos y religiosos del nuevo mundo de las Indias y crónica de la provincia del santo evangelio de México. Porrúa, México, 224 pp.

Villarreal M., 1995, Estudios de Deformacion del Popocatepetl. Licenciatura en Ingenieria Geodesica. Facultad. de Ingeniería. UNAM.50pp.

Wolfe, E.W., Hoblitt, R.P., 1996, Overview of the eruptions, Fire and mud: Eruptions and lahars of Mount Pinatubo, Philippines. Newhall C.G., Punongbayan R. S., University of Washington Press, 3-20.

Yokoyama I., 1988, Seismic energy relases from volcanoes. *Bull. Vulcanol.,* 50, 1-13.

Yokoyama I., De la Cruz Reyna S., 1990, Precursory earthquakes of the 1943 eruption of Paricutin volcano, Michoacán, Mexico. *J. Volcanol. Geotherm. Res.,* 44, 265- 281.

Zlotnicki J., Bof M., 1998, Volcanomagnetic signals associated with the quasi-continuous activity of andesitic Merapi volcano, Indonesia: 1990-1995. *Phys. Earth Planet Inter.,* 105, 119-130.

Zobin V.M., Luhr J.F., Taran Y.A., Breton M., Cortes A., De La Cruz Reyna S., Domínguez T., Galindo I., Gavilanes J.C., Muñiz J.J., Navarro C., Ramírez J.J., Reyes G.A., Ursua M., Velasco J., Alatorre E., Santiago H., 2002, Overview of the 1997-2000 activity of Volcán de Colima, Mexico. *J. Volcanol. Geotherm. Res*., 117, 1-19.